Friedrich-Alexander-Universität
Faculty of Sciences

Dissertation

2025

Katrin Streil

A Comprehensive Study of the Galactic Centre with H.E.S.S.: Systematic Uncertainties, Diffuse Emission and WIMP Annihilation

A Comprehensive Study of the Galactic Centre with H.E.S.S.: Systematic Uncertainties, Diffuse Emission and WIMP Annihilation

Umfassende Untersuchung des Galaktischen Zentrums mit H.E.S.S.: Systematische Unsicherheiten, Diffuse Emission und WIMP-Annihilation

Der Naturwissenschaftlichen Fakultät
der Friedrich-Alexander-Universität Erlangen-Nürnberg
zur Erlangung des Doktorgrades Dr. rer. nat.

Vorgelegt von
Katrin Streil
aus Augsburg

Abstract

The Galactic Centre contains multiple astrophysical objects, representing a promising region for the study of the most extreme accelerators and physics beyond the standard model. The region hosts a supermassive black hole, which is surrounded by dense gas clouds known as the central molecular zone. It has been proposed that the region harbours a source capable of accelerating cosmic rays to ultra high energies, which is known as a PeVatron. The accelerated cosmic rays diffuse and interact with the particles in the central molecular zone, resulting in γ rays detectable on Earth. Moreover, the Galactic Centre is a prime target for searches for Dark Matter, given its anticipated high concentration. The indirect detection of Dark Matter particles may be achieved through the annihilation of these particles, which could result in the production of γ rays. The aim of this thesis is to examine the spectral characteristics of the proposed PeVatron and to identify potential evidence of Dark Matter in the Galactic Centre.

This thesis employs a three-dimensional likelihood analysis method, which addresses issues in background estimation and source disentanglement. This approach allows for the simultaneous fitting of the spatial morphology and spectral shape of all γ-ray sources within the field of view. This method is applied to data from the only operating ground-based γ-ray telescope in the southern hemisphere, the High Energy Stereoscopic System (H.E.S.S.) in Namibia. The analysis incorporates the handling of systematic uncertainties through the utilisation of priors and nuisance parameters, thereby ensuring an accurate modelling of the measured data.

The Galactic Centre has been modelled and investigated in three dimensions using the H.E.S.S. data. A comprehensive analysis of the spectral characteristics of the hypothesized PeVatron is conducted, with a particular emphasis on addressing systematic uncertainties arising from the background, telescope properties, and other γ-ray model components. A cutoff at $23.59 \pm 6.79\,\mathrm{TeV}$ with a significance of 4.77σ in the γ-ray spectrum was revealed, raising doubts about the PeVatron hypothesis as the central cosmic ray source in the Galactic Centre. The results demonstrate the advantages of the three-dimensional approach over traditional ON/OFF analysis methods, particularly in the complex and crowded region of the Galactic Centre.

Furthermore, the search for the potential presence of Dark Matter in the Galactic Centre yielded results comparable to, and in some channels even more sensitive than, those obtained from an ON/OFF analysis.

Zusammenfassung

Das galaktische Zentrum beinhaltet eine Vielzahl astrophysikalischer Objekte und stellt eine vielversprechende Region für die Untersuchung der extremsten Beschleuniger und der Physik jenseits des Standardmodells dar. Die Region enthält ein supermassereiches Schwarzes Loch, das von dichten Gaswolken umgeben ist, die als zentrale molekulare Zone bekannt ist. Vorherige Untersuchungen ergaben Hinweise darauf, dass die Region eine Quelle beherbergt, die in der Lage ist, kosmische Strahlung auf extrem hohe Energien zu beschleunigen. Solch eine Quelle wird PeVatron genannt. Die beschleunigten Protonen diffundieren und interagieren mit den Teilchen der zentralen molekularen Zone, was zu γ-Strahlung führt, die auf der Erde nachweisbar ist. Darüber hinaus ist das galaktische Zentrum ein bevorzugtes Ziel für die Suche nach Dunkler Materie, da eine hoche Konzentration in dieser Region erwartet wird. Der indirekte Nachweis von Dunkler Materie kann durch deren Annihilation erfolgen, was zur Produktion von γ-Strahlung führen könnte. Ziel dieser Arbeit ist es, die spektralen Eigenschaften des vorgeschlagenen PeVatrons zu untersuchen und mögliche Hinweise auf Dunkle Materie im galaktischen Zentrum zu identifizieren.

In dieser Arbeit wird eine dreidimensionale Likelihood-Analysemethode verwendet, die Probleme bei der Hintergrundabschätzung und dem Auseinanderhalten von Quellen angeht. Dieser Ansatz ermöglicht den gleichzeitigen Fit der räumlichen Morphologie und der spektralen Form aller Quellen innerhalb des Sichtfeldes. Diese Methode wird auf Daten des einzigen bodengebundenen γ-Strahlungsteleskops auf der Südhalbkugel, dem High Energy Stereoscopic System (H.E.S.S.) in Namibia, angewendet. Die Analyse umfasst die Behandlung systematischer Unsicherheiten durch die Verwendung von A-priori-Wahrscheinlichkeiten und Störparametern, wodurch eine genaue Modellierung der gemessenen Daten gewährleistet wird.

Das galaktische Zentrum wurde anhand der H.E.S.S.-Daten genau und detailliert in drei Dimensionen modelliert. Es wurde eine umfassende Analyse der spektralen Eigenschaften des hypothetischen PeVatrons durchgeführt, wobei ein besonderer Schwerpunkt auf die systematischen Unsicherheiten gelegt wurde, die sich aus dem Hintergrund, den Teleskopeigenschaften und anderen γ-Strahlungsmodellkomponenten ergeben. Es wurde ein Cutoff bei $23.59 \pm 6.79\,\mathrm{TeV}$ mit einer statistischen Signifikanz von 4.77σ im γ-Strahlungsspektrum aufgedeckt, der Zweifel an der PeVatron-Hypothese bezüglich der zentralen kosmischen Strahlungsquelle im galaktische Zentrum aufkommen lässt. Die Ergebnisse zeigen die Vorteile des dreidimensionalen Ansatzes gegenüber der traditionellen ON/OFF-Analyse, insbesondere in der komplexen und überfüllten Region des galaktische Zentrum.

Darüber hinaus wurde die Suche nach dem möglichen Vorhandensein von Dunkler Materie im galaktische Zentrum durchgeführt, wobei die Ergebnisse in ihrer Empfindlichkeit mit denen der ON/OFF-Analyse vergleichbar, in manchen Annihilationskanälen sogar besser, sind.

Contents

INTRODUCTION

PeVatrons with γ-ray Astronomy Over the past two decades, the VHE (very high energy, $\gtrapprox 100\,\mathrm{GeV}$) γ-ray catalogue has been expanded to encompass more than 250 sources, thereby establishing it as a powerful tool for the study of the sources of cosmic rays (CRs) [1]. These γ rays are produced via interactions of cosmic rays with interstellar gas and radiation fields, primarily through pion decay in hadronic processes, and also via Bremsstrahlung and inverse Compton scattering in the case of high-energy electrons.

As a consequence of their charge, CRs are isotropised and the information regarding their original direction is lost due to their interactions with turbulent magnetic fields. This is not the case for γ rays, however. They interact with Earth's atmosphere, resulting in the production of $e^- e^+$ pairs. These particles emit secondary photons via Bremsstrahlung, which then undergo pair production and so forth, resulting in an air shower of multiple secondary particles. The latter can be observed directly with surface arrays (SA) or water Cherenkov detectors (WCD). As an alternative approach, the Cherenkov radiation emitted by particles in the atmosphere can be detected by Imaging Atmospheric Cherenkov Telescopes (IACTs). Figure 1 illustrates the latitude and the energy range to which current operating γ-ray telescopes are sensitive: H.E.S.S., MAGIC, VERITAS, LHAASO, and HAWC. The latter two have identified more than 40 UHE (ultra high energy, $\gtrapprox 100\,\mathrm{TeV}$) sources, indicating that there is an acceleration of CRs to energies up to the PeV regime [2, 3]. The sources are designated as PeVatrons and they are closely related to a break in the CR spectrum at approximately 4 PeV, which is known as the knee. This marks the transition from Galactic to extragalactic CRs and is therefore formed by Galactic PeVatrons [4]. Additionally, the upcoming telescopes CTA and SWGO will play a crucial role in the detection and investigation of these UHE γ-ray sources (see Figure 1).
In 2016, the H.E.S.S. collaboration proposed the existence of a Galactic PeVatron in the Galactic Centre (GC) [5]. The GC is the centre of the Milky Way (MW) and is home to a supermassive black hole (SMBH), multiple supernova remnants (SNR), pulsar wind nebulae and stellar clusters. The inner region is defined as the central molecular zone (CMZ) which contains very dense gas clouds. The PeVatron in the centre injects protons into this CMZ, resulting in the production of diffuse γ rays due to the interaction with the molecules. In the spectrum of this emission as measured by H.E.S.S. no significant cutoff was found, which led to the PeVatron hypothesis. The aim of this thesis is to investigate the spectral properties of this PeVatron candidate in the GC with H.E.S.S. data. Although this has been done before, what distinguishes this work from previous studies is the method of analysis used.

Analysis Method In general, the spatial morphology or the position of a γ-ray source is modelled and the counts as a function of the energy can be extracted from a specific region resulting in the source spectrum. The isotropically arriving CRs are also producing air showers, which are measured by an IACT. This background can be estimated in the field of view (FoV)

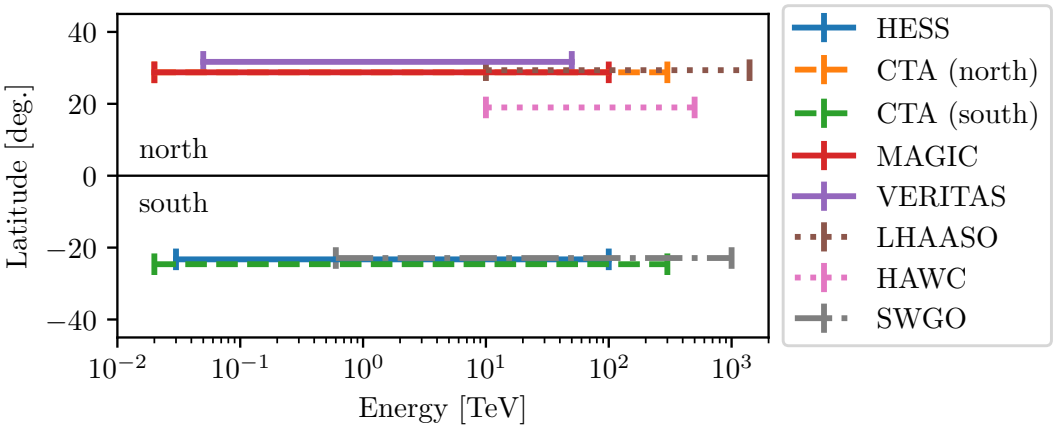

Figure 1: Energy range and latitude of operating (solid lines) and planned (dashed lines) ground-based γ-ray telescopes. Dotted lines indicate WCD and SA, while others are IACTs [6, 7, 8, 9, 10, 11, 12] .

with no γ-ray emission and subsequently be subtracted from the measured signal. However, in the complex and crowded region of the GC, it is challenging to identify these regions due to the presence of large extended sources. Additionally, the spectra of overlapping sources cannot be distinguished. Both of these issues can be addressed through a 3D likelihood analysis, which simultaneously fits the morphology or position of the sources with the spectral shape of all sources in the FoV. The template-based background is estimated from archival observations.

However, systematic uncertainties arise from both the background estimation and the detectors' response and energy scale. Both must be considered during the analysis process to ensure that the measured data are correctly modeled. This thesis focuses on the appropriate treatment of systematic uncertainties through the use of a statistically motivated approach that incorporates priors and nuisance parameters to quantify the systematic uncertainties. The method is applied to the analysis of CMZ diffuse emission and the results are compared to those previously published by H.E.S.S.

Dark Matter Search in the GC Furthermore, the GC is a key target for advancing our understanding of physics beyond the Standard Model, such as the search for Dark Matter (DM). DM is a form of matter that interacts very differently from ordinary matter. Unlike ordinary matter, DM does not interact via strong or electromagnetic forces (hence the term 'dark'). Instead, it interacts through gravity and weak interactions, albeit with a very small cross section, which makes detections challenging. It follows that the target region should exhibit exceedingly high concentrations of DM, a condition that is met by the GC. In the annihilation process of two DM particles, a pair of Standard Model particles is created, which subsequently leads to the emission of γ rays. This allows for an indirect detection of DM with γ-ray telescopes which is carried out in this thesis through the application of the 3D analysis method with a focus on incorporating systematic uncertainties through the use of nuisance parameters and priors.

Structure of the Thesis The thesis is divided into four parts. In each part a relevant theoretical introduction is given, followed by a physical analysis and a discussion of the results. Part I presents a discussion of the analysis method of fitting systematic uncertainties with

nuisance parameters and priors in γ-ray astronomy. First an introduction to ground-based γ-ray astronomy is provided, followed by the analysis methods used in the field. The use of priors is then explained, applied and verified with simulated datasets. Finally, a summary is given. The second part of the thesis presents the GC with H.E.S.S., starting with a brief overview of the GC and the H.E.S.S. dataset. Thereafter, the physical outcomes of the modelling are presented, and finally, the systematic uncertainties due to the background model are discussed. Part III analyses the diffuse emission in the CMZ in three dimensions. First, an introduction to diffuse γ-ray emission is provided, including a discussion of CRs, the γ-ray production mechanism and the CMZ. Next, a physical model of diffuse CRs and their interactions with the gas is presented, followed by a discussion of the results from fitting this model. This is followed by a discussion of the systematic uncertainties arising from telescope properties and other model components. Finally, the implications for the PeVatron hypothesis are discussed. The last part addresses the search for DM in the GC. A brief introduction to DM is given, followed by an overview of indirect searches in the GC. The results obtained in 3D with the H.E.S.S. dataset are then presented and compared to published limits. The thesis is concluded with a summary.

Part I

FITTING SYSTEMATIC UNCERTAINTIES WITH NUISANCE PARAMETERS AND PRIORS IN γ-RAY ASTRONOMY

In the field of γ-ray astronomy, the accurate modelling of observed data is crucial for the understanding and interpretation of astrophysical phenomena. However, any set of measured data will be subject to a certain degree of uncertainty. There are two principal categories of uncertainty: statistical and systematic. The former are a consequence of the Poisson statistics governing photon counts, reflecting the stochastic nature of γ-ray detection events. These are unavoidable, but they can be included in a statistical manner with relative ease. In contrast, systematic uncertainties can arise from various sources. For a γ-ray astronomy analysis, this includes instrumental effects, background estimations and atmospheric conditions, but also uncertainties in the astrophysical models. Generally, these systematic uncertainties are estimated using pseudo-experiments. In this approach, the analysis is repeated many times on simulated datasets in which key inputs such as the instrumental effects and background models are intentionally varied within their expected uncertainty ranges. This helps assess how sensitive the results are to these variations. While effective, this method can be very computationally intensive and may sometimes fail to fully capture the complexity of the real data. In this study, an alternative approach is proposed: fitting systematic uncertainties using nuisance parameters and priors. Unlike the model parameters, nuisance parameters are not of direct interest; however, their inclusion improves the accuracy of the model and enhances the reliability of the results. Prior distributions represent the prior knowledge or assumptions about the parameters before the data are analysed. Here, priors provide a quantitative description of the systematic uncertainties that can be incorporated into the analysis.

Although this approach is a common practice in other fields of particle physics (for instance ATLAS collaboration [13], multiwavelength astronomy [14]), it is not the standard approach in γ-ray astronomy. This first part of the thesis examines the methodology and applies it to γ-ray observations. Following an introduction to γ-ray astronomy, the analysis method is introduced and expanded to include nuisance parameters and priors. The method is then applied to γ-ray data from the H.E.S.S. telescope.

Chapter 1

Instrumentation and Data Reduction in Ground-based γ-ray Astronomy

γ-ray astronomy can be performed with two classes of telescopes: satellite-based detectors and ground-based detectors. The former class of telescopes is effective in detecting γ rays in the high energy range ($0.1\,\mathrm{GeV} \leq \mathrm{E}_\gamma \leq 100\,\mathrm{GeV}$) [15]. The flux of γ rays decreases extremely with increasing energy, as the spectrum follows a steep power law. The limited collection area of satellite-based telescopes is therefore insufficient for significant detection in the very high energy range (VHE, $100\,\mathrm{GeV} \leq \mathrm{E}_\gamma \leq 100\,\mathrm{TeV}$). In contrast, ground-based telescope systems can have larger detection areas since they are not restricted by the payload capacities of launch vehicles. Additionally, they can be spread on a wider area on the ground. However, the transparency of the atmosphere depends on the radiation energy. For VHE the atmosphere is opaque to γ rays, therefore, allowing only an indirect detection on the ground. This is achieved by collecting the Cherenkov light produced by the particle showers initiated by the original γ ray entering the Earth's atmosphere.

First an introction to the field of ground-based γ-ray astronomy will be given followed by a discussion of IACTs. The principle behind IACTs was initially developed by the Whipple Collaboration and is still used by today's third generation of ground-based telescopes (H.E.S.S., VERITAS, and MAGIC) [16]. Since the data used in this work are from H.E.S.S. the instrument will be discussed in the second part of this chapter.

In order to detect ultra-high energy γ rays (UHE, with energies greater than 100 TeV), even larger detection areas, FoVs, and duty cycles are required due to the ever reducing flux at higher energies. In this energy range, detector arrays which sample particles produced in air showers are in operation (HAWC, LHAASO, and the future SWGO) [17].

1.1 Introduction to Ground-based γ-ray Astronomy

γ-ray astronomy has become an essential tool for exploring the most energetic processes in the Universe. Unlike photons with longer wavelengths, γ-ray in the MeV to TeV range cannot be produced by thermal emission. Instead, their existence implies non-thermal mechanisms by which large amounts of energy are concentrated into single photons. γ-ray observations therefore provide a direct insight into environments where CRs are accelerated and interact with matter, magnetic fields or radiation [18].

The origin and the acceleration mechanisms of CRs are a long-standing questions in HE

astrophysics. Their energy spectrum shows features that indicate complex acceleration and propagation mechanisms. However, CRs do not travel in straight lines due to magnetic deflections, which obscure their sources. By contrast, γ rays travel essentially undeflected, making them ideal tracers of CR production sites.

Ground-based γ-ray astronomy began in the late 1980s with the first successful detections using IACT. Short-lived flashes of Cherenkov light produced when HE γ rays initiate air showers in the Earth's atmosphere, were observed. In 1989, the Whipple 10 m telescope provided the first unambiguous detection of a TeV γ-ray source (the Crab Nebula). This milestone established the technique's viability and paved the way for the next generation of observatories [16].

Since then, the field has advanced rapidly with major IACT arrays such as HEGRA, H.E.S.S., MAGIC and VERITAS being developed. These instruments have increased both the sensitivity and angular resolution of γ-ray observations. They have made significant contributions to Galactic astrophysics, including mapping a large population of sources, such as supernova remnants, pulsar wind nebulae, and regions of diffuse emission. These discoveries provide direct evidence for CR acceleration at various astrophysical sites [19].

In addition to identifying accelerations, γ-ray observations also facilitate the study of the transport of CRs through the interstellar medium. Extended or diffuse γ-ray emission reveals how relativistic particles propagate through the Galactic magnetic fields and interact with their surroundings [20].

Furthermore, γ-ray astronomy provides insight into several other fundamental questions, such as the search for indirect signatures of DM annihilation or decay.

In summary, ground-based γ-ray astronomy is a well-established and rapidly evolving field. By capturing the highest-energy photons from astrophysical sources, it continues to deepen our understanding of the HE universe. This thesis has two central objectives: identifying of CR acceleration sites in the GC and the search for possible γ-ray signatures of DM.

1.2 Imaging Atmospheric Cherenkov Telescopes

Air showers A high energy γ ray entering the Earth's atmosphere collides with atmospheric nuclei or molecules, resulting in the production of an e^-e^+ pair. Hereby, the nucleus is absorbing some of the momentum, ensuring that the conservation law is satisfied. This conversion of γ-ray energy into the rest mass and the kinetic energy of the two fermions is accompanied by the emission of more γ rays via Bremsstrahlung, which occurs due to the deceleration of the particles in the Coulomb field of the atmospheric nuclei. A cascading process is initiated as a result of the secondary γ rays producing new e^-e^+ pairs [20]. After traversing the radiation length of Bremsstrahlung and pair production, the number of particles on average doubles, causing a cascade of particles, known as an air shower. The secondary particle production ceases when energy losses due to ionization exceed those caused by Bremsstrahlung losses. This typically occurs at the critical energy of 84 MeV [16]. The energy of the primary γ ray, E_γ, is proportional to the number of particles created in the shower. A cascade of this nature is referred to as an electromagnetic air shower due to the underlying fundamental interaction. For incoming γ rays approaching the zenith, the maximum of the shower intensity occurs at an altitude of approximately 10 km. The projection of a simulated electromagnetic air shower is shown in Figure 1.1 (left).

Nevertheless, it is important to note that γ rays are not the only particles capable of initiating air showers in the atmosphere. High energy CRs, predominantly protons, can also initiate hadronic cascades through nucleonic interactions with atmospheric molecules. This initial

collision results in the production of charged and neutral pions and kaons. Additionally, hadronic spallation products are generated, contributing to the complex appearance of the particle shower, see Figure 1.1 (right). The mesons undergo rapid decay into other particles, including muons, which in turn result in the production of additional secondary particles. Neutral pions in the shower decay into photons, which induce an electromagnetic subshower.

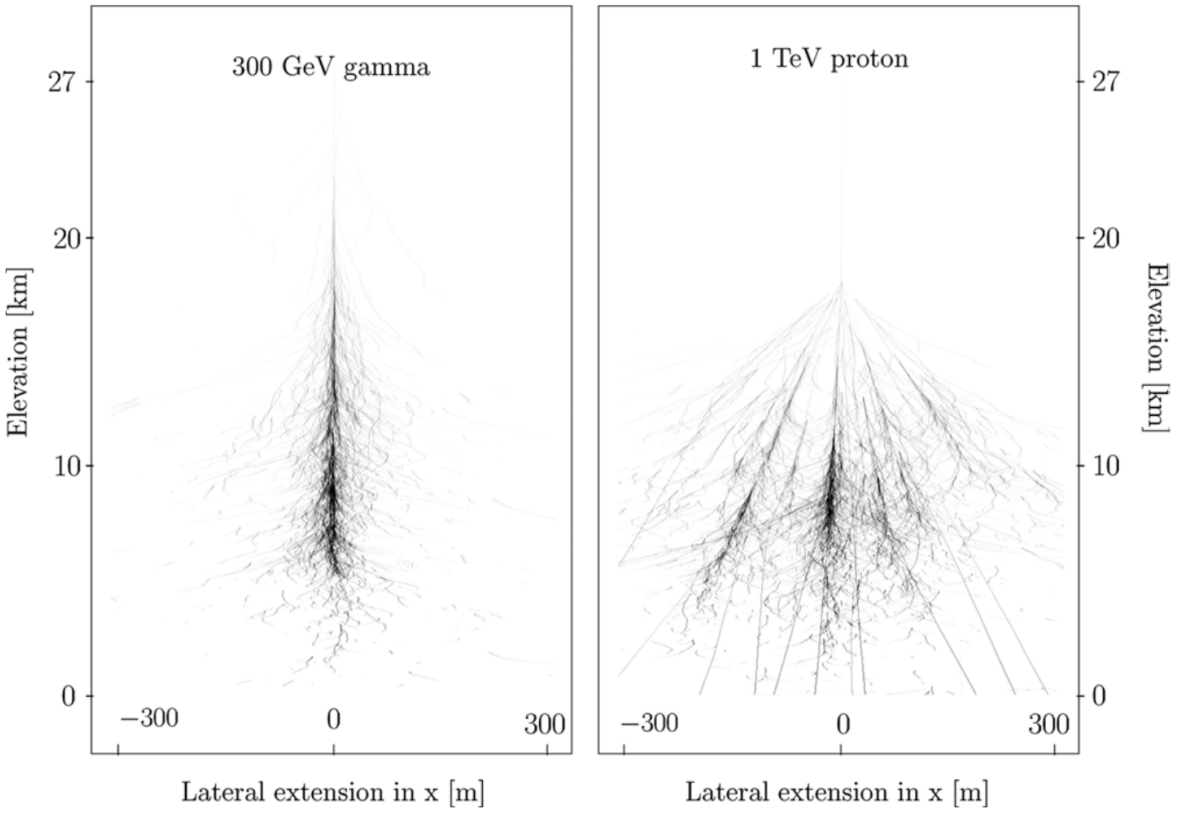

Figure 1.1: Particle tracks of a simulated air shower initiated by a 300 GeV γ ray (left) and a 1 TeV proton (right) using the Monte Carlo technique. Figure taken from [18].

Cherenkov Radiation Charged particles, which are faster than the local speed of light in the atmosphere, emit Cherenkov radiation. This radiation is emitted when a charged particle moves through a dielectric medium at a speed greater than the phase velocity of light in that medium, thereby perturbing the electromagnetic field and polarising the molecules. The polarisation of the molecules is rapidly reversed, resulting in the emission of electromagnetic waves. If the particles are faster than the local speed of light, the emission is coherent due to constructive interference of the emitted photons. The radiation forms the characteristic Cherenkov angle of approximately 1.4° in air; this results in the formation of a pool of light on the ground with a radius of approximately 125 m. In the case of a primary γ ray with an energy of 1 TeV, the Cherenkov radiation is composed of approximately 100 photons $m^{-2}s^{-1}$ in the air at sea level arriving within a few nanoseconds [16].

The Cherenkov radiation emitted by the hadronic shower is measured by a ground-based γ-ray telescope as background. However, due to their differing shapes, a pure electromagnetic shower can be distinguished from a hadronic shower. The hadronic shower has a wider lateral

distribution due to the strong interactions transferring a large transverse momentum (see Figure 1.2). It is evident that a robust γ-hadron separation and, therefore, background rejection are crucial for the performance of a ground-based γ-ray telescope, given that there are approximately 10^4 times more air showers of hadronic nature than those induced by primary γ rays. However, it is not always possible to distinguish between electromagnetic and hadronic air showers, since, under certain circumstances, such as large impact distances, they have a similar shape. Therefore, a fraction of the hadronic events remain in the data as background, which must be taken into account in the analysis.

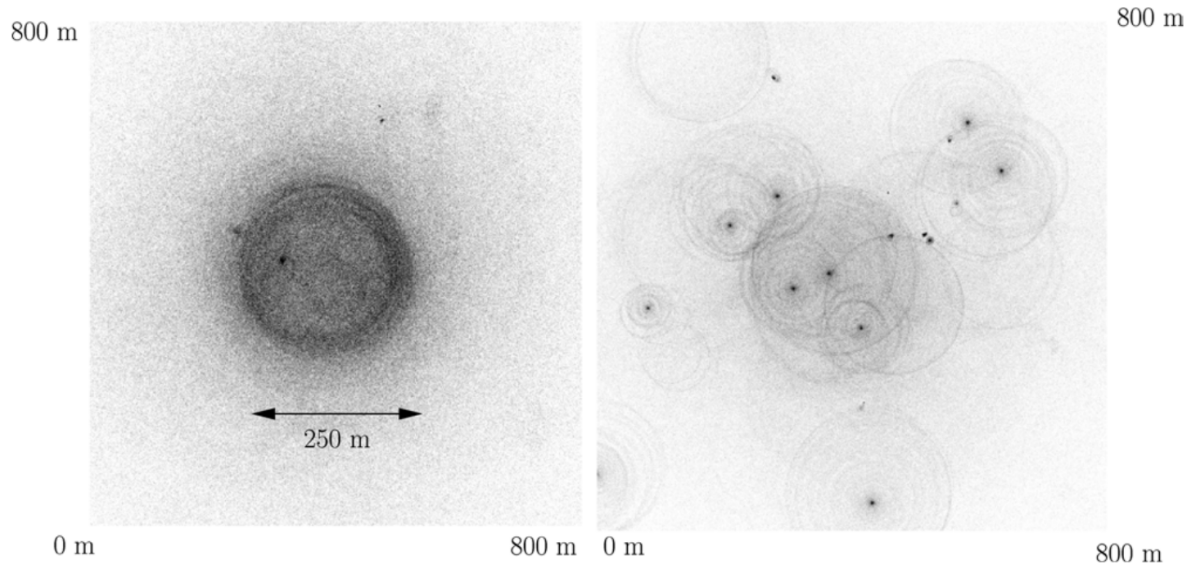

Figure 1.2: Monte Carlo simulations of the distribution of Cherenkov light on the ground from an electromagnetic air shower initiatied by a 300 GeV γ ray (left) and an hadronic air shower due to a 1 TeV proton (right)hower. Picure taken from [18].

Stereoscopic Imaging Atmospheric Cherenkov Telescopes The Cherenkov light is collected by the large mirrors of IACTs and focused on a camera. The goal is to reconstruct the arrival direction and energy of the primary particle. In order to collect a sufficient number of Cherenkov photons the mirror surface per telescope is typically $\gtrapprox 100\,\mathrm{m}^2$ [16]. The camera must provide a reasonable photon detection efficiency, clean amplification and response in the nanosecond range. Often it is composed of multiple photomultiplier tubes, which employ the photoelectric effect to convert the measured Cherenkov photons to an amplified, electrical signal. In other cases cameras based on Silicon photomulitpliers are employed.

The camera is used to capture and analyse the angular distribution of Cherenkov light. Therefore, the electromagnetic shower is visualised as an ellipse in the image of the focal plane when recorded (see Figure 1.3). The longitudinal shower development is mapped on the ellipse's major axis which coincides with the shower direction. The geometrical properties of the ellipse are used to differentiate between an electromagnetic and a hadronic air shower. Consequently, so-called Hillas parameters are defined, which are then subjected to certain cut criteria in order to perform the γ-hadron separation. Hadronic events that survive the separation process exhibit an isotropic arrival direction. Consequently, the extent of background contamination of the γ-ray

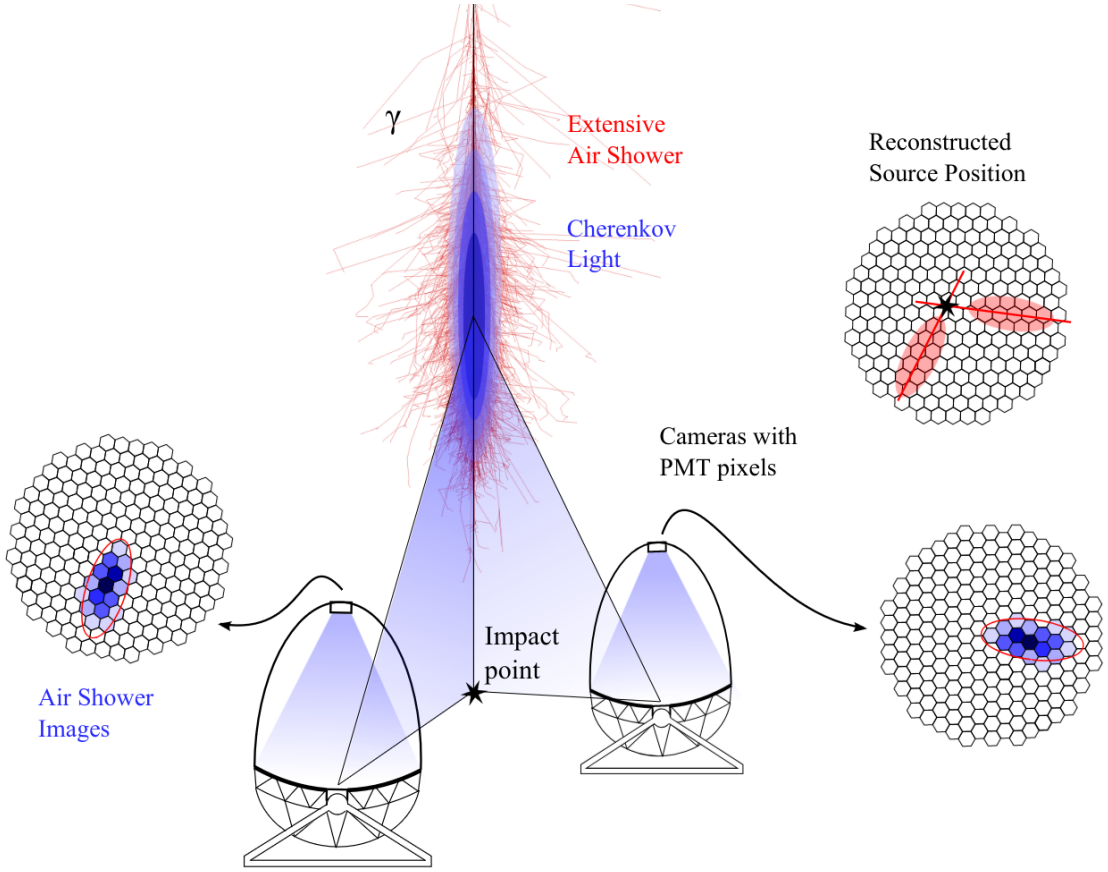

Figure 1.3: Illustration of a stereoscopic IACT. The Cherenkov light emitted by the air shower is observed by two telescopes and the source position is reconstructed by intersecting the major axes of the cleaned images. Figure taken from [21].

signals can be estimated in regions where no expected γ-ray source is present.

In order to reduce the night sky background, the IACTs only trigger if a certain number of pixels record a signal exceeding a certain discrimination threshold within a certain timeframe. This is because lower-energetic primary particles produce fewer secondary particles whose Cherenkov radiation might not be sufficient to trigger the telescope. Consequently, a lower limit on the IACTs energy range is set.

The geometric reconstruction of the shower can be enhanced by utilising multiple telescopes. This stereoscopic imaging technique involves capturing the same shower from different perspectives. The reconstruction of the direction of the primary particle is improved by intersecting the major axes computed from the single camera images. By requiring more than one telescope to trigger an event, the contamination from the night sky background can be further minimised. Consequently, the optimal spacing between the telescopes must be determined by considering the size of the Cherenkov cone to maximise the telescope array's sensitivity. The size of the cone is dependent on the energy of the primary particle and the local index of refraction, which in turn makes the optimal setup dependent on the desired energy range.

Due to their relatively small FoV, IACTs are pointing instruments and therefore provided with an altitude-azimuth mount to adjust the pointing direction quantified by the zenith angle θ

and azimuth angle ϕ . Hereby, a zenith angle of zero defines upward pointing. As the zenith angle increases (pointing towards the ground) the line-of-sight distance to the shower maximum $z_{\max}$ increases as $l_{\max} \propto z_{\max}/\cos\theta$. Therefore, the projected size and width of the shower decrease by $\cos\theta$ and the radius of the Cherenkov cone increases by a factor of $\propto 1/\cos\theta$. As a result, the intensity of the images decreases by $\cos\theta^2$. Hence, the energy threshold has to be increased by $1/\cos\theta^2$ [18].

1.3 Data Reduction

The objective is to reconstruct scientific results from the raw output of the telescope cameras. This is achieved through a data reduction process, which can be divided into five data levels (DLs) representing the common workflow of IACTs (see Figure 1.4).

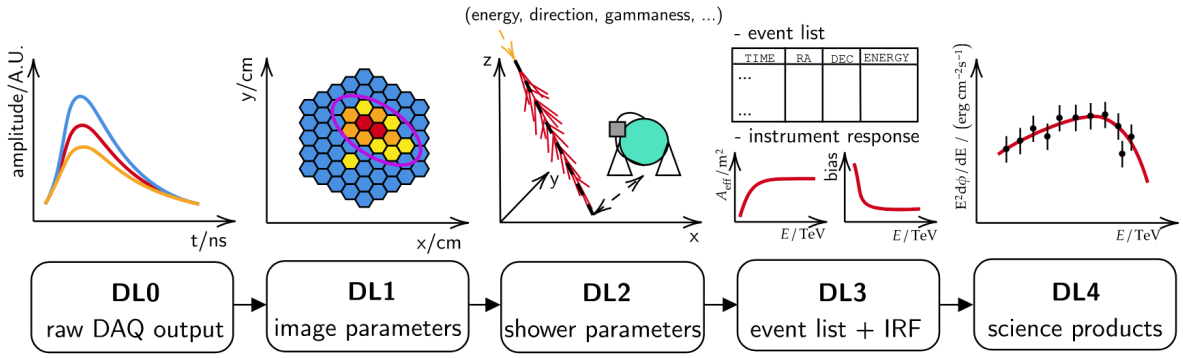

Figure 1.4: Illustration of the typical data levels for an IACT [22].

The raw signal measured by the telescope camera is designated DL0. The central trigger system is responsible for searching for coincident signals between the triggered signals from the individual telescopes. If a sufficient number of coincident signals are found, the telescope is read out. The number of telescopes triggered by an event is referred to as the multiplicity.

A single telescope is triggered if the signal brightness exceeds a certain threshold, designated as P, in a specified number of pixels, N, within a defined camera segment within a time interval of 1.5 nanoseconds. For the smaller cameras of the telescope array H.E.S.S. for instance, the read-out criterion is N = 3 pixels with a threshold of P = 5.5 photo-electrons (p.e.) [16]. Consequently, the majority of the signal that does not originate from a γ-ray event, such as the night sky background or PMT noise, is eliminated. The remaining noise is removed using the tail cut method. This process involves the rejection of pixels that do not have an amplitude of at least 5 p.e. and a next neighbour with an amplitude of 10 p.e. Conversely, pixels with an amplitude of at least 5 p.e. and a next neighbour with an amplitude of 10 p.e. are retained [16]. Note, that these values are again for the smaller telescopes of H.E.S.S. This cleaned and pixelated image corresponds to DL1.

From this image, the shower properties, including the arrival direction, are determined (DL2). The Hillas parameters are computed from the signal in the image [23]. This includes the centre of gravity, the width, length, and size of the image. Images that have been truncated, in which partial information is lost, are excluded by setting an upper cut on the distance between the centre of gravity and the camera centre. The reconstruction of very faint signals is error-prone and therefore excluded by setting a lower cut on the size of the image. The value of the cut has

an effect on the lower energy threshold.

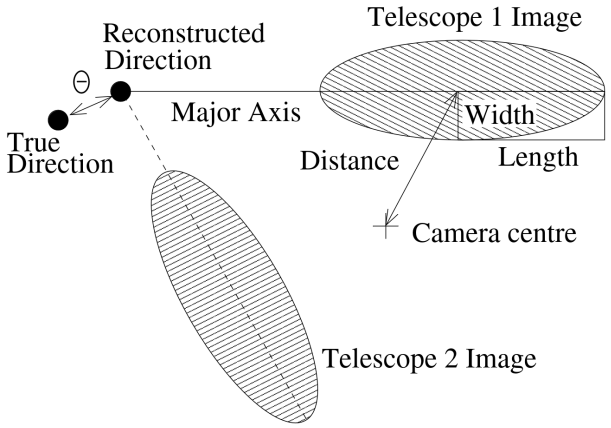

Figure 1.5: Scheme of the Hillas parameterisation of the picture of one electromagnetic air shower in two cameras. By intersecting the two major axes the direction of the primary γ ray is reconstructed. The distance to the true direction is denoted as θ [24].

Figure 1.5 illustrates the configuration of a single event observed by two cameras and the associated Hillas parameters. The point of intersection between the two major axes represents the reconstructed arrival direction of the primary particle on the ground (DL2).

In order to reconstruct the energy of primary particles, it is necessary to determine the image size and the impact distance. Hence lookup tables are created from Monte Carlo simulations of air showers and the telescope response. Since both are dependent on the zenith angle, the simulations are carried out in different zenith angle bins (from 0° to 70° as well as for different sizes and offsets from the camera centre). Furthermore, it is necessary to update the lookup tables on a regular basis due to changes in the optical efficiency over time. This is also based on Monte Carlo simulations.

The Hillas parameters are also employed to ascertain the probability that the recorded event is attributable to a γ ray as the primary particle and not a charged CR. The Hillas parameters are used by a multivariate, tree classification method, whereby multiple failed or passed criteria determine the overall signal- or background likelihood of an event. The output is the parameter ζ. Once more, Monte Carlo simulations are utilised to determine the requisite cuts to be applied to the final parameter ζ in order to achieve optimal γ-ray sensitivity [25]. There are three different sets of selection cuts, each of which is optimised for a specific analysis goal. The "standard" cuts (std) are designed for a 10% Crab source. For a 1% Crab source with a spectrum following $\sim E^{-2}$, the "hard" cuts are deemed appropriate. In the case of a source as strong as the Crab, the "loose" cuts are recommended [26].

Another reconstruction method is the Image Pixel-wise fit for Atmospheric Cherenkov Telescopes (ImPACT) [27]. This method generates expected camera images through Monte Carlo simulations of air showers with varying properties, including energy, zenith angle and impact distance. Subsequently, the image templates are then fitted pixel-wise to the observed image, with each pixel's contribution to the overall image considered. This process allows for the reconstruction of the primary particle properties (direction and energy).

Once all γ-ray events have been filtered out, the resulting information is saved in an event list, which contains the energy, time of detection, direction, and other relevant data (DL3). The telescope properties are summarised in instrument response functions (IRFs), which will be

discussed in the following section.

1.4 Instrument Response Functions

In general, IRFs are mathematical representations that are employed to relate the observed properties of γ-ray events to their true properties. Extensive Monte Carlo simulations are utilised to model the interactions of the γ rays with the Earth's atmosphere and the detection by the IACT. Given that both are highly dependent on the observation conditions (pointing direction, optical efficiency, atmospheric conditions), multiple simulations are collected in lookup tables from which the expected properties can be interpolated.

In the following text, the denotation *true* and *reco* are used to indicate whether a parameter is true or reconstructed. The IRFs comprise three components: the effective area, the energy dispersion and the point spread function (PSF).

1.4.1 Effective Area

The effective area, $A_{\text{eff}}(p_{\text{true}}, E_{\text{true}})$ of a telescope array is the collection area weighted by the detector's efficiency where p_{true} is the true position. The latter depends on the observation (pointing, atmosphere, etc.) and detector conditions (mirror reflectivity, etc.). In general, the effective area of an IACT is larger than its physical extension of the telescope, due to the large size of the Cherenkov cones. The product of the effective area and the observation time t_{obs} is the so-called exposure in terms of [m^2s]. An exemplary effective area map is shown in Figure 1.6. It is based on the publicly available dataset of the point source PKS 2155-304 observed by the H.E.S.S. collaboration [28]. The source was observed with four different pointing positions offset to the actual source position.

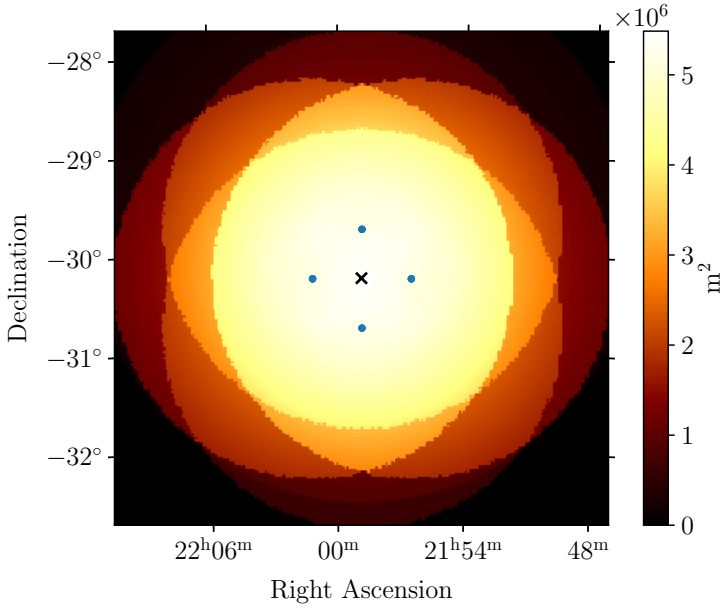

Figure 1.6: Effective area of PKS 2155-304 measured by H.E.S.S. The blue points denote the four pointing positions and the black cross the position of the source.

1.4.2 Energy Dispersion

The energy dispersion, $E_{\mathrm{disp}}(E_{\mathrm{reco}}|p_{\mathrm{true}}, E_{\mathrm{true}})$, is the probability of reconstructing an energy E_{reco} given that the true γ-ray energy is E_{true}. It can be visualised in a 2D matrix as in Figure 1.7 for the PKS 2155-304 dataset.

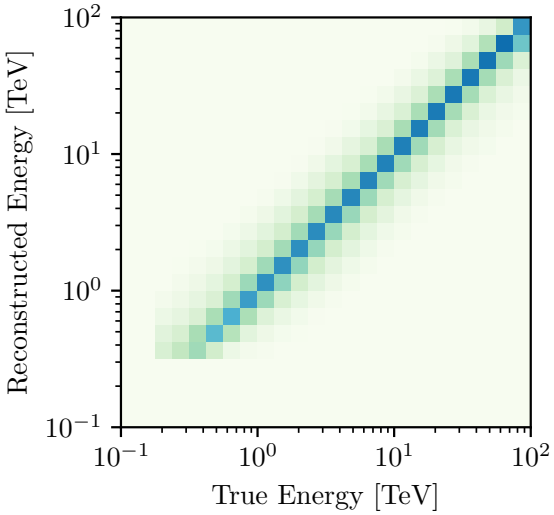

Figure 1.7: Energy dispersion matrix of the H.E.S.S. observation of PKS 2155-304.

To quantify the properties of the energy dispersion of a certain instrument or observation, the energy bias and the energy resolution can be defined. Hereby, the energy bias is:

$$\Delta E = \langle \frac{E_{\mathrm{reco}} - E_{\mathrm{true}}}{E_{\mathrm{true}}} \rangle (E_{\mathrm{true}}) \tag{1.1}$$

and the energy resolution is:

$$\delta E = \frac{\sqrt{\mathrm{Var}(E_{\mathrm{reco}})}}{E_{\mathrm{true}}} (E_{\mathrm{true}}) \tag{1.2}$$

Both quantities are computed from the energy dispersion matrix and shown in Figure 1.8.

It should be noted that the absolute value of the energy bias is the strongest at the lowest and highest energies. The reason for the former is as follows: the image sizes are subject to fluctuations, and under fluctuations do not create enough light for the telescope to be triggered. However, over fluctuations result in the telescope being triggered, leading to an overestimation of the reconstructed energy and, consequently, a higher energy bias. Conversely, for very high-energy γ rays, the reconstruction can suffer from increased uncertainty due to partial containment of the light pool or limitations in the reconstruction algorithm. Therefore, the reconstructed energy is lower than the underlying true energy, resulting in a negative bias. In order to mitigate the potential for systematic uncertainties to arise from an inaccurate reconstruction of the γ-ray energy, lower and upper energy thresholds are set on the dataset.

1.4.3 Point Spread Function

The point spread function, $\mathrm{PSF}(p_{\mathrm{reco}}|p_{\mathrm{true}}, E_{\mathrm{true}})$, is defined as the probability density of the angular separation between the true and reconstructed directions, $\theta = (p_{\mathrm{reco}} - p_{\mathrm{true}})$. The PSF

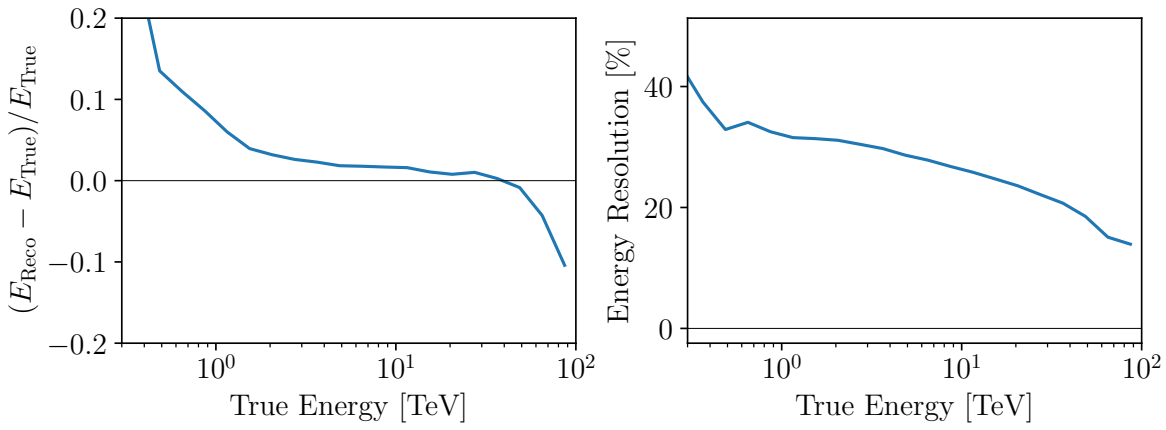

Figure 1.8: Energy bias (left) and energy resolution (right) as a function of true energy of the PKS 2155-304 dataset measured by H.E.S.S. Both quantities are computed for the energy dispersion matrix shown in Figure 1.7.

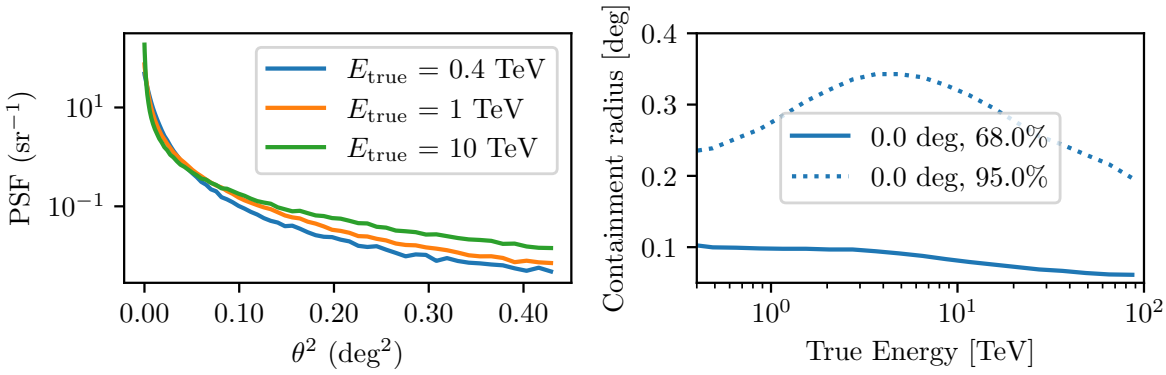

Figure 1.9: PSF of H.E.S.S. from PKS 2155-304 observations. Left panel: as a function of the squared distance between p_{true} and p_{reco} for different true energies. Right panel: 68% and the 95% Containment radii as a function of true energy at the center of the FoV.

is a function of the true energy and offset angle from the field of view centre and depends on the zenith angle. It describes how the IACT responds to a point source and thereby reflects the telescope's ability to reconstruct the image with angular resolution. Figure 1.9 (left) illustrates the PSF of the source PKS 2155-304 as measured with the H.E.S.S. telesocope array as a function of θ^2 for different true energies. By representing the angular offset as θ^2 the area covered by each sky map bin is standardised, ensuring uniformity in the measurement of the sky's solid angle. The containment radius is defined as the radius within which a certain percentage of the γ rays is measured. This quantifies the resolution of the telescope. The 68% and the 95% containment radii are presented as a function of true energy in Figure 1.9 (right). At the highest energies, the increase in containment radius is due to the broader spatial extent of the air showers, which leads to greater angular dispersion in the reconstructed directions. The precision is more accurate at the centre of the field of view (0° offset) and less so with increasing distance.

1.5 Hadronic Background

In the process of γ-hadron separation, there is a tendency for some of the hadronic air showers to be misclassified as γ-ray events. Such events remain in the data as a residual hadronic background. The background rate depends on a number of variables, including the zenith and azimuth angle of the observations, the separation technique employed and the reconstructed primary energy [29].

In order to obtain the γ-ray excess, the background must be taken into account by subtraction from the measured counts. There are two general approaches to this: the ON/OFF method, which estimates the background rate in the FoV where no γ-ray sources are expected; and the FoV background method, which estimates the background from different FoVs observed during similar observation conditions which also do not contain γ-ray sources. The former method is illustrated in Figure 1.10. In the **ON/OFF** background estimation method, regions are defined within FoV where γ-ray emission is absent (the OFF region) and present (the ON region). The number of counts within the OFF region can be subtracted from the counts within the ON region, yielding the excess counts attributed to γ-ray events. To reduce statistical errors the size of the OFF region is typically larger which must be accounted for when performing the subtraction. Since the IRFs of the telescope are radially symmetric, the OFF-and-ON regions are symmetrically located relative to the pointing direction. However, this method is only suitable for an analysis of sources with small extensions. For regions like the GC with very extended and overlapping γ-ray sources, an alternative background estimation is more appropriate.

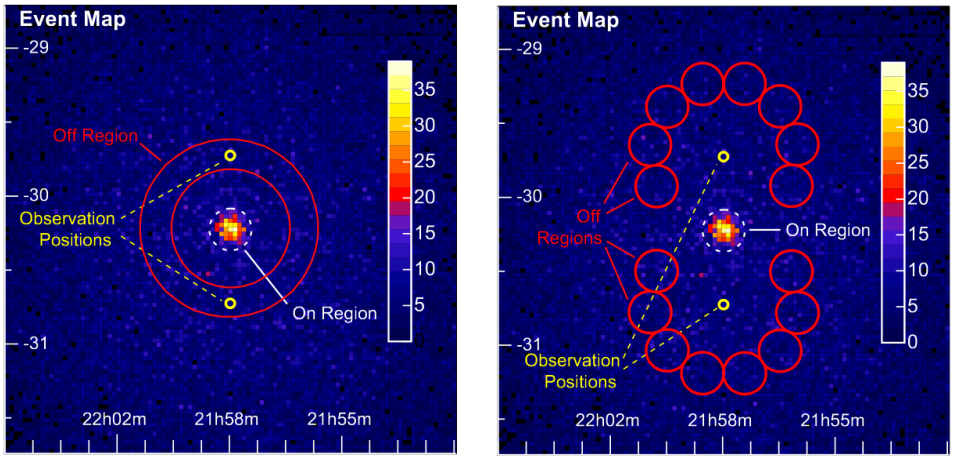

Figure 1.10: Illustration of the ring (left) and reflected (right) background estimation method. The colorbar shows the counts measured. Figure taken from [29].

The following section is based on [30]. A background estimation method suitable for complicated region of interest (ROI) is the **FoV background model**. Here, the expected background rate in the γ-ray observations is estimated from archival observations not containing any γ-ray sources and a 3D template is constructed. Since various observational parameters affect the background rate, a tailored background model for each observation is used. One dominating parameter is the zenith angle of the pointing. Accordingly, the archival observations are grouped into seven zenith bins (0°, 15°, 25°, 35°, 42.5°, 47.5°, 52.5°, 60°). The effect of the azimuth angle ϕ is weaker and thus only two bins are used ($-90° < \phi < 90°$ and $90° < \phi < 270°$). The average

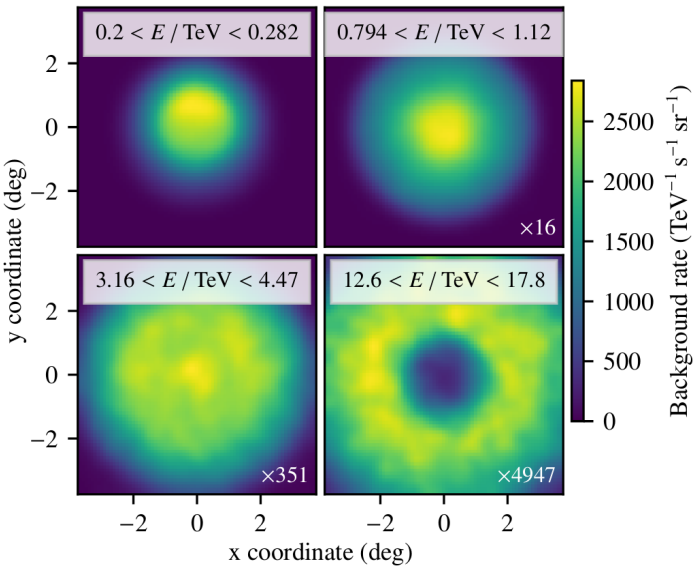

Figure 1.11: Background model in the FoV coordinate system in four different energy bins. Figure taken from [30].

background rate from all archival observations in each bin is computed, and the different pointing positions are accounted for. The result is a 3D background rate. An example of the background rate is shown in Figure 1.11. The energy binning was fixed to 20 logarithmically spaced bins between 100 GeV and 100 TeV. In newer models, the energy binning is chosen depending on the available statistics in the bin. The remaining statistical fluctuations are smoothed out.

As a quality check, the background normalization was determined for each individual observation run in every energy bin. A residual dependence on zenith angle was observed within the defined zenith bins. This effect was corrected by applying a linear interpolation across the zenith angle range.

In addition, the background model was corrected for a dependency on the transparency coefficient which quantifies the optical transparency of the atmosphere. In the case of a larger value, that is to say a more transparent atmosphere and, therefore, less absorption, the background rate increases and, therefore, the normalisation is fitted to higher values. Finally, in a last correction, varying optical efficiencies of the telescopes, for instance due to mirror degradation, are accounted for. The background model was validated for sources in the public H.E.S.S. dataset, demonstrating that the reconstruction of source parameters is feasible and comparable to the results obtained with the classical ON/OFF analysis. At low energies, limited statistics can cause fluctuations in the background estimation, which may propagate as systematic uncertainties in the reconstructed spectra. To mitigate this, a lower energy threshold must be applied. The upper edge of the energy bin containing the maximum of the predicted background rate is typically defined as the threshold.

Chapter 2

Binned Likelihood Fitting in γ-ray Astronomy

As previously stated, the FoV background model allows for a 3D analysis of the γ-ray data. The H.E.S.S. collaboration has adopted this methodology as a standard analysis method (i.e. [31], [32]). The method is based on the following principle: the measured data is reconstructed in terms of energy and position, whereas the underlying physical properties of the sources like its spectrum are in terms of true energy and position. Consequently, the detector response is applied to the theoretical models describing the true physical properties in order to predict the observed data. This forward folding by the IRFs allows a comparison between the model and the actual observations. Figure 2.1 illustrates the modelling in two dimensions. The observed excess in the H.E.S.S. Galactic Plane scan is illustrated in the upper panel, expressed in terms of the measured counts at reconstructed positions. Although the full analysis is performed in three dimensions (energy and position), the figure presents a 2D spatial projection for visualisation. The excess is modelled using a combination of multiple model components. Subsequently, the spatial shape and spectra are forward folded through the H.E.S.S. IRFs for obtaining the model prediction. The correct representation of the excess is ensured by using both single- and multi-component sources. In order to optimise the physical parameters of the source, a Poisson likelihood fit is utilised. Subsequently, the quality of the FoV description or the fit is evaluated, resulting in the generation of the residual map. Any remaining measured excess not accounted for will be clearly discernible from the overall flat residual map (Figure 2.1 lower panel).

In the majority of cases, 3D H.E.S.S. analyses employ the open-source tool *gammapy* [34]. The python-based software is capable of handling DL3 γ-ray data based on the GADF format and is facilitating a 3D analysis through the incorporation of multiple γ-ray emission models.

In the beginning of this chapter, the 3D maximum likelihood fit will be explained in more detail. Thereafter, the focus will be shifted to an examination of the nature of systematic uncertainties and the determination of parameter uncertainties.

2.1 Maximum Likelihood Estimation

The following section in based on [34]. Let us define a geometry for our data with an energy axis and a spatial grid. A single bin of this geometry is indexed by i, in the spatial and spectral dimension. The measured counts within this bin i, denoted by c_i, are observed. The predicted number of photons measured within bin i is denoted as μ_i. The measurement of γ-ray data is

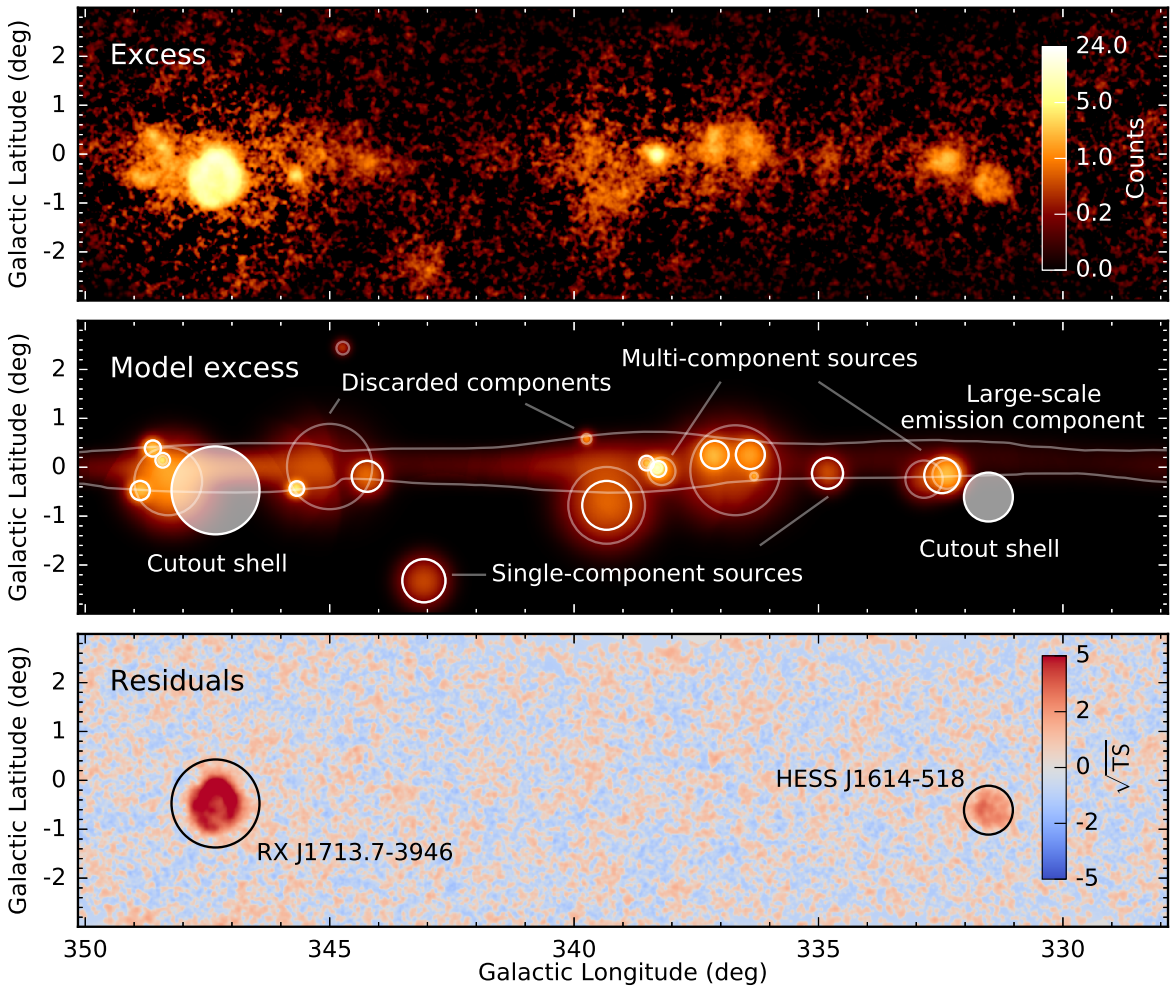

Figure 2.1: Upper panel: Morphology of the γ-ray excess as observed by H.E.S.S. along the Galactic Plane in terms of counts. Centre panel: Different model components used to describe the excess. Lower panel: Residual map computed after the excess is accounted for by the model components. The map is in terms of $\sqrt{\mathrm{TS}}$. The two sources not included in the model are clearly visible. Image has been adapted from [33].

Poisson distribution with the probability mass function given by:

$$P_i(c_i;\mu_i) = \frac{\mu_i^{c_i} e^{-\mu_i}}{c_i!} \tag{2.1}$$

The likelihood function is the probability of observing the data given a specific model. Given that the measured data in each bin follow a Poisson distribution, the likelihood function is the product of the probability mass function in each bin:

$$\mathcal{L}(c;\mu) = \prod_{i=1}^{n} P_i = \prod_{i=1}^{n} \frac{\mu_i^{c_i} e^{-\mu_i}}{c_i!}, \tag{2.2}$$

where n is the total number of bins in spatial and spectral dimensions.

Assuming that the intrinsic flux of gamma rays from the source is given by $\phi(E_{\text{true}}, p_{\text{true}}; \vec{\theta})$, where the model can be separated into a spatial and a spectral model as:

$$\phi(E_{\text{true}}, p_{\text{true}}; \vec{\theta}) = \phi_{\text{spec}}(E_{\text{true}}; \vec{\theta}_{\text{spec}}) \cdot \phi_{\text{spat}}(p_{\text{true}}; \vec{\theta}_{\text{spat}}), \tag{2.3}$$

where $\vec{\theta}$ is the set of model parameters. It should be noted that in certain instances, a distinction between the spatial and spectral model components is not feasible, particularly in the case of an energy-dependent morphology. A point source is a common spatial model, characterised by a single set of parameters, namely the source positions. Alternatively, a Gaussian spatial model may be employed, wherein both the source position and spatial extent are treated as parameters. Spectral models frequently take the form of power laws, with occasional features such as an exponential cutoff or a break. The unit of the flux model is $\text{TeV}^{-1}\text{cm}^{-2}\text{s}^{-1}$. The predicted number of signal events is calculated from the flux models by forward folding through the IRFs:

$$\begin{aligned}\mu_i(p_{\text{reco}}, E_{\text{reco}}|\vec{\theta})\ \mathrm{d}p_{\text{reco}}\ \mathrm{d}E_{\text{reco}} = E_{\text{disp}}(E_{\text{reco}}|E_{\text{true}}, p_{\text{true}}) \circledast [\text{PSF}(p_{\text{reco}}|E_{\text{true}}, p_{\text{true}}) \\ \circledast (A_{\text{eff}}(E_{\text{true}}, p_{\text{true}}) \cdot t_{\text{obs}} \cdot \phi(E_{\text{true}}, p_{\text{true}}; \vec{\theta}))]\end{aligned} \tag{2.4}$$

Inserting equation 2.4 into equation 2.2 the likelihood as a function of the model parameters is obtained: $\mathcal{L} = \mathcal{L}(\vec{\theta})$. If the number of model parameters is k, the likelihood is therefore a function defined on a k-dimensional parameter space.

The set of parameters $\hat{\vec{\theta}}_{ML}$, which best describe the data best can be found by maximising the likelihood:

$$\vec{\theta}_{ML} = \arg\max\left(\mathcal{L}(c; \vec{\theta})\right) \tag{2.5}$$

The set $\vec{\theta}_{ML}$ is called the maximum likelihood estimate of the parameters or the best-fit parameters.

In practice, one often works with the log-likelihood function rather than with the likelihood function itself:

$$-2\log\mathcal{L}(c; \mu(\vec{\theta})) = -2\sum_{i=1}^{n}\left(c_i \log\mu_i(\vec{\theta}) - \mu_i(\vec{\theta})\right), \tag{2.6}$$

Note that the constant $\log(c_i!)$ term can be omitted since it is not relevant to the optimisation process. The products of the probabilities become sums that are more straightforward to work with resulting in numerical stability and better differentiation. The factor 2 is employed to ensure that the resulting statistic follows a chi-squared distribution in the asymptotic limit of very large samples (Wilk's theorem [35]). To obtain the maximum likelihood estimate of $\vec{\theta}$, it is therefore necessary to minimise $-2\log L(c; \mu(\vec{\theta}))$:

$$\vec{\theta}_{ML} = \arg\min\left(-2\log\mathcal{L}(c; \mu(\vec{\theta}))\right) \tag{2.7}$$

When using *gammapy* to fit the model parameters, the optimisation is performed using the *iminuit* package, which provides a Python interface to the MINUIT algorithm [36, 37].

2.2 The Ratio Likelihood Test and Statistical Uncertainties

The 1σ error of a model parameter defines a confidence interval such that, under repeated identical experiments, approximately 68% of the constructed intervals would contain the true parameter value. The following section is deriving the computation of the parameter uncertainties

and is based on [38, 39]. The likelihood on its own does not quantify the goodness of fit. However, since it reflects how well a model explains the observed data, it can be compared to the likelihood computed under another model, for example using likelihood ratios. One, thereby, defines hypotheses. The so-called null hypotheses H_0 is that model M_0 which only consist of the background model and no source models describes the data best. The second hypothesis H_1 states that background model and a specific source model (M_1) describe the data best. The best maximum likelihood estimates of the model parameters are $\hat{\theta}_{0,1}$ for M_0 and M_1, respectively.

One defines the ratio of the two likelihoods:

$$\lambda(\mu) = \frac{\mathcal{L}(H_0)}{\mathcal{L}(H_1)} = \frac{\mathcal{L}(M_0(\mu = 0, \theta = \hat{\theta}_0))}{\mathcal{L}(M_1(\mu = \hat{\mu}, \theta = \hat{\theta}_1))} \tag{2.8}$$

The larger $\lambda(\mu)$ the better H_0 in comparison to H_1. By taking the negative logarithm of $\lambda(\mu)$ one defines the observed test statistic, denoted as $t_{\mu,obs}$ (also known as ΔTS):

$$t_{\mu,obs} = -2\log\left(\lambda(\mu)\right) = 2\log\mathcal{L}(H_1) - 2\log\mathcal{L}(H_0) \tag{2.9}$$

If the null hypothesis is preferred, t_μ has a positive value. The value itself can be related to the p-value by:

$$p_\mu = \int_{t_{\mu,obs}}^{\infty} f(t_\mu|\mu)dt_\mu \tag{2.10}$$

where $t_{\mu,obs}$ is the observed test statistic and $f(t_\mu|\mu)$ is the probability density function (pdf) of t_μ assuming signal strength μ. The relation between the p-value and the test statistic t_μ is illustrated in Figure 2.2 (a). One rejects H_0 if its p-value is below a specific threshold α, e.g. $\alpha = 0.05$. By testing different values for the signal strength μ, the confidence interval is defined. In the case of $\alpha = 0.05$, it would be the 95% confidence interval.
Instead of using the p-value, it is very common in particle physics to use the significance Z. It is defined such that the Gaussian distributed variable is found within Z standard deviations. The relation to the p-value is:

$$Z = \Phi^{-1}(1 - p) \tag{2.11}$$

where Φ^{-1} is the inverse of the cumulative distribution of the standard Gaussian. For $p = 0.05$, the significance is $Z = 1.64$. The relation is illustrated in Figure 2.2 (b). Note, that one can also use a one-sided definition where $Z = 0$ gives $p = 0.5$.

In equation 2.10, the pdf $f(t_\mu|\mu)$ is assumed. If the sample size N approaches infinity, Wilks theorem can be used which states that under H_0, the distribution of the test statistic t_μ approaches the χ^2 distribution with k degrees of freedom where k is the difference in parameters of M_0 and M_1. For example, if $k = 1$ and the test statistic is $t_\mu = 25$, the p-value corresponding to a χ^2 distribution of 25 with one degree of freedom is $3 \cdot 10^{-7}$. Inserting in equation 2.11, results in a significance of 5. For $k = 1$, the significance can therefore be approximated as the square root of the test statistic. In Figure 2.1 lower panel, the test statistic was computed in each bin and the squared values are plotted. The source RX J1713.7 − 3946 has entries with $\sqrt{\mathrm{TS}} > 5$ which is the standard criterion for a source detection. The other source HESS J1614 − 518 is weaker and therefore the $\sqrt{\mathrm{TS}} \sim 2$ is smaller. The other sources in the excess map are well modelled and hence, no significant excess can be seen.

The test statistics $t_{\mu,obs}$, which asymptotically follows a $\chi^2_{k=1}$ distribution, can be further simplified using Wald's approximation [39]:

$$t_{\mu,obs} = \frac{(\mu - \hat{\mu})^2}{\sigma^2} + \mathcal{O}(1/\sqrt{N}), \tag{2.12}$$

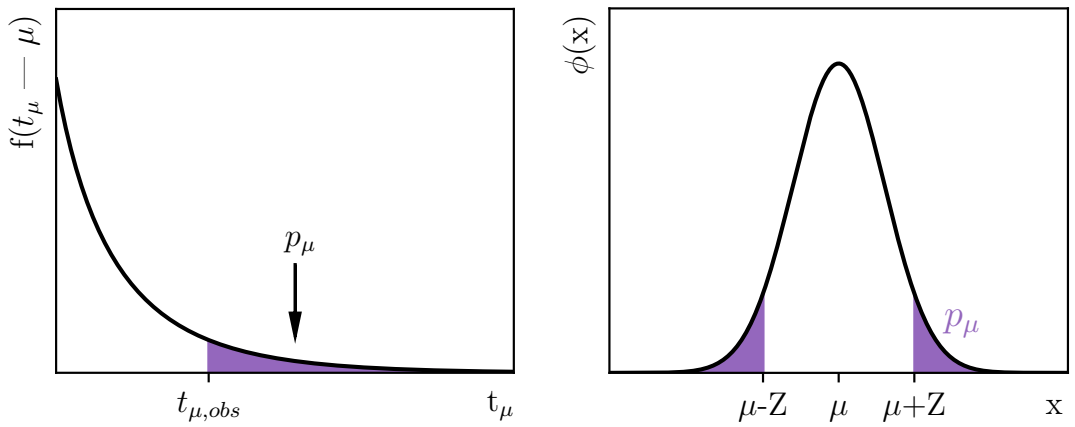

(a) (b)

Figure 2.2: Illustration of the relation between the p-value (purple area) and (a) the observed test statistics $t_{\mu,\text{obs}}$ and (b) the significance Z. Figure adapted from [39].

where $\hat{\mu}$ follows a Gaussian distribution with mean μ' and standard deviation σ. The latter can be obtained by scanning the t_μ as shown in Figure 2.3. The $n\sigma$ uncertainty of $\hat{\mu}$ is such that

$$t_{\hat{\mu}+1\sigma} = t_{\hat{\mu}} + n^2 \tag{2.13}$$

Note that this quadratic approximation only holds when the parameters are within the interior of their allowed range. If any parameter, such as μ, lies at the boundary (e.g., $\mu = 0$), the distribution of t_μ deviates from the $\chi^2_{k=1}$ form, and the relation in equation 2.13 no longer holds.

Instead of scanning the test statistics to derive the standard deviation σ based on equation 2.12, it can be computed from the covariance matrix of the estimators $V_{ij} = \text{cov}[\hat{\theta}_i, \hat{\theta}_j]$. The inverse of the covariance matrix can be computed by neglecting the $\mathcal{O}(1/\sqrt{N})$ term:

$$V^{-1}_{ij} = -E\left[\frac{\partial^2 \ln L}{\partial\theta_i \partial\theta_j}\right] \approx \left[\frac{\partial^2 \ln L}{\partial\hat{\theta}_i \partial\hat{\theta}_j}\right] \tag{2.14}$$

where E is the expectation value and the expression in the brackets is the Hessian matrix. The uncertainty on parameter $\vec{\theta}_i$ is $\sqrt{V_{ii}}$.
The MINUIT framework employed in *gammapy* uses this approach to compute the per definition symmetric hesse errors. Note, that non-linearities cannot be taken into account. On the other hand, using Minos in the MINUIT framework performs likelihood scans to obtain the parameter uncertainties based on equation 2.13 and therefore asymmetric uncertainties can be obtained. However, the correlation between the parameters can not be computed this way.

It is important to note, that here only the statistical uncertainty on the parameter μ is quantified since it is intrinsically accounted for by the Poisson assumption made. However, total amount of uncertainties is a composition of statistical and systematical uncertainties:

$$\sigma^2_{\text{tot}} = \sigma^2_{\text{stat}} + \sigma^2_{\text{sys}} \tag{2.15}$$

For a count experiment the relative statistical uncertainty decreases with $\sqrt{N}$ due to the underlying Poisson behavior where N is the sample size. This is not the case for systematic

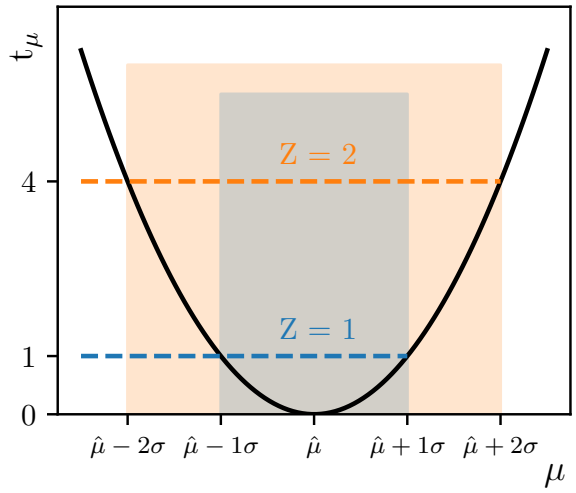

Figure 2.3: Illustration of a test statistic as a function of the parameter μ. The determination of the 1σ and 2σ error is shown.

uncertainties which makes them dominant especially for large sample sizes. In the next chapter, a method is discussed that allows the inclusion of systematic uncertainties in the likelihood, so that when the uncertainties of the model parameters are derived from the likelihood, they are intrinsically included.

Chapter 3

Using Priors to Include Systematic Uncertainties in the Fit

Systematic uncertainties are defined as reproducible inaccuracies that consistently affect measurements. These inconsistencies may originate from a number of sources, including instrument calibration errors, external environmental factors, or inherent limitations in theoretical models. It is not possible to guarantee the robustness and reliability of a physical result in the absence of an appropriate analysis of the uncertainties. Systematic uncertainties can be incorporated into the likelihood function through the use of priors. Priors reflect the initial beliefs or assumptions about a physical parameter that are made prior to the observation of data. The incorporation of priors during the modelling process represents a more nuanced approach to the handling of systematic uncertainties.

3.1 Maximum A Posteriori Estimation

Bayes's theorem can be derived from the conditional probability of two events, A and B, occurring [40]:

$$\mathcal{P}(A|B) = \frac{\mathcal{P}(B|A) \cdot \mathcal{P}(A)}{\mathcal{P}(B)} \tag{3.1}$$

Setting the event B as the measured data c and event A as the model prediction depending on multiple parameters $\mu(\vec{\theta})$, results in:

$$\mathcal{P}(\mu(\vec{\theta}), c) \propto \mathcal{L}(c, \mu(\vec{\theta})) \cdot \pi(\vec{\theta}) \tag{3.2}$$

Here, the probability P(B,A) equals the likelihood defined in equation 2.6. The term $\pi(\vec{\theta})$ denotes the assumed prior probability density of the model parameters. The posterior $\mathcal{P}(\vec{\theta}|c)$ represents the updated probability of the model parameters after observing the data. The denominator is dropped because it is only a normalising factor under the assumption that it is finite and non-zero. As with the determination of the maximum likelihood estimator $\vec{\theta}_{ML}$, the value maximising the a posteriori probability is the maximum a posteriori estimator $\vec{\theta}_{MAP}$ [41]:

$$\vec{\theta}_{\mathrm{MAP}} = \arg\min \left(-2 \ln \mathcal{P}(\vec{\theta}) \right) \tag{3.3}$$

The uncertainties on the model parameters are computed in accordance with the methodology outlined in equation 2.13. It should be noted that for a non-informative prior distribution, the maximum a posteriori estimator $\vec{\theta}_{MAP}$ is equal to the maximum likelihood estimator $\vec{\theta}_{ML}$.

As the complexity of the model increases, the number of parameters rises, thereby facilitating a more precise representation of the data. These supplementary models modify the background template and the IRFs in order to account for the systematic uncertainties associated to the corresponding model component. The respective parameters are designated as nuisance parameters, $\vec{\theta_n}$, since they are not employed for physical interpretations. Knowledge about the systematic uncertainties of the instrument or the dataset exists due to dedicated Monte Carlo simulations and instrumental studies. This knowledge can be incorporated into the fit with the help of a prior probability $\pi(\vec{\theta_n})$. Assuming the systematic uncertainty follows a Gaussian distribution around μ with a variance σ^2, the prior takes the form:

$$\pi(\vec{\theta_n}) = G(\vec{\theta_n}, \vec{\mu}, \vec{\sigma}^2), \tag{3.4}$$

where $\vec{\mu}$ are the expected values of the nuisance parameters. In the absense of systematic uncertainties, $\vec{\mu} = \vec{0}$. The variance of the distribution is equivalent to the magnitude of the underlying systematic uncertainty, i.e. a 10% systematic uncertainty on energy bias results in $\sigma = 0.1$ for the prior set on the nuisance parameter shifting the energy dispersion matrix. In instances where there are correlated systematic uncertainties, a multidimensional Gaussian distribution is employed as the prior:

$$\pi_m(\vec{\theta_n}) = G(\vec{\theta_n}, \vec{0}, K), \tag{3.5}$$

where K is the correlation matrix containing the magnitudes and correlations between the nuisance parameters $\vec{\theta_n}$. I.e. if the background template is normalised in every energy bin with a nuisance parameter, one can quantify the correlation between the bins in the correlation matrix.

The inclusion of additional nuisance parameters with their priors results in an expansion of the parameter space. This directly affects the model parameters' uncertainties due to the wider minimum in the posterior function compared to the likelihood function. The uncertainty is now of a statistical and systematic nature simultaneously. As a byproduct of the fit, one obtains the correlation between all fitted parameters. This allows an investigation of which model parameters are affected by which source of systematic uncertainty. This information could be used in future analyses to minimise the systematic uncertainties for particular studies.

3.2 Application to an Exemplary Case

Assume a simple counting experiment where the energy of multiple photons is measured and reconstructed. The true energies of the photons were simulated by sampling from a Gaussian distribution with a mean of $\mu = 20, \mathrm{TeV}$ and a standard deviation reflecting only statistical variation (see Figure 3.1). However, the energy dispersion of the experiment introduces an additional Gaussian uncertainty with a mean (energy bias) of zero and a standard deviation (energy resolution) of $\delta E = 3, \mathrm{TeV}$. The probability density function is shown in Figure 3.2 (left). This results in a widening of the distribution of the measured energies.

A one-dimensional Gaussian model is fitted to the data:

$$\mu(E) = N \exp\left(\frac{(E - E_c)}{2\sigma}\right)^2 \tag{3.6}$$

where $N = 1/\sigma\sqrt{2\pi}$ is the normalisation, E_c is the mean of the distribution and σ the standard deviation. The parameters $\theta = (N, E_c, \sigma)$ are fitted with the maximum likelihood method to the data. The best-fit value of the mean of the distribution was found to be $20.1 \pm 0.252\,\mathrm{TeV}$.

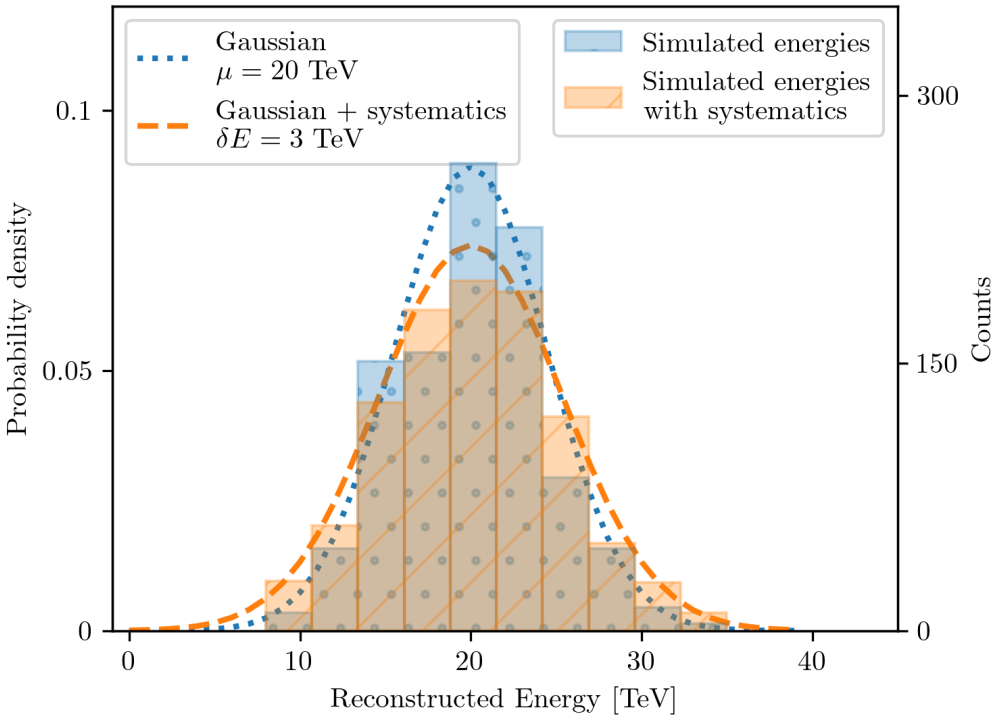

Figure 3.1: Photon energies were randomly drawn from a Gaussian distribution with a mean of 20 TeV. An additional Gaussian smearing with a standard deviation of 3 TeV was applied to simulate the experimental energy resolution. The probability density is represented on the left axis, while the drawn counts are indicated on the right.

This is in good agreement with the injected mean of the distribution $\lambda = 20\,\text{TeV}$. The likelihood scan as a function of the parameter E_c is shown in Figure 3.2 (left). It can be observed that the uncertainty computed from the covariance matrix (error bar) is in agreement with the Minos uncertainty where the $-2\log\mathcal{L}$ is $+1$ from the minimum. However, the parameter uncertainty is only statistical.

In order to account for the systematic uncertainty resulting from the energy resolution in the fitting process, a nuisance parameter is introduced. This nuisance parameter has the ability to shift the energy axis and is therefore highly correlated with the fitted position of the centre of the Gaussian distribution.

$$\mu'(E) = N \exp\left(\frac{(E - E_c - \Delta E)^2}{2\sigma^2}\right) \tag{3.7}$$

where ΔE is the energy bias.

Since the underlying shape of the systematic uncertainty is known, a prior can be set on the nuisance parameter ΔE with the same properties: Gaussian distributed, with the expected value of the nuisance parameter being $\mu = 0\,\text{TeV}$ and standard deviation of $\sigma = \delta E = 3\,\text{TeV}$:

$$\pi(\Delta E) = G(\Delta E, \mu = 0\,\text{TeV}, \sigma^2 = (3\,\text{TeV})^2), \tag{3.8}$$

The $-2\log\pi$ is shown as a function of the nuisance parameter ΔE in Figure 3.2 (right). It should be noted that the assumed distribution around zero is a consequence of the absence

of a systematic uncertainty on the energy bias. The parameters of the Gaussian distribution employed to describe the signal and the nuisance parameter are fitted by maximising the a posteriori probability which is the sum of $-2\log\mathcal{L}$ and $-2\log\pi$. The mean of the Gaussian distribution was determined to be $20.0 \pm 3.06\,\text{TeV}$. Given that a systematic uncertainty has now been incorporated, the uncertainty associated with the measurement of $E_{c,MAP}$ has increased. Due to the direct correlation between fitted E_c and the energy scale, the uncertainty equals the square root of the quadratic sum of the statistical uncertainty and the energy resolution (see equation 3.7). This is also the uncertainty resulting from the fitting process. The scan of the a posteriori distribution as a function of E_c is shown in Figure 3.2 (left). It is evident that the function $-2\log\mathcal{P}$ is considerably narrower than $-2\log\mathcal{L}$ which results in the larger uncertainty. The bias was fitted to $0.03 \pm 3.052\,\text{TeV}$ which perfectly agrees with the prior the bias is supposed to follow.

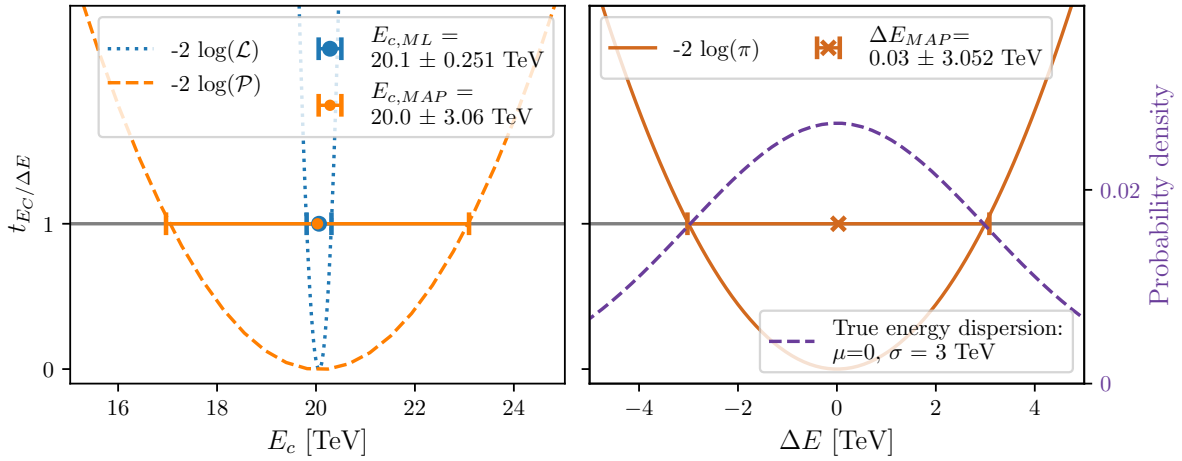

Figure 3.2: Left panel: Likelihood and a posteriori scan of the model parameter E_c. The 1σ errors of the covariance matrix are illustrated as error bars which match the width of the scan 1 offset of the minimum (Minos error). Right panel: Distribution of the prior and the best-fit nuisance parameter bias on which the prior was set with best-fit 1σ error and the true underlying energy dispersion probability density.

This straightforward example of a one-dimensional count distribution demonstrates how incorporating a nuisance parameter to quantify the systematic uncertainty on the energy dispersion results in an increase in the uncertainty associated with the model parameter of interest. It is crucial to emphasise that for the increase to align with the actual underlying systematic uncertainty, the prior must be correctly identified. If the standard deviation of the prior π is underestimated (overestimated), the same holds for the increase and therefore the effect of the systematic uncertainty is underestimated (overestimated).

Chapter 4

Systematic Uncertainties due to the Instrument Response Function

In a γ-ray analysis, the flux models are forward folded with the IRF of the telescope. Systematic uncertainties in the IRF, therefore, will directly lead to systematic uncertainties in the flux models, which in turn can have an influence on the interpretation of the physical results. It is important to not only have reliable IRFs for the instrument but to also incorporate any potential systematic uncertainties into the analytical process. With that in mind, the previously introduced method of using nuisance parameters and priors can be employed. In this approach, the nuisance parameters are used to parameterise the systematic uncertainties in the IRFs, where the estimate of the strength of the systematic uncertainties is used as prior. This chapter will demonstrate the application of the method to an exemplary dataset from the H.E.S.S. telescope.

4.1 Setup

In section 1.4 the IRFs of H.E.S.S. observations of PKS 2155-304 were introduced. These are subsequently employed in the following chapter to construct an illustrative dataset. As the public dataset comprises only 9.14 hours of data, the statistics are limited, which causes the statistical uncertainties to dominante. Given the focus of this work on systematic uncertainties, the statistics of the dataset are artificially increased with simulations, to a total of 100 hours. A flux model is forward folded through the IRFs to generate an artificial excess. The flux model consists of a point source (positions in longitude and latitude) and a power law:

$$\frac{d\phi}{dE_{\text{true}}} = \phi_0 \left(\frac{E_{\text{true}}}{E_0} \right)^{-\Gamma} \tag{4.1}$$

where ϕ_0 is the amplitude at the reference energy $E_0 = 1\,\text{TeV}$ and Γ is the spectral index. For the amplitude and the spectral index $\phi_0 = 10^{-12}\,\text{TeV}^{-1}\text{s}^{-1}\text{cm}^{-2}$ and $\Gamma = 2.3$ are used if not stated otherwise. Moreover, the background rates of the individual observations are considered. To this simulated data, artificial statistical fluctuations are added. An illustrative example is presented in Figure 4.1 (a). The model, which is comprised of a point source with a power law and a normalisation of the background template, is fitted to the excess data using the 3D likelihood method. The model prediction is illustrated in Figure 4.1 (b). In an ideal scenario, the input values are recovered with their associated uncertainties, and the residuals are flat and distributed around zero, indicating no residual excess or underprediction. In this relatively simple example, this is indeed the case, as can be seen in Figure 4.1 (c).

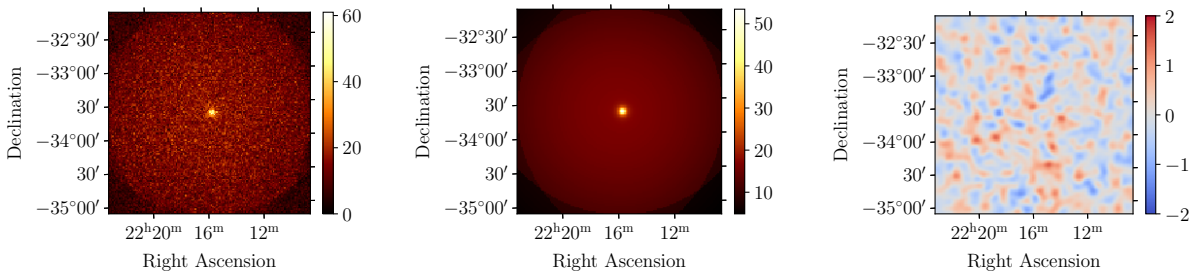

(a) Counts (b) Model prediction (c) Residuals

Figure 4.1: Artificial counts, model prediction and resulting residuals of the dataset based on H.E.S.S. observations of PKS 2155-304 with a simulated point source with a power law.

The following demonstration employs this dataset to illustrate the impact of IRF systematic uncertainties on a γ-ray analysis.

4.2 Effective Area

The effective area is proportional to the measured γ-ray intensity in true energy. Consequently, if the intensity is mismodelled, it will result in a systematic underestimation or overestimation, which causes an incorrect description of the effective area. Since the model prediction is directly proportional to the telescope's effective area (see equation 2.4), this affects the best-fit properties of the source. The effective area is determined through Monte Carlo simulations of air showers and their Cherenkov radiation. Additionally, the instrument efficiency is simulated. Any discrepancy between the simulated instrument and the real one results in a systematic uncertainty in the effective area. A parameterising model is required in order to modify the effective area $A_{\mathrm{eff}}(E_{\mathrm{true}})$. In this instance, a simple, energy-dependent power law is employed. However, the method is applicable to models of any complexity. The modified effective area $\bar{A}_{\mathrm{eff}}(E_{\mathrm{true}})$ used to compute the count prediction from a flux model based on equation 2.4 is, therefore:

$$\bar{A}_{\mathrm{eff}}(E_{\mathrm{true}}) = (a+1) A_{\mathrm{eff}}(E_{\mathrm{true}}) \left(\frac{E_{\mathrm{true}}}{E_0} \right)^{-b}, \tag{4.2}$$

the two introduced nuisance parameters are the normalisation factor a and the spectral tilt b. The reference energy E_0 is set to 1 TeV. Note that $(a+1)$ is used as the normalisation factor to ensure that the nuisance parameter a is distributed around zero. Consequently, $a = 0$ corresponds to the absence of a systematic uncertainty on the normalisation of the effective area. The same holds true for the spectral tilt, b. The magnitude of the systematic uncertainties is typically estimated based on the characteristics of the instrument, the datasets, the quality of the data, and other relevant factors. In the majority of cases, the assumption is that the systematic is distributed according to a Gaussian function around zero, with a particular width, which is referred to as the magnitude of the systematic uncertainty.

In the following analyses, we assume that the magnitude of the overall normalisation of the effective area is 10% and that the magnitude of the spectral shape is 2%. It should be noted that these are exemplary values specifically for the PKS 2155-304 dataset measured by H.E.S.S.

Exemplary Dataset with Statistical Fluctuations For the purposes of clarification, the method is elucidated in detail with respect to an example case. The objective is the realistic simulation of a dataset comprising a background, a source, and both systematic and statistical uncertainties. The source model is fitted to the data, and the impact of the artificial systematic on the fit result is discussed.

It is assumed that the systematic uncertainty in the effective area on the normalisation is exemplary value of $a_{sys} = 3\%$ and on the tilt is $b_{sys} = 0.1\%$. These values are incorporated into equation 4.2, thereby yielding a modified effective area. This modified effective area is then employed in the IRFs used to create the artificial excess including the background prediction and statistical fluctuations. The resulting excess, with systematic and statistical uncertainties, represents a real measurement of the source.

In order to compute the model excess, the unmodified effective area is employed in the forward folding process. The maximum likelihood method is employed for the purpose of fitting the model parameters. In this illustrative example, the spectral index was fitted to 2.249 ± 0.046 and the amplitude was found to be $(9.07 \pm 0.49) \cdot 10^{-12}\,\mathrm{TeV}^{-1}\mathrm{s}^{-1}\mathrm{cm}^{-2}$. The resulting spectrum, along with the 1σ error band and the input spectrum, is shown in Figure 4.2. Moreover, the flux points have been calculated. In this manner, the amplitude has been refitted in each energy bin, and the uncertainty on the amplitude has been computed. In accordance with the definition, the spectrum is expected to fall within the 68% of the error bars. In this particular example case, this is only the case for five of the ten flux points. This can be attributed to the fact that in both the flux point uncertainties and the error band encompass solely the statistical uncertainties. The systematic uncertainty due to the effective area is not included in the fit, which results in an underestimation of the parameter uncertainties and highlights the need for accounting for such effects.

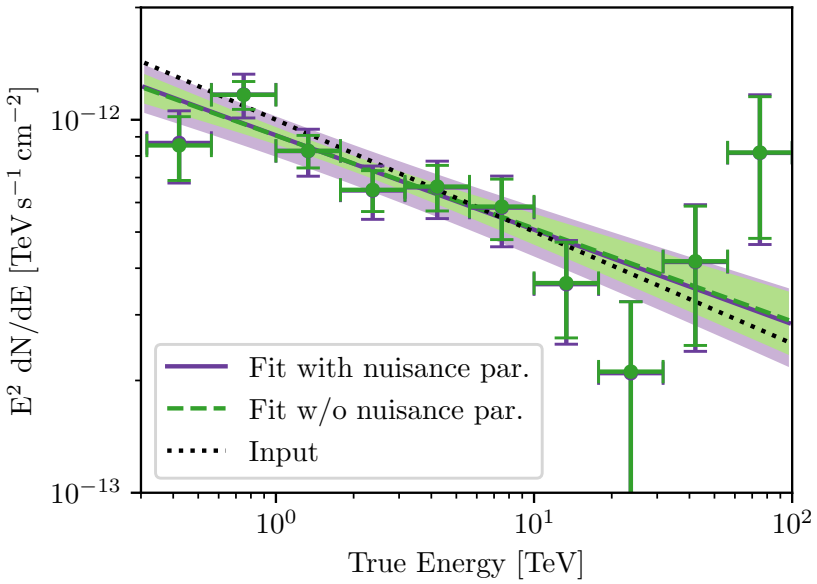

Figure 4.2: Input power law employed in the generation of the artificial excess and the best-fit spectra and flux points, both with and without the fitting of the effective area nuisance parameters.

This issue can be circumvented by refitting the two nuisance parameters a and b alongside

the model parameters, utilising the maximum a-posteriori estimation method. This yields the best-fit values for the nuisance parameters, which are 0.0 ± 0.1 and 0.0 ± 0.02, in accordance with the specified prior. As a consequence of the expansion in the dimensionality of the parameter space, the uncertainties associated with the model parameters increased. The resulting values are as follows: $\Gamma = 2.249 \pm 0.050$ and $\phi_0 = (9.07 \pm 1.13) \cdot 10^{-12}\,\mathrm{TeV}^{-1}\mathrm{s}^{-1}\mathrm{cm}^{-2}$. The spectrum with the 1σ errroband is shown in Figure 4.2. In the process of computing the flux points, the two nuisance parameters are reoptimised together with the source amplitude, resulting in the generation of larger error bars (see Figure 4.2). The increase in the model parameter uncertainties can be attributed to the incorporation of the systematic uncertainty into the fitting process. It is noteworthy that the input spectrum is now consistent within the 1σ error band for the majority of energies and within seven of the ten flux point errors, indicating a more precise estimation of the uncertainties inherent in the dataset.

Analysis of the Asimov Dataset It is important to note, however, that the dataset in question also contains statistical uncertainties, which make it unpredictable and not reproducible. In order to make quantitative estimates of the extent to which systematic uncertainties have been correctly included, it would be necessary to use multiple artificial datasets. An alternative approach would be to analyse a representative sample from these datasets with statistical uncertainties. This is called an Asimov dataset[1]. The dataset is analogous to that of the previously mentioned example, namely the simulated signal (point source, power law) and the background. It should be noted, however, that no Poisson statistic or systematic effect has been included. The model parameters are fitted to this Asimov dataset via the maximum likelihood method. The input values are accurately recovered; however, the uncertainties do not encompass the systematic uncertainties ($\Gamma = 2.30 \pm 0.05$, $\Phi_0 = (1.00 \pm 0.05) \cdot 10^{-12}\,\mathrm{TeV}^{-1}\mathrm{s}^{-1}\mathrm{cm}^{-2}$). Figure 4.3 depicts the spectrum with the addition of error bars and flux points. If the nuisance parameters, a and b, are also refitted along with the model parameters and the parameter uncertainties are computed based on the maximum a posteriori method, the results are as follows: $\Gamma = 2.30 \pm 0.05$, $\Phi_0 = (1.00 \pm 0.12) \cdot 10^{-12}\,\mathrm{TeV}^{-1}\mathrm{s}^{-1}\mathrm{cm}^{-2}$. The increase in parameter uncertainty is reflected in the widening of the error band and the resulting increase in the flux point errors (see Figure 4.3).

Figure 4.4 illustrates the likelihood (without nuisance parameters) and the a-posteriori (with nuisance parameters) as a function of the source amplitude, ϕ_0. It is evident that the wider range resulting from the larger parameter space is clearly visible, which in turn leads to a larger uncertainty regarding the parameter ϕ_0. Note that the scanning process revealed a slight asymmetry, resulting in asymmetric errors.

Multiple Realisations of Artificial Datasets Lastly, the representativeness of the Asimov datasets is confirmed through the analysis of multiple realisations of the exemplary datasets, taking into account both systematic and statistical uncertainties. Hereby, 1000 datasets were created by modifying the effective area with values of a and b being drawn from Gaussian distributions, with a mean of zero and standard deviations of $\sigma_a = 10\%$ and $\sigma_b = 2\%$. The modified effective area was then used to set the counts of the dataset equal to the model prediction with additional statistical fluctuations. The model parameters and the nuisance parameters with a prior set on them are fitted to the aforementioned counts, resulting in a best-fit flux prediction. In accordance with the definition, it is anticipated that 68% of these flux predictions will fall within the Asimov 1σ error band. The aforementioned coverage is computed for each energy

[1] An 'Asimov dataset' takes its name from the American science fiction writer Isaac Asimov. In his short story 'Franchise', one 'voter of the year' is randomly chosen to represent the entire electorate [**likelihoodbased˙tests**].

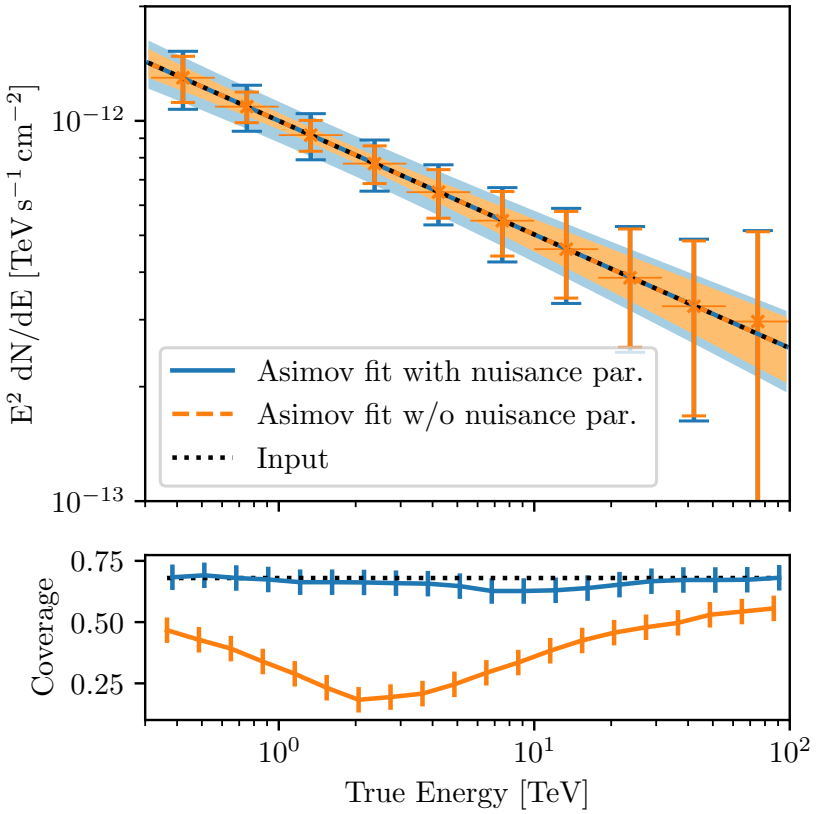

Figure 4.3: Upper panel: Input power law and the best-fit of the Asimov dataset with and without nuisance parameters quantifying the systematic uncertainties in the effective area and flux points. Lower panel: Coverage of the error band computed with the Asimov dataset with and without the nuisance parameters of the flux models of the 1000 datasets with artificial statistical and systematic uncertainties.

bin and is plotted in the lower panel of Figure 4.3. The use of the Asimov error band without nuisance parameters results in a limited coverage of approximately 50%. For certain energies (approximately 2 TeV) only 25% of the flux predictions are encompassed within the Asimov error band, indicating a pronounced underprediction. Conversely, when utilising the Asimov error band in conjunction with nuisance parameters, the coverage is highly accurate at the anticipated value of 68%.

It is important to note that the use of multiple simulated datasets with an added systematic is a common method for estimating the impact of this specific systematic on the parameters in question. In this case, the width of the optimal indices and amplitudes across the 1000 datasets would be regarded as the combination of the systematic and statistical error. As demonstrated, this would yield the same conclusions regarding the systematics as presented here. However, the simulated datasets must be based on the best-fit results derived from the actual data. As illustrated in the example, the true characteristics of the source may not be accurately represented in the fitted model. Based on these results, all simulations may potentially lead to a loss of information about additional systematics.

This is not the case if the actual data, which includes intrinsic systematic uncertainties, is

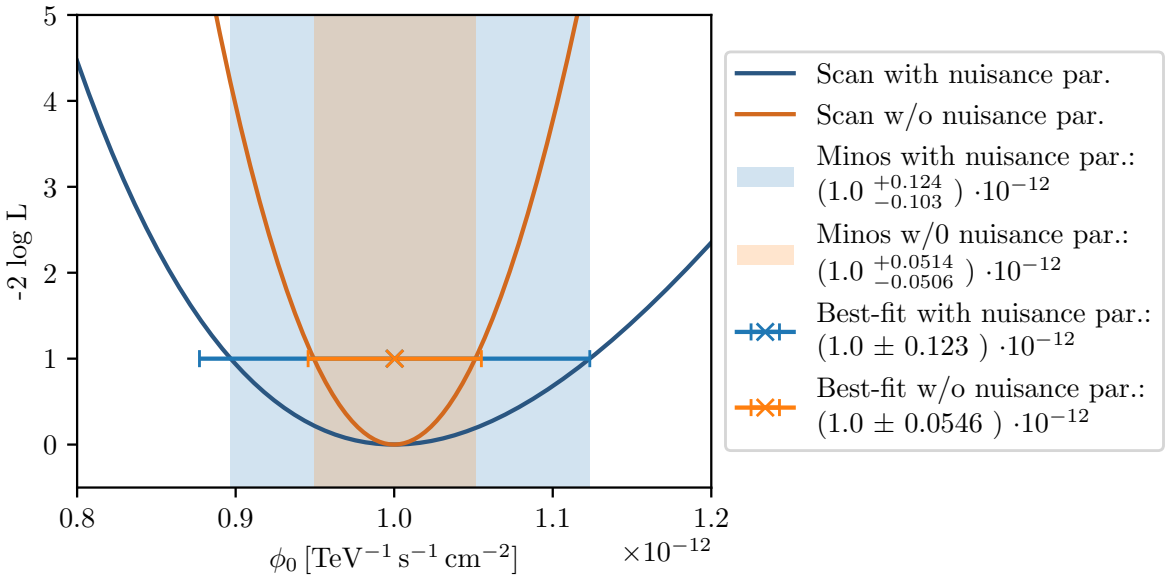

Figure 4.4: Scan of the likelihood with and without nuisance parameters as a function of the amplitude. The best-fit values and uncertainties are indicated, as are the 1σ uncertainties (Minos) based on equation 2.13.

fitted with nuisance parameters. As a consequence of this process one obtains the correlation matrix, which facilitates a more better understanding of the complex connections between the systematic uncertainties and the source properties. Moreover, the reduced computation time represents an additional advantage. The CPU time required for the 1,000 simulations was 4.03 hours, whereas the single fit with the additional parameters was completed in 49.2 seconds.

4.3 Energy Dispersion

The energy dispersion is related to energy-dependent source properties, such as the spectral index, breaks or cutoffs in the spectrum. Potential systematic uncertainties directly impact these properties, creating the possibility of erroneous physical interpretations if they are not carefully considered. In general, the energy dispersion is quantified by two properties: the energy bias and the energy resolution. In this context, a simplified model is employed, wherein only the energy bias is associated with systematic uncertainties.

As previously stated, the systematic uncertainties can be incorporated into the model by parameterising it with a nuisance parameter, which is fitted alongside the model parameters.

$$\bar{E}_{\text{disp}}(E_{\text{reco}}|p_{\text{true}}, E_{\text{true}}) = E_{\text{disp}}(E_{\text{reco}}|p_{\text{true}}, E_{\text{true}} \cdot (1 + \Delta E)) \tag{4.3}$$

where the nuisance parameter, ΔE, represents a shift in the energy bias[2]. It should be noted that for $\Delta E = 0$, the energy dispersion is unmodified. While the nuisance parameter ΔE could

[2]In the implementation the energy dispersion matrix is multiplied with a diagonal matrix. The matrix is defined as the Kronecker delta function $\delta_{i+\Delta E,j}$, which is 1 if $i + \Delta E = j$ and 0 otherwise. To make the nuisance parameter ΔE continuous, both the energy dispersion and the diagonal matrix are upsampled before the multiplication and downsampled back to the original dimensions.

in principle be a function of the true energy, for the sake of simplicity, it is chosen not to be in the following.

It is once more assumed that the systematic uncertainty on the energy bias is distributed according to a Gaussian function around zero, with a width that quantifies the magnitude, denoted as $\sigma_{\Delta E}$. In the following $\sigma_{\Delta E} = 10\%$ is chosen.

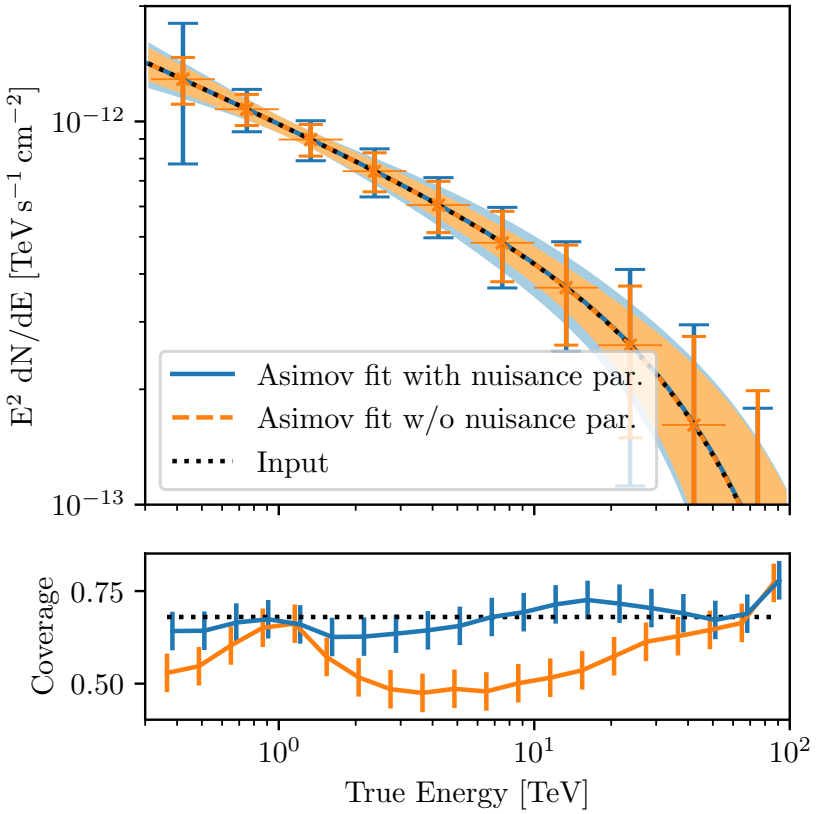

Figure 4.5: Upper panel: Input power law and the best-fit of the Asimov dataset with and without nuisance parameters, which quantify the systematic uncertainties in the energy dispersion and flux points. Lower panel: Coverage of the error band computed with the Asimov dataset with and without the nuisance parameters of the flux models of the 1000 datasets with artificially introduced statistical and systematic uncertainties.

The principle is now discussed in an analogous manner, as was done previously with regard to the effective area. Initially, an artificial dataset is created comprising a flux model consisting of a point source (positions in longitude and latitude) and a power law with exponential cutoff:

$$\frac{d\phi}{dE_{\text{true}}} = \phi_0 \left(\frac{E_{\text{true}}}{E_0} \right)^{-\Gamma} \cdot \exp(-\lambda E_{\text{true}}) \tag{4.4}$$

where $\phi_0 = 10^{-12}\,\text{TeV}^{-1}\text{s}^{-1}\text{cm}^{-2}$ is the amplitude at the reference energy $E_0 = 1\,\text{TeV}$, $\Gamma = 2.3$ is the spectral index and $\lambda = 1/60\,\text{TeV}$ is the inverse cutoff energy. In contrast to the analysis of systematic uncertainties in the effective area, the cutoff in the spectrum is now chosen since systematic uncertainties of the energy dispersion have a strong effect on highly energy-dependent parameters. Therefore, in addition to the spectral index, the additional energy cutoff is employed.

Analysis of the Asimov Dataset Firstly, an Asimov dataset is created by setting the model predictions of the artificial dataset containing the source model, the background template and the correct IRFs as the counts. The model parameters are then fitted to these counts, resulting in the best-fit spectral parameters, namely the spectral index $\Gamma = 2.30 \pm^{0.08}_{0.08}$, the source amplitude $\phi_0 = (1.00 \pm^{0.06}_{0.05}) \cdot 10^{-12}$, and the inverse cutoff energy $\lambda = (1/60.0 \pm^{1/65.0}_{1/53.0})$1/TeV. As anticipated, all input values have been successfully recovered. However, it is important to note that the parameter uncertainties only quantify the statistical uncertainties. The asymmetric uncertainties have been obtained through the scanning of the likelihood function and the application of equation 2.13. In a second fit, the bias parameter is reoptimised along with the model parameters. The input values are still recovered, but due to the larger parameter space, the parameter uncertainties increase: the spectral index $\Gamma = 2.30 \pm^{0.12}_{0.11}$, the source amplitude $\phi_0 = (1.00 \pm^{0.06}_{0.05}) \cdot 10^{-12}$, and the inverse cutoff energy $\lambda = (1/60.0 \pm^{1/68.2}_{1/58.3})$1/TeV. The systematic uncertainties of the energy dispersion have now been incorporated. As anticipated, the effect is more pronounced for the two highly energy-dependent parameters, namely, Γ and λ.

The increased parameter uncertainties are reflected in the 1σ error band and the flux point errors, as illustrated in Figure 4.5.

Multiple Realisations of Artificial Datasets In order to compute the coverage of the Asimov error band, it is necessary to calculate the flux prediction of multiple datasets that contain both systematic and statistical uncertainties. Once more, 1000 datasets are generated with an energy dispersion incorporating a systematic error drawn from a Gaussian distribution with a width $\sigma_{\Delta E} = 10\%$ and Poissonian statistics. The coverage of both the Asimov error band with and without the fitted bias is calculated in each energy bin and presented in Figure 4.5 lower panel. In the absence of the nuisance parameter, the coverage, with the exception of the reference energy at 1 TeV, is smaller than anticipated. Approximately 50% of the flux predictions are contained. Upon fitting the nuisance parameter, the correct amount of flux predictions are contained within the Asimov error band, indicating an accurate estimation of uncertainty. However, at the highest energy bin, the coverage is overestimated due to the limitations of statistics in the flux prediction, resulting in the end of the Gaussian regime. Nevertheless, the method was proven to be successful.

4.4 Combined Application to an Example Dataset

Given that a dataset is characterised by systematic uncertainties with regard to both the effective area and energy dispersion, it is not necessary or realistic to conduct a separate analysis. Consequently, in this chapter, the two IRF sources of systematic uncertainties are simulated and accounted for simultaneously. However, the setup is equivalent to that employed in the preceding two sections.

Analysis of the Asimov Dataset The initial step is to create an Asimov dataset comprising the model prediction of a point source with an exponential cutoff power law as the counts, with the inclusion of both statistical and systematic uncertainties. If the model parameters are fitted using the maximum likelihood method, the resulting parameter uncertainties serve to quantify the statistical uncertainties present within the dataset. When both the model parameters and the nuisance parameters (effective area norm and tilt, a and b, and energy bias ΔE) are fitted with priors included in the likelihood, the resulting uncertainties encompass both the statistical

	Φ_0 $[10^{-12}\,\mathrm{cm}^{-2}\,\mathrm{s}^{-1}\,\mathrm{TeV}^{-1}]$	Γ	$1/\lambda = E_c$ [TeV]
Input	1.0	2.30	60.0
Without fitting sys.	$1.00\pm^{0.06}_{0.05}$	$2.30\pm^{0.08}_{0.08}$	$60.0\pm^{65.0}_{53.0}$
Fitting eff. area sys.	$1.0\pm^{0.13}_{0.11}$	$2.30\pm^{0.08}_{0.09}$	$60.0\pm^{66.1}_{53.9}$
Fitting energy bias sys.	$1.00\pm^{0.06}_{0.05}$	$2.30\pm^{0.12}_{0.11}$	$60.0\pm^{68.2}_{58.3}$
Fitting eff. area & energy bias	$1.00\pm^{0.13}_{0.11}$	$2.30\pm^{0.12}_{0.11}$	$60.0\pm^{68.2}_{58.3}$

Table 4.1: The flux model input parameters of the simulated datasets and the best-fit results with and without IRF systematic uncertainties are presented. The asymmetric parameter uncertainties are obtained through scanning the likelihood and posterior functions.

and the systematic aspects. It should be noted that both the input parameters of the flux model and the priors remain unchanged from the previous iteration. The input and best-fit parameters are presented in Table 4.1.

As previously observed, the effective area systematic primarily serves to enhance the uncertainty associated with the source amplitude. In contrast, the energy bias is responsible for both an increase in the spectral index and an elevation in the cutoff energy uncertainties.

The correlation between the sources of systematic uncertainties and the model parameters can be quantified further in the symmetric correlation matrix, which is a byproduct of the optimisation process. This is shown in Figure 4.6. The strongest correlation is between the effective area normalisation, represented by the variable a, and the source amplitude. The effective area tilt is correlated with the source's spectral index. However, due to the relatively small systematic magnitude of 2%, the overall effect on the model uncertainty is minimal. Obtaining a correlation matrix of this nature from the fitting process can assist in optimising the dataset and the instrument for specific purposes. For instance, if the parameter of interest is the cutoff energy, one can directly gain information about possible systematic uncertainties that might reduce the sensitivity.

Multiple Realisations of Artificial Datasets Lastly, the results obtained with the Asimov datasets are validated by fitting multiple realisations of the datasets, which contain IRF systematic effects (effective area and energy bias) and statistical uncertainties. The 1000 datasets were fitted, and the resulting best-fit parameters are presented as two- and one-dimensional histograms in Figure 4.7. The 1σ contours of the Asimov datasets with and without nuisance parameters are computed. As the number of sources of systematic uncertainties incorporated into the fit increases, the width of the contour correspondingly increases due to the larger parameter space. The asymmetric errors are indicated as error bars, which are aligned with the contours by definition. The one-dimensional projection of the contours is indicated in the one-dimensional histograms. As a means of evaluating the efficacy of the proposed coverage test, it is possible to ascertain the number of the optimal values of the draws that fall within the asymmetric 1σ error bounds of the Asimov bands. In the absence of nuisance parameters, only 35.8% of the best-fit amplitudes, 42.7% of the indices and 64.9% of the inverse cutoff energy are contained.

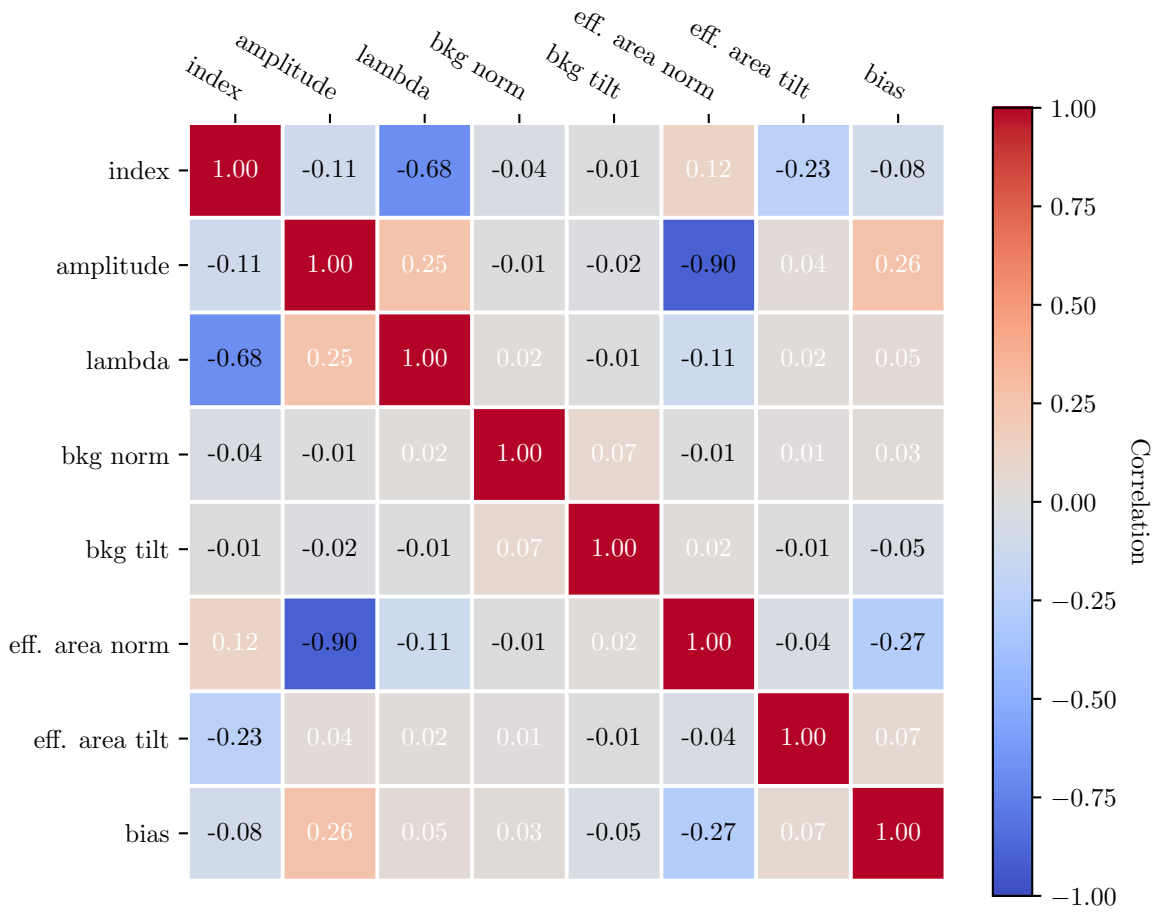

Figure 4.6: Symmetric correlation matrix of the spectral flux model parameters, the IRF nuisance parameters quantifying the effective area and the energy dispersion and the background model parameters.

This differs from the expected 68%. When the nuisance parameters, a, b and ΔE, are included, these values increase to 65.8%, 66.0% and 64.5%, respectively. This is as expected and it can be concluded that the Asimov errors are considered correct.

In this chapter, the IRF systematic uncertainties were incorporated into a mock dataset through parameterisation with nuisance parameters, which were fitted alongside the model parameters. In a real dataset, the behaviour of the systematic uncertainty must be inferred based on prior knowledge and estimated. Here, it was assumed that the distribution followed a Gaussian with a specific width, which was set to 10% for both the effective area and the energy dispersion. The outcomes yielded by the Asimov datasets were contrasted with those obtained from randomly selected subsets of the original dataset, wherein the IRF systematic uncertainty was incorporated. This latter approach represents a traditional methodology for estimating systematic uncertainties. As both results are compatible, the nuisance parameter and prior method is deemed to have been successful. Furthermore, the correlation matrix and saved computation time are additional benefits. In real scientific cases, creating multiple realisations of the dataset based on the best-fit description can result in mismodelling of the data, and in the

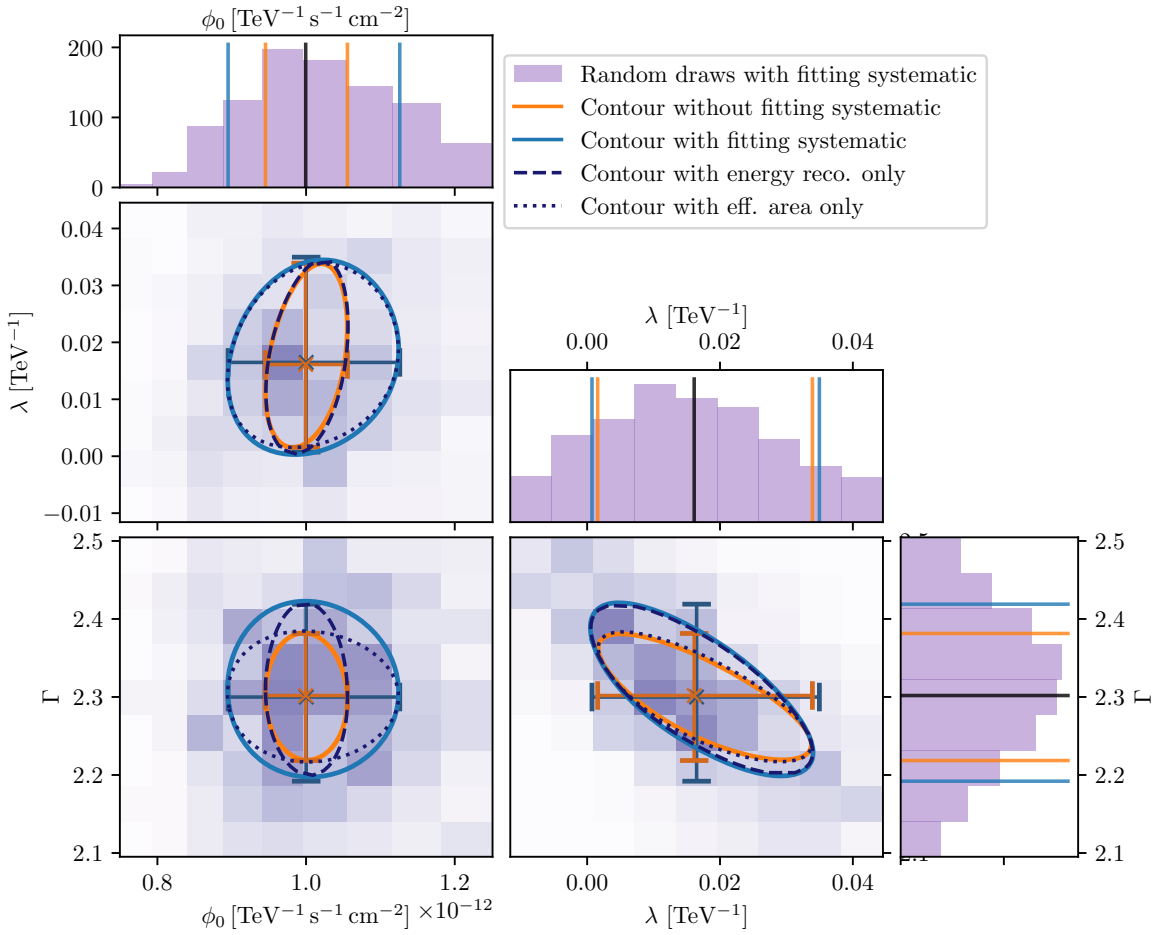

Figure 4.7: Best-fit results of the 1000 artificial datasets with systematic and statistical uncertainties. Additionally the 1σ contours and errors of the Asimov datasets are shown with and without fitting the nuisance parameters.

worst case, an underestimation of the systematic uncertainty. Therefore, the introduced method is not only statistically correct, but also a superior solution for complex γ-ray data.

Chapter 5

Systematic Uncertainties of the Hadronic Background

In a 3D γ-ray analysis, the hadronic background is incorporated through the use of a template derived from archival data. This template is initially fitted to the individual runs prior to stacking and utilisation in the comprehensive analysis. Given the significant influence of the background rate on the telescope's pointing position, the background is categorised according to both zenith and azimuth angle, in addition to the conventional energy binning. The construction of the background template may be subject to systematic effects resulting from the mismodelling of muon efficiency or binning effects observed in the BDT training, among other factors. At lower energies, in particular, systematic uncertainties tend to exert a dominant influence, potentially impacting the modelling of γ-ray sources. This chapter will explore the use of nuisance parameters and priors to modify the template at varying energy bins, thereby accounting for the aforementioned systematic uncertainties. A mock dataset based on the H.E.S.S. IRFs of PKS 2155-304 is employed in this study. The methodology is elucidated in the initial section, which is followed by an examination of a representative sample from this dataset. Subsequently, multiple realisations are discussed and compared to the Asimov dataset.

5.1 Setup

In general, the background template is modified with a simple power law function during the bin-wise fit and after the stacking in the overall analysis, along with the other flux models. The power law spectrum is defined as follows:

$$\bar{r}(E_i, p) = n \cdot r(E_i, p)^{-\Gamma}, \tag{5.1}$$

where $r(E_i, p)$ is the background rate predicted by the template at energy E_i and position p. The two nuisance parameters n and Γ are the normalisation and the spectral tilt.

Nevertheless, a basic tilt may be insufficient to account for the various effects observed in specific energy bins. By incorporating additional parameters beyond the two nuisance parameters, namely one normalisation term in each energy bin, systematic uncertainties associated with factors such as binning or low statistics at the highest energy bins can be addressed. This piece-wise spectral model is defined as follows:

$$\bar{r}(E_i, p) = (1 + \delta_i) \cdot r(E_i, p), \tag{5.2}$$

where $\vec{\delta} = (\delta_1, \delta_2, .., \delta_N)$ is the set of newly introduced nuisance parameters with N being the number of energy bins. Note that again $(1 + \delta_i)$ is used as the normalising factor to ensure that $\delta_i = 0$ corresponds to no systematic shift in energy bin i. In this instance, one nuisance parameter is introduced for each energy bin, resulting in a total of 24 parameters. This value depends on the specific dataset and the analytical approach employed. Given that the systematic effects are inherently correlated between the energy bins, it is reasonable to assume that the nuisance parameters will also exhibit this correlation. This information is contained in the correlation matrix, which is part of the prior term via an inverted version thereof. The prior is of Gaussian form and defined by the expected magnitude of the background systematic σ_i at energy E_i and the length of the correlations between the bins l. Given these parameters, the correlation matrix is as follows:

$$V_{ij} = \frac{\sigma_i}{\sqrt{2\pi}l} \exp\left(-\frac{(\delta_i - \delta_j)^2}{2l^2}\right). \tag{5.3}$$

As in the preceding chapters, a simulated dataset based on the IRFs of PKS 2155-304 is employed to illustrate how these nuisance parameters contribute to systematic uncertainties associated with the hadronic background. The estimation of the expected magnitude and correlation of the systematic is initiated with the assumption that $\sigma_i = \sigma = 10\%$ in every energy bin and $l = 2.5$. It should be noted that, in principle, both the magnitude and the correlation length may be dependent on energy. For the sake of simplicity, this assumption is not made here. The resulting correlation matrix is illustrated in Figure 5.1. As the initial four energy bins are situated below the energy threshold of 0.4 TeV, no correlation can be observed between them. Consequently, the correlation matrix is set to an identity matrix.

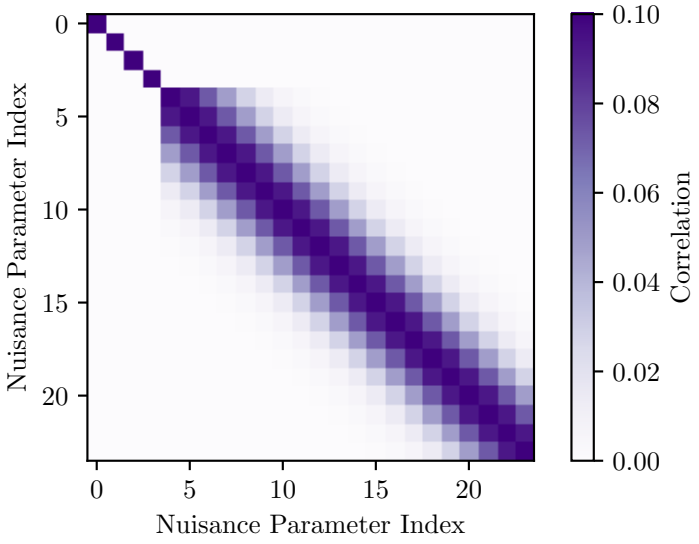

Figure 5.1: Covariance matrix computed based on equation 5.3 for $\sigma = 0.1$ and $l = 2.5$.

5.2 Application to an Example Dataset

The simulated flux models comprise a Gaussian source with a size of $\sigma = 0.3°$ and an exponential cutoff power law ($\phi_0 = 10^{-12}\,\mathrm{cm}^{-2}\,\mathrm{s}^{-1}$, $\Gamma = 2.3$, $\lambda = 1/60\,\mathrm{TeV}^{-1}$). Furthermore, an additional background systematic is simulated and incorporated into the template. Consequently, a set of

nuisance parameters is drawn from the correlation matrix depicted in Figure 5.1. The random values are illustrated in Figure 5.2. By defining these values as the nuisance parameters of the background model, the background rate is modified in accordance with the equation 5.2.

The modified background, in conjunction with the model prediction and Poissonian statistics, has now been designated as the counts of a dataset. The dataset is fitted with the source parameters and only the background normalisation and tilt are treated as free parameters. This approach could be interpreted as the standard way of fitting the background template. Given the strength of the source itself, all source parameters are adequately recovered. The simple power law also attempts to emulate the random input nuisance parameters, as illustrated in Figure 5.2. However, due to the stiffness of the model, the hadronic background systematic uncertainty remains unaccounted for.

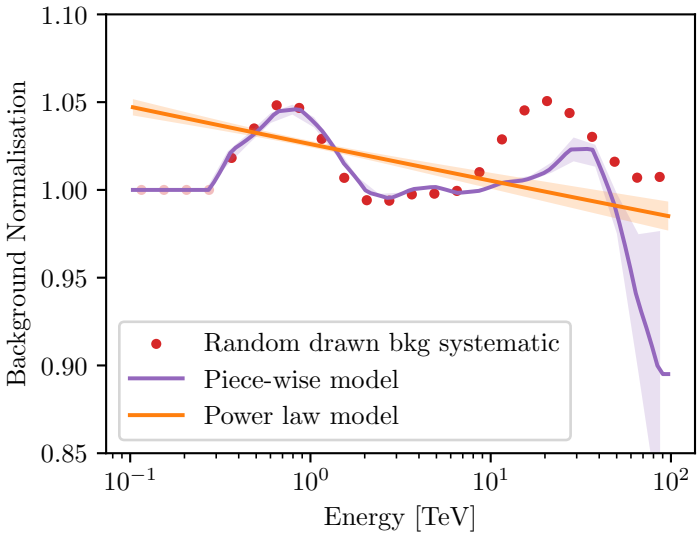

Figure 5.2: Input nuisance parameters drawn from the correlation matrix and the two best-fit models (power law and piece-wise) modifying the background template.

This is particularly evident when calculating the residual points or the z-score in the off-region, thereby ensuring that any mismodelling of the γ-ray emitting sources does not impact the background study. Let X be a random variable with an expected value of $E(X) = \mu$ and positive variance $Var(X) = \sigma^2$, then Z is defined as follows [42]:

$$Z_i = (X_i - \mu_i)/\sigma_i \tag{5.4}$$

In this context, the random variable is the total number of counts in energy bin i, c_i, while the expected value is the total prediction of all model components, μ_i. Consequently, σ_i is the square root of μ_i and represents the statistical error. The counts are distributed according to a Poisson distribution. However, since the expected values μ are considered to be large, the central limit theorem holds, and the Poisson distribution can thus be approximated by a normal distribution. In the event that the counts are normally distributed, the expected value of the random variable Z is zero and the variance is distributed around 1. If the model prediction is indeed the expected value of the counts and the standard deviation is solely attributable to statistical fluctuations, any potential for systematic uncertainty is effectively negated. In other

words, if the z-score variance is approximately equal to one, it can be inferred that the inherent systematic uncertainties in the data have been adequately addressed.

Figure 5.3 illustrates the z-score for the exemplary dataset. The variance was calculated to be 4.71, indicating the residual systematic uncertainties in the background template.

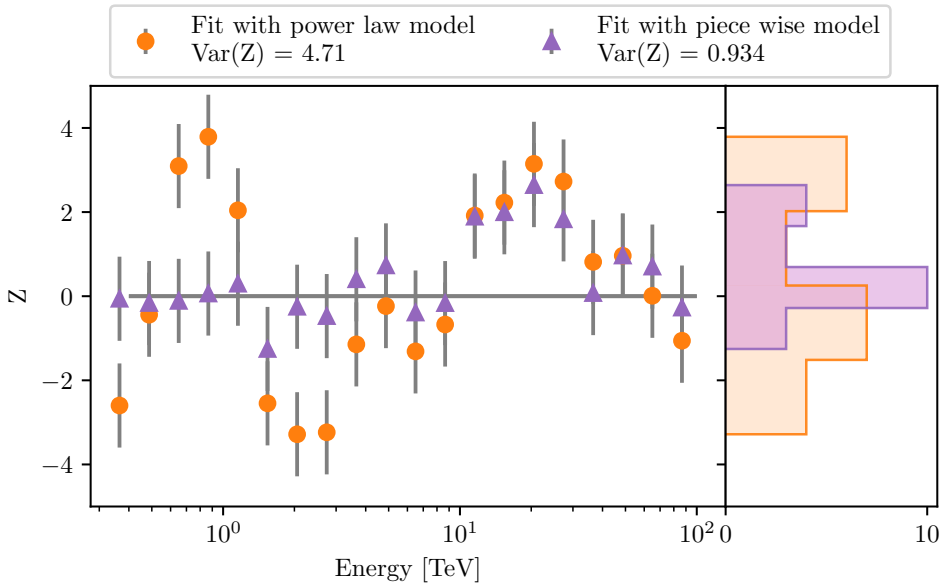

Figure 5.3: Z-score as a function of the energy and the distribution for different background models (power law and piece-wise)

To circumvent this issue, the piece-wise background model is fitted in place of the power law spectrum, along with the model parameters. The inverted correlation matrix with standard deviation $\sigma = 0.1$ and $l = 2.5$ is employed as the prior. The latter are successfully recovered, and the optimal background nuisance parameters are illustrated in Figure 5.2. The results are in good agreement with the input values, except for the higher energy ranges, where the statistical uncertainties become more dominant. The z-score is recomputed and also shown in Figure 5.3. The variance of 0.934 indicates that the only remaining uncertainty is of a statistical nature. The exemplary dataset demonstrated how systematic uncertainties due to the hadronic background manifest in the residuals if they are not accounted for in the modelling process. Given that this example relies on statistical fluctuations and the systematic itself was generated, the fitting process will be repeated multiple times to reduce the fluctuations and illustrate the overall effect.

5.3 Multiple Realisations of Artificial Datasets

An example dataset comprising a Gaussian source with an exponential cutoff power law and artificial background systematics and statistical fluctuations was generated 1,000 times. The same correlation matrix was employed to derive the input nuisance parameters. The dataset was fitted with both a power law and a piece-wise model with prior, along with the flux model. The best-fit parameters of the flux model are illustrated in Figure 5.4 for both background models. The mean of the distributions aligns with the input values in all cases, indicating a good recovery of the source model. However, the width of the distribution differs between the background models, with the distribution based on a power law exhibiting greater variability,

particularly for the source strength and inverse cutoff value. It can be observed that the input is only contained within the 1σ uncertainty in 56.1% (59.6%) of the cases for ϕ_0 (λ). Therefore, even for a very strong source with a significance of 420σ, the source strength is erroneous for a non-negligible number of example datasets. Moreover, a strong energy cutoff (24σ) is influenced by a background systematic of 10%. If the latter is incorporated by the nuisance parameters of the piece-wise model, the input amplitude (inverted cutoff) is contained within 71.0% (79.8%) of the 1σ uncertainties. It should be noted that the slight deviation from the expected 68% is due to the symmetric errors obtained from the fit, which are less accurate than the asymmetric errors from a likelihood scan. However, they are considerably less computationally expensive. The background systematic also affects the source's spectral index and extension, but to a lesser extent than the other two parameters.

Furthermore, an Asimov dataset was generated and the flux model and the piece-wise background model were fitted. The 1σ uncertainties on the model parameters are indicated in Figure 5.4. The standard deviation of the distributions with nuisance parameters is in close agreement with the latter, indicating a robust result.

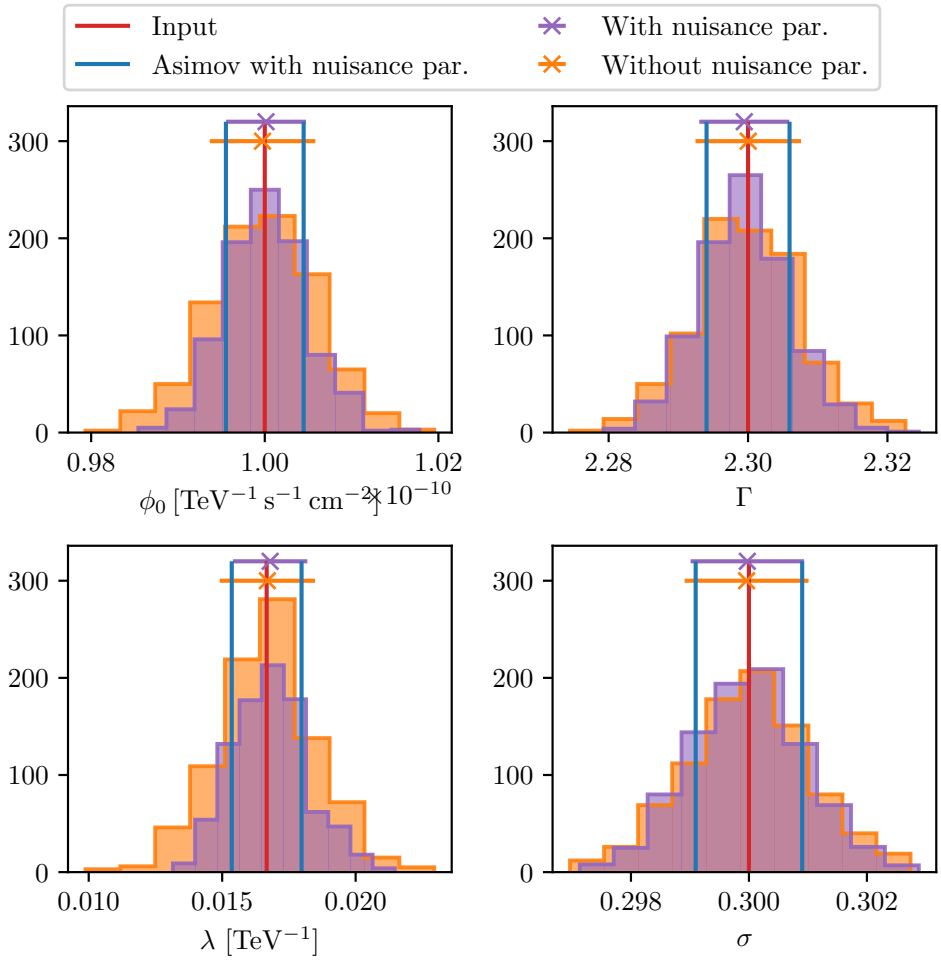

Figure 5.4: Best-fit source model parameters obtained from a fit with a power law and a piece-wise model as the spectral model for the background template. The input values are indicated as well as the 1σ uncertainties obtained from the Asimov dataset with nuisance parameters.

Prior to the fitting process, the z-score was calculated for each dataset. This was then repeated after the application of both the power law and the piece-wise model to the background data. The resulting data is presented in Figure 5.5. It can be observed that prior to fitting, the mean variance of the z-scores is markedly high. Following the fitting of the source model and the power law, the value is observed to be slightly reduced. However, the mean continues to exhibit a notable deviation from 1. When the piece-wise model is employed, the systematic uncertainties are incorporated into the data, leaving only statistical fluctuations. This results in a mean variance of 1. Finally, it is demonstrated that when a dataset is subjected to statistical fluctuations alone, the mean is observed to be at the expected value of 1. This further illustrates the inadequacy of a power law spectral model in accounting for the systematic uncertainties inherent to the background model.

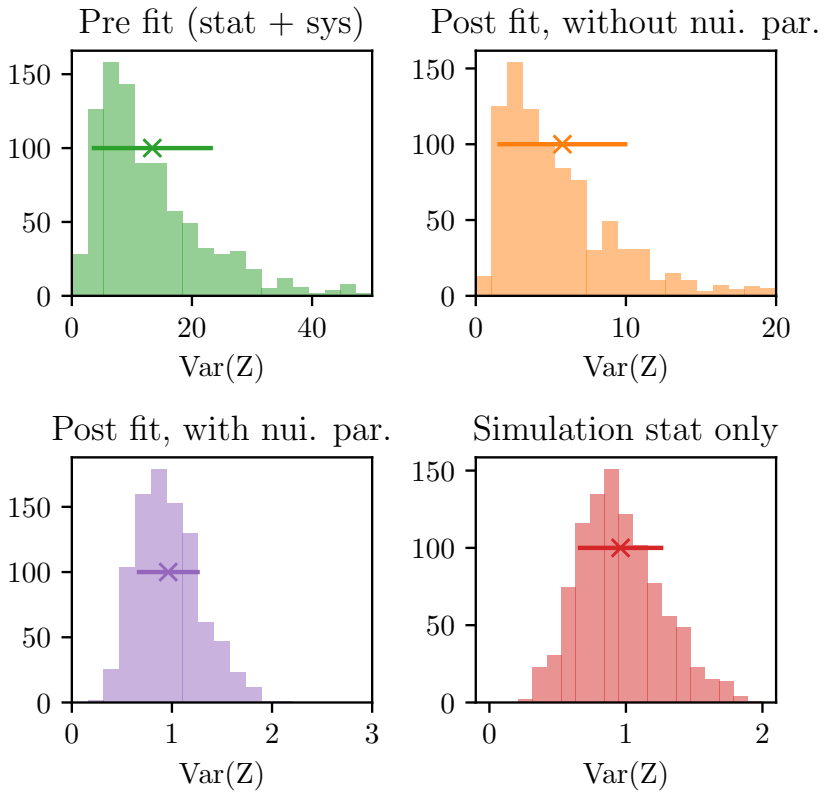

Figure 5.5: Variance of the z-scores calculated for the multiple realisations of the datasets prior to the fit, after fitting with the power law and the piece-wise model to modify the background. Lastly, the variances of the z-scores of a dataset containing only statistical fluctuations.

It is important to note that, in the case of a real dataset, it is not straightforward to ascertain whether there is a residual degree of uncertainty or if all potential factors have been taken into account. This is due to the fact that the variance of the z-score is expected to be approximately 1 on average; however, due to statistical fluctuations, there is a spread in the distribution. Nevertheless, the variance can still be used as a general indicator and can be compared to the results obtained from more straightforward background models or different input values for the prior in order to interpret the results.

Chapter 6

Summary

The observed properties of the γ rays are related to the true properties through the IRFs of the detector. This encompasses the effective area, the energy dispersion and the point spread function. By forward folding the flux models of the γ-ray sources through the IRFs, the observed excess can be fitted. Hence the parameters of the models can provide further inside into the properties of the source. The fitting is achieved by maximising the likelihood, which quantifies the accuracy of the flux models in predicting the observed counts. The data is binned in three dimensions: two spatial and one spectral. This allows for a simultaneous fitting of the morphology and spectral properties of the sources.

Nevertheless, the systematic uncertainties inherent to the IRFs are propagated to the fitted source parameters. It is crucial to quantify this by incorporating it into the parameter uncertainties. In this approach, a statistical Bayesian methodology is employed, where systematic uncertainties are incorporated into the fitting process through the introduction of additional nuisance parameters and a prior term that quantifies the estimated systematic uncertainty. This methodology was demonstrated using illustrative datasets from the ground-based telescope H.E.S.S. It was demonstrated how systematic uncertainties in the effective area and in the energy scale affect the spectral properties of the artificial source, and the method was validated using multiple realisations of mock datasets. The benefits include a reduction in computation time, the generation of a correlation matrix that illustrates the relationship between the model and nuisance parameters, and the elimination of the need for the creation of mock datasets based on the best-fit predictions, which could result in the loss of crucial information from the true dataset.

In the 3D analysis approach, a background template is constructed from archival observations. The template is then fitted to the measurements of the individual runs and subsequently stacked and employed in the final analysis. Usually, a simple power law model is employed during the fitting process to modify the background template. This approach may be too inflexible to account for minor variations between different energies. A more complex model is employed here, introducing a nuisance parameter in each energy bin. By incorporating the correlation matrix in the prior, the magnitude and correlation between energy bins are integrated into the fitting process. The efficacy of this method was demonstrated using mock datasets, with the flux model parameters successfully reconstructed. Additionally, the correct statistical behaviour of background counts from γ-ray sources was verified.

The utilisation of nuisance parameters and a prior to account for systematic uncertainties of the IRF and the hadronic background model was highly successful and will be employed throughout the remainder of this thesis for the analysis of data measured by H.E.S.S.

Part II

THE GALACTIC CENTRE REGION WITH H.E.S.S.

The GC is defined as the innermost region of the MW and is the host of multiple sources emitting VHE γ rays. This provides a unique opportunity to study the extreme processes occurring in the GC. The γ rays are generated through a number of different mechanisms, including interactions between accelerated particles and the surrounding medium, the decay of pions, and inverse Compton scattering. These VHE γ rays facilitate the investigation of particle acceleration mechanisms and the propagation of CRs within the GC. This section of the thesis concentrates on an analysis of the VHE γ-ray emissions from the GC as observed by the IACT array H.E.S.S. Given its location in the southern hemisphere, the H.E.S.S. instrument is ideally positioned to observe the inner GC. First, a brief introduction of the GC region is given. Secondly, the H.E.S.S. telescope array in Namibia is presented. This section focuses on the technical details of the instrument, data acquisition and data processing. Then the characteristics of the dataset are discussed and the results of the analysis are then presented. Finally, a study of the systematic uncertainties due to the hadronic background and a cross-check are presented, followed by a final discussion and interpretation of the results.

Chapter 7

Brief Overview of the Galactic Centre Region

7.1 Multi-Wavelength Observations

The GC has been the subject of extensive multi-wavelength observations. Its first detection in radio band was made by Jansky in the 1930s, marking the first radio detection from outer space [43]. Radio emission in the GC originates from hot gas, star-forming regions and the interaction of CRs with magnetic fields. Radio waves are able to penetrate the dust and gas prevalent in this region due to their long wavelengths, thereby providing a clear view of the underlying astrophysical phenomena. Figure 7.1 shows a survey of the GC conducted with the MeerKAT radio telescope in South Africa in 2020. The exceptional angular resolution reveals a very complex and challenging morphology. Multiple Supernova Remnants (SNRs) are indicated, which emit radio waves through synchrotron radiation. In this process, the supernova shock wave accelerates electrons which spiral along magnetic fields and emit radiation due to the change of direction. Furthermore, specific features have been identified, including the Mouse, the Snake, the Christmas tree and the arc source [44].

The strongest emission is generated by the complex Sgr A source, which comprises three superimposed components: Sgr A east (a SNR), Sgr A west (a spiral structure) and Sgr A* (a bright and compact radio source). The latter is at the centre of Sgr A west and is known to be a supermassive black hole (SMBH). In 2024, the Event Horizon Telescope captured the first image of the accretion disk around the event horizon of Sgr A* [45]. The mass of Sgr A* can be estimated from infrared (IR) observations for which dust clouds are transparent providing a clear view on faint stars. By tracing their motion and accelerations the position and mass of the central source of gravity, Sgr A*, can be measured with great precision. The mass is estimated to be approximately $4 \cdot 10^6 M_\odot$ [46].

Besides radio measurements the GC is studied in the X-ray band. For instance NASA's Chandra X-ray observatory measures a very faint signal from Sgr A*. Additionally, flares of approximately 60 minuets were found in near-infrared and X-ray bands. These are caused by synchrotron emission of non-thermal particles which are accelerated in the accretion flow [47].

In the 1990s, the γ-ray telescope EGRET detected excess in the GC on top of the diffuse emission [48]. The latter is due to diffusing protons from the centre which are interacting with gas and thereby produce γ rays. Due to worse angular resolution compared to X-ray and radio observatories, a coincident position of the point source with Sgr A* could not be confirmed. The satellite based γ-ray telescope Fermi LAT which is continuously monitoring the whole sky has

taken data of the GC for more than a decade. Nowadays, the Fermi LAT collaboration confirms a coinciding position between the γ-ray source and Sgr A*. However, no definitive association between the two sources is drawn [49].
Fermi LAT also detected vast structures that extend above and below the Galactic plane, emitting high energy γ rays and covering a distance of about 50,000 light-years. They are called Fermi bubbles, and it is believed that their origin is connected to past energetic events involving the supermassive black hole at the center of our galaxy [50]. Similarly, the eROSITA bubbles are enormous X-ray structures that surround the Fermi bubbles, extending even further into the circumgalactic medium. These bubbles are thought to be the result of large-scale outflows from the GC [51].

The GC is subdivided into distinct regions, see Figure 7.2. The Galactic disk extends along the Galactic Longitude. Assuming a cylindrical shape, the height of the region is approximately $\sim 1\,\mathrm{kpc}$ and its density can be approximated with $n_{\mathrm{gas}} \sim 1\,\mathrm{cm}^{-3}$. The inner region with a radius of $2-3\,\mathrm{kpc}$ constitutes the bulge of the Galaxy and exhibits a similar density to that of the Galactic disk. Within the bulge, the central molecular zone (CMZ) is defined. This region hosts multiple molecular clouds and is more dense, with a gas density of approximately $n_{\mathrm{gas}} \sim 100\,\mathrm{cm}^{-3}$. It extends from the molecular cloud Sgr D to the radio source Sgr E, with an approximate length of 200 pc in Galactic Longitude and only a few tens of parsecs in Galactic Latitude. The dynamics of the gas content of the CMZ can be observed via carbon monosulfide (CS) radio emissions. Hereby, molecules of CS transition from higher energy states to lower and emit light in radio wavelengths [53]. The complex morphology of the gas can be investigated with OH measurements. About 10% of the total molecular material of the Milky Way is found in the CMZ. Because of the high density, CRs entering the region will interact with the gas and produce γ rays from neutral pion decay. Therefore, the diffuse emission measured by e.g., Fermi LAT is tracing the gas with a gradient towards the central source. While being considered background when studying point sources, the diffuse emission can be used to investigate the underlying properties of the CRs [54].

7.2 Very High Energy Observations

The detection of TeV γ-ray emissions from the GC was first achieved by the Whipple γ-ray telescope in 2004 with a statistical significance of 3.7σ [55]. In the same year, H.E.S.S. detected a point-like source spatially aligned with Sgr A* within one arcsecond, designated HESS J1745-290, with a spectral index close to 2 [56]. Subsequent analysis revealed an exponential cutoff in its emission spectrum at about 10 TeV and no time variability [57]. With improved instrument pointing, the H.E.S.S. collaboration further confirmed a coincident localisation with the SMBH Sgr A* and additionally with the then newly discovered pulsar wind nebula (PWN) candidate G359.95-0.04 [58].

The point source HESS J1747−281 coinciding with the composite supernova remnant (SNR) G0.9+0.1 was first detected by H.E.S.S. in 2005 [59].

In 2016, the H.E.S.S. collaboration analysed the γ-ray diffuse emission extracted from an annulus centred on Sgr A* and found no evidence for a significant cutoff or break. The γ-ray signatures, inferred from neutral pion decay following proton-proton interactions, suggested the presence of a PeVatron - a cosmic accelerator capable of driving particles to PeV energies. A definitive correlation between the hypothesised PeVatron and HESS J1745-290 remained elusive [5].

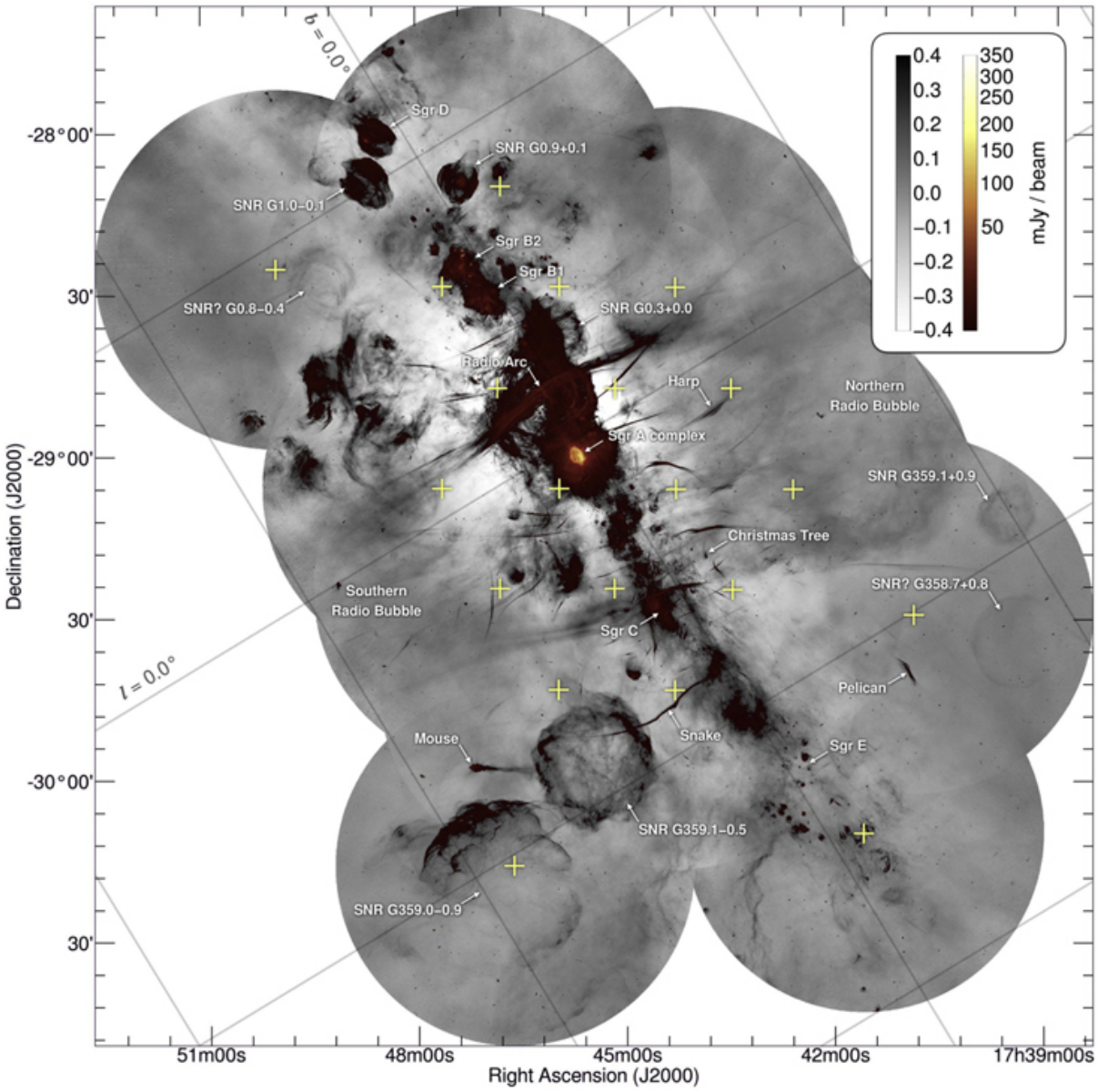

Figure 7.1: Radio image of the GC region: 1.28 GHz MeerKAT Mosaic 7 covering a 6.5° × 6.5° FoV. The mosaic is formed from 20 pointings, marked in the figure as '+', with an angular resolution of 4″. A dual colour scheme is employed to illustrate the faint end (linear greyscale) and the bright end (square-root stretched coloured scale). The projection is in equatorial coordinates and an overlaid grid shows the Galactic coordinates. The GC is located inside the Sgr A complex. Figure taken from [44].

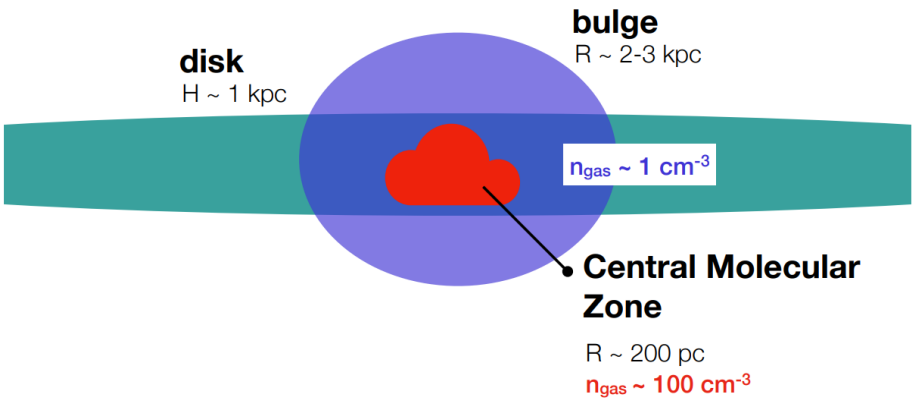

Figure 7.2: Sketch of the regions of the Galactic Centre with their respective sizes and gas densities. Illustration taken from [52].

Subsequent studies in 2018 analysed the morphology of the innermost 200 parsecs of the MW in detail [60]. Figure 7.3 shows the significance map from this study. The detected emission was found to be out of two components: one with a larger latitude extension not correlating with the dense matter in the CMZ, large-scale emission (LSC), and one of smaller extension which followed the dense matter distribution, CMZ diffuse emission. In addition for the latter, a strong gradient towards the GC was found. Since the CMZ diffuse emission originates from cosmic proton interaction with dense molecular gas, it can be inferred that the protons come from a single, central proton source. Again, spectral analysis of this diffuse emission revealed no significant cutoffs or curvatures, hinting towards a PeVatron in the centre of the MW. The LSC is due to CRs originating not from the GC itself but from the isotropic CR sea hence the lack of a gradient.

In the same paper, the detection of the point-like source HESS J1746-285 coincident with the GC radio arc has been published for the first time. The position of the source is consistent with that of the PWN candidate G0.13−0.11.

In comparison to the previously discussed H.E.S.S. publications on the GC, there is now more data available from this region. Furthermore, the 3D approach allows for the simultaneous analysis of the morphology and spectrum of γ-ray sources, which can help to distinguish overlapping sources, many of which are present in the GC, such as large-scale and CMZ diffuse emission. For this reason, the GC is revisited in the following chapter.

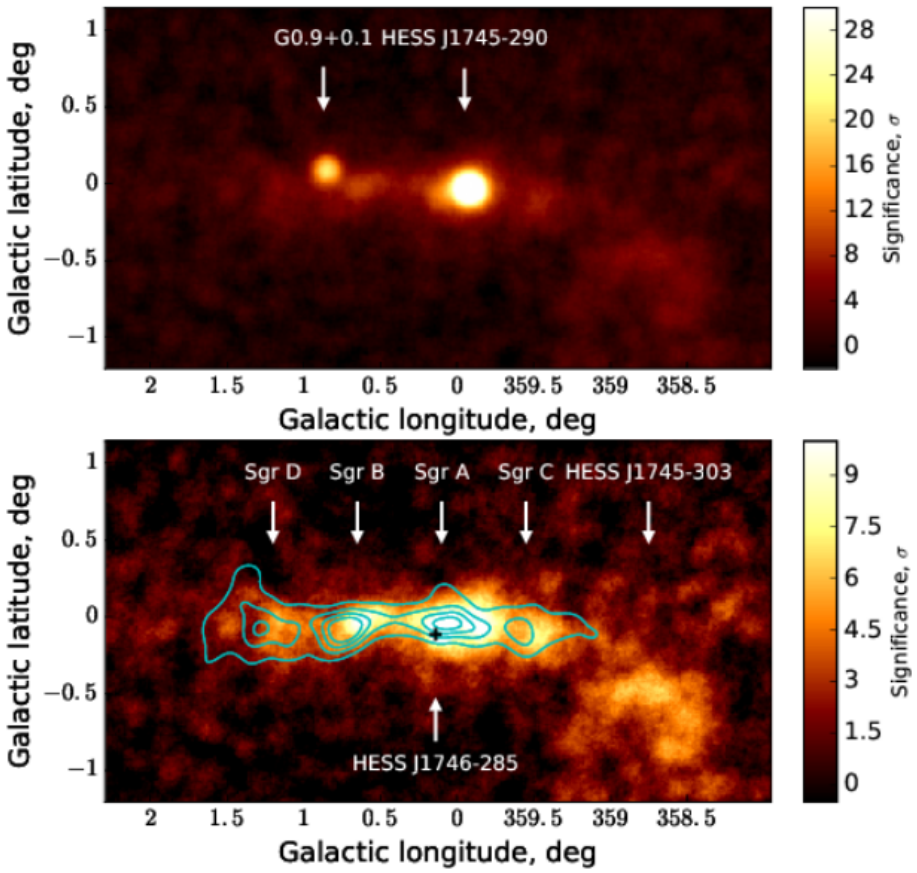

Figure 7.3: VHE γ-ray images of the GC region. Upper panel: Significance map. Lower panel: Significance map after the two strongest point sources, HESS J1745-290 and G0.9+0.1, are subtracted. The light blue contour indicates the density of the molecular clouds in the CMZ. Figure taken from [60].

Chapter 8

H.E.S.S. Dataset of the Galactic Centre

H.E.S.S. is an IACT array and its location in the southern hemisphere makes it an optimal site for observing the GC. This chapter will present the obtained dataset. Initially, the H.E.S.S. instrument will be introduced, followed by the data selection. Subsequently, the results of the run-wise fit of the background template in 3D in a region without γ-ray emitting sources will be presented. Finally, the single runs will be stacked in 3D into one dataset, and the properties of the dataset will be discussed.

8.1 The H.E.S.S. Instrument

The H.E.S.S. telescope system is located in the Khomas Highland in Namibia (see Figure 8.1). The rationale behind this choice was the minimal impact of light pollution from urban areas, the availability of an adequate infrastructure, a favourable climate with low cloud coverage and minimal precipitation, and political stability. Construction at an altitude of approximately 1800 m above sea level represents an optimal compromise between the maximum width of the shower development and atmospheric transparency [61]. Furthermore, the location in the southern hemisphere ensures the observation of the central part of the MW.

The telescope array consists of five telescopes, four of which (CT1-4) are smaller in size with 12 m (H.E.S.S. I era) and the larger CT5 with 28 m, which has been operational since 2012 (H.E.S.S. II era). In 2016 the cameras of the four smaller telescopes were upgraded (H.E.S.S. IU era). The four smaller telescopes are arranged in a grid with a side length of 120 m, with CT5 situated in the grid's centre.

The total tessellated mirror area of the CT1-4 telescopes is 107 m^2, comprising 380 round mirrors. The layout is based on a Davies-Cotton design with a 12 m diameter and a focal length of 15 m resulting in an f/d ratio of approximately 1.2. CT5's 876 hexagonal mirror facets result in a total area of 614 m^2. Instead of a Davies-Cotton layout, a parabolic layout was chosen to minimise the time dispersion. The f/d ratio is 1.3 since the focal length of the mirror is 28 m [16]. In order to ensure that all the mirror facets reflect into a single focus spot, a control system can be used to align each mirror facet. This allows the mirrored image of a star in the focal plane to be viewed by a CCD camera, with each mirror being adjusted until perfect coverage is achieved in the centre of the dish. This is crucial since the mirror alignment is closely related to the pointing accuracy and the optical PSF of the telescope.

Figure 8.1: Picture of the H.E.S.S. telescope array with the four smaller CT1-4 telescopes and the central CT5. Image credit: H.E.S.S. Collaboration, Clementina Medina[62].

The cameras of the CT1-4 telescopes have a field of view of 5° and consist of 960 photodetector elements. The larger camera of CT5 contains 2058 photomultipliers resulting in a field of view of 3.2° [62].

The H.E.S.S. telescope system is sensitive within an energy range from ∼30 GeV to ∼100 TeV. Observations of the target are conducted in 'runs' of 28 minutes. This allows the source of interest to be offset from the centre, which improves the estimation of the background due to symmetry. The quality of the data is monitored to ensure the reliability of the results of the high-level analysis.

8.2 Data Selection

The data employed in this work is from the H.E.S.S. I (March 2004 and October 2012) and H.E.S.S. II era (June 2013 and June 2015). The observation IDs of all runs used are listed in Tables 4 and 5. Data taken by CT5 is excluded in order to utilise the excellent stability of CT1-4. The benefit of CT5 is its lower energy threshold which is not a significant factor in the present analysis since the focus is on the higher energy range. Consequently, the data can be excluded without further consideration. The total number of runs utilised in both areas, along with the cumulative livetime, is presented in Table 8.1. The runs were selected via the internal H.E.S.S. analysis pipeline (*hap*) and the standard quality criteria were applied. This includes a maximum angular offset angle of 2° between the pointing direction and the Galactic Centre and a minimum run duration of 10 minutes. The required multiplicity was set to 4, i.e. all four telescopes took data. No runs with a zenith angle exceeding 42.5° were included. This value was selected to ensure a fair comparison and to verify the results with an addional dataset created with the *hap-fr* analysis chain, where this upper bound is set to avoid potential systematic uncertainties [63].

The distribution of zenith angles of the pointing positions is shown in Figure 8.2. Due to the geographical location of H.E.S.S. in the southern hemisphere, the average zenith angle is

	Number of runs	Livetime [hr]
H.E.S.S. I	375	174.5
H.E.S.S. II	200	89.9
Total	575	264.4

Table 8.1: Number of runs and resulting livetime for the H.E.S.S. I and H.E.S.S. II phase with a maximum zenith angle of 42.5°.

relatively small with 18.1° (17.6°) for H.E.S.S. I. (H.E.S.S. II).

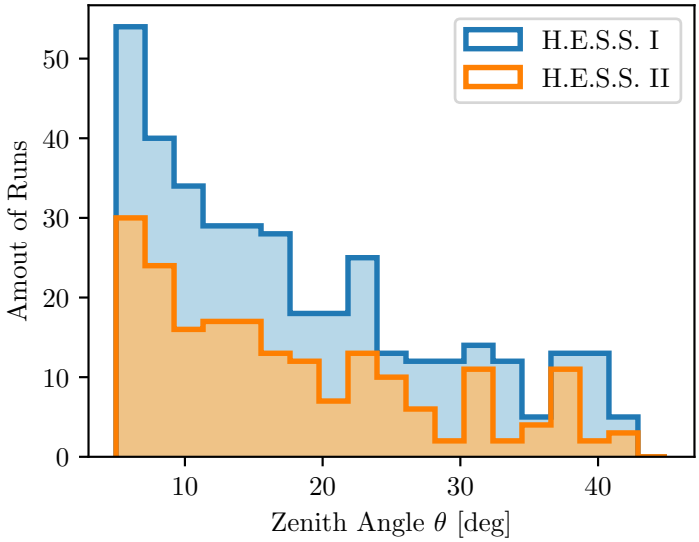

Figure 8.2: Zenith angle distribution of the pointing positions for the H.E.S.S. I and H.E.S.S. II observations of the GC

The dataset was created with two different configurations, designated as *std-zeta* and *std-ImPACT*. As previously described in the preceding chapter, in the *std-zeta* configuration the γ-hadron separation is performed with boosted decision trees, whereas in the *std-ImPACT* configuration image template fitting is used. The analysis of the GC is performed with both configurations to cross-check the physical results.

8.3 Run-wise Fit of the Background Template

A background template is assigned to each observation based on the pointing position. To correct for observational, atmospheric and telescope specific effects, the background normalisation is fitted to the data of the run, with regions exhibiting γ-ray emission excluded. Prior to this, a safe energy range must be defined.

In a 3D analysis as it is used here, two distinct types of thresholds are identified: the background threshold and the energy bias threshold. The former is set to avoid the background

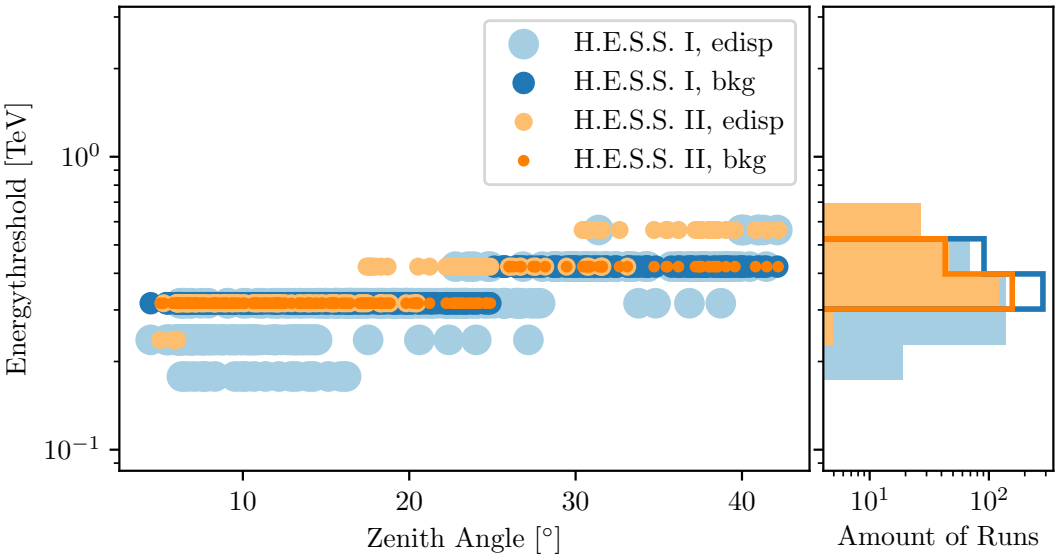

Figure 8.3: Energy threshold based on the background and the energy bias as a function of zenith angle for H.E.S.S. I and H.E.S.S. II

rate's statistical fluctuations which are more pronounced at energies proximate to the instrument threshold. Accordingly, the background energy threshold is defined as the upper edge of the energy bin containing the peak in the background rate (see section 1.5). The energy bias increases strongly at the lower energies. The energy threshold is selected in such a way that the energy bias does not exceed 10%. The two thresholds are calculated for all runs and are presented as a function of the zenith angle of the pointing direction in Figure 8.3. Both thresholds demonstrate a dependency on the zenith angle, which is to be expected given the observed decrease in the shower amplitude (see section 1.2). For both H.E.S.S. I and H.E.S.S. II, the energy bias threshold is lower compared to the background threshold for lower zenith angles and vice versa for the higher angles. It should be noted that an additional energy threshold of 0.4 TeV has been set in order to facilitate a more comprehensive comparison with other published studies of the GC. For each run the energy threshold is set to the maximum value of the background threshold, the energy dispersion threshold and the additional threshold.

In each run, the γ-ray emitting region along the Galactic Plane is excluded with a rectangular mask centred around the GC with width 4.3° and height 1.6°. The extended source HESS J1747-248 with a size of $0.061 \pm 0.012°$ is located within the FoV [33]. A circular mask with a radius of 0.28° is set around its position to remove contamination. Analogously, the excess from the source HESS J1745-303 is excluded with a circular mask with a radius of 0.7°. Assuming a Gaussian shape the source has an extension of $0.179 \pm 0.020°$ [33].

Furthermore, a mask is applied to exclude data that is not within a radius of two degrees of the pointing direction. This is to avoid systematic uncertainties arising from the PSF at larger angles.

The background template is modified by a power law:

$$\bar{b}(E) = nb(E) \cdot \left(\frac{E}{E_0}\right)^{-\Gamma}, \tag{8.1}$$

where $b(E)$ is the original background rate prediction at energy E, n is a normalisation, Γ a

spectral tilt and the reference energy E_0 is set to 1 TeV and fixed.

The best-fit normalisation and tilt for each run are presented in the histograms in Figure 8.4. In case of $n = 1$ and $\Gamma = 0$, the background rate remains unaltered, indicating an accurate description of the background in the run by the template. This is expected since the background rate is already pre-fitted during the creation. In the case of H.E.S.S. II the values are very close to the expected ones. In contrast, for H.E.S.S. I, the mean background normalisation is smaller than one. This indicates the need to account for atmospheric variations or mirror degradation and the resulting reduction in detected background photons. Furthermore, the background tilt is on average fitted to a value larger than 0. Given that the observed discrepancies are minimal and that the potential implications of background systematics remain under discussion, it seems appropriate at this stage to disregard these discrepancies.

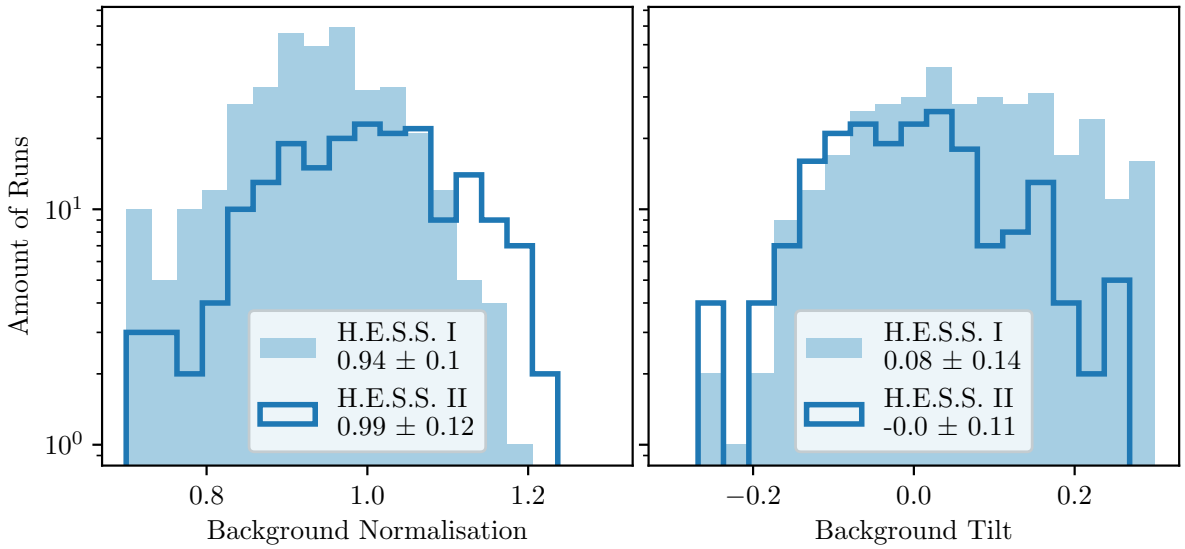

Figure 8.4: Distribution of the best-fit background normalisations and title in the run-wise fit for H.E.S.S. I and H.E.S.S. II

8.4 Significance Map and IRFs of the Stacked Dataset

Once the background of each run has been fitted, the observations are stacked to create a single final dataset. Hereby the individual energy thresholds and the circular mask with a radius of 2° around the pointing direction are preserved. The dataset is then cropped to a 6° × 4° FoV with a spatial bin size of 0.02°. The energy bins are logarithmically spaced between 0.1 TeV and 100 TeV, with 24 bins in total (both true and reconstructed energy). The resulting counts and background map summed along the energy axis is shown in Figure 8.5. The central source is clearly the strongest emission in the FoV. If the background is subtracted from the counts, the γ-ray excess is obtained.

This excess can be expressed in terms of significance. The significance map of the stacked dataset is shown in Figure 8.6. In the upper panel, the strongest point source in the centre HESS J1745-290 can be seen. The second strongest emission is measured from the SNR G0.9+0.1.

To visualise the weaker emission in the region, these two strong point sources and the large-scale emission are accounted for with a 3D likelihood fit and the significance map is recomputed

which is shown in the lower panel of Figure 8.6. The large-scale emission is due to the isotropic CR sea producing γ rays through interactions with gas. The leftover diffuse emission traces the dense gas component of the CMZ visualized as a light blue contour.

Note that the region around HESS J1745-303 (at $l = 358.9°$, $b = -0.5°$ [64]) is excluded in both the published analysis from 2018 [60] and in this present study. The extended source has no confirmed counterpart and is due to its complex morphology difficult to model. To avoid contamination from this unrelated emission, a circular mask with a radius of 0.7° is used unless otherwise specified.

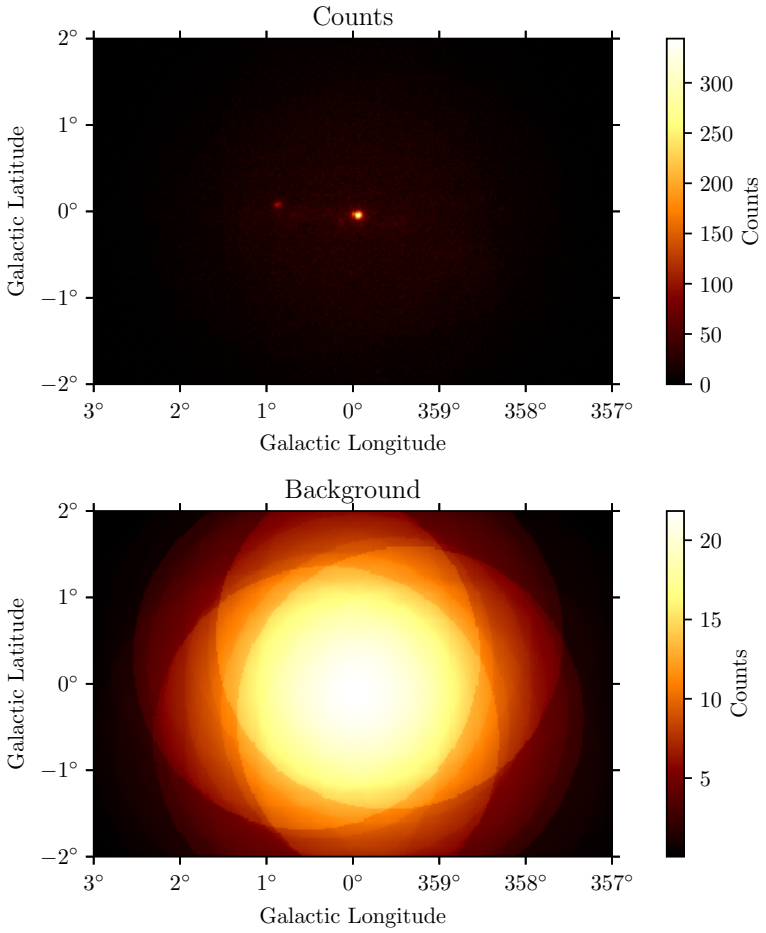

Figure 8.5: Upper panel: Counts of the stacked dataset summed along all energy bins; Lower panel: Background prediction the stacked datasets summed along all energy bins

In order to account for the measured excess the predicted count for the different model components, the flux prediction is forward folded through the IRFs (see section 2.1). The IRFs of the H.E.S.S. GC dataset are now presented.

Figure 8.7 illustrates the effective area, calculated as a cumulative sum across all true energy levels. The data were obtained with the telescope pointed at various positions, indicated by the blue dots on the map. The effective area is dependent on the offset angle relative to the centre. To illustrate this, the effective area at the centre of the FoV (0° offset) and at 1° offset are shown

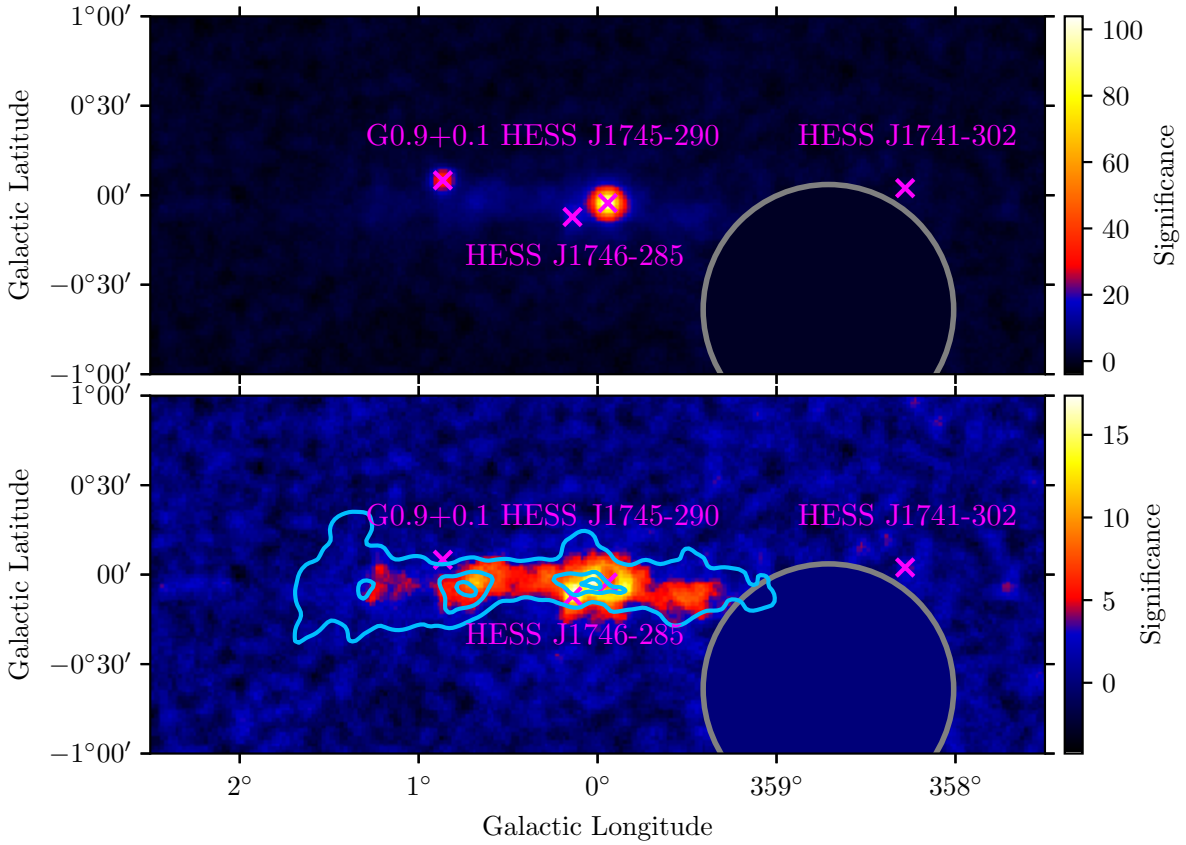

Figure 8.6: H.E.S.S. significance map for energies >0.4 TeV with a 2D top-hat filter of the size of the 68% containment radius at E_{true} = 1 TeV (0.05°). The positions of the four H.E.S.S. point-like sources are indicated as magenta crosses. The lower panel shows the excess map after modelling the two strongest point sources (HESS J1745-290 and G0.9+0.1) and the large-scale component. The light blue contour illustrates the distribution of the gas in the CMZ. The region within the grey circle is masked to exclude emission from HESS J1745-303.

as a function of true energy in Figure 8.8. As lower energy events are less likely to trigger the system, the effective area is smaller at the lowest energies.

The energy dispersion matrix of the stacked GC dataset is shown in Figure 8.9 (a). For each true energy the energy bias was computed and plotted in Figure 8.9 (b). The sharp increase of the energy bias at lower energies is due to downward fluctuations in Cherenkov light that cause some low-energy events to fall below the trigger threshold. At the highest energies, the negative bias arises from saturation effects in the camera, where the signal exceeds the dynamic range of the readout system, as well as from image leakage, where part of the shower image extends beyond the camera edge and is therefore not fully reconstructed, both leading to an underestimation of the reconstructed energy.

The PSF as a function of the θ^2, the squared distance between p_{true} and p_{reco} is shown for different true energies in Figure 8.10 (a). As expected, for higher energies the PSF degrades progressively. The 68% and 95% containment radii are computed for each true energy and shown in Figure 8.10 (b). The containment radius at higher energies is better for positions at the centre

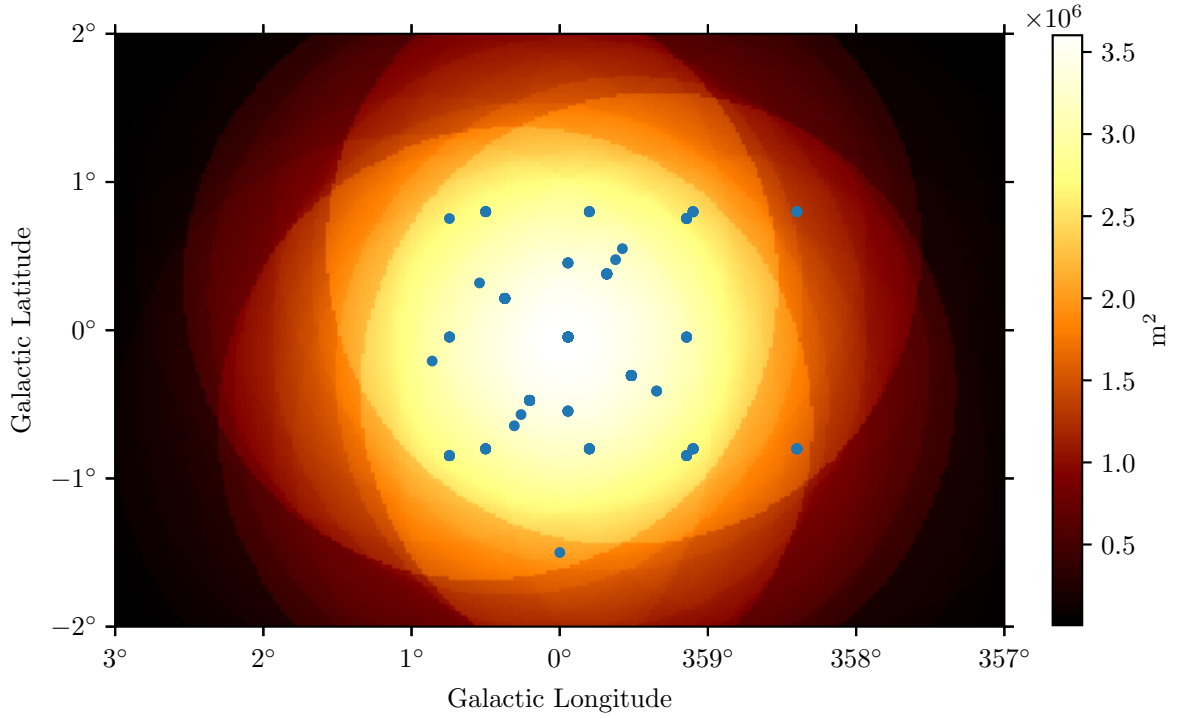

Figure 8.7: The effective area of the H.E.S.S. dataset used in this work. The different pointing positions of the runs are illustrated as blue dots.

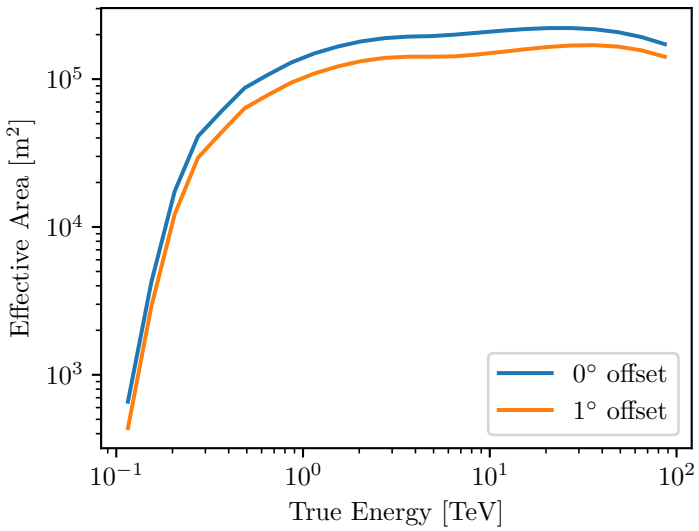

Figure 8.8: The effective area as a function of true energy at 0° offset from the centre of the FoV and at 1° offset.

of the FoV compared to a position with a 1° offset. At $E_{\text{true}} = 1\,\text{TeV}$ the 68% containment radius is 0.05°.

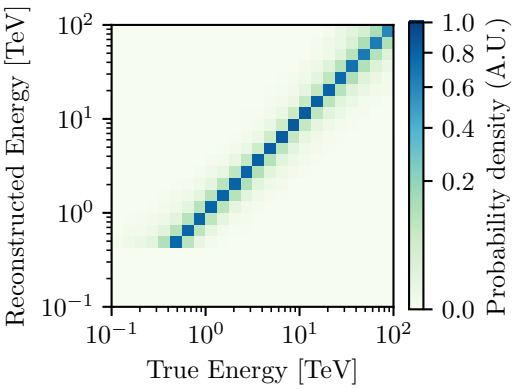

(a) Energy dispersion matrix

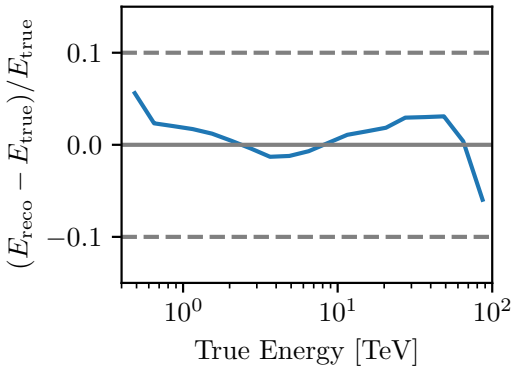

(b) Energy bias as a function of true energy

Figure 8.9: Energy dispersion from H.E.S.S observations of the GC with CT1-4 used in this work.

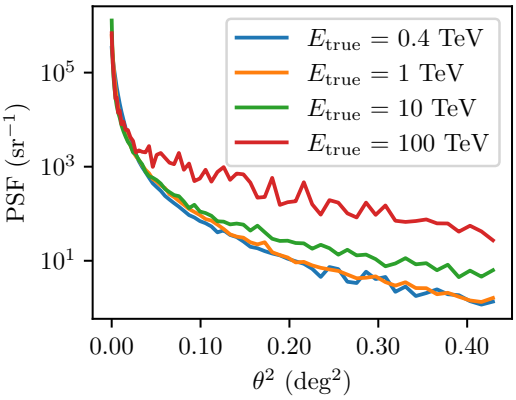

(a) PSF as a function of the squared distance between p_{true} and p_{reco} for different true energies.

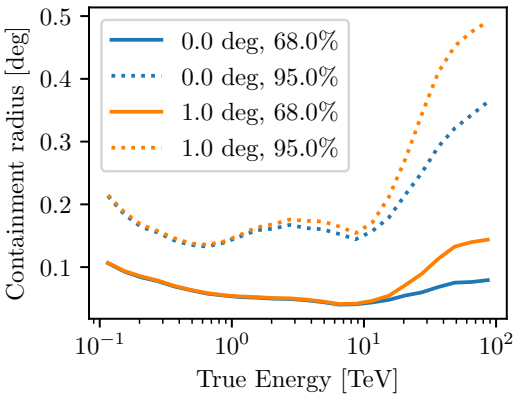

(b) 68% and the 95% Containment radii as a function of true energy at the center of the FoV and at 1 deg offset.

Figure 8.10: PSF from H.E.S.S observations of the GC with CT1-4 used in this work.

Chapter 9

Analysis of the γ-ray Sources in the Galactic Centre

This section presents the results of the application of different source models to the data of the GC region. First, the individual model components are presented in detail and afterwards, the fit qualitiy is reviewed.

The model components are:

- the four known point sources: HESS J1745−290, HESS J1747−281 (the PWN G0.9+0.1), HESS J1741−302 and HESS J1746−285
- the large-scale foreground emission (LSC)
- the diffuse emission in the CMZ
- the hadronic background.

The latter is modified with a piece-wise model consisting of normalising nuisance parameters with priors as described in part I. Details will be discussed in the following chapter about the treatment of systematic uncertainties.

9.1 Point Sources

Four known γ-ray sources are within the FoV: HESS J1745−290, HESS J1747−281 (the PWN G0.9+0.1), HESS J1741−302 and HESS J1746−285. Due to their spatial extent being smaller than that of the H.E.S.S. PSF, these sources are considered point-like. Consequently, only their position (longitude, latitude) is fitted. The relevant parameters are listed in Table 9.1 and shown in Figure 9.1. In the latter the best-fit positions are compared to values published in [33] which demonstrates a high level of compatibility.

The spectra of the point sources are modelled per default with a simple power law:

$$\frac{d\phi}{dE_{\mathrm{true}}} = \phi_0 \left(\frac{E_{\mathrm{true}}}{E_0} \right)^{-\Gamma} \tag{9.1}$$

with ϕ_0 and Γ being respectively the normalization (in TeV^{-1} cm^{-2} s^{-1}) and the spectral index. The reference energy E_0 is fixed to 1 TeV for all the sources.

Source	lon [°], lat [°]	N_0 [TeV^{-1} cm^{-2} s^{-1}]	Γ	$1/\lambda = E_{\mathrm{cut}}$ [TeV]
HESS J1745-290	359.943° ± 0.001°	$(2.08 \pm 0.06) \times 10^{-12}$	2.00 ± 0.05	10.63 ± 1.77
	-0.044° ± 0.001°			
G0.9+0.1	0.865° ± 0.001°	$(0.83 \pm 0.06) \times 10^{-12}$	2.06 ± 0.10	6.93 ± 2.10
	0.083° ± 0.001°			
HESS J1746-285	0.140° ± 0.004°	$(0.11 \pm 0.02) \times 10^{-12}$	2.02 ± 0.10	
	-0.121° ± 0.004°			
HESS J1741-302	358.281° ± 0.008°	$(0.08 \pm 0.02) \times 10^{-12}$	2.07 ± 0.20	
	0.040° ± 0.008°			

Table 9.1: Best-fit spatial and spectral parameters of the known H.E.S.S. point sources. In addition to these point source models, the LSC, the diffuse emission in the CMZ, and the hadronic background - modelled with nuisance parameters - were included in the fit.

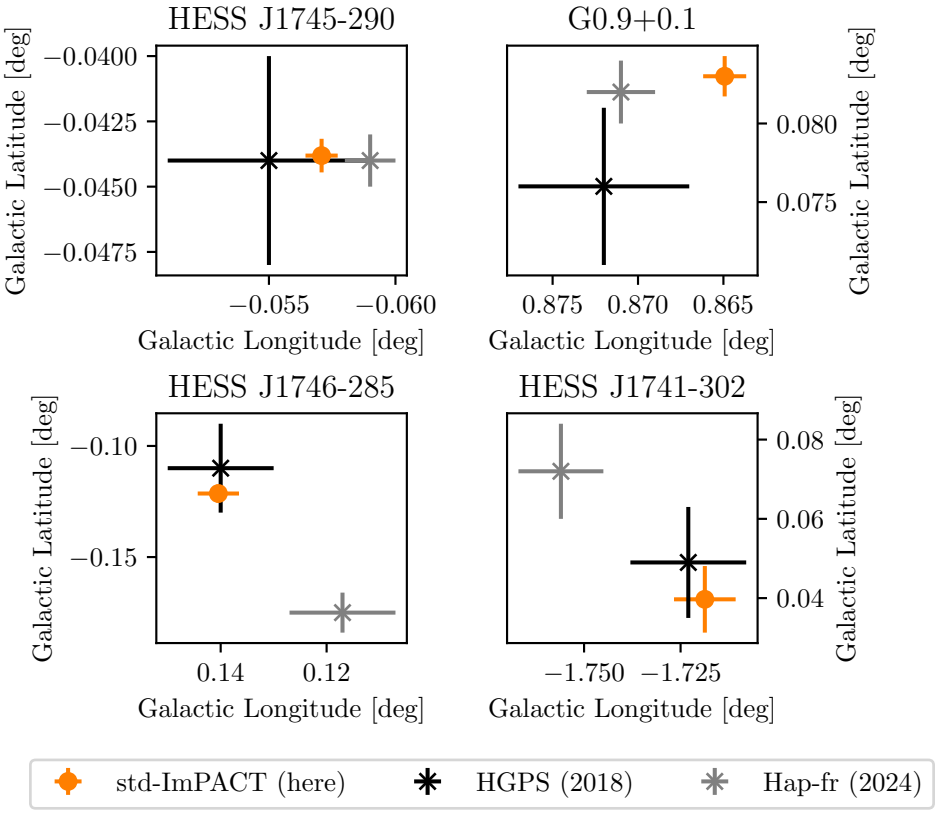

Figure 9.1: Best-fit position of the four point sources compared to the H.E.S.S. galactic plane survey [33] and to an analog analysis performed with the *hap-fr* chain [63].

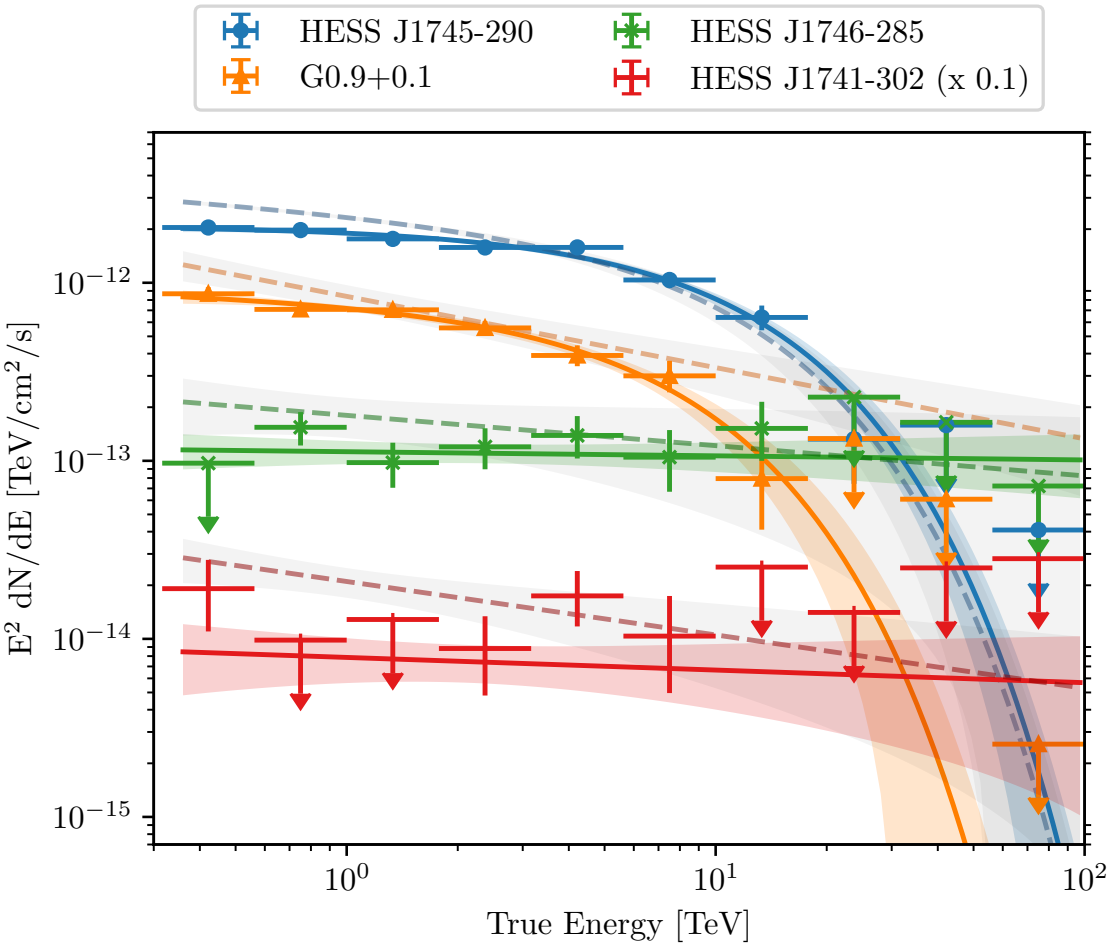

Figure 9.2: Best-fit spectra of the point sources with flux points and 1σ error band compared to the spectra from [33] shown as the dashed darker line with 1σ error indicated as the grey error band.

HESS J1745-290 is known to have a significant cutoff and therefore a power law with exponential cutoff (ECPL) is used:

$$\frac{d\phi}{dE_{\text{true}}} = \phi_0 \left(\frac{E_{\text{true}}}{E_0} \right)^{-\Gamma} \exp(-\lambda E_{\text{true}})) \tag{9.2}$$

where λ is the inverted cutoff energy E_{cut} (in 1/TeV).

The obtained best-fit spectral values are listed in Table 9.1. The resulting spectra with 1σ error band and flux points are shown in Figure 9.2. Note that in this thesis, the flux points are shown as upper limits if their $\Delta TS < 4$. The parameters are compared to the values cited in [33] and are consistent within approximatly 2σ. Deviations are due to the different analysis techniques employed. The flux points at the higher energies for G0.9+0.1 were significantly below the spectrum and therefore an exponential cutoff at 6.93 ± 2.10 TeV was introduced in the spectrum. By doing so the results improved with a significance of 4.41σ. Figure 8 shows the best-fit spectrum with and without exponential cutoff.

9.2 Large-Scale Diffuse Emission

The first investigation of the diffuse emission in the TeV range was conduced by H.E.S.S. (2006) [60]. Hereby, data from the Galactic Plane Survey in regions without known γ-ray sources was analysed. Prior, this kind of excess has been investigated only in the GeV range.

The emission observed along the Galactic Plane was interpreted as a superposition of diffuse γ-ray emission from CRs interacting with interstellar matter (i.e. the Galactic diffuse component) and contributions from unresolved γ-ray sources located in the GC region. It was found that the decay of neutral pions into γ rays, a process occurring when CRs interact with interstellar matter, contributes significantly to the large-scale γ-ray emission. Within the inner region of the GC the diffuse γ-ray emission can be split into two components: one with a larger latitude extension not correlating with dense gas tracers (large-scale emission) and one with a smaller latitude and longitude extension distributed like dense gas with a gradient towards the central source (CMZ) [60]. The main difference between the two components is the origin of the parent CRs. Generally, once CRs travel sufficiently far from their origin, they become isotropised due to the Galactic magnetic fields [65]. This forms the isotropic CR sea, which generates large-scale γ-ray emission in the GC through interactions with interstellar matter, primarily via neutral pion decay. The CMZ emission is due to CR diffusion from the central source, hence the gradient.

Here the morphology of the LSC is modelled as a 2D Gaussian along the Galactic Longitude, where the latitude extension is a free parameter. The width is fitted to $\sigma = 0.46° \pm 0.03°$. The resulting morphology of the count prediction is shown in Figure 9.3 (a). The spectral shape of the LSC was assumed to be a simple power law which resulted in a best-fit index of 2.46 ± 0.05. The spectrum and the flux points are shown in Figure 9.3 (b). Note, how the highest fluxpoint is below the spectrum indicating a cutoff. Indeed when exchanging the simple power law with an exponential cutoff power law, there is an improvement with a statisical significance of 5.13σ. The spectral index is decreased to 2.01 ± 0.10 and the cutoff is found to be at 10.83 ± 2.94 TeV. The recomputed flux points are in a good agreement with the best-fit spectrum.

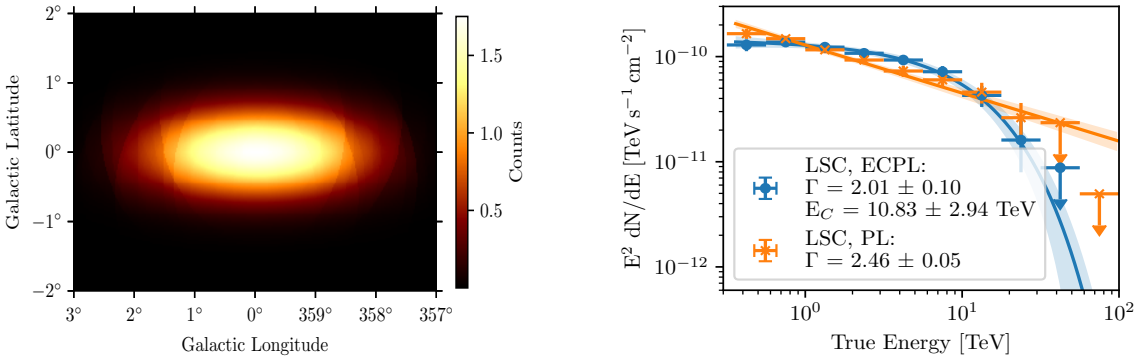

(a) Spatial morphology of the best-fit count prediction summed over all energies

(b) Best-fit spectra of the LSC with and without cutoff.

Figure 9.3: Best-fit results of the LSC modelled with a band model and a power law with and without exponential cutoff. In addition the point osources, the CMZ and the hadronic background - modelled with nuisance parameters - were included in the fit.

9.3 Diffuse Emission in the CMZ

The last component neccersary to fully describe the data of the GC measured by H.E.S.S. is the diffuse emission in the CMZ. The emission is assumed to be the reusult of a proton source at the position of Sgr A* which is continuously injecting protons in the surrounding neighbourhood. These protons diffuse outwards until they interact with the dense gas in the CMZ. In these interactions, neutral pions are produced which decay into γ rays which travel directy to Earth where they are measured. The morphology of the γ-ray emission therefore traces the gas with a gradient towards the GC where the source of protons is. Figures 9.4 and 9.5 illustrate the two components needed to construct a model of the γ-ray morphology. The former shows the dense gas distribution. This is based on two different measurement of emission and absoption lines (CS, CO) which are present in the gas. Note that the gas distribution is in three dimensions (Galactic Longitude, Galactic Latitude and the line-of-sight position z) but is here shown in only two dimensions (Galactic Longitude and latitude). Here z is the depth of the gas clouds. The three dimensional distribution is result of a mapping of 'edge-on' (Galactic Longitude and latitude) and 'face-on' (Galactic Longitude and z) information obtained from different measurement principles.

The continuous diffusing protons have a $1/r$ distribution centered around Sgr A* as shown in Figure 9.5. The product of the gas distribution and the diffused protons results in Figure 9.6, the morphology of the γ rays. This approach to model the morphology of the CMZ will in the following be referred to as the template-based model.

The spectrum of the CMZ γ rays is determined by the spectrum of the inital proton source. The spectral index Γ_γ is depending on the spectral index of the proton source and on the energy dependence of their diffusion. If the inital source has a cutoff E_c, this would translate to a cutoff in the γ ray spectrum at $E_{c,\gamma} \approx 10\% E_c$. This relation arises because, in hadronic interactions, only about 10% of the primary proton energy is transferred to neutral pions that decay into γ rays.

If the γ ray spectrum is modelled with a simple power law, the spectral index was fitted to 2.42 ± 0.03 with an amplitude of $(7.82 \pm 2.23) \cdot 10^{-14}$ TeV^{-1} cm^{-2} s^{-1}. The best-fit spectrum with the 1σ error bar and the flux points are shown in Figure 9.7. Note how the last three flux points are below the spectrum. At the highest energybin $[54, 100]$ TeV, the upper limit is smaller by at least a factor of 3. This indicates an incorrect and overpredicting description of the CMZ. Therfore, an exponential cutoff is introduced in the power law. When fitting with the maximum likelihood method, a smaller spectral index of 2.24 ± 0.05 is revealed and an exponential cutoff at 23.59 ± 6.79 TeV. The γ-ray spectrum with the exponential cutoff is preferred by 4.77σ. Figure 9.8 shows the likelihood scan as a function of the γ-ray cutoff energy. The asymetric uncertainties are computed to $23.6^{+8.46}_{-5.6}$ TeV and the 95% upper limit is 40.3 TeV. From this result it can be concluded that a cutoff < 1000 TeV is also favoured for the proton spectrum. This cutoff represents a new finding in comparison to the published H.E.S.S. results from 2018 [60]. In the previous study, the absence of a cutoff led to the conclusion that the initial proton source is a PeVatron, which is a source that accelerates CRs up to PeV energies, resulting in γ-ray energies of 100 TeV. The presence of this cutoff with a significance of almost 5σ calls for further investigation to confirm or reject the hypothesis.

9.4 Fit Quality

The Li&Ma significance map computed over all energy bins after the fit of all model components is shown in Figure 9.9. The positions and contours of the individual model components are

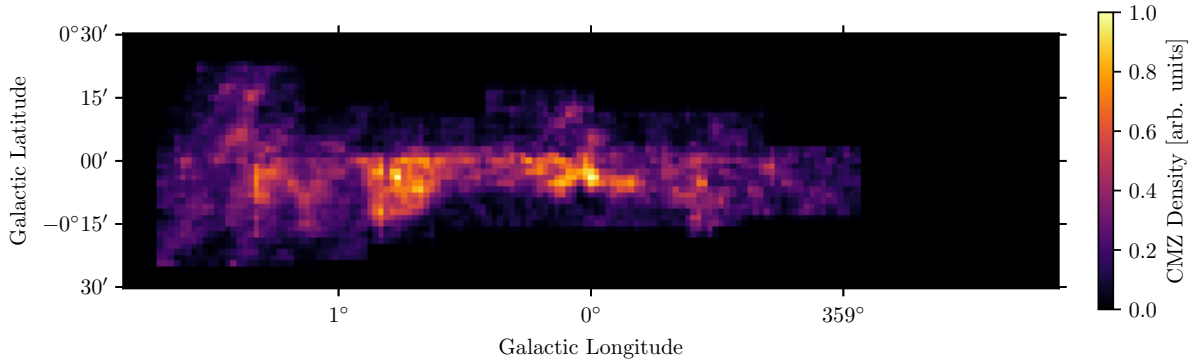

Figure 9.4: Gas distribution in the CMZ constructed from the measurements by [66] and [67]

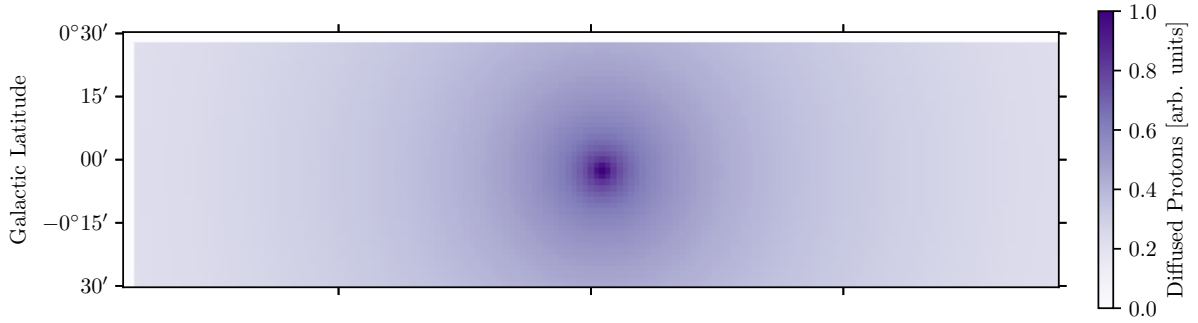

Figure 9.5: Diffused protons following a $1/r$ distribution of the continous diffuse emission scenario

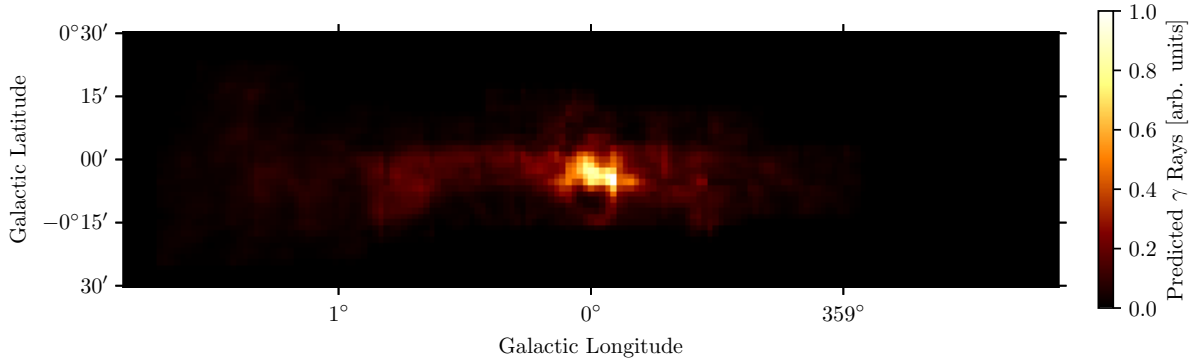

Figure 9.6: γ-ray emission resulting from the interaction of the diffused protons with the gas.

indicated. The mean of the significance distribution is -0.04 and the standard deviation 1.06. If only the statistical uncertainties are left in the data and all the excess is correctly modelled, one expects these values to be close to 0 and 1, respectively. Since the observed values are close and spatial distribution is flat a very good description of the data is indicated. The only excess left unmodelled in the dataset is at the positions of the molecular complexes Sgr B and Sgr C. This will be discussed in part III.

In order to ensure a comprehensive description of the data at different energies, the significance

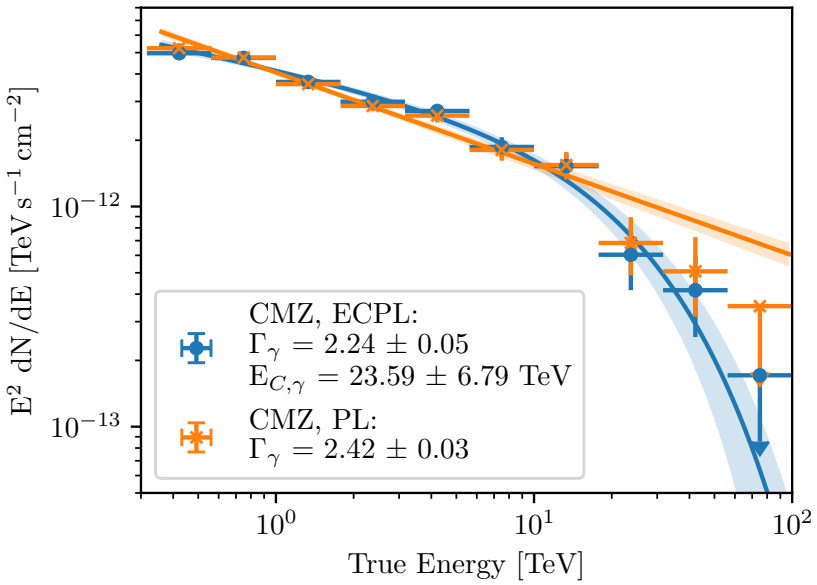

Figure 9.7: Best-fit spectrum and flux points of the CMZ modelled with a template diffusion model of Galactic protons with and without an initial exponential cutoff. Note that the spectral parameters relate to the γ-ray spectrum and not the initial proton spectrum.

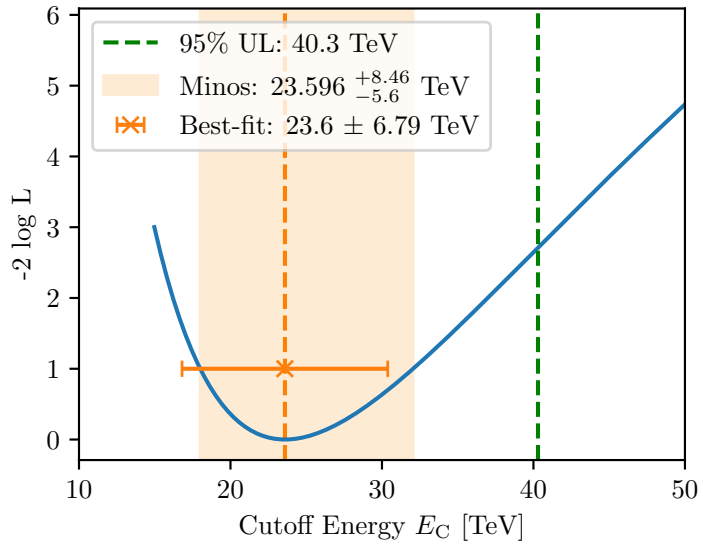

Figure 9.8: Likelihood scan as a function of the γ-ray cutoff energy. The symmetric 1σ uncertainty obtained from the fit and the asymmetric uncertainty from the scan are indicated. Additionally, the 95% upper limit is computed.

of the Li&Ma distribution is computed within three energy bins (Figure 9.10). In all bins, the distribution is flat indicating that the excess is well modelled. This is further verified by the distribution of the significance maps which are shown in Figure 9.11. The mean and standard deviation values are in close proximity to the expected values. However, for the last energy bin

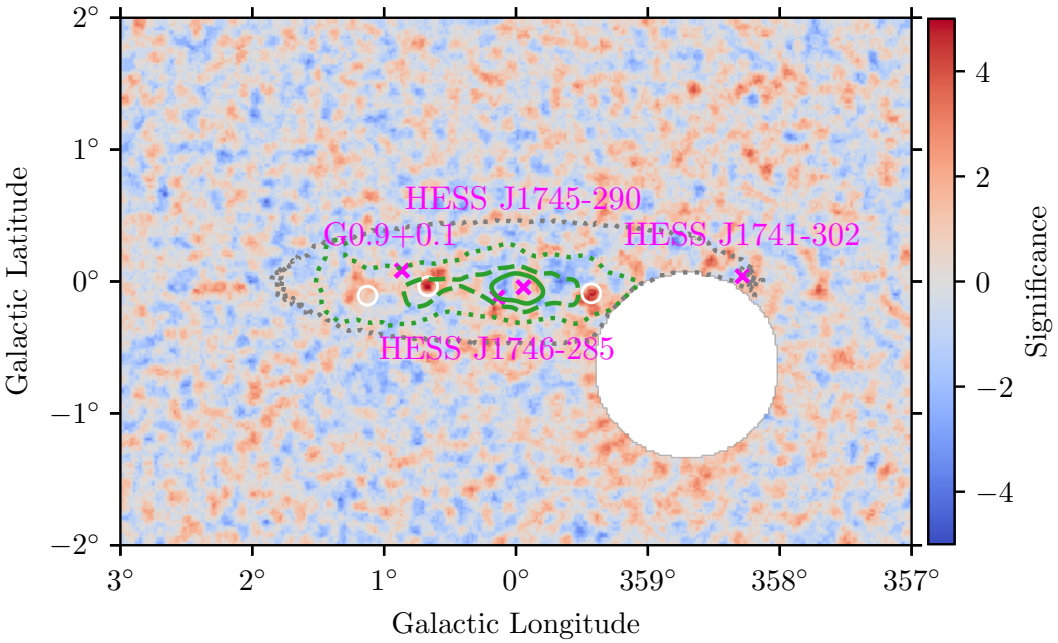

Figure 9.9: Li&Ma significance map of the dataset after the fit of all listed model components. A 2D top-hat filter is applied, averaging the values within a circular region of radius 0.05° (68% containment radius of the PSF). The positions of the point sources are indicated with magenta crosses. The green dotted, dashed and solid lines are the 1σ, 5σ, and 10σ contours of the CMZ diffuse emission, respectively. The dotted grey contour is the 1σ contour of the large-scale emission. The white circles indicate the location of the molecular complexes (Sgr D, Sgr B and Sgr C from left to right).

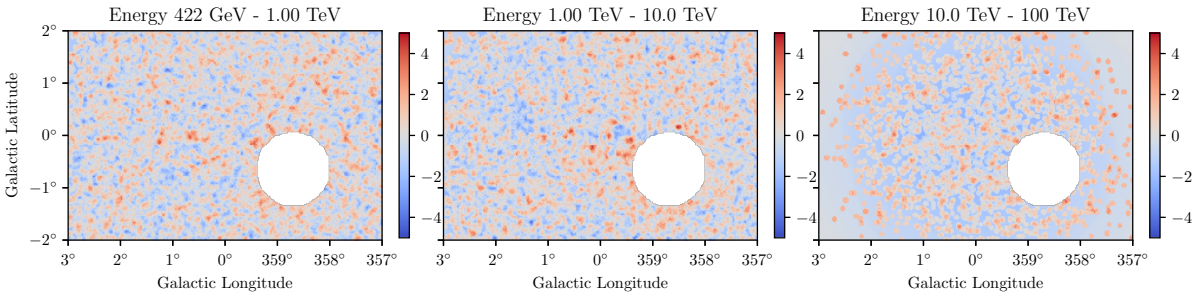

Figure 9.10: Li&Ma significance map in three energy bins with a 2D top-hat filter with radius 0.05° applied.

between 10 TeV and 100 TeV the reduced available statistics are causing deviations from the normal distribution.

To further verify the fitting of the modelling components, a spatial profile along the Galactic Latitude and Longitude is computed (Figure 9.12). In the latter, the reduced excess is due to the applied mask around HESS J1745-303. The strong contributions of the point sources HESS J1745-290 and HESS J1747-281 can be seen. Both the CMZ diffuse emission and the large-scale emission exhibit an extended distribution along the Galactic Longitude, with the

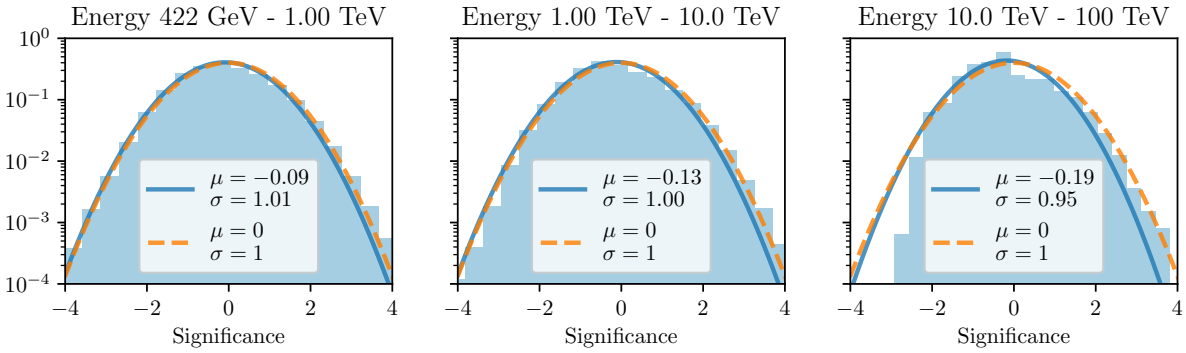

Figure 9.11: The distribution of the Li&Ma significance map in three energy bins with a 2D top-hat filter with radius 0.05° applied shown in Figure 9.10. The mean and standard deviation of the distribution were calculated and a Gaussian with the corresponding values is shown (blue). As a comparison, the normal distribution is shown in dashed orange.

latter exhibiting a larger extent also along the Galactic Latitude. The residual points are evenly distributed around zero, which again demonstrates a very good description of the FoV.

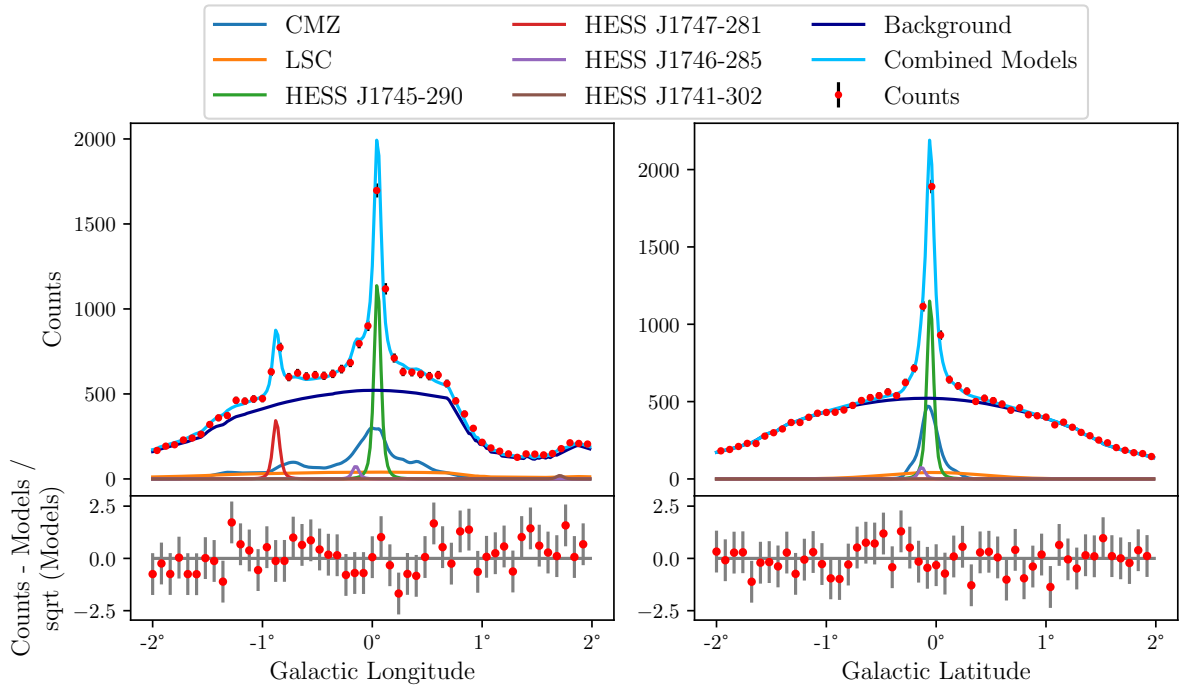

Figure 9.12: Profiles of the counts and the model prediction maps computed within a (left) 0.5° x 4° and (right) 4° x 0.5° region. The maps are summed up along all energies. For better visibility, the counts are rebinned by a factor of 4 resulting in a spatial binning of 0.08°. The lower panels show the residuals of the counts with the combined models.

Figure 9.13 illustrates the counts of the total FoV as a function of the energy. The hadronic background is the dominating model component followed by the CMZ and the large-scale emission. The residual points are close to zero indicating a good description of the data in every energy

bin.

In conclusion, it can be stated that the GC dataset is accurately modelled. This was done through the utilisation of significance maps and their distribution, as well as through the analysis of spatial and spectral profiles.

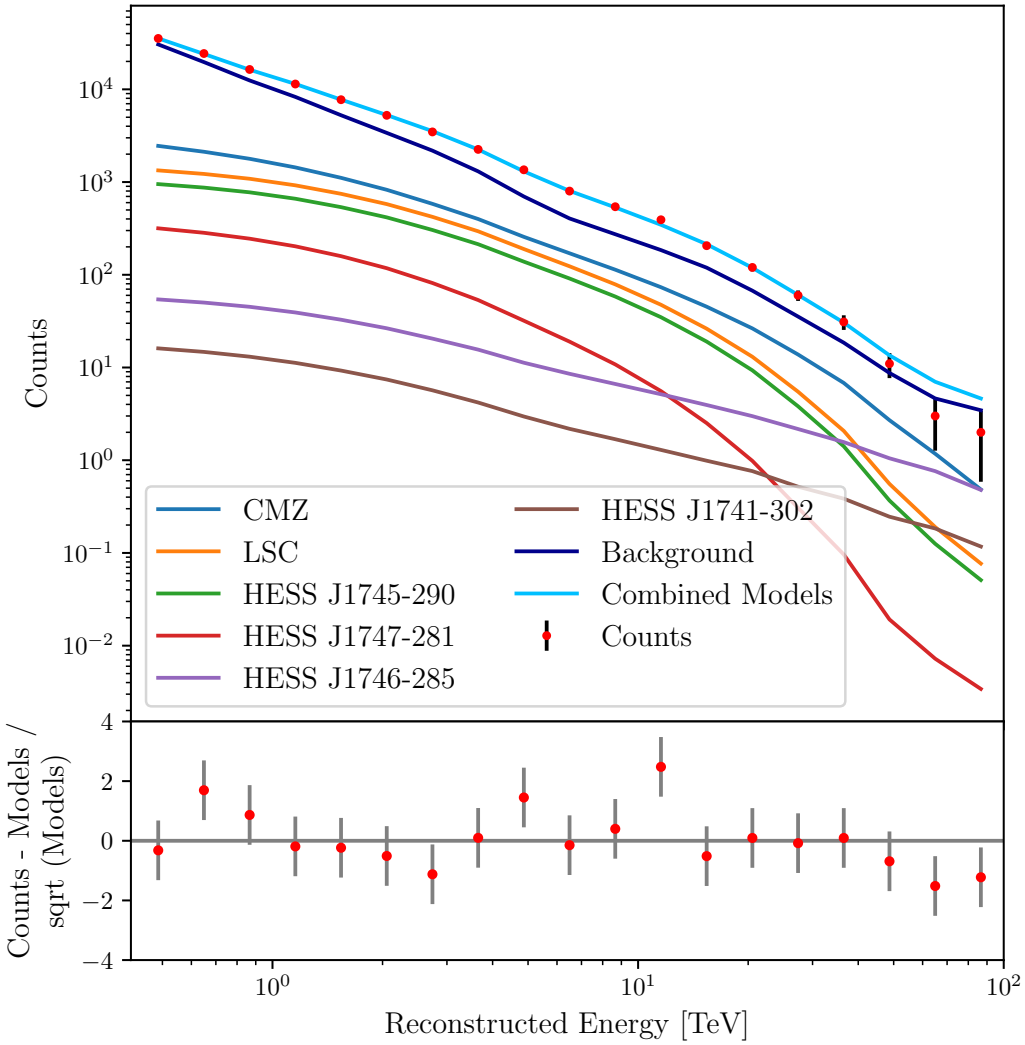

Figure 9.13: Counts and model prediction of the single components within the complete FoV as a function of reconstructed energy. The residual points in the lower panel are computed with the combined models.

In other energy ranges, giant structures in the Galactic Halo have been measured, such as the Fermi and eROSITA bubbles [50],[51]. It is believed that energetic outflow from the GC is the cause. A recent H.E.S.S. study revealed excess spatially coincident with the base of the Fermi bubbles [68]. The region where this excess was found is partially within the FoV analysed here at approximate $l = 359° - 358°$ and $b = 1° - 3°$. In the residual maps no excess in this region can be seen. This might be due to the fact, that the study uses about twice as much data than here and is therefore about 1.4 times more sensitive to the relatively weak excess. Additionally, the pointing positions of the data used here is more centred within the inner $\sim 2°$. Therefore,

the effective area is a lot smaller at the region were the excess was found. The study's additional data is from the H.E.S.S. IU era where the pointing was more in the direction of the excess. It can therefore be concluded, that there is no reason to assume that not taking the modelling of the Fermi bubbles into account would significantly change the results found here.

Chapter 10

Systematic Uncertainties and Cross-checks

This chapter is dedicated to the study of systematic uncertainties and cross-checks. In the default configuration, the hadronic background template is modified with a normalising power law characterised by a specific spectral index. However, there is no clear physical rationale for this spectral shape, and the lack of flexibility of the model is causing mismodelling. The issue of mismodelling was addressed by exchanging the power law model with a more complex piece-wise model, in which a normalising nuisance parameter was introduced in each energy bin. Note that this was already done in the previous chapter and now the choice is validated by comparing the utilised piece-wise model to the power law. The results of this comparison are presented in the first section of this chapter. Subsequently, the analysis was repeated with a different H.E.S.S. reconstruction, *std-zeta*, in which a different γ-hadron separation was employed.

10.1 Hadronic Background Template

As described in section 1.5, the background template is obtained for each run from archival H.E.S.S. observations off γ-ray sources or masked γ-ray emitting regions which are applied to each run. Afterwards, the background template is fitted with a normalised power law to the run before stacking them to a dataset. During the fitting of the stacked dataset, the background is again allowed to vary. This variation is per default parameterised by a PL (see equation 8.1). The choice of the power law as the modifying spectrum is however not physically motivated and is with its simplicity not able to account for smaller-scaled discrepancies between model and data.

If all the introduced model components (point sources, CMZ and LSC) as well as the power law to modify the background are fitted to the data, the best-fit values of the PL are 0.992 ± 0.003 for the normalisation and 0.013 ± 0.004 for the spectral tilt. The spectral residuals are non-neglectable (see Figure 10.1 (a)). Especially in the two lowest energy bins the models do not match the data well. The background modification as a function of energy is shown in Figure 10.1 (b).

To better describe the data a more complex spectral model was used to modify the hadronic background. In each energy bin i a normalising nuisance parameter δ_i is introduced. The magnitude and the correlation between the energy bins of the hadronic systematic uncertainties are quantified in a correlation matrix which is included in the prior. This was already introduced

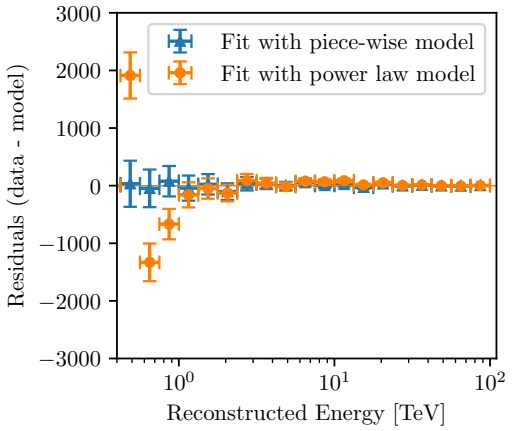

(a) Residual points computed in the source free region for each energy bin.

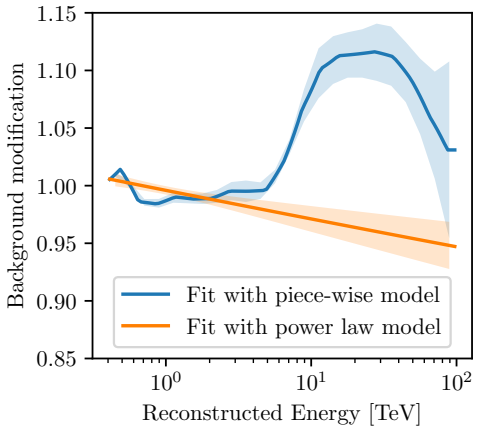

(b) Best-fit spectral modification as a function of energy

Figure 10.1: Results obtained with different spectral models to modify the background: power law (PL), piece-wise spectral model with $\sigma_{\mathrm{bkg}} = 10\%$ and $\mathrm{l}_{\mathrm{corr}} = 2$

in chapter 5.

The covariance matrix is of Gaussian shape with magnitude σ_{bkg} and correlation length $\mathrm{l}_{\mathrm{corr}}$. σ_{bkg} quantifies the systematic uncertainties of the background and is in terms of percentage. The value is estimated based on previous studies on background systematic uncertainties of a 3D background template by K. Nakashima [69]. In the reference, the systematic error is calculated for a H.E.S.S. dataset containing almost the same observations of the GC as are used in this work. The magnitude was found to be in the order of 10% which is adapted for σ_{bkg} here.

The optimal $\mathrm{l}_{\mathrm{corr}}$ is determined in the following. As an initial starting point $\mathrm{l}_{\mathrm{corr}} = 2$ is chosen. The resulting covariance matrix is shown in Figure 10.2. As a reminder, the dataset has 24 energy bins logarithmically spaced between 0.1 TeV and 100 TeV, yet a minimal energy threshold of 0.4 TeV. Therefore, the first four nuisance parameters modifying the background are frozen and the covariance matrix is such that there is no correlation between the frozen and free parameters. With this covariance matrix set in the prior, the dataset is refitted. In the absence of the nuisance parameters, the spectral residual points are of a poor quality. However, when these are included in the fit, the resiudal points are small indicating a good result (see Figure 10.1 (a)).

The best-fit modification of the background as a function of energy is shown in Figure 10.1 (b). At lower energies the values of the best-fit nuisance parameters are smaller. Above 1 TeV, the modifications are in the order of 10%.

To quantify how well the data is described the z-score is used, see chapter 5. If the counts are normally distributed, i.e. there is only statistical uncertainties in the data, the expected value of the random variable Z is zero and the variance distributed around 1. The mean of the variance is larger than 1, if both systematic and statistical uncertainties are present.

Figure 10.3 shows the z-score computed for different spectral models used in the fit to modify the background. If the power law is used the variance of Z is a lot larger than 1, since the background systematic uncertainty is not sufficiently described. Using the piece-wise spectral model with a correlation length of 2, results in variance very close to 1. In this successful fit result, the model description is the expected value of the counts and the scattering of the residual

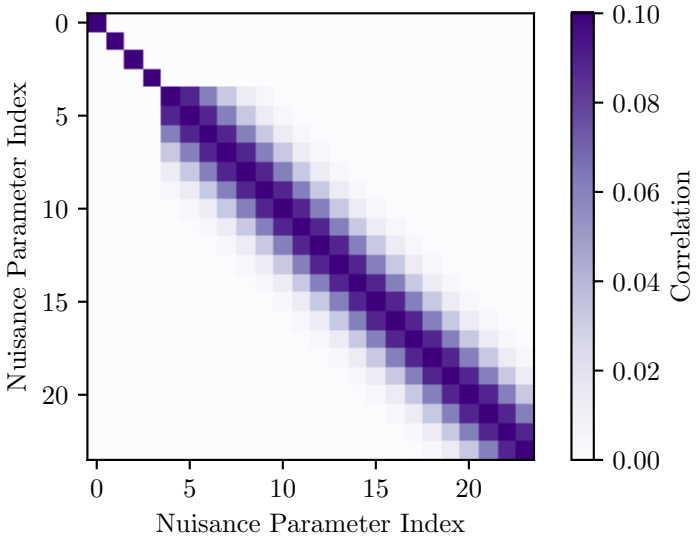

Figure 10.2: Covariance matrix with $l_{corr} = 2$ and $\sigma_{bkg} = 10\%$ used in the prior to correlate the nuisance parameters of the piece-wise background modification model.

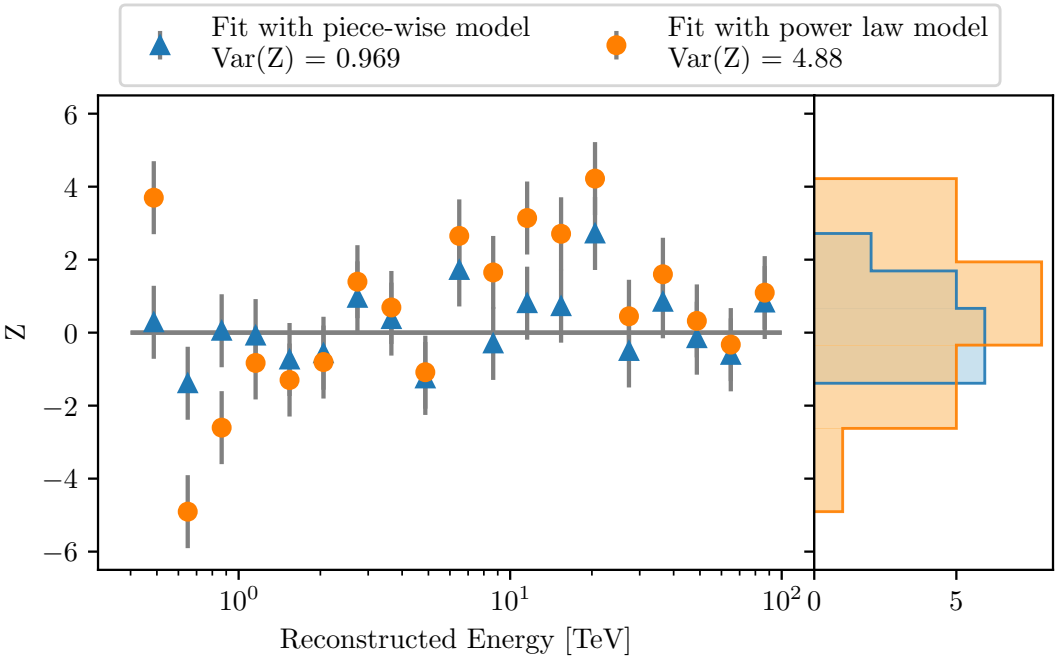

Figure 10.3: Z-score computed in each energy bin with different background modification models and the distribution.

points is only due to the statistical fluctuations and not due to systematic uncertainties. If the correlation length is decreased to one, the nuisance parameters are allowed to vary more independently with respect to their neighbours which results in stronger fluctuations. Now the nuisance parameters are not only accounting for the correlated systematic uncertainty in the

data but also for statistical fluctuations. As a result, the square root of the expected value overestimates the statistical error: $\sigma > \sigma_{\mathrm{stat}}$ and the variance of the z-score is < 1. On the other side, if the correlation length is chosen too large, the nuisance parameters are forced into correlations stronger than the underlying systematic uncertainty and $Var(Z) > 1$. For instance, $\mathrm{l_{corr}} = 3$ results in $Var(Z) = 3.23$. Several values for the correlation length between 1 and 3 have been tested, to obtain the one where $Var(Z) = 1$. The initial guess of $\mathrm{l_{corr}} = 2$ was found to be the best. For the rest of the analysis of the GC with H.E.S.S. data the background will be modified with nuisance parameters. A Gaussian multidimensional prior is used to enforce a correlation of $\mathrm{l_{corr}} = 2$ and a magnitude of $\sigma_{\mathrm{bkg}} = 10\%$.

Effect of the Background Modification on the Other Model Components The effect of the addition of the piece-wise correction on the other physical model components is studied in the following.

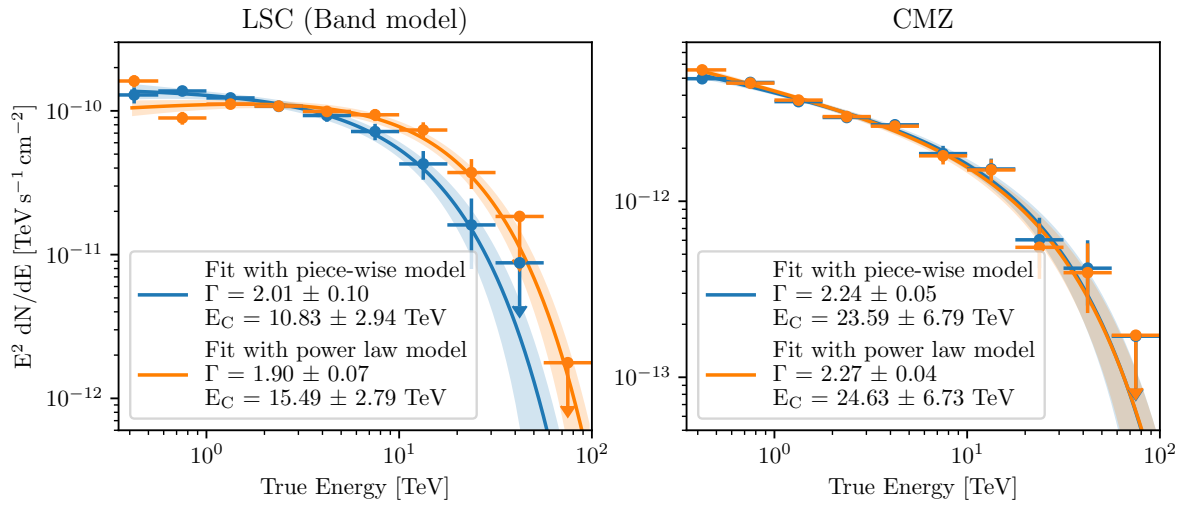

Figure 10.4: Best-fit spectrum and flux points of the LSC (left) and CMZ (right) computed for a PL modification of the background and a piece-wise modification with $\mathrm{l_{corr}} = 2$ and $\sigma_{\mathrm{bkg}} = 10\%$.

The effect on the point sources is as expected negligible. All positions and spectral parameters are consistent within the 1σ errors (see Figure 10 and 11 in the appendix).
The modelling of the CMZ is also unaffected by the choice of the background model. The best-fit spectrum together with the flux points with the two spectral background models, power law and piece-wise model, is shown in Figure 10.4 (right). There are only minor changes in the best-fit index and cutoff value. This is not the case for the larger-scaled model. Due to the large morphology which is very strongly correlated with the morphology of the effective area and therefore the background, this is expected. The spectra and flux points are shown in Figure 10.4 (left). The cutoff energy increases if the PL is used instead of the piece-wise model. When comparing the best-fit modification shown in Figure 10.1 (left), one can see how the PL is underpredicting the background for energies higher than $\sim 0.8\,\mathrm{TeV}$. Especially the LSC emission is therefore overestimated at $> 0.8\,\mathrm{TeV}$ which results in a higher cutoff value.

This is further confirmed by computing the spectral residuals in different regions of the FoV. The regions are chosen so that each one contains the γ-ray emitting regions which are modelled

by the physical models and two control regions mainly containing background. The former is centred around the GC with a size of ($6° \times 1°$) and the two latter are at above and below with a size of ($6° \times 1.5°$). The regions are shown in Figure 9. The resulting spectral residuals within this region computed with the PL and the piece-wise model are shown in Figure 10.5. In the background dominating regions, the residuals are mainly positive at $> 0.8\,\mathrm{TeV}$ confirming the underprediction. In the central region, this is not the case, since here the LSC can 'correct' the background underestimation. This results in the observed larger cutoff value. Note, how the residuals in all regions in the first few energy bins are decreased with the piece-wise model. To summarize it was shown how a simple power law spectral model is not sufficient to fit the background template to the data. This leads to the large-scaled model component compensating the missmodelled background by increased cutoff values. This is prevented by using a spectral piece-wise model which is used through out the thesis.

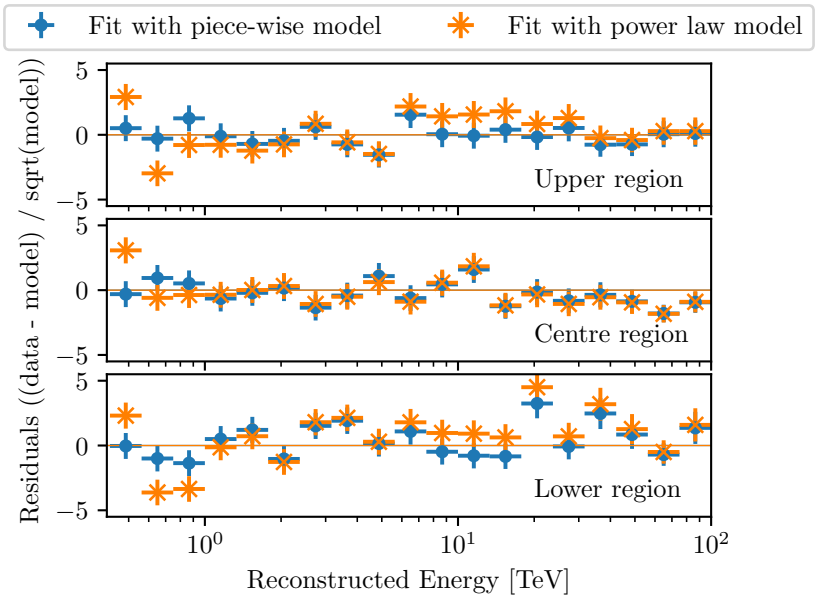

Figure 10.5: Spectral residuals computed for a PL modification of the background and a piece-wise modification with $\mathrm{l_{corr}} = 2$ and $\sigma_{\mathrm{bkg}} = 10\%$. The residuals were computed within different regions of the FoV: Upper panel: Upper region ($6° \times 1.5°$) containing background only. Centre panel: Centre region ($6° \times 1°$) containing γ-ray sources. Lower panel: Lower region ($6° \times 1.5°$) containing background only.

10.2 Cross-check with the std-zeta Configuration

To test whether the physical results show a dependency on the γ-hadron separation technique, the analysis is repeated with the *std-zeta* configuration. The dataset consists of the same runs and is created analoguous to the *std-ImPACT* datasets, i.e. pre-fitting the background for each run before stacking. The same model components are fitted to the dataset (point sources, LSC, CMZ). The background rate is modified by a piece-wise spectral model with an assumed background systematic magnitude of 10% and a correlation length of 2. The best-fit values of the spectral model parameters are listed in Table 10.1 and the positions of the point sources in

Table 1 in the appendix. The counts and background map of the stacked dataset, the residual maps and distributions and profiles are shown in the appendix (Figure 12, 13, 14, 15, 16, 17). The residuals show a norm-like distribution and based on the profiles the data is well described by the model components.

In Figure 10.6 the best-fit position of the point sources is shown. The positions are consistent within the 2σ error. Note, that the *std-zeta* dataset has a worse 68% containment radius of 0.08° at $E_{\mathrm{true}} = 1\,\mathrm{TeV}$ compared to the *std-ImPACT* dataset with 0.05°. Therefore, the uncertainties on the source position are generally larger.

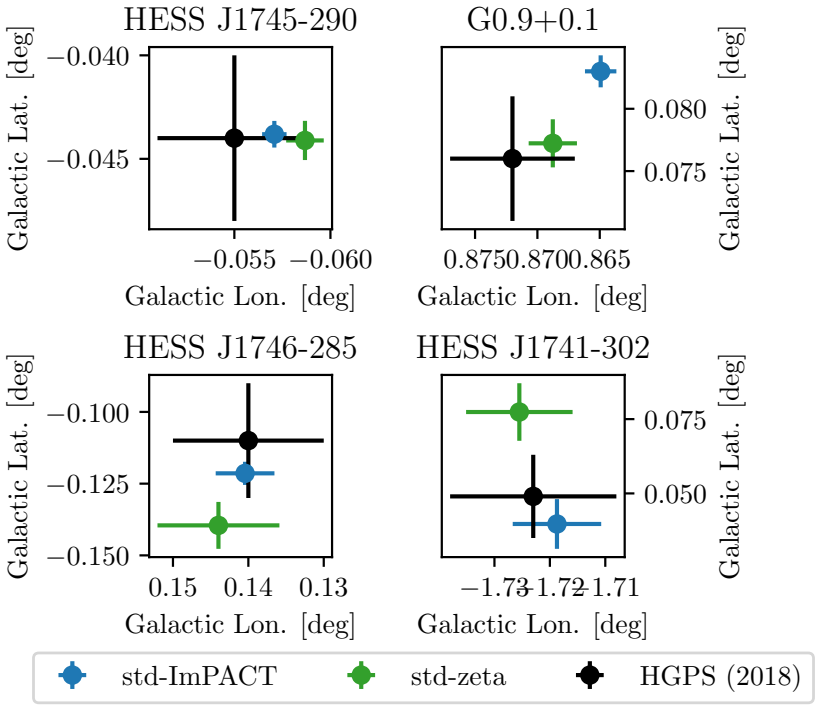

Figure 10.6: The best-fit positions of the four point sources with computed using the *std-zeta* configuration and the *std-ImPACT* configuration.

Figure 10.7 shows the spectra of the four point sources fitted to the *std-zeta* and the *std-ImPACT* dataset. Both the spectral shapes and the flux points are consistent with each other. The best-fit parameters are listed in Table 10.1.

Finally, the properties of the two large-scale components are analysed and compared. The LSC is modelled with the band model ($\sigma = 0.55° \pm 0.06°$) and an exponential cutoff power law with amplitude $(1.28 \pm 0.85) \times 10^{-10}$ TeV^{-1} cm^{-2} s^{-1}. The values are compatible with the *std-ImPACT* result within the 1σ errors. The same holds for the index and the cutoff value, which are listed in the legend in Figure 10.8 (left). In the latter, the resulting spectra and flux points are shown which have a very nice agreement. The exponential cutoff in the LSC is preferred by 4.76σ compared to the simple power law.

To model the diffuse emission in the CMZ, a combination of a power law with and without exponential cutoff and a template model of the morphology was used. The latter is the product of the gas distribution in the CMZ and a $1/r$ profile. In Figure 10.8 (right) the γ-ray spectrum resulting from the diffused protons from the central source is shown. The spectrum and the

Source	N_0 (TeV^{-1} cm^{-2} s^{-1})	Γ	$1/\lambda = E_{\mathrm{cut}}$ (TeV)
HESS J1745−290	$(2.08 \pm 0.06) \times 10^{-12}$	2.02 ± 0.06	10.35 ± 2.02
	$[(2.08 \pm 0.06) \times 10^{-12}]$	$[2.00 \pm 0.05]$	$[10.63 \pm 1.77]$
G0.9+0.1	$(8.29 \pm 0.56) \times 10^{-13}$	1.91 ± 0.14	4.81 ± 1.42
	$[(8.29 \pm 0.56) \times 10^{-13}]$	$[2.06 \pm 0.10]$	$[6.93 \pm 2.11]$
HESS J1746−285	$(1.11 \pm 0.16) \times 10^{-13}$	2.04 ± 0.14	
	$[(1.11 \pm 0.16) \times 10^{-13}]$	$[2.02 \pm 0.10]$	
HESS J1741−302	$(7.86 \pm 2.21) \times 10^{-14}$	2.00 ± 0.21	
	$[(7.86 \pm 2.21) \times 10^{-14}]$	$[2.07 \pm 0.20]$	
CMZ	$(4.58 \pm 0.17) \times 10^{-12}$	2.19 ± 0.05	17.01 ± 4.41
	$[(4.31 \pm 0.14) \times 10^{-12}]$	$[2.24 \pm 0.05]$	$[23.59 \pm 6.79]$
LSC	$(1.31 \pm 0.10) \times 10^{-10}$	1.91 ± 0.12	8.91 ± 2.39
	$[(1.41 \pm 0.10) \times 10^{-10}]$	$[2.01 \pm 0.10]$	$[10.83 \pm 2.94]$

Table 10.1: Best-fit spectral parameters of the H.E.S.S. point sources found with the *std-zeta* configuration. The *std-ImPACT* values are in squared brackets.

flux points are compatible with the results obtained with the *std-ImPACT* configuration. The spectral properties of the γ rays are listed in the legend. Both the index and the cutoff value are compatible within the 1σ statistical errors. The cutoff in the γ-ray spectrum and therefore in the initial spectrum of the proton source is preferred by 5.77σ.

Overall, there is a good agreement between the two configuration chains. Most of the model parameters are consistent and most importantly the same properties are reconstructed. Due to the better IRF properties, the *std-ImPACT* dataset is chosen as the main dataset in this thesis.

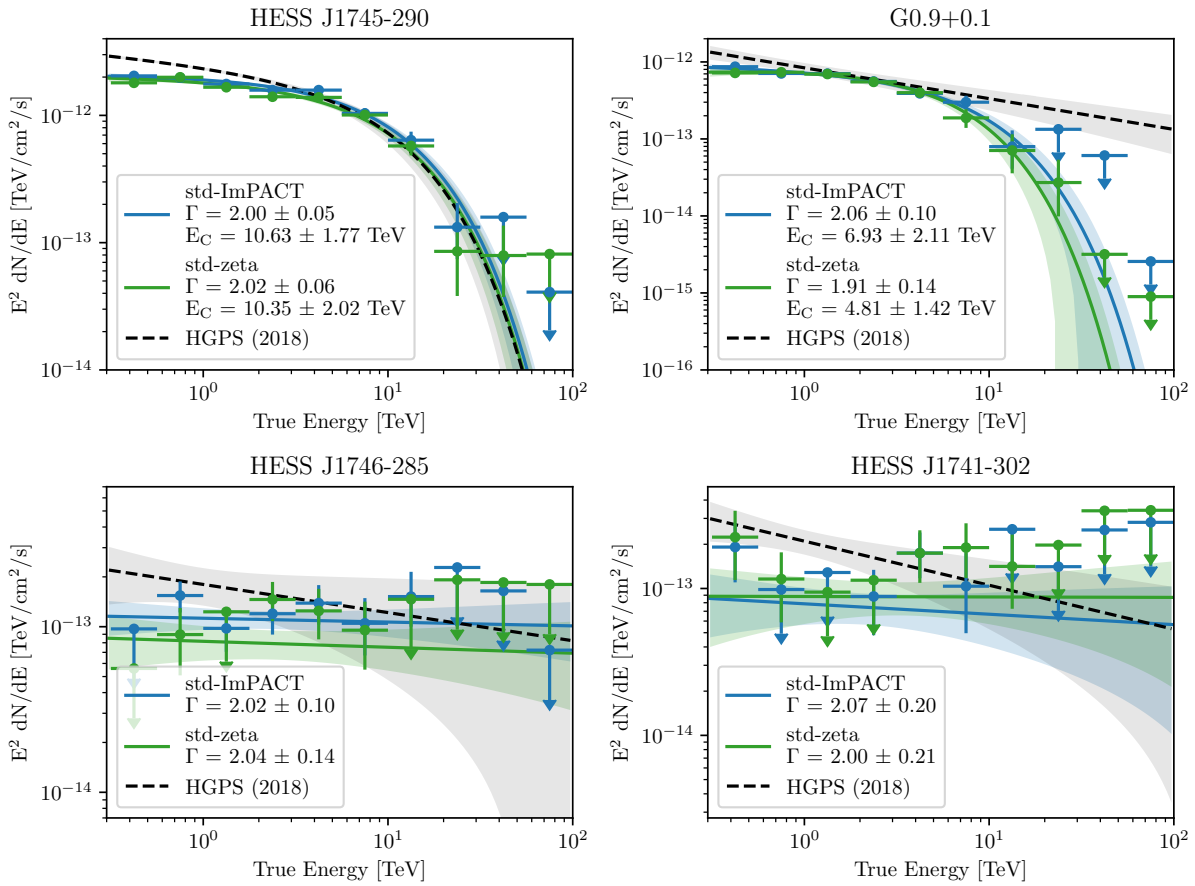

Figure 10.7: The best-fit positions of the four point sources with computed with the *std-zeta* configuration and the *std-ImPACT* configuration.

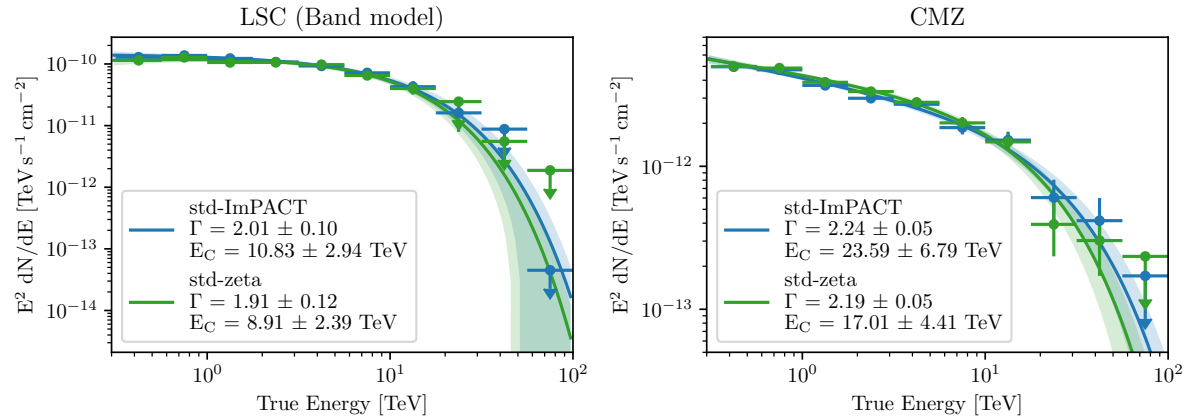

Figure 10.8: Best-fit spectrum of the CMZ and the LSC modelled as a band and flux points obtained with the *std-zeta* and the *std-ImPACT* configuration

Chapter 11

Summary

In earlier studies of the GC, the region was examined using 2D likelihood analyses or template fitting methods. This implies that spectral and spatial modelling were typically performed in separate steps, such as fitting the morphology in energy slices and extracting spectra independently. The GC region contains a multitude of sources, some of which overlap. Consequently, such 2D analyses do not permit the acquisition of a disentangled spectrum or a morphology of the diverse sources in a single, joint fit. However, this is now feasible as a full 3D likelihood analysis, using a background template created from archival observations, can be carried out. As a result, the properties of all model components, including the background, can be retrieved simultaneously in both the spatial and the spectral dimension.

In the FoV, a number of model components were taken into account, including four known H.E.S.S. sources, such as the strong source designated HESS J1745-290 located at the centre of the FoV. Two of the point sources have a significant cutoff: HESS J1745-290 which is compatible with the findings of the H.E.S.S. Galactic plane survey and G0.9+0.1 which in previous publications has not shown a significant cutoff. Generally, the position and the spectra of the point sources are compatible with previously published results.

Diffuse γ-ray emission is observed to be prevalent along the Galactic Plane, exhibiting a two-component structure. The first component is a large-scale structure that does not trace the dense gas, while the second component is observed to trace gas with a gradient towards the GC. The latter is attributable to protons injected continuously into their surrounding medium by a source positioned at the centre. These protons diffuse outwards and interact with the dense gas in the CMZ, which causes γ-ray emission via neutral pion decay. The resulting morphology is described by a template comprising the distribution of the dense gas and a $1/r$ profile, which quantifies the outward diffusion of protons. The morphology of the other large-scale components is modelled with a band along the Galactic Plane, with a Gaussian extension along the Galactic Latitude.

The analysis that utilising a basic power law with a normalising and a spectral tilting parameter is insufficient for modelling the hadronic background. The description of the data in the region where no γ-ray emission was expected was inadequate. This was corrected for by exchanging the power law with a spectral model that offers more flexibility. This piece-wise model introduces a normalising nuisance parameter in each energy bin. The correlation between the energy bins and the magnitude of the background systematic was estimated and quantified in a multi-dimensional prior. This is how the systematics were accounted for in the fit. The spectral residuals computed in the OFF region significantly improved by the employment of the piece-wise model.

While the position and spectra of the point sources and the CMZ were largely unaffected by this change in the background modelling, discrepancies were observed in the best-fit results for the large-scale component. By computing the residuals in different regions of the FoV, the more accurate description was quantified and verified.

Fitting the two large-scale components in 3D revealed that both sources have a significant cutoff in their spectra. For the large-scale component the cutoff was found at 10.83 ± 2.94 TeV with a significance of 5.13σ. The diffuse emission in the CMZ showed a cutoff at 23.59 ± 6.79 TeV. The exponential cutoff spectrum was preferred over the simple power law by 4.77σ. This implies that the underlying proton spectrum is also not a simple power law. Before, the central source was postulated to be a Pevatron accelerating protons up to 1000 TeV [5]. If here a cutoff is suggested by these indirect measurements, the PeVatron hypothesis is weakened. It is clear that this subject requires further investigations and systematic tests, i.e. the influence of the large-scale emission model. Therefore, the γ-ray emission in the CMZ will be the focus of the following part of the thesis.

The results were cross-checked by another analysis chain: *std-zeta*. Here, the γ-hadron separation is performed with boosted decision trees, whereas in the *std-ImPACT* configuration image template fitting is used. Both the point sources and the large-scale components are compatible. Using the *std-zeta* configuration also revealed significant cutoffs in the large-scale and the CMZ spectra with $\sim 5\sigma$.

In conclusion, the modelling of the GC with H.E.S.S. has been successful in representing the complex region of the GC with the different astrophysical models and a detailed and flexible model for the hadronic background.

Part III

DIFFUSE EMISSION IN THE CENTRAL MOLECULAR ZONE

In the preceding section, the GC was analysed using a 3D approach with data obtained by the H.E.S.S. telescope. By employing this analytical approach, the diffuse γ-ray emission was distinguished from the other components, and a significant cutoff in the γ-ray spectrum was identified. This cutoff is now being subjected to further investigation. Prior to this, the model of the CMZ was relatively straightforward: it comprised a morphology based on the product of the gas distribution and a $1/r$ distribution, as well as a power law with an exponential cutoff describing the γ-ray spectrum. The template-based model is being replaced with one that is more physically motivated. Instead of modelling the γ-ray spectrum, the spectrum of the initial protons and their diffusion is modelled. Subsequently, the diffusing protons interact with the gas in the CMZ, resulting in a transformation of the proton spectrum into a γ-ray spectrum based on proton-proton interactions. When the aforementioned model is fitted alongside the other source models within the field of view, the proton properties are reconstructed. The question of a cutoff in the proton spectrum will be addressed, as will the implications regarding the PeVatron.

This section is structured as follows: first, a theoretical background is provided regarding CRs and the production mechanisms of γ rays. Subsequently, the CMZ is the subject of discussion, with a particular focus on the diffusion of protons and the findings of previous studies conducted in this area. The second chapter presents and compares the results of the physical modelling of the CMZ with those obtained with the template model and other telescopes. In the final chapter, the systematic uncertainties are evaluated. Given the substantial overlap and similarity between the models, the systematic uncertainties associated with the large-scale emission are considered to be significant. To test the impact of different spectral and spatial shapes of the LSC model on the parameters of the CMZ model, the analysis is repeated with varying assumptions. Subsequently, the systematic uncertainties related to the IRF are evaluated, and the results are compared to theoretical predictions of the diffuse properties of CRs. Finally, the results are summarised and discussed.

Chapter 12

Introduction to Diffuse γ-Ray Emission

In general, the emission of γ rays is described as diffuse if it spreads out over a large area of the sky. The production of galactic diffuse γ rays is due to the interaction of CRs with the interstellar medium and low-energy photons. A brief introduction to CRs is therefore provided at the outset of this chapter, followed by a discussion of the two principal production mechanisms of γ-ray emission: the leptonic and hadronic scenarios. While diffuse γ rays are detected along the entire Galactic band, this thesis focuses on the inner part of the MW, the CMZ, which is introduced in section 12.3. Afterwards, the source of the CRs and the diffusion of the injected protons causing the diffuse γ-ray emission in the CMZ is discussed. Lastly, publications about the topic from various γ-ray telescopes are presented.

12.1 Cosmic Rays

CRs are particles that originate from outside the Earth's atmosphere and have been accelerated to nearly the speed of light by a range of astrophysical processes. One of the fundamental questions concerning CR is that of their origin. The majority of the CRs exhibit an anti-correlation with solar activity, which rules out the possibility that they originate within our solar system. Indeed, the majority of CRs are believed to originate from the Milky Way, with supernova remnants being a popular source of acceleration. The charged nature of CRs allows them to be deflected by magnetic fields. The deflection is quantified by the Larmor radius, which is given by the equation $r = E/qB$, where E is the particle's energy, q is the charge and B is the magnetic field strength. Assuming $B \sim 4\,\mu$G, the Larmor radius of a 10^{18} eV proton is 300 pc which is comparable to the dimensions of the MW (thickness of the thin disk of $\sim 200 - 300$ pc) [70]. It can be concluded that the high energy CRs are not confined by the galactic magnetic field, which indicates that their origin must be extragalactic [71].

The collision of primary CRs with atomic nuclei in the interstellar medium results in the production of secondary CRs. By studying the relative amounts, conclusions can be drawn about the propagation of the CRs and the matter and fields they encountered. Additionally, other chargeless secondary particles, such as photons and neutrinos, are produced. Consequently, γ-ray and neutrino astronomy enable the study of the properties of CR sources and the acceleration mechanisms.

This chapter provides an overview of CRs, beginning with the measured spectrum and

subsequently presenting a theory that explains their acceleration.

Cosmic Ray Spectrum The majority of CRs (98%) are composed of protons and nuclei, while the remaining fraction is composed of electrons [20]. The spectrum of CRs is shown in Figure 12.1. In order to obtain an overall spectrum of this kind, a number of experiments are necessary, given that the energies span a very large range from $\sim 10^9\,\mathrm{eV}$ to $\sim 10^{20}\,\mathrm{eV}$. The energies attained by CR exceed those currently achieved by the Large Hadron Collider. The flux can be described by a power law with an index of ~ 2.7, spanning almost 30 orders of magnitude. At specific energies, a spectral break is observed. These features include the knee at $\sim 10^{15}\,\mathrm{GeV}$ and the ankle at $10^{18}\,\mathrm{GeV}$. After the former, the spectral index increases to ~ 3 which is attributed to the maximum energy CRs are accelerated to by the most common sources (SNRs) through shock waves. Beyond the knee energy, the efficiency declines, resulting in a reduction in CRs at higher energies and a change in the spectral slope. Conversely, the ankle corresponds to a flattening of the spectrum where the origin of CRs is primarily extragalactic which increases the rate at energies beyond the ankle. The energy range between the knee and the ankle therefore marks the transition of CRs originating from within and outside the MW [20].

The Pierre Auger Observatory observed a significant suppression of the CR flux beyond $4 \cdot 10^{19}\,\mathrm{eV}$ [72]. This finding is in accordance with the predicted upper limit of CRs (GZK cutoff). At these energies, the CRs interact with the cosmic microwave background, producing low-energy protons and pions and losing energy.

The lower limit of the spectrum is a consequence of solar modulation. Low-energy CRs are affected by the solar wind when entering the heliosphere, resulting in a loss of energy.

Mechanisms of Particle Acceleration The following section is based on [20]. In order to elucidate the mechanism of CR acceleration, Fermi proposed a mechanism in 1949, which is now referred to as second-order Fermi acceleration. Hereby, the particles are reflected by irregularities in the Galactic magnetic field ('magnetic mirrors'). Assuming that the mirrors move randomly with velocity V, then the particles gain energy with each reflection. The average energy gain is proportional to $(V/c)^2$, which is not an efficient process due to the low value of V. Furthermore, the energy loss in some collisions and the large mean free path make the second-order Fermi acceleration less favourable as an explanation for the observed CRs.

In the 1970s, the first-order Fermi acceleration model, also known as the diffusive shock acceleration, was postulated. The fundamental premise is the existence of a disturbance that propagates at a velocity exceeding the local speed of sound through a medium (shock). The particles gain energy through repeated crossing of the shock boundary, resulting in a high efficiency. As the name suggests, the energy gain is proportional to the shock velocity in first order. The result yields a power law spectrum with a spectral index of 2. This has attracted considerable interest as a means of explaining the presence of power law energy spectra with a unique spectral index in a range of astrophysical environments. The underlying conditions are characterised by the presence of strong shock waves and randomised velocity vectors of high energy particles, which are observed in sources such as supernova remnants, active galactic nuclei and extragalactic radio sources.

In both first- and second-order Fermi acceleration, the high energy particles do not affect the shock itself. It is therefore only the linear effects that are taken into account. In reality,

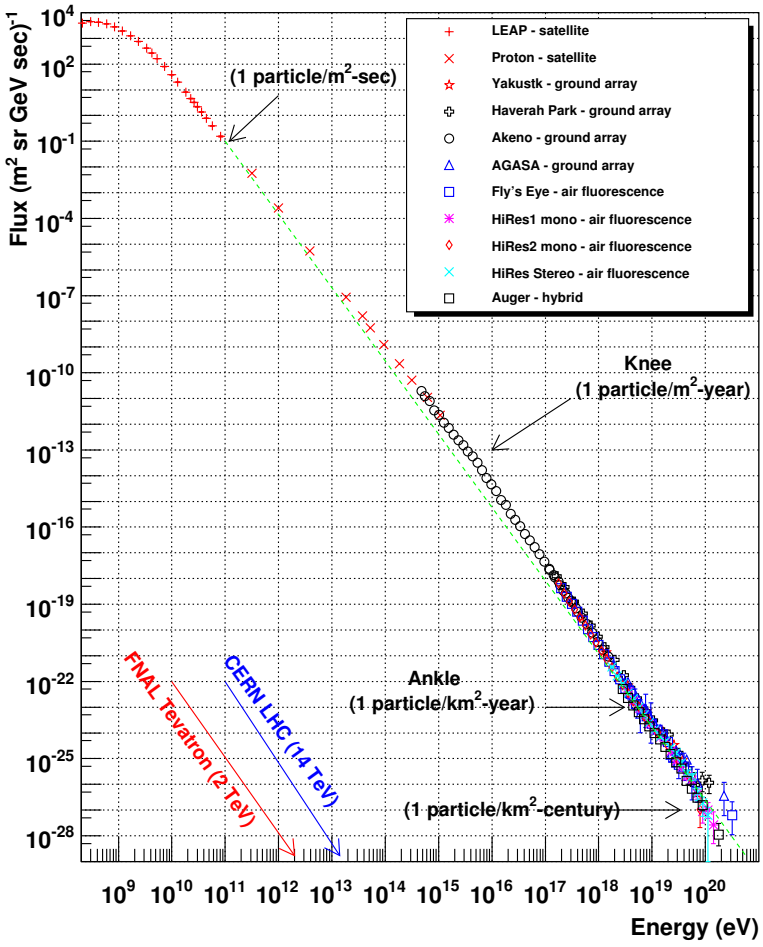

Figure 12.1: CR spectrum of varios experiments. The green dashed line corresponds to a power law with index 2.7. Figure taken from [73].

however, the shock structure and magnetic fields are significantly modified by the accelerated particles, which leads to more complex, non-linear interactions. These modified shock conditions are considered in the non-linear theory of diffusive shock acceleration, which leads to predictions that are in better agreement with spectral observations. Further details about the non-linear theory can be found in Reference [74].

12.2 γ-ray Production Mechanisms

While the study of CRs can elucidate their properties, composition, and interactions, one challenge persists: due to their electric charge, they arrive isotopically on Earth as a consequence of interactions with interstellar magnetic fields. As a result, it is not possible to reconstruct their original direction. However, interactions with the interstellar medium and electromagnetic fields result in the production of γ rays (and neutrinos), which are not deflected. Consequently, a positional reconstruction is feasible. This establishes an intrinsic link between CR production mechanisms and γ-ray astrophysics.

12.2.1 Leptonic Scenario

γ rays are produced by relativistic electrons via a number of processes, including inverse Compton scattering, synchrotron emission, Bremsstrahlung and curvature radiation. The following section is based on [75].

Inverse Compton Scattering In inverse Compton scattering (IC), low-energy photons (i.e. cosmic microwave background (CMB), infrared, X-ray or optical photons) gain energy by scattering off energetic electrons, whereby part of the electron's energy is transferred to the photon.

$$e^- + \gamma_{low} \rightarrow e^- + \gamma_{high} \tag{12.1}$$

The distinction between the two regimes hinges on the energy of the photon prior to scattering, designated as E_{low}. When this energy is less than the electron rest mass energy, represented by $E_{low} < m_e c^2$, the Thomson regime is observed. In this scenario, the cross section is

$$\sigma_T = \frac{8}{3}\pi r_0^2, \tag{12.2}$$

where r_0 is the classical radius of the electron. After the scattering the photon spectrum follows

$$\frac{dN_\gamma}{dE_\gamma} \propto E_\gamma^{-(a+1)/2} \tag{12.3}$$

assuming the electron spectrum followed the power law $\frac{dN_e}{dE_e} \propto E_\gamma^{-a}$, where energy E_e relates to the electron's energy in the electron's restframe.

In the Klein-Nishima regime, $E_{low} >> m_e c^2$, the cross-section is:

$$\sigma_{KN} = \frac{3}{8}\sigma_T x^{-1} \ln(4x), \tag{12.4}$$

where

$$x = \frac{E_e E_{low}}{(m_e c^2)^2}. \tag{12.5}$$

The energy of the photon after the scattering is approximately equal to the electron energy. Under the assumption of a constant electron power law spectrum, the spectrum of the scattered photons can be described by the following equation:

$$\frac{dN_\gamma}{dE_\gamma} \propto E_\gamma^{-(a+1)}. \tag{12.6}$$

In comparison to the Thomson regime, the proportion of energy transferred from the electron to the photon is significantly greater. In instances where high Lorentz factors are present ($\gamma = 10^2 - 10^3$), the photons attain energies in the GeV-TeV range, with the maximum energy equating to approximately $E_{\gamma,max} \approx 4\gamma^2 E_{low}$.

Synchrotron Radiation A charged particle that moves in a helical trajectory along magnetic field lines emits electromagnetic radiation, which is known as synchrotron radiation. As a consequence of the Lorentz force, the trajectory of the particle is perpendicular to the direction of the magnetic field. Both electrons and protons are capable of emitting synchrotron radiation.

However, the latter is significantly suppressed due to its higher mass and the fact that the synchrotron power is proportional to the fourth power of the mass. Without considering cooling, the resulting photon spectrum is

$$\frac{dN_\gamma}{dE_\gamma} \propto E_\gamma^{-(a+1)/2}. \tag{12.7}$$

The resulting photon emission is typically in the infrared/X-ray regime. However, these low-energy photons can undergo Compton scattering with the relativistic parent electrons, thereby producing high energy photons. This process is referred to as synchrotron self-Compton scattering [76].

Bremsstrahlung A charged particle experiencing strong nuclear force i.e, close at an atomic nucleus, is accelerated and therefore emits radiation. The emitted intensity is inversely proportional to the mass of the particle, which again makes this process effective for electrons and positrons. The resulting photon spectrum is

$$\frac{dN_\gamma}{dE_\gamma} \propto E_\gamma^{-a}. \tag{12.8}$$

12.2.2 Hadronic Scenario

Protons (or, in general, ions) are capable of emitting radiation in a manner analogous to electrons, due to their charge, via the aforementioned leptonic processes. However, given that the mass of a proton is approximately 1836 times greater than that of an electron, the radiation power is considerably lower. However, protons are capable of producing γ rays through both strong and weak interactions [77]. The simplest of these is the $p\gamma$ interaction, in which an energetic proton interacts with a photon of sufficient energy. Thereby a a Δ^+ resonance can be produced, whereby the proton (uud) undergoes a transition to its higher-energy equivalent state with spin 3/2. The Δ^+ subsequently decays into mesons. Mesons of different multiplicity Σ are produced in the scattering process without Δ^+. The processes are shown below:

$$p\gamma \rightarrow \begin{cases} \Delta^+ \rightarrow p\pi^0/n\pi^+ \\ \Sigma\pi^{\pm 0} \end{cases} \tag{12.9}$$

The interaction of energetic protons with other protons present in the surrounding gas at the production site results in the creation of pions:

$$pp \rightarrow \Sigma\pi^{\pm,0} \tag{12.10}$$

The pions created via equations 12.9 and 12.10 subsequently undergo further decay. Neutral pions decay electromagnetically and almost instantaneously with a branching ratio of $> 98\%$ into two high-energetic photons. Charged pions decay almost exclusively via the weak interaction into a muon with a muon neutrino ($BR > 99\%$) [78]. The muon then rapidly decays into an electron/positron with accompanied neutrinos. The processes can be summarised as follows:

$$\pi^0 \rightarrow \gamma\gamma \tag{12.11}$$

$$\pi^+ \rightarrow \mu^+\nu_\mu \rightarrow (e^+\nu_e\bar{\nu}_\mu) + \nu_\mu \tag{12.12}$$

$$\pi^- \rightarrow \mu^-\bar{\nu_\mu} \rightarrow (e^-\bar{\nu}_e\nu_\mu) + \bar{\nu_\mu} \tag{12.13}$$

The production of a neutral pion results in the transfer of approximately $10 - 20\%$ of the proton's energy. Via 12.11 the total energy is conserved, leading to the conclusion that approximately $5 - 10\%$ of the proton's energy is transferred to the photon.

In a proton-proton interaction eta mesons (η) are produced via excitation and subsequent decay of a nucleon resonance $N^*(1535)$. The primary modes of the decay of the η mesons are [79]:

$$(pp \to pN^*(1535) \to pp\eta) \to \eta \begin{cases} 2\gamma & \\ 3\pi^0 & \to 6\gamma \\ \pi^+\pi^-\pi^0 & \to 2\gamma + \dots \\ \pi^+\pi^-\gamma & \to \gamma + \dots \end{cases} \tag{12.14}$$

Approximately 3.2 γ-ray photons are produced per decay, with 81% of the energy of the η transferred to all γs. Assuming a proton spectrum with an exponential cutoff, the energy spectrum of a γ-ray can be computed while considering all aforementioned production mechanisms. The computations and simulations are carried out in accordance with the methodology outlined in Kelner (2006) [79]. Figure 12.2 illustrates the resulting γ-ray spectra from two distinct proton spectra. It can be observed that the cutoff energy is approximately 10% of the original proton cutoff.

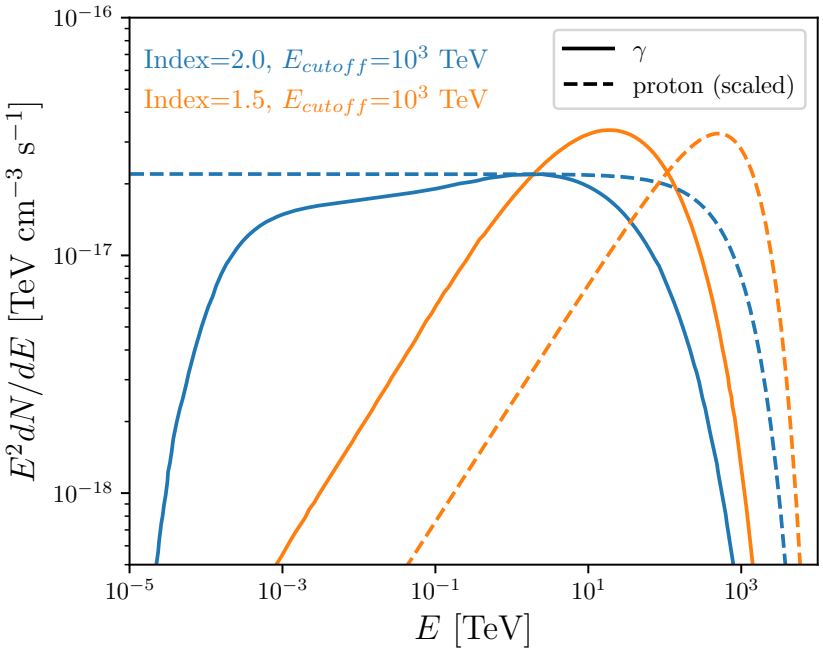

Figure 12.2: Simulation of a γ-ray spectrum based on two proton spectra with different spectral indices. Figure adapted from [80] and based on the calculations from [79].

12.3 The Central Molecular Zone

The Central Molecular Zone (CMZ) is a ring-like concentration of molecular gas located within the innermost few hundred parsecs of the Milky Way. The Galactic bar drives matter inward and causes extreme conditions. Within the inner $\sim 600\,\mathrm{pc}$, the mass of the molecular gas is

estimated to be $2 - 6 \cdot 10^7 M_\odot$ [81]. Despite the small region, this equals 10% of all the gas in the MW. Its density found to be several orders of magnitude above the average density in the Galactic disk [82]. The gas in the CMZ is highly turbulent and can reach temperatures as high as $400 - 600\,\mathrm{K}$ [82]. The CMZ is the most extreme star forming region in the MW since the star forming rate is proportional to the amount of molecular gas.

The CMZ contains a variety of molecules, including molecular hydrogen (H_2), carbon monoxide (CO), carbon monosulfide (CS) and methanol (CH_3OH). While H_2 is by far the most abundant molecule, it is not directly observable in cold gas. CO, being the second-most abundant molecule and easily observable, is commonly used as a tracer for molecular hydrogen. On the other hand, CS is less abundant but has a higher critical density which makes it beneficial for tracing dense gas distributions like the CMZ. The CS molecules transition between energy levels and thereby emit emission which is detectable with radio telescopes. The molecular clouds traced with CS by [67] are shown in Figure 12.3. Hereby, the CS(J=1-0) line was targeted which refers to the rotational transition between the first excited rotation state (J = 1) and the ground state (J = 0). For CS (J=1-0), this frequency is around 49.5 GHz. The 45-meter telescope at Nobeyama Radio Observatory was used, which provides high spatial resolution and sensitivity. The intensity of the emission lines is measured in units of brightness temperature (K). The width of the emission lines is broadened by several effects: thermal and turbulent motion of the gas, collisions in high-density regions and natural broadening due to inherent uncertainties in the energy levels. Hence, the linewidth is a measurement of the turbulence and velocities [83]. In [67], absolute velocities of 200 km/s were found. Compared with the velocities measured in the Galactic disk ($1 - 10\,\mathrm{km/s}$), shows the extreme condition in the CMZ [82]. Note, that a negative velocity in spectral line broadening indicates that the source is moving towards the observer, causing a blueshift in the light's wavelength. The distribution of the gas with respect to the GC is asymmetric. It is estimated that there is three times more gas at positive Galactic Longitude which have a positive velocity, i.e. moving away from the observer [82].

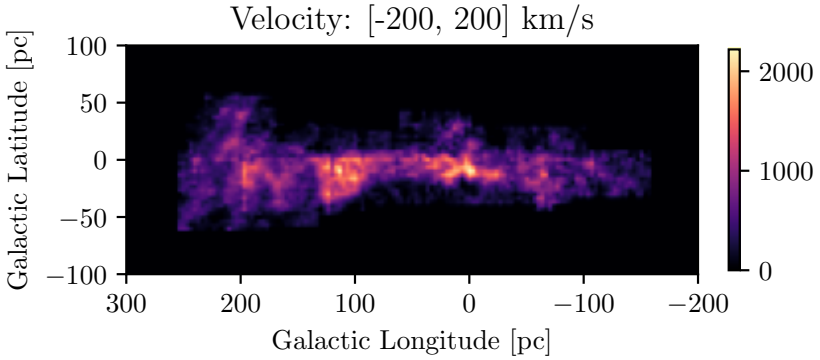

Figure 12.3: Mapping of the molecular clouds of the CMZ with CS measurements. The map is integrated over velocitys between $-200\,\mathrm{km/s}$ and $200\,\mathrm{km/s}$ and is in units of Kkm/s [67].

The CS map shown in Figure 12.3 lacks the information of the distribution of the gas in the z-direction. To overcome this 'edge-on' only view of the CMZ, 'face-on' information from another molecule tracing has to be taken into account. This can be done by using the OH/CO ratio [66]. As mentioned CO emission lines are used to trace the distribution and velocity of the

molecular gas. OH (hydroxyl) molecules on the other hand absorb specific wavelengths of IR light due to vibrations of the O-H bond. By comparing the absorption lines to the emission lines, the line of sight position of the clouds can be reconstructed. Then a face-on distribution of the CO brightness and velocity can be created (see Figure 12.4). A elongated and inclined structure is revealed. The information of the two maps is joined by matching the observed velocities and a three dimensional map of the gas distribution is created.

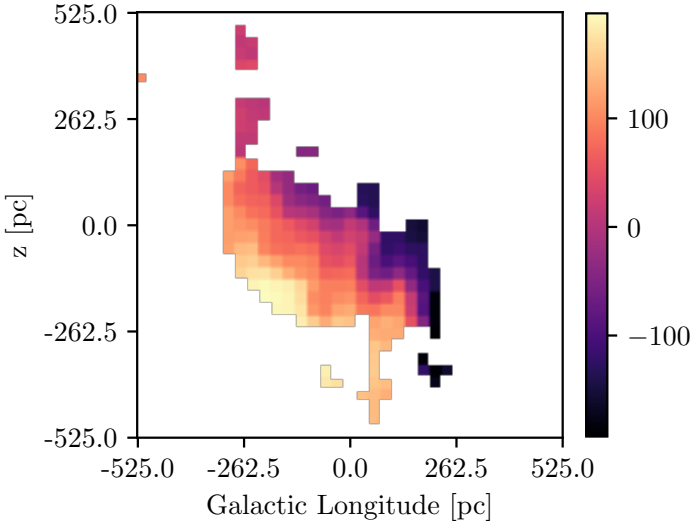

Figure 12.4: Face-on distribution of the gas in the CMZ in units of km/s as obtained by [66].

12.4 Diffuse Protons in the CMZ

In the centre of the MW multiple sources are capable of accelerating CRs to high energies. This includes a supernova remnant, a pulsar wind nebula and a compact cluster of massive stars [5]. The super massive black hole Sgr A* might be the source of PeV protons. The acceleration could be in the immediate vicinity of the black hole or due to a fraction of the accreting matter by being ejected back into the environment when falling into the black hole.

As previously stated, the trajectories of charged CRs are isotropised as a result of turbulent Galactic magnetic fields. Consequently, it is not feasible to reconstruct the position of their source. However, since they produce secondary particles that do not carry charge, namely photons and neutrinos, an indirect reconstruction is possible. By measuring the spectral shape of the secondary particles, conclusions can be drawn about the initial CR spectrum of the source.

However, the charged CRs are not confined to a limited region; rather, they exhibit a diffused distribution contingent upon their energy and the characteristics of their surrounding environment. In the absence of convection and energy loss, the diffusion of protons can be described by Fick's law.

$$\vec{q}(\vec{r}, E, t) = -D(\vec{r}, E, t)\nabla n(\vec{r}, E, t), \tag{12.15}$$

hereby $\vec{q}(\vec{r}, E, t)$ is the proton flux, $n(\vec{r}, E, t)$ the proton density and $D(\vec{r}, E, t)$ the diffusion coefficient which quanifies the rate at which the protons spread out into their enviroment.

Assuming that the diffusion coefficient is only energy dependet ($D(\vec{r}, E, t) = D(E)$) and that the total number of particles is conserved:

$$\frac{\partial n(\vec{r}, E, t)}{\partial t} = -\nabla \cdot \vec{q}(\vec{r}, E, t) \tag{12.16}$$

the classical diffusion equation can be derived:

$$\frac{\partial n(\vec{r}, E, t)}{\partial t} = D(E)\nabla^2 n(\vec{r}, E, t) \tag{12.17}$$

In the case of spherical symmetry:

$$\frac{\partial n(E, t)}{\partial t} = D(E)\frac{1}{r^2}\frac{\partial}{\partial r}\left[r^2\frac{\partial n}{\partial r}\right] \tag{12.18}$$

Note, that reacceleration is neglected, as the energy gain is much slower than the regular acceleration in shock fronts [20], [84]. The cooling time of CRs is much longer than the time the protons spend in the highly dense CMZ region. Therefore, the proton cooling can also be neglected [85].

In general, two principal categories of proton-injecting types can be distinguished: impulsive and continuous. During the former the protons are injected into the surrounding medium with a short burst. In the latter scenario, the protons are continuously injected which maintains a constant supply of high energy particles.

Solving the diffuse equation for the impulsive scenario results in [86]:

$$n(r, E, t) = \frac{N_p}{[4\pi D(E)t]^{3/2}} \exp\left(-\frac{r^2}{4D(E)t}\right), \tag{12.19}$$

where N_p is number of injected protons. The proton density has a Gaussian shape.

To obtain the proton density in the continuous scenario, one integrates over the time, and $\dot{N}_p$ is the injection rate of the protons:

$$n(r, E, t) = \frac{1}{(4\pi D(E)t)^{3/2}} \int_0^t \dot{N}_p(t') \exp\left(-\frac{r^2}{4D(E)(t-t')}\right) \frac{dt'}{(t-t')^{3/2}} \tag{12.20}$$

$$= \frac{\dot{N}_p}{4\pi D(E)r}\mathrm{erfc}\left(\frac{r}{\sqrt{4D(E)t}}\right) \tag{12.21}$$

Note, that the proton density now follows $1/r$.

The diffusion coefficient depends on the rigidity of the particle (momentum per unit charge). Since here protons are the main focus, the rigidity is approximated by the protons energy. The diffusion coefficient is typically presented in the form [87]:

$$D(E) = D_0 \left(\frac{E}{10\,\mathrm{GeV}}\right)^{\delta}, \tag{12.22}$$

where the D_0 is a normalising constant in terms of $\mathrm{pc}^2/\mathrm{yr} \approx 3.02 \cdot 10^{29}\mathrm{cm}^2/\mathrm{s}$ and δ describes the energy dependency. The diffusion inside the CMZ is considered to be slower $D_0 \sim 10^{26}\mathrm{cm}^2/\mathrm{yr}$ compared to the rest of the interstellar medium [85]. This is due to its high gas density, temperatures and the presence of strong magnetic, turbulent fields. Outside the CMZ the value is estimated to be larger by a factor of 100.

The energy dependency of the diffusion coefficient δ reflects the nature of the turbulence in the medium and therefore affects the energy spectrum of the CRs. Therefore, the theoretical prediction dependent on on the turbulence model. The value $\delta = 1/3$ is derived from Kolmogorov's concept of turbulence. Hereby, energy is transferred from larger to smaller structures of turbulences with a certain energy dissipation rate. This energy spectrum follows a power law as a function of the wavelength, the inverse of the length of the structures known as Kolmogorov's 5/3 law: $E(k) \propto k^{-5/3}$. It follows a diffusion coefficient which scales with the rigidity as $D \propto R^{1/3}$ [88]. An experimental way of determining the spectral index of the diffusion coefficient is by measuring the ratio of flux of boron to carbon. The latter are accelerated in astrophysical sources, while boron is created through spallation, where heavier nuclei are broken into lighter elements due to collision with matter. By measuring the ratio information about the CR propagation is provided. A high B/C ratio indicates more material that the CR encountered which results in a low diffusion coefficient ($B/C \propto 1/D \propto R^{-\delta}$). A measurement by AMS-02 in 2016 of the spectral index revealed $\delta = -0.33 \pm 0.02$ which is in excellent agreement with the Kolmogorov prediction [89]. Using Kraichnan's model of turbulence, where the velocity field in a turbulent flow is treated as a random process, results in a $\delta = 1/2$ [90]. This prediction was confirmed with data taken by the TRACER CR detector measuring the B/C ratio and finding $\delta = 0.53 \pm 0.06$ [91]. Generally, δ is quoted to be $0.3 - 0.6$ [70], [92].

12.5 Past Studies of the CMZ

H.E.S.S. first detected the diffuse emission in the GC in 2006 [93]. In 2016, both VERITAS and MAGIC reported emission in the CMZ [94],[95]. In the same year, the H.E.S.S. collaboration published the paper "Acceleration of petaelectronvolt protons in the Galactic Centre" [5]. The diffuse emission spectrum was extracted from an annulus around Sgr A* and a power law with spectral index $\Gamma = 2.32 \pm 0.05_{stat} \pm 0.11_{sys}$ was fitted over an energy range up to 45 TeV. No indications of a cutoff or a curvature were found. Since the γ-ray emission is due to hadronic interactions followed by the production and the decay of a neutral pion, the conclusion was that the underlying proton spectrum also has no cutoff and can thereby be extrapolated to PeV energies. As the initial proton source, Sgr A* was proposed. The spectrum with flux points of the diffuse emission and HESS J1745-290 is shown in Figure 12.5.

The H.E.S.S. collaboration published "Characterising the VHE diffuse emission in the central 200 parsecs of our Galaxy with H.E.S.S." in 2018 [60]. The morphology of the GC was modelled with multiple components, including G0.9+0.1, HESS J1745-290, Dense Gas (DGC) which corresponds to the CMZ, an additional central Gaussian component, HESS J1746-285 and an extended large-scale component (LSC). The spectrum of the diffuse emission along the Galactic ridge ($|l| < 1°$, $|b| < 0.3°$, with exclusion of the point sources) was fitted with a power law up to 45 TeV with a spectral index of $2.28 \pm 0.03_{stat} \pm 0.2_{sys}$. No significant cutoff was found. The CR density followed $1/r$ (see Figure 12.6)

In 2020, MAGIC published an analysis of the diffuse γ-ray emission in the CMZ [96]. The flux points obtained within 400 GeV-50 TeV in a similar region to the Galactic ridge are consistent with the ones obtained in H.E.S.S. (2018) [60]. The spectrum was fitted with an exponential cutoff power law: spectral index of $1.98^{+0.26}_{-0.23}$ and a cutoff energy of $17.5^{+59.3}_{-9}$ TeV. The exponential cutoff was found to be preferred by 2σ over the simple power law. This raised questions about the existence of a PeVatron. However, since the 1σ confidence on the photon cutoff value was $10 - 80$ TeV, the PeVatron scenario is still marginally compatible. The CR density decreased inversely with distance to Sgr A*, as shown in Figure 12.6, which is compatible with the H.E.S.S.

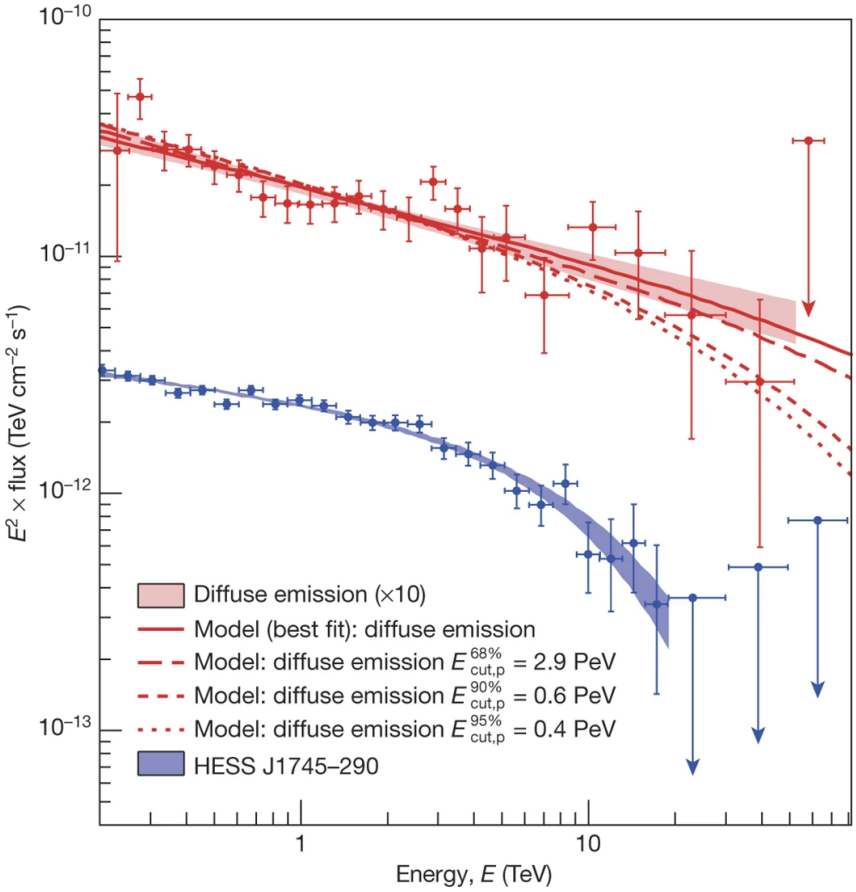

Figure 12.5: Best-fit spectrum of the diffuse emission and HESS J1745-290 with flux points. The 1σ statistical error band is shown as well as diffuse emission spectra resulting from different inital proton spectra with cutoff energies between 0.4 PeV and 2.9 TeV. The spectra deviate from the best-fit spectrum at the 68%, 90% and 95% CL. However, the index was fixed to 2.4 during these computations. Figure taken from [5].

result.

In 2021, the VERITAS collaboration found the spectral index of the diffuse emission in the CMZ to be 2.19 ± 0.20 which is compatible with the published results by then [97]. No significant cutoff was found, however, at the 95% confindence level the lower bound of the cutoff energy was reported as 10.3 TeV. This value is compatible with the MAGIC (2020) result.

The latest publication about the CMZ is from the HAWC collaboration in 2024 [98]. The spectrum of the diffuse emission was fitted with a power law within 6 to 114 TeV. The spectral index is $2.88 \pm 0.15_{stat} \pm 0.1_{sys}$ and is thereby softer than the other reported indices. Since no significant cutoff or curvature was found and photons beyond 100 TeV were observed, this confirmed the presence of a PeVatron.

It should be noted that all the reported results use the ON/OFF analysis method where the spectrum is extracted from a defined region. None of the publications account for the LSC, which was found to be very significant. The key question is whether the diffuse emission exhibits a curvature or cutoff in its spectrum. This is essential to determine whether the GC is capable of

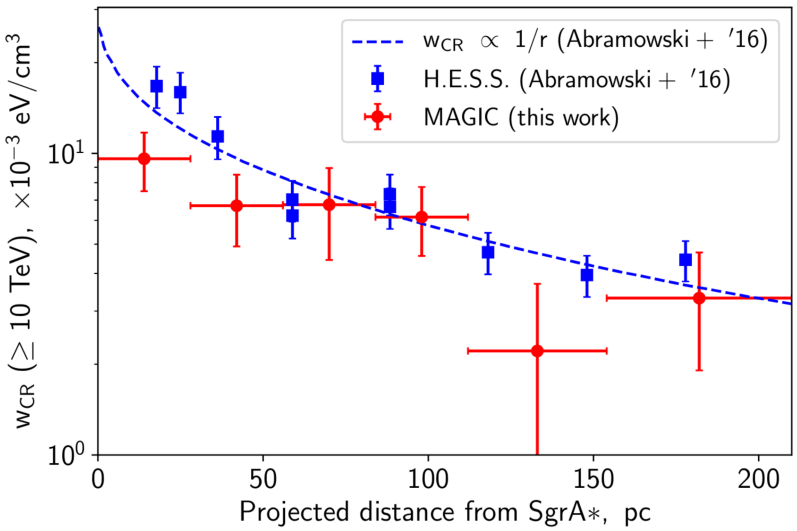

Figure 12.6: CR density obtained from MAGIC (2020) and H.E.S.S. (2016) as a function of the projected distance to Sgr A*. Figure taken from [96]

accelerating protons up to PeV. Summarizing the results from the various telescopes is difficult since they are not fully compatible. While none reports a statistically significant cutoff of $> 5\sigma$, excluding some softening or a break in the spectrum seems incorrect. Otherwise, the reported soft index from the HAWC (2024) observation would not be compatible with the other indices $\sim 2 - 2.2$. In 2023, LHAASO measured the spectrum of the diffuse emission of the Galactic plane from 10 TeV and 1 PeV [99]. Unfortunately, the Galactic Centre is not within their field of view, and the measurement was limited to the region $15° < l < 125°$, $|b| < 5°$. They found a spectral index of 2.99 ± 0.04. This soft index matches the one observed by HAWC (2024) in the GC in a comparable energyrange and indicates the need of a spectral break or curvature from the hard to the soft spectra. Note, however, that due to the different ROI, a comparison between LHAASO (2023) and HAWC (2024) should be taken with a great deal of caution.

Chapter 13

Physical Motivated Model of the Diffuse Emission

In part II it was shown that modelling the CMZ in three dimensions and fitting morphology and the spectrum simultaneously with all the other model components results in a significant cutoff in the γ-ray emission spectrum. This γ-ray emission is attributed to protons diffusing from a central source and interacting with the gas in the CMZ. In contrast to the previous approach, which employed a template-based methodology, this part utilises a physically motivated model. The advantage of this approach is that the properties of the protons are fitted, rather than the best-fit γ-ray properties. This includes the spectral parameter of the initial proton source and the diffusion properties. This chapter outlines the configuration of the physical model and presents the fit results of said model. These results will be compared to the template-based fit and to published results from other telescopes. Finally, the individual clouds and two complexes are analysed.

13.1 Model Setup

The γ-ray diffuse emission observed in the GC is due to interaction with protons and the molecular gas. The protons are originating from a central point source with a power law spectrum [with exponential cutoff]:

$$N_{\mathrm{proton}}(E) = N_0 \left(\frac{E}{E_0}\right)^{-\Gamma_p} [\exp(-E\lambda_p)] \tag{13.1}$$

where N_0 is the total number of protons injected in the CMZ, the reference energy E_0 is fixed to 1 TeV, Γ_p is the spectral index and in case of a cutoff $\lambda_p = 1/E_{\mathrm{C,p}}$ is the inverse of the cutoff energy.

These injected protons are diffusing into their surrounding medium where a continuous scenario is assumed. The observations made by H.E.S.S. (2016) and MAGIC (2020) lend support to the choice of this scenario over impulsive injections, as they found the $1/r$ distribution. This results in a proton distribution based on equation 12.20. The distribution is plotted for different diffusion coefficients D_0 and $\delta = 0$ in Figure 13.1 (upper panel). The diffusion time was set to 10^7 years. For a given number of injected protons, the larger the diffuse emission coefficient, the more the protons spread out. It should be noted that this diffusion is modelled in four dimensions: three spatial (Galactic Longitude, Latitude, and z) and in the proton energy dimension.

The diffused protons interact with the gas distribution in the CMZ, resulting in a profile as shown in Figure 13.1 (lower panel). Once more, the larger the diffusion coefficient, the greater the spreading. Subsequently, the proton spectrum is transformed into a γ-ray spectrum. This is based on reference [79].

This process yields a physically motivated model of the γ-ray diffuse emission in the CMZ. The physical model was implemented by Dr. Yu Wun Wong and described in her PhD thesis [100, 80].

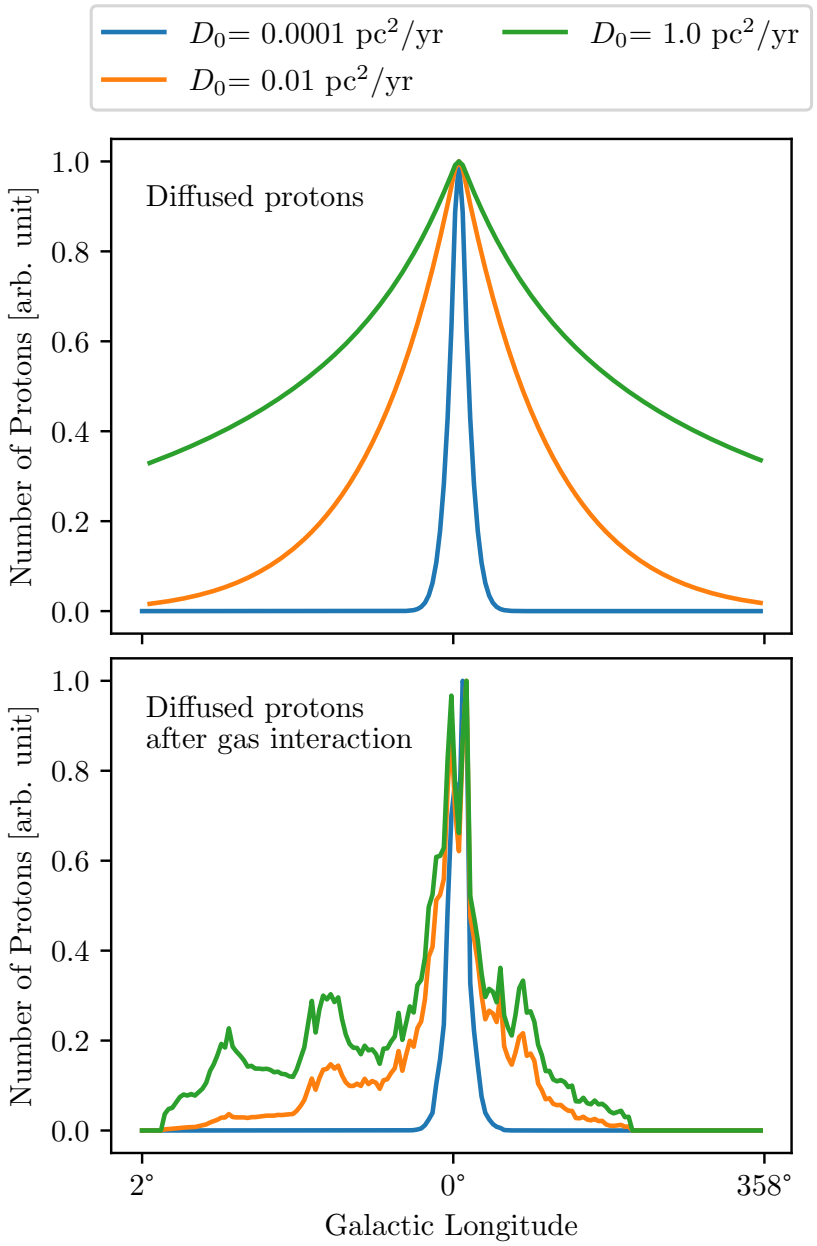

Figure 13.1: Upper panel: Profile along the Galactic Longitude of the protons after diffusion for different diffusion coefficients with no energy dependency ($\delta = 0.0$). Lower panel: Profile along Galactic Longitude of the protons that have diffused and interacted with the molecular gas.

13.2 Fit Results

The model is fitted together with the four point sources, the band model for the LSC and the background template with the nuisance parameters.

Previously, modelling the CMZ with the template-based approach lead to the detection of a cutoff in the γ-ray spectrum, the implication is that the initial proton spectrum also has a cutoff. Using a power law with exponential cutoff resulted in a best-fit spectral index of 1.51 ± 0.04 and a cutoff energy of $164.61 \pm 32.71\,\mathrm{TeV}$. The scaled, resulting spectrum is shown in Figure 13.3. The total number of injected protons is determined to be $(0.34 \pm 0.05) \cdot 10^{52}$. The energy-dependent diffusion coefficient is $D(E) = (0.11 \pm 0.01) \cdot (E_\mathrm{p}/10\,\mathrm{GeV})^{0.71\pm0.01}\mathrm{pc}^2/\mathrm{yr}$. The proton spectrum after diffusion according to $D(E)$ is shown in the same figure. The spectral index of the diffused protons is $\Gamma_p + \delta$. This softening can be observed when comparing the spectral shapes. The cutoff energy remains unchanged. Following the diffusion process the protons interact with the molecular gas, resulting in the production of γ rays. The morphology of the resulting γ-ray emission is shown in Figure 13.2. The resulting spectrum is shown in Figure 13.3. The spectral index is identical to that of the diffused protons, however since the photons have in approximation 10% of the proton energy, the cutoff shifts to $\sim 10 - 20\,\mathrm{TeV}$. The flux points are computed and exhibit a well-distributed pattern around the spectrum.

Figure 13.4 shows the symmetric correlation matrix of the diffuse emission model parameters. As anticipated, the number of injected protons is significantly correlated with D_0. The same holds for the two parameters quantifying the spectral slopes: δ and Γ_p. Additionally, the index of the initial proton spectrum is found to be strongly dependent on the cutoff energy.

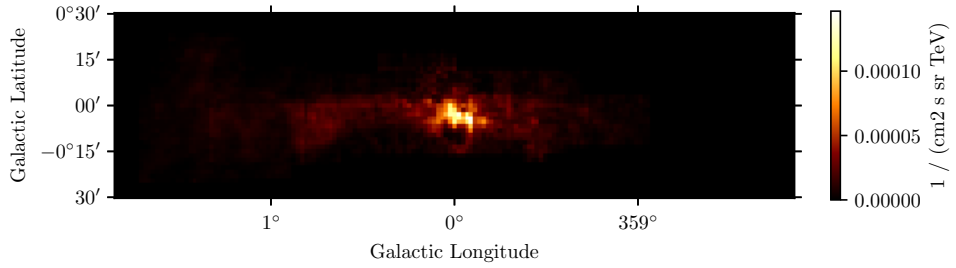

Figure 13.2: Best-fit γ-ray morphology due to protons diffusing from the central source. The map is summed along all energies.

To test the hypothesis that the initial proton spectrum has a cutoff, the fitting process has to be repeated with different spectra. Using a simple power law results in an spectral index of 1.81 ± 0.05. The spectral shape is not favoured compared to the exponential cutoff by 4.44σ. The other diffuse emission parameters slightly change. Additional to an exponential cutoff in the spectrum, there might be a less restrictive curvature, which can be parameterised by a log parabola spectrum. This spectrum is defined as:

$$N_\mathrm{proton}(E) = N_0 \left(\frac{E}{E_0}\right)^{-\alpha-\beta\log\left(\frac{E}{E_0}\right)} \tag{13.2}$$

The inclusion of the curvature is preferred over the simple power law with a statistical significance of 3.78σ. All the best-fit values are listed in Table 13.1. Note how the value for δ increases in the case of the log parabola spectrum.

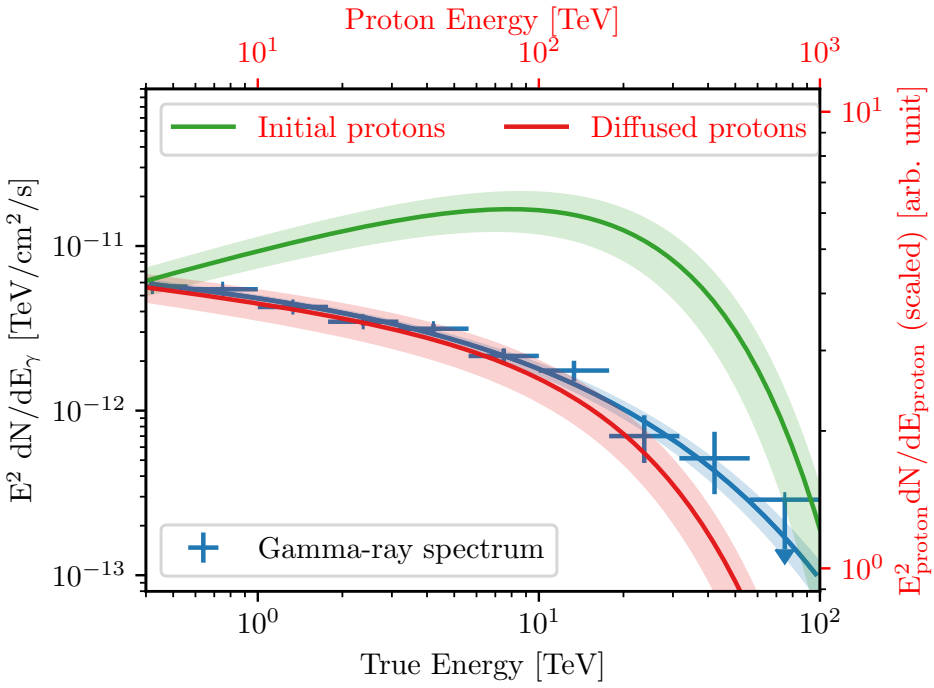

Figure 13.3: Best-fit spectrum of the inital proton source and spectrum of the protons after diffusion. Resulting γ-ray spectrum with flux points as measured by H.E.S.S.

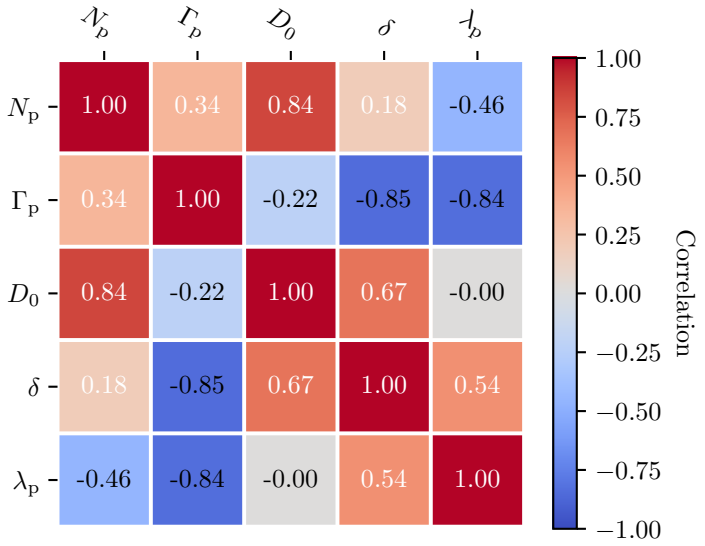

Figure 13.4: Correlation matrix of the diffuse emission model parameters.

In Figure 13.5 the γ-ray spectra resulting from different initial spectra of the proton source are shown with the corresponding flux points. Once again, it is evident that a simple power law does not provide an adequate description of the data at higher energies. This is indicated by the fact that both the flux points and the upper limits lie below the spectrum. Including an

Parameter	PL	ECPL	LogP
$\dot{N}_{\mathrm{D}}[10^{45}/\mathrm{s}]$	6.37 ± 1.47	0.34 ± 0.05	2.36 ± 0.78
Γ_{p}	1.81 ± 0.05	1.51 ± 0.04	
$D_0[\mathrm{pc}^2/\mathrm{yr}]$	0.99 ± 0.17	0.11 ± 0.01	0.31 ± 0.08
δ	0.69 ± 0.03	0.71 ± 0.01	0.99 ± 0.02
$1/\lambda_{\mathrm{p}}[\mathrm{TeV}]$		164.61 ± 32.71	
α_{p}			1.33 ± 0.07
β_{p}			0.10 ± 0.03
Significance		4.44σ	3.78σ

Table 13.1: Best-fit diffuse emission parameters for different initial proton spectra: power law (PL), power law with exponential cutoff (ECPL) and log-parabola (LogP). Note that the significance computed with respect to the power law.

exponential cutoff or a curvature in the spectrum results in a better description. The inclusion of an exponential cutoff or curvature in the spectrum results in a superior description. It is notable that the power law with an exponential cutoff and the log parabola spectrum are compatible within the 1σ errors, despite the diffusion parameters listed in Table 13.1 are not, an inconsistency that is not expected. This discrepancy can be attributed to the degeneracy of certain parameters.

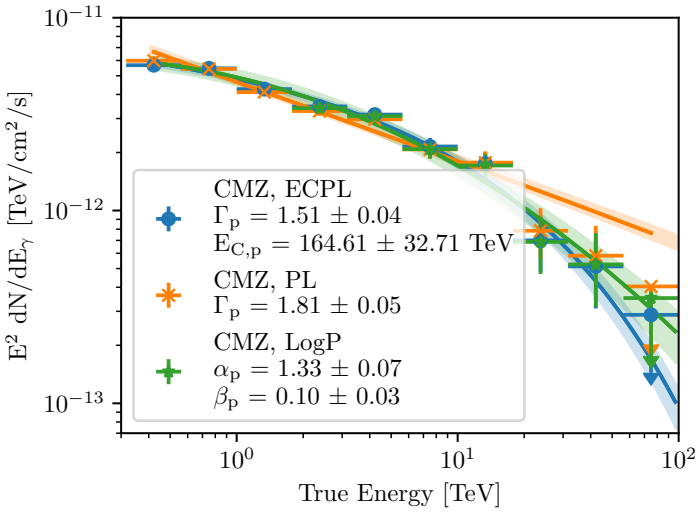

Figure 13.5: γ-ray spectra and flux points resulting from different initial proton spectral shapes inserted in the CMZ modelling.

The outcome of the analysis conducted in Part II was validated: the hypothesis that the γ-ray emission in the CMZ follows a simple power law was not substantiated. An exponential cutoff in the spectrum is slightly preferred over a curvature.

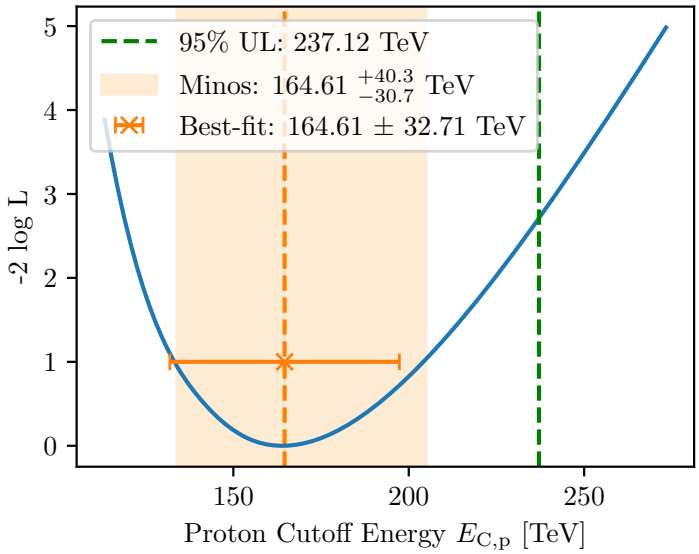

Figure 13.6: Likelihood scan as a function of the proton cutoff energy. The 1σ uncertainties from the fitting process and from the scanning are indicated, as well as the 95% upper limit.

13.3 Comparison with Published Results from Other Telescopes

In previous studies of the diffuse emission in the CMZ measured by H.E.S.S., no significant cutoff was found [60]. This led to the conclusion, that the underlying proton source should be capable of accelerating protons to PeV energies, thereby classifying it as a PeVatron. Upon initial examination, the current result is inconsistent with this prediction. A comparison of the analysis methods and datasets may, however, provide an explanation for the discrepancy in results. The study in 2018 utilised a slightly smaller dataset (250 hours) and an ON/OFF analysis technique. In this case, the background is not incorporated into the template, which is created from archival data, but is evaluated in the OFF regions. A comprehensive overview of the diverse background model techniques can be found in section 1.4. The morphology of the CMZ was modelled as the product of the molecular gas and a 2D Gaussian function with a standard deviation of $\sigma = 1.11° \pm 0.17°$ and the spectrum was modelled as a simple power law. The spectral γ-ray index was determined to be 2.28 ± 0.20. It is important to note, however, that the morphology and the spectrum are not modelled and fitted simultaneously. Consequently, the various components cannot be disentangled as it is possible with the 3D template-based analysis presented here. Especially, the CMZ and the LSC components have a large overlapping region. The γ-ray flux is estimated as a function of the energy in the so-called ridge region. Hereby, a rectangle box of dimensions ($1° \times 0.3°$) is used with a mask around all known point sources is meant. The flux points are shown in Figure 13.7. They are now compared to the CMZ γ-ray flux points and the best-fit model. It is evident that there is a slight discrepancy in the source strength at the lower energies. This discrepancy is attributable to the disparate analytical techniques and modelling approaches employed in the analysis of the CMZ, LSC, and the additional central component. However, the spectral shape of the distribution of the flux points is however in a good agreement. The spectral index of the γ-ray emission here is $\sim \Gamma + \delta = 2.22$ which is within the uncertainties of the value found in [60] ($\Gamma = 2.32 \pm 0.05_{stat} \pm 0.11_{sys}$).

The flux points obtained by MAGIC (2020) are highly consistent with those obtained by

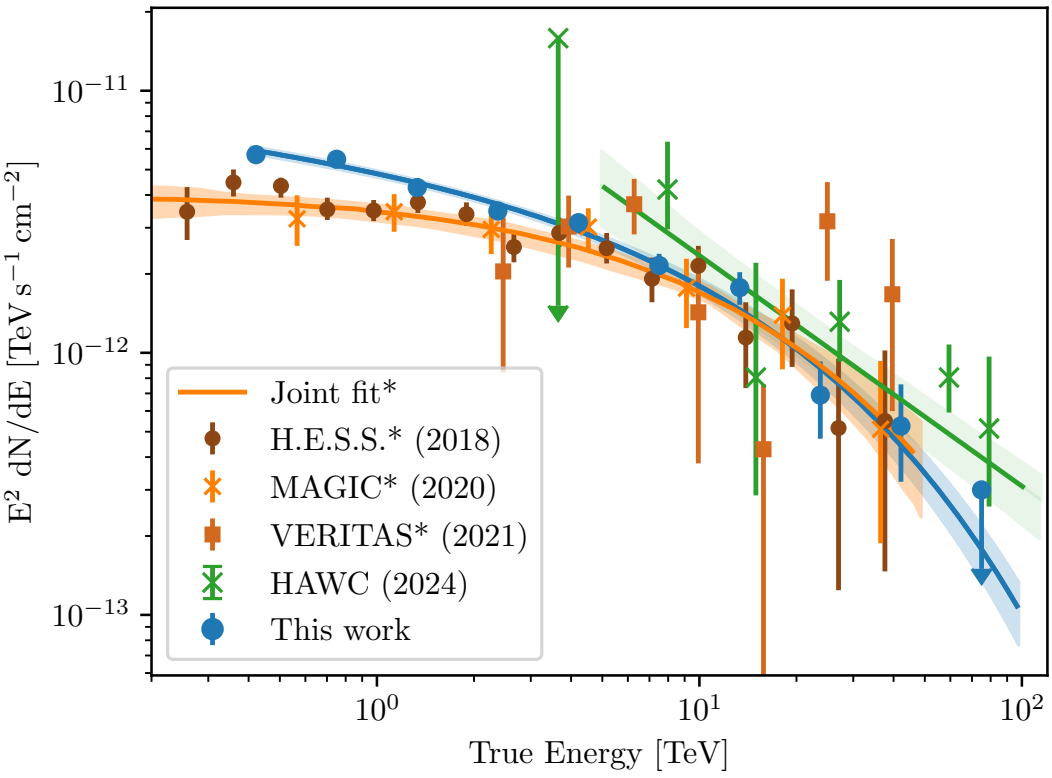

Figure 13.7: Comparison of the CMZ γ-ray flux points to different observations in a similar region. Data taken from H.E.S.S. (2018)[60], MAGIC (2020)[96], VERITAS (2021)[97], HAWC (2024)[98]. The joint fit of the flux points of H.E.S.S. (2018), MAGIC (2020) and VERITAS (2021) taken from [101].

H.E.S.S. (2018)[96] (see Figure 13.7). Assuming $E_{\mathrm{C},\,\gamma} \approx 10\% \cdot E_{\mathrm{C},\,\mathrm{proton}} \approx 16.4 \pm 3.3\,\mathrm{TeV}$, the cutoff values are in very good agreement with the one found by MAGIC (2020) at $17.5^{+59.3}_{-9}$ TeV with 2σ significance [102].

In [101], a joint fit of the flux points obtained by H.E.S.S. (2018), MAGIC (2020) and VERITAS (2021) was reported.

The γ-ray spectrum was modelled assuming hadronic emission, with the proton spectral index and exponential cutoff energy as free parameters of the fit (see Figure 13.7). A conservative systematic uncertainty is added to the flux points and the fitting range is $[0.26, 39.8]\,\mathrm{TeV}$. The best-fit value of the proton index was found to be 2.03 ± 0.14 with an exponential cutoff in the proton spectrum of $157 \pm 87\,\mathrm{TeV}$. While the index slightly deviates from the value found here, the cutoff value is in excellent agreement. In the publication, a PeVatron test statistic (PTS) is defined as a likelihood ratio test between the best-fit cutoff value in the proton spectrum and a cutoff at 1000 TeV. The significance S_{PTS} is defined as the square root of PTS and for $S_{\mathrm{PTS}} < 5$ an association with a PeVatron with at least 5σ. On the other hand, $S_{\mathrm{PTS}} \geq 5$ ensures that the underlying proton spectrum reaches beyond 1 PeV. For $|S_{\mathrm{PTS}}| \leq 5$, the Pevatron cannot be excluded nor confirmed due to the statistics being not sufficient. The latter is the case for the joint fit, since $S_{\mathrm{PTS}} = -2.3$ was found. Note however, that the results tend to a rejection of the PeVatron hypothesis.

Beside the different analysis technique (3D vs ON/OFF) the main difference between H.E.S.S. (2018) and the results here, is the upper limit of the energy range in which the diffuse emission was analysed. If the upper limit of 100 TeV used in this work is reduced to the 45 TeV used in H.E.S.S. (2018), the best-fit proton spectrum slightly changes. The index was fitted $\Gamma = 1.53 \pm 0.03$ and the cutoff to $E_C = 215.29 \pm 59.32$ TeV which is compatible to the value obtained before within the 1σ statistical uncertainty. The significance of the cutoff decreases from the mentioned 4.44σ to 3.57σ. This highlights the importance of the last two energy bins of the analysis and explains the lack of a significant cutoff in the H.E.S.S. 2018 publication.

In conclusion it can be stated that the flux points obtained from the diffuse emission are consistent in their spectral shape when considering the different analysis techniques and regions where the spectrum was extracted. The best-fit spectrum and the significance of a cutoff are dependent upon on the energy range and the available statistics. However, if only data > 10 TeV is considered, the index becomes softer. Consequently, it is evident that a break, cutoff or curvature is necessary to explain the softening of the spectrum.

It is challenging to ascertain whether the source injecting protons into the CMZ can be classified as a PeVatron, given the vague definition of this phenomenon. In [98], it is stated that the occurrence of 98 events with energies of ~ 100 TeV indicates that the source is a PeVatron. However, the threshold is never discussed. In [60], the proton source is considered a PeVatron since the γ-ray spectrum does not indicate a spectral break or a cutoff. Nevertheless, this spectral shape should be questioned which makes the argument unconvincing. To answer the question of a PeVatron in the GC with statistical certainty, more data needs to be collected, especially in the higher energy range.

13.4 Spectra of the Individual Gas Clouds

As mentioned in section 12.3 the CMZ consists of different clouds. In addition to an overall analysis of the region as a whole, the individual regions can also be analysed. This enables the quality of the overall fit to be evaluated and regional variations in the spectrum of the CMZ to be identified. The individual cloud regions are illustrated in Figure 13.8. The total number of regions is seven, and they vary in size. The majority of the excess is situated within the compact cloud structure designated as Sgr B2. The definitions and spatial gas templates for the cloud regions were provided via personal communication hghg[62], and are based on the gas distribution commonly used in CMZ studies.

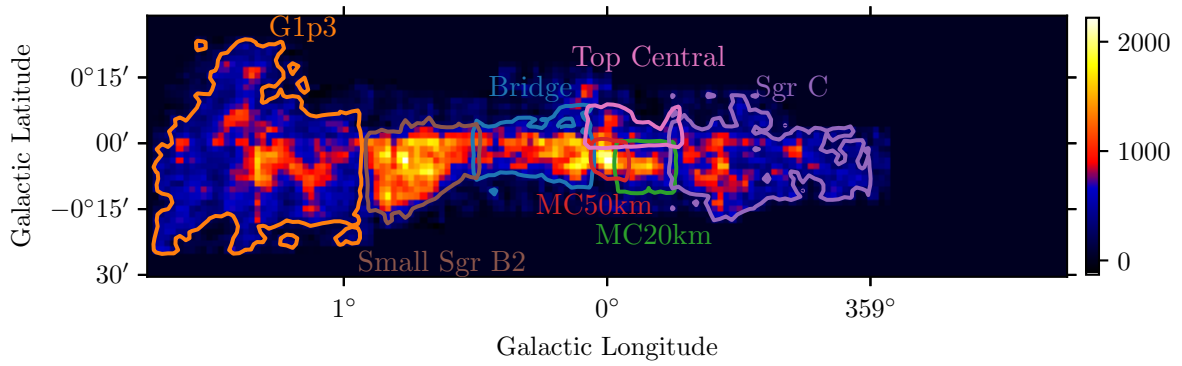

Figure 13.8: The seven cloud regions defined in the CMZ overlaid over the gas distribution.

To enable comparison of the quality, the flux points were calculated in two different ways.

First, the flux points obtained for the entire CMZ were rescaled for each cloud region using the fraction of the expected flux attributed to that region, as determined from the spatial emission templates. Secondly, the flux points were recalculated within the region. Both flux points are presented for all regions in Figure 13.9. Due to the limited statistics within the clouds, the cutoff at high energies cannot be discerned, and upper limits were employed. In general, however, the two types of flux points align well. This indicates that the description of the CMZ is not only accurate for the entire region but also for the individual clouds.

13.5 Fitting of the Complexes

As shown in the residual map presented in Figure 9.9, two point-like structures stand out as being more significant than the rest of the FoV. These structures are spatially aligned with the two cloud complexes, designated B and C, which are part of Sgr B and C, respectively. It is possible that the positive excess is the result of a misreconstruction of the position of the clouds or complexes with respect to Sgr A*. This information is derived from the face-on distribution of the gas, as determined from CO measurements. However, it should be noted that uncertainties may arise due to instrumental limitations, binning effects, or incorrect differentiation between sources along the line of sight. Given that the residual maps of the FoV are essentially flat, it can be assumed that the effects are minimal and confined to the individual complexes. In order to ascertain whether this can be accounted for in the fit, two point sources with a simple power law have been included.

The spatial residual map is shown in Figure 13.10. At the locations indicated by magenta circles, no residual excess is observed. The statistical significance of Complex B (C) is 6.25σ (5.46σ). The best-fit spectra with flux points for the two complexes are shown in Figure 13.11. Given the limited statistical data available, the flux points beyond 1 TeV are upper limits. The spectral index is relatively large and matches the γ-ray index observed in the CMZ. The incorporation of the complexes has no impact on the optimal fit position or spectrum of the point sources. The spectral index of the LSC remains unaltered; however, the cutoff energy is reduced from 11.87 ± 2.90 TeV to 10.96 ± 2.57 TeV. Similarly, the cutoff energy of the CMZ is slightly reduced from 164.61 ± 32.71 TeV to 161.09 ± 36.44 TeV. The sum of the spectral index of the initial source and the spectral slope of the diffusion coefficient $\Gamma + \delta$ demonstrates minimal variation: 2.22 in the absence of the complexes and 2.21 with the complexes included in the fit.

Parameter	Complex B	Complex C
$\Phi_0[10^{-14}\mathrm{TeV}^{-1}\mathrm{s}^{-1}\mathrm{cm}^{-2}]$	8.97 ± 1.59	6.65 ± 1.41
Γ	2.69 ± 0.26	2.41 ± 0.23
Lon [°]	0.67 ± 0.01	359.42 ± 0.01
Lat [°]	-0.03 ± 0.01	-0.09 ± 0.01

Table 13.2: Best-fit parameters of the complexes B and C.

The location of the clouds and complexes in relation to Sgr A* is subject to systematic uncertainties that have an impact on the morphology of the CMZ model. In the event that the reconstructed face-on position is erroneous, the γ-ray excess will be either over- or underestimated.

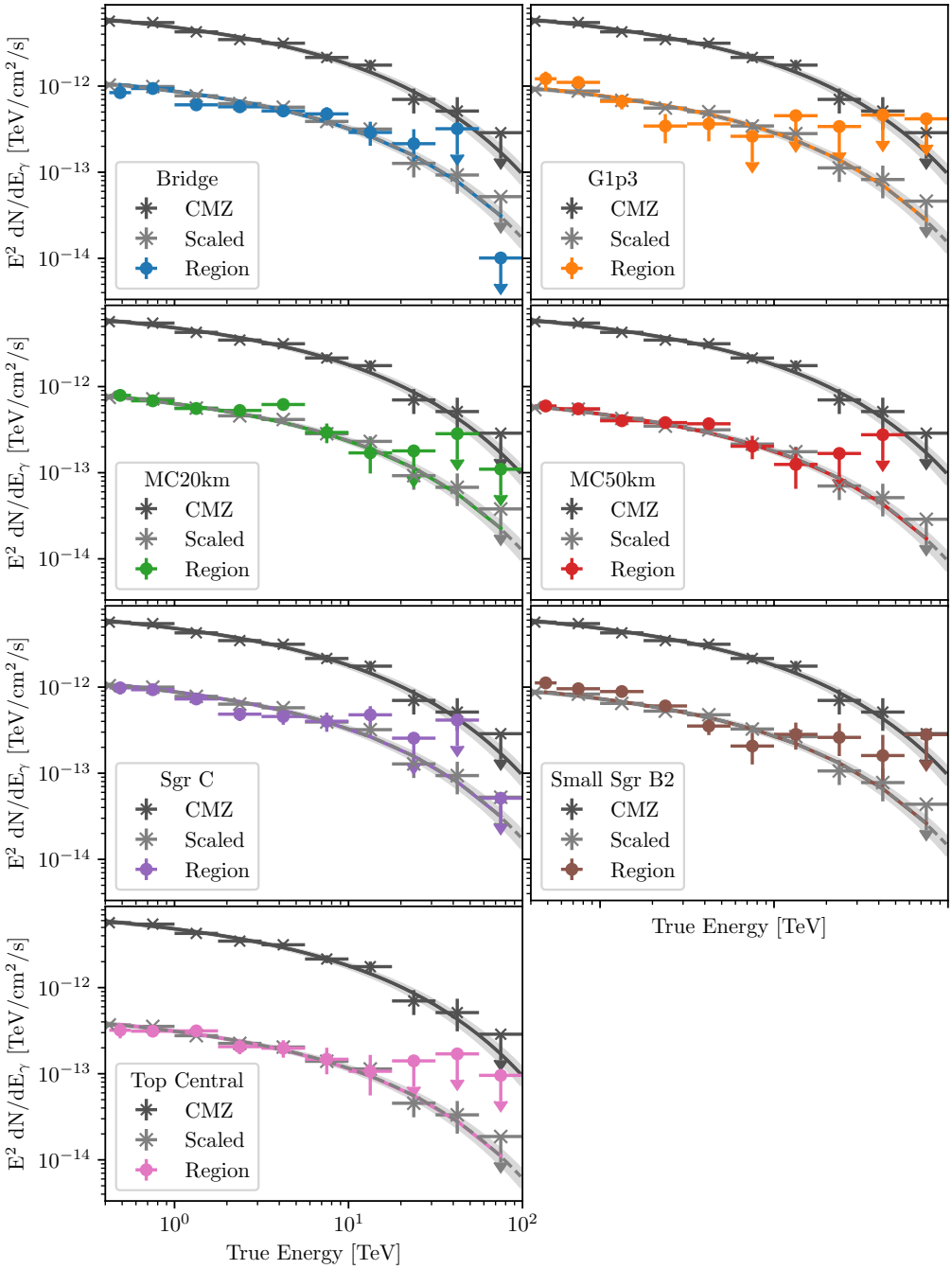

Figure 13.9: γ-ray spectrum of the whole CMZ (dark grey) and the different clouds computed by scaling the spectrum according to the flux within the cloud region (colored lines). The flux points computed in the whole CMZ are also scaled (light grey) and additionally recomputed in the cloud region (colored).

As evidenced by the residual maps, this is also the case for complexes B and C. The inclusion of point source models with power laws in the dataset led to an improvement in the overall description of the data without altering the fact that a cutoff is present in both the LSC and

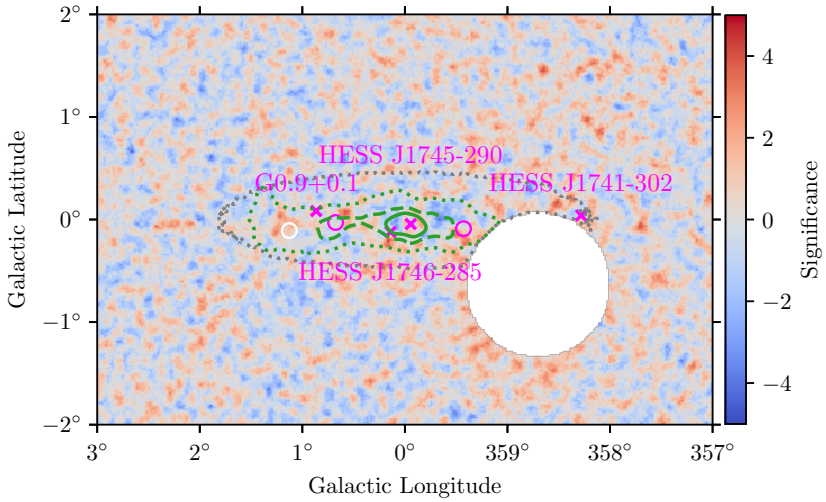

Figure 13.10: Residual map after including complex B and C. Modelled as a power law and a point source. The position of the two fitted complexes is indicated as a magenta circle.

the CMZ. A different measurement of the face-on distribution of the gas by Yan et al. [103] indicates that the cutoff in the CMZ remains as demonstrated by Y.W. Wong [80]. The Sawada measurement [66] provides the optimal description of the data and is therefore employed here.

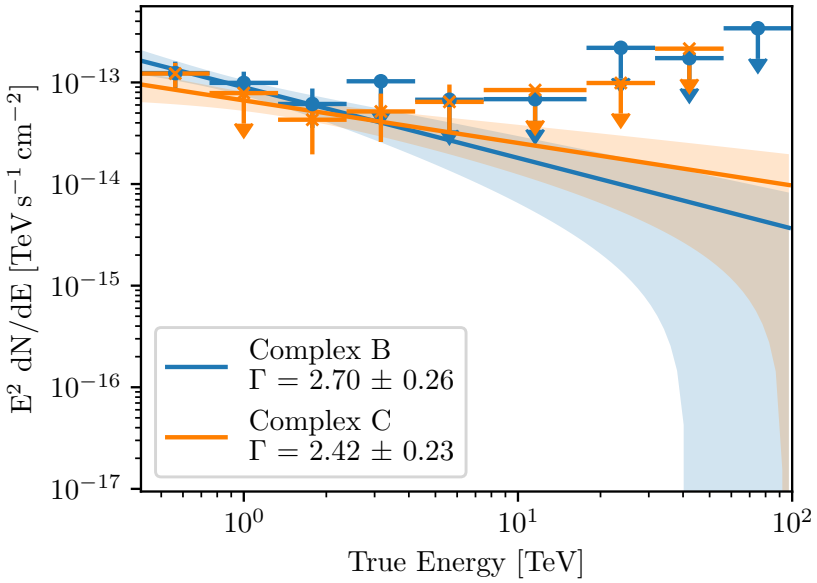

Figure 13.11: Best-fit spectrum with flux points of the two complexes.

Chapter 14

Systematic Uncertainties and Cross-checks

In order to further verify the existence of a cutoff in the γ-ray spectrum of the CMZ, systematic uncertainties are discussed and cross-checks are performed. In section 14.1, the results are compared to the fit results obtained with the template-based model of the CMZ. The modelling of the LSC emission is regarded as a significant source of systematic uncertainty, with a notable impact on the spectrum of the CMZ. Before the LSC's morphology was modelled with a band model and its spectrum with a power law with an exponential cutoff. Both the model components are replaced in section 14.2. First, the exponential cutoff power law is replaced by a simple power law and a log parabola spectral model, and the other model components are refitted to test the effect on the CMZ (section 14.2.1). Furthermore, the band model is replaced with a more physical morphology (section 14.2.2). Additionally, the systematic uncertainties due to the IRF are included in the fitting with nuisance parameters and priors (section 14.3). Lastly in section 14.4, the diffuse emission parameters are fixed to theoretical predictions to test whether the degeneracy has an effect on the CMZ.

14.1 Comparison with the Template-based CMZ Modelling

In part II of the thesis, the CMZ was accounted for using a template-based model. In this instance, the morphology is defined as the distribution of gas, which is multiplied by a distribution of the form $1/r$. The γ-ray spectrum was either a simple power law or a power law with exponential cutoff. The latter was selected as the preferred model by a significance level of 4.77σ, with a best-fit cutoff value of $23.59 \pm 6.79\,\mathrm{TeV}$. The results obtained with the template-based approach can now be compared to those obtained with the physical model. Additionally, the effect of the CMZ model on the other physical models is evaluated. As anticipated, the choice of CMZ model has no impact on the point sources (see Figure 18). The best-fit spectrum and the associated flux points of the LSC are shown in Figure 14.1 (left). A slight alteration in the cutoff value is evident, yet the compatibility remains high. The γ-ray spectra of the CMZ obtained with the different models with flux points is shown in Figure 14.1 (right). Assuming that the spectral index of the γ-ray spectrum is similar to the proton index after diffusion ($\sim \Gamma_p + \delta = 2.22$), the value is compatible with the best-fit of the template. The exponential cutoff value of the proton spectrum is $E_{c,p} = 164.61 \pm 32.71\,\mathrm{TeV}$. Assuming that the γ-ray energy is 10% of the initial proton energy, the γ-ray cutoff energy is $E_{c,\gamma} \approx 16.4 \pm 3.2\,\mathrm{TeV}$. This is slightly lower than the

value obtained with the template. However, it should be noted that the strength of the γ-ray cutoff differs between the models. A power law with an exponential cutoff can be expressed as:

$$\phi(E_\gamma) = \phi_0 \left(\frac{E_\gamma}{E_0}\right)^{-\Gamma_\gamma} \exp(-(\lambda_\gamma E_\gamma)^\alpha) \tag{14.1}$$

where α is the cutoff strength parameter which is 1 per default. If the proton spectrum is modelled with such a model, during the transformation to the γ-ray spectrum the cutoff strength is weakened. Fitting equation 14.1 to the γ-ray spectrum obtained with the physical model yields $\alpha = 0.57 \pm 0.05$, which can also be observed by comparing the spectra. This is the reason for the slight change in both the CMZ and the LSC spectral cutoff value where the latter is compensating. Nevertheless, in both instances, a cutoff of some strength is preferable to a simple power law, and the results are deemed consistent.

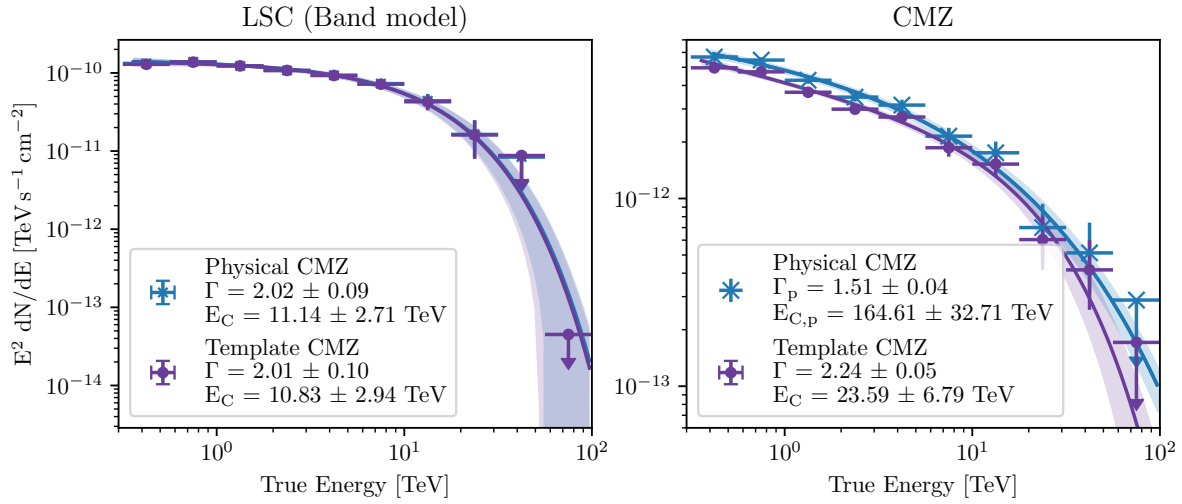

Figure 14.1: Best-fit spectra and flux points of the LSC (left) and the CMZ (right) obtained with different models for the CMZ. The physical model refers to the morphology parameterising the diffusion of the protons and the proton spectrum. The template model consists of a $1/r$ distribution multiplied with the gas distribution and a γ-ray spectrum. Note that in the CMZ spectrum Γ and E_C refer to the properties of the γ rays.

14.2 Effect of the Large-Scale Emission

As documented in the H.E.S.S. publication from 2018 about the CMZ, the measured γ-ray flux necessitates the incorporation of a large-scale model component for an accurate description. It was thus demonstrated that this component accounts for 30% of the measured flux, thereby emphasising the importance of accurately describing this model component for the purpose of facilitating further physical interpretations. In comparison to the diffuse emission observed in the CMZ, the emission in question displays a considerably larger extension in both latitude and longitude, and does not fully trace the distribution of molecular gas. Given that 30% of the molecular gas within the region of interest is in a diffuse hydrogen phase, it was anticipated that the large-scale emission would be attributable to CRs interacting with this gas [60].

In [60], the LSC is modelled as a Gaussian distribution centered around ($l = 0°$, $b = 0°$) and with a power law spectrum. The extension of the Gaussian was fitted to the following values: $\sigma_x = 0.97° \pm 0.13°$ and $\sigma_x = 0.22° \pm 0.07°$. The basis of the LSC model component is adapted here: a simple power law and a band model with Gaussian extension in latitude. The longitude extension is along the whole ROI. The longitude extension is applied to the entire ROI, thus aligning with the distribution of the effective area. It should be noted that, due to the extensive nature of the LSC, it is significantly influenced by background systematic uncertainties.

In this chapter, the impact of the spectral and spatial shape of the LSC has on the CMZ, in particular the proton cutoff value, is tested. Initially, the spectrum is modelled with a power law with and without an exponential cutoff and a logparabola spectrum. Subsequently, the relatively simple band-like morphology is exchanged for a more complex, detailed template.

14.2.1 Different Spectral Shapes

Fitting the LSC with a band model and a simple power law results in an index of 2.46 ± 0.05. In this scenario the initial proton spectrum causing the diffuse emission shows to have an spectral index of 1.54 ± 0.03 and an exponential cutoff of 114.14 ± 22.30 TeV. The cutoff has a significance of 6.26σ. The best-fit γ-ray spectra with flux points of the LSC and the CMZ are shown in Figure 14.2. The last fluxpoint of the LSC computed with the power law indicates the need for a cutoff or curvature by being located way below the best-fit spectrum. The spectral residual at the highest energies also indicated a slight overprediction of the model (see Figure 14.3). Therefore, a exponential cutoff was introduced to the LSC spectral model. The value was fitted to 11.87 ± 2.90 TeV and the spectral index slighly hardens. The overall description of the data improved by 5.13σ and the cutoff is therefore considered significant. The upper limits of the flux points are now above/on the spectrum. Due to the large spatial overlap, is expected that the spectral modeling of the LSC has a strong effect on the spectral properties of the diffuse emission. Indeed the introduction of an exponential cutoff in the LSC spectrum, increases to 164.61 ± 32.71 TeV with a slightly softer spectral index. The significance of the proton cutoff of the CMZ is reduced to 4.44σ.

Instead of using an exponential cutoff in the LSC spectrum a curvature can be included by employing a log parabola model. The best-fit values for α and β are listed in the legend in Figure 14.2. The log parabola spectrum is preferred compared to the simple power law with a statistical significance of 4.89σ. The curvature in the LSC is causing the exponential cutoff in the proton spectrum of the CMZ to increase slightly to 209.16 ± 72.39 TeV. If the LSC is modelled with a log parabola spectrum, the exponential cutoff in the initial proton spectrum has a significance of 4.52σ.

The curvature is however, slightly less preferred compared to the exponential cutoff (2.09σ). The improvement of the description of the highest energies can be seen in the smaller residual points.

The diffusion parameters are less affected by the shape of the LSC spectrum. The spectral slope of the diffusion coefficient is increased slightly from 0.56 (PL) to 0.71 (ECPL) and 0.674 (LogP). The four point sources are not affected, see Figure 19.

Due the fact, that the ECPL is signficantly (slightly) perferred over the PL (LogP), it will be used as the default spectrum for the LSC in the following, unless stated otherwise. The spectral shape of the LSC has an effect on the exact value of the CMZ cutoff ($\sim 100 - 200$ TeV). The values are, however, compatible within the 1σ uncertainties and in all cases the cutoff has a significance of $> 4\sigma$.

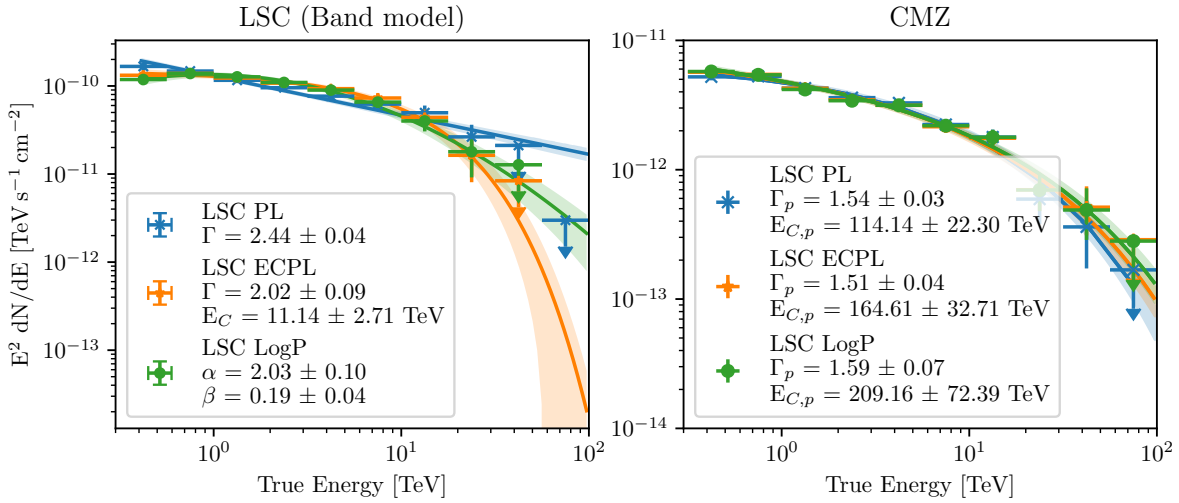

Figure 14.2: Left panel: Best-fit spectrum with error band and flux points obtained by fitting the LSC with a band model and three different spectral shapes. Right panel: Best-fit spectrum of the γ rays due to the diffuse emission modelled with an exponential cutoff power law and the LSC with the spectral shapes indicated in the legend. The best-fit values in the legend correspond to the intial proton spectrum.

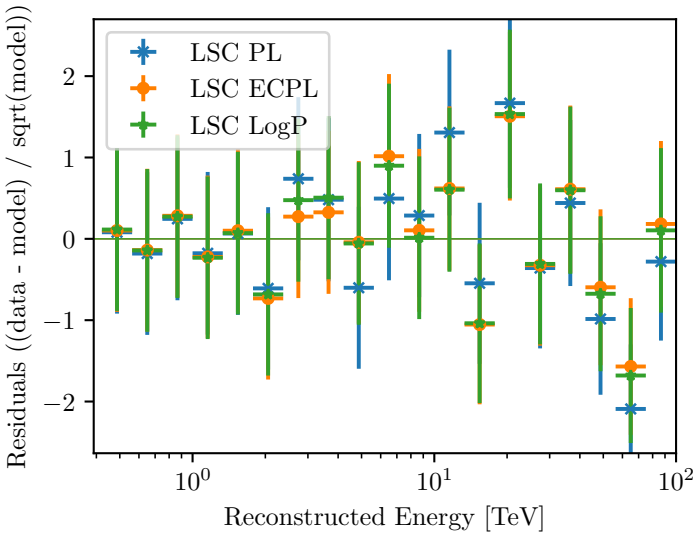

Figure 14.3: Spectral residual points computed with different spectral models of the LSC (power law, exponential cutoff power law and log parabola.)

14.2.2 Different Morphological Shapes

The assumed morphology of the LSC is very simplistic; however, it revealed good results based on the spectral and spatial residuals. Nonetheless, another morphology is tested to rule out any systematic effects on the diffuse emission. To obtain a more physical motivated model, HERMES is used [104]. It is a publicly available framework where multi-wavelength skymaps of galactic emission are modelled based on muliple physical processes. The template to describe the LSC

in the GC region was produced by Dr. Justine Devin ([63]). Figure 14.4 shows the Li&Ma significance map computed if no LSC is taken into account. The excess is clearly shown. In the second row the LSC was modelled with the simple band model and an exponential cutoff power law. The latitude extension was fitted to $0.460^\circ \pm 0.03^\circ$. The residual drastically improve. In the last row, the 2D HERMES template is shown. Fitting it with an exponential cutoff power law to the data results again in good residuals. The mean value is slightly lower than the value obtained with the band model, while the standard deviation slighly increased. Based on these values, the band model is slightly preferred. The excess of the two complexes, Sgr B and C, is visible in both cases, as discussed in section 13.5.

The best-fit spectrum of the two different LSC morphologies is shown in Figure 14.5. The spectral index and cutoff values are in excellent agreement with each other. The significance of the cutoff with the band model was already stated (5.13σ). In the case of the HERMES template the cutoff significance is 5.46σ. The morphology of the LSC does not have a strong effect on the CMZ. The diffuse γ-ray spectrum is shown for both morphologies in Figure 14.5 (right). Both the spectral index and the proton cutoff are in very good agreement. The proton cutoff values have a significance of 4.44σ (4.22σ) for the band (2D HERMES) model. In the central energy range two of the flux points deviate from the spectrum for the HERMES template. This indicates a slight deviation from the model to the data. The overall description of the model, however, seems to be sufficient in both cases. This can be seen in the spectral residual points (see Figure 14.6).

In conclusion, both modelling the LSCs morphology with the 2D HERMES and the band model yield very good results. The effect on the diffuse emission is negligible. In the following, the band model will be used to model the LSC unless stated otherwise. This due to its simplicity and the closeness to the models used in previous publications [60].

The conclusion drawn from this chapter is that the spectral shape of the LSC does have a very strong effect on the spectral shape of the CMZ, especially on the cutoff value, not however on its signficance. When the LSC is modelled with a power law the cutoff value is the lowest, since the diffuse emission tries to compensate for the overprediction of the LSC model. This is possible since they have a large overlapping region. A cutoff or curvature in the LSC is however signficantly preferred.

Modelling the morphology of the LSC with a physical motivated 2D HERMES model instead of the simple band model, does not affect the description of the CMZ. The spectral shape of the initial protons is incomplete agreement.

14.3 Systematic Uncertainties due to the IRF

Systematic uncertainties due to mismodelling of the hadronic background were always taken into account in the previous fitting. The effect on the large-scale components (CMZ and LSC) was discussed in part II. However, systematic uncertainties due to the IRF have not been included yet. For a sufficient description, nuisance parameters and priors are used to quantify the errors. Similarly, to the modelling of the background, a piece-wise spectral model is used for the effective area, see equation 5.2. Seven normalising nuisance parameters logarithmically spaced within the range of [0.1, 100] TeV are used. On each nuisance parameter a Gaussian prior is set with an energy dependent standard deviation σ. Since the systematic uncertainties of the effective areas are larger at lower energies, the standard deviation has been conservatively set to 30 % for

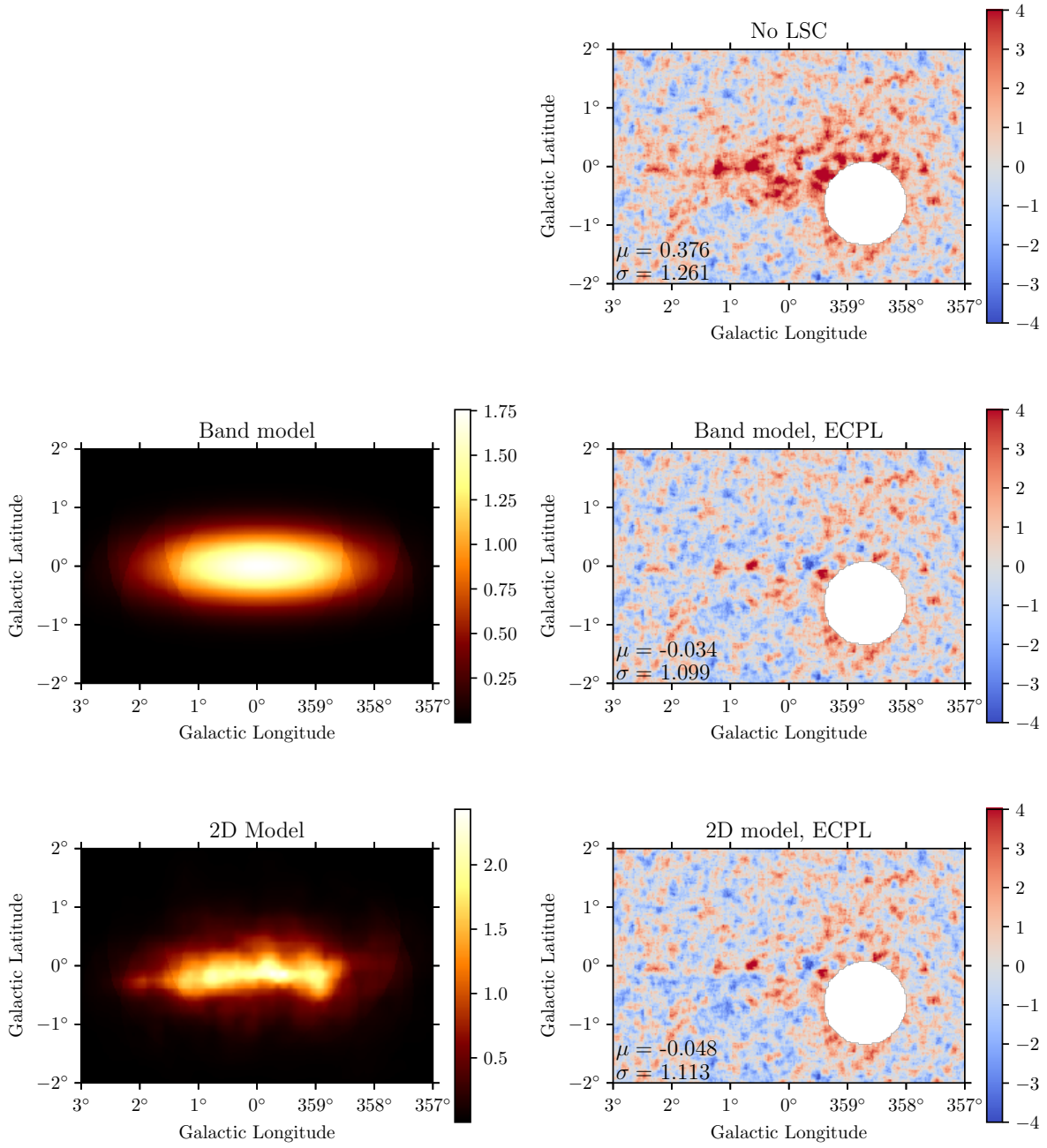

Figure 14.4: Left panel: Best-fit CMZ model summed over all energy bins before convolution with the PSF. Right panel: Li&Ma significance computed over all energy bins with the LSCs morphology modelled with the template shown in the same row. In the first row, the LSC is not modelled. The mean and the standard deviation of the Li&Ma distribution is shown.

energies below 3 TeV. For energies above 3 TeV, 10% was chosen. To account for the systematic uncertainty in the energy dispersion, the bias nuisance parameter Δb is included in the fit with a Gaussian prior with a standard deviation of 10%.
The bias was fitted to 0.03 ± 0.012 and the best-fit nuisance parameters modifying the effective

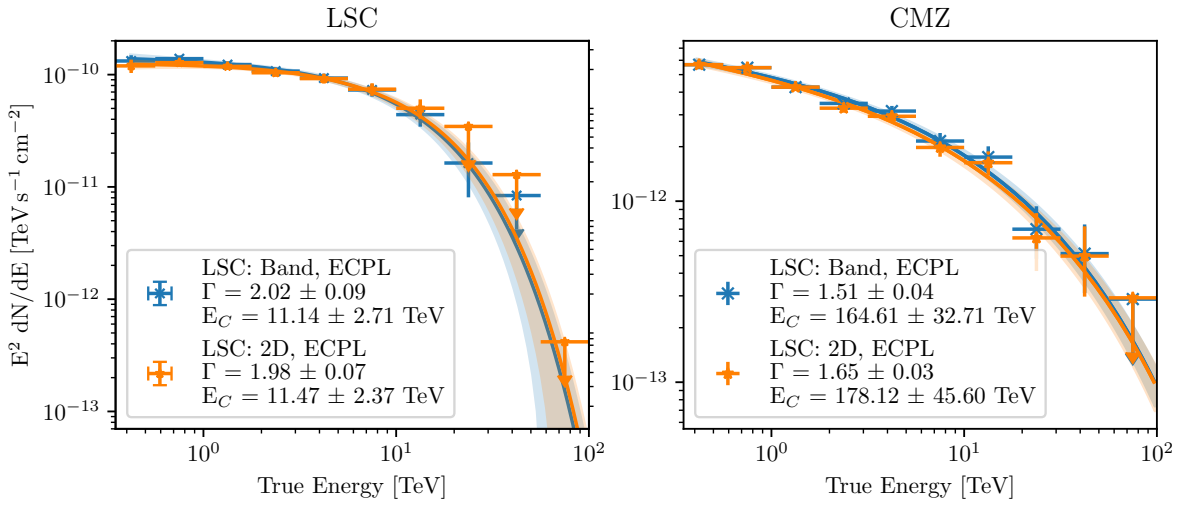

Figure 14.5: Left panel: LSC best-fit spectrum modelled with an exponential cutoff power law and the band model or the 2D HERMES template. The spectral best-fit values are listed in the legend. Right panel: Best-fit spectrum of the γ-ray diffuse emission modelled with a exponential power law as the initial proton spectrum. The LSC was modelled with the band model and the 2D HERMES template as indicated in the legend. The values in the legend refer to the proton spectrum.

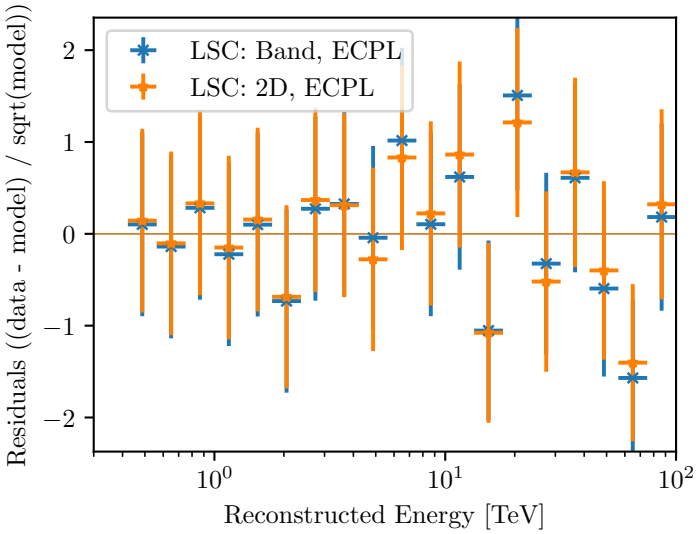

Figure 14.6: Spectral residual points computed for the case where the LSC is modelled with the band model and the 2D HERMES template. In both cases the spectrum is an exponential cutoff power law.

area are plotted as a function of true energy in Figure 14.7. As expected the strongest modification is found at the lower energies. The effect on the point sources is relatively negligible, the spectral results are shown in Figure 19. However, the two large-scale components LSC and CMZ are, however, slightly affected. Both spectra and flux points are shown and compared with the fit without IRF systematics in Figure 14.8. The spectral parameters of the LSC change only slightly,

with the relative errors increasing slightly. The index of the CMZ softens by 0.08 which is within the 1σ error and is due to the upward correction of the effective area model. This also results in a lower cutoff value of 130.15 ± 47.70 TeV compared to 164.61 ± 32.71 TeV in the case of no IRF systematics. The significance of the cutoff is slightly reduced to 3.66σ.
In summary, the inclusion of the systematic uncertainties of the IRF in a rather conservative prior estimate leads to an even lower proton cutoff with a significance greater than 3σ. This further reinforces the fact that there is a cutoff in the γ-ray spectrum that weakens the PeVatron hypothesis.

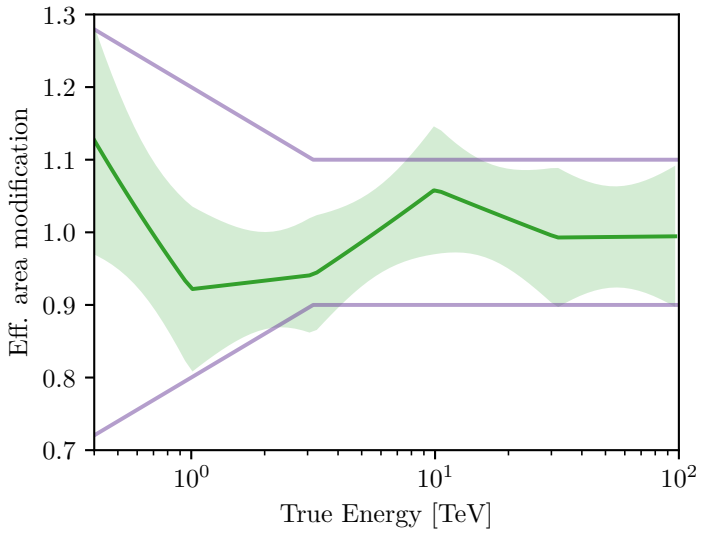

Figure 14.7: Best-fit nuisance parameters modifying the effective area as a function of energy. The purple lines indicate the magnitude of the systematic uncertainty used in the prior distribution.

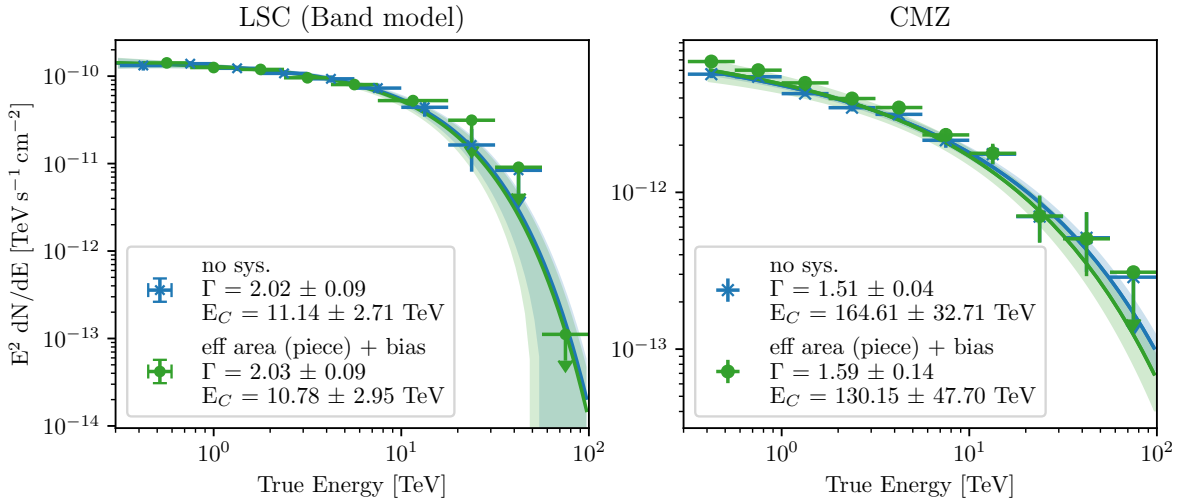

Figure 14.8: Best-fit spectrum with flux points of the LSC modelled with the band model and ECPL (left) and the CMZ (right) when no IRF systematic is taken into account and the effective area is modified by a piece-wise power law with Gaussian priors set on the nuisance parameters.

14.4 Diffuse Emission Parameterisation

In the diffuse emission model the spectral index of the proton source Γ and the slope of the diffusion coefficient δ are highly correlated since the measured γ-ray spectral index is equal to $\Gamma + \delta$. This was seen in the correlation matrix of the best-fit diffuse emission parameters, see Figure 13.4. An interpretation of Γ or δ alone is therefore not possible. The same is true with regard to the relationship between the number of protons, N_p, and the normalising diffusion coefficient, D_0. In order to ascertain whether this degeneracy presents an issue in the description of the data, theoretically motivated values have been adopted for δ and D_0. A plain diffusion (PD) is assumed with $\delta = 0.6$ and $D_0 = 3.0 \cdot 10^{28}\,\mathrm{cm}^2/\mathrm{s}$ at rigidity $\rho = 4\,\mathrm{GV}$ which is based on B/C measurements [105]. The latter is equivalent to $D_0 \approx 0.17\,\mathrm{pc}^2/\mathrm{yr}$. The two parameters δ and D_0 were fixed, while the remaining parameters were optimised using the maximum likelihood method. As anticipated, the effect on point sources was found to be negligible. The spectra and flux points of the LSC and the CMZ are shown in Figure 14.9. The parameters of the LSC remain unaltered. The difference between the best-fit spectral slope $\delta = 0.71 \pm 0.01$ and the δ_{PD} is 0.11, which is almost equal to the difference between the best-fit spectral index $\Gamma = 1.51 \pm 0.04$ and $\Gamma_{PD} = 1.63 \pm 0.02$. A slight change was observed in the proton cutoff value, with the significance of the cutoff increasing from 4.44σ to 4.53σ. The best-fit diffusion coefficient $D_0 = 0.11 \pm 0.01\,\mathrm{pc}^2/\mathrm{yr}$ slightly differs from the PD value $D_{0,\mathrm{PD}} = 0.17\,\mathrm{pc}^2/\mathrm{yr}$. The rate of injected protons is highly consistent: $\dot{N}_\mathrm{D} = 0.34 \pm 0.05 \cdot 10^{45}/\mathrm{s}$ and $\dot{N}_{\mathrm{D,PD}} = 0.35 \pm 0.03 \cdot 10^{45}/\mathrm{s}$. The ratio of the injection rate and the diffuse emission coefficient is plotted as a function of the proton energy for both the best-fit case and the PD model in Figure 14.10. The ratios are compatible within the 2σ errors.

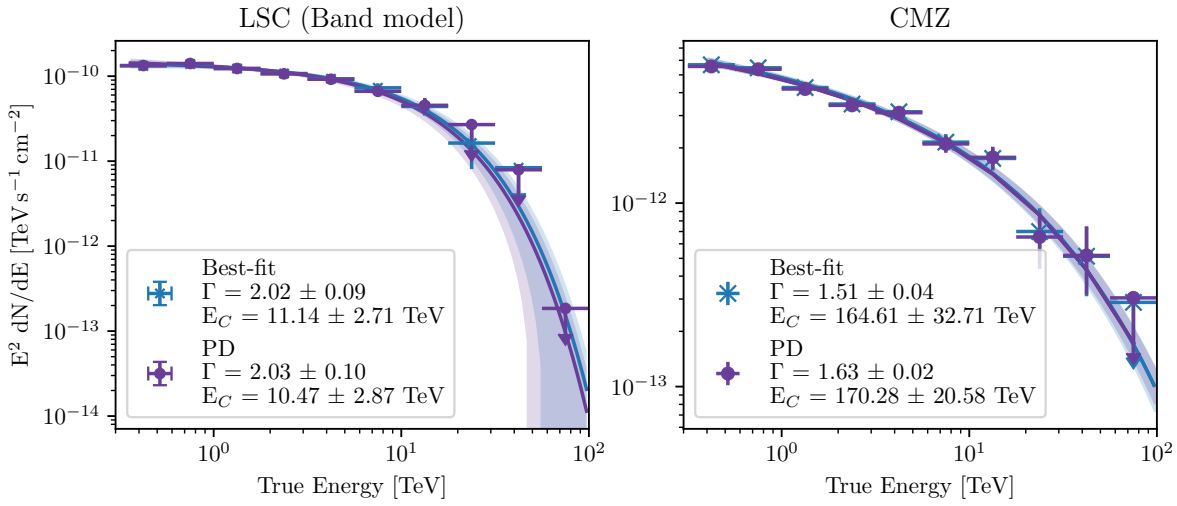

Figure 14.9: Best-fit spectrum and flux points of the LSC and the diffuse emission in the CMZ obtained with all diffusion parameters optimised (best-fit) and the plain diffusion (PD) assumption where $\delta = 0.60$ (fixed) and $D_0 = 0.17$ (fixed).

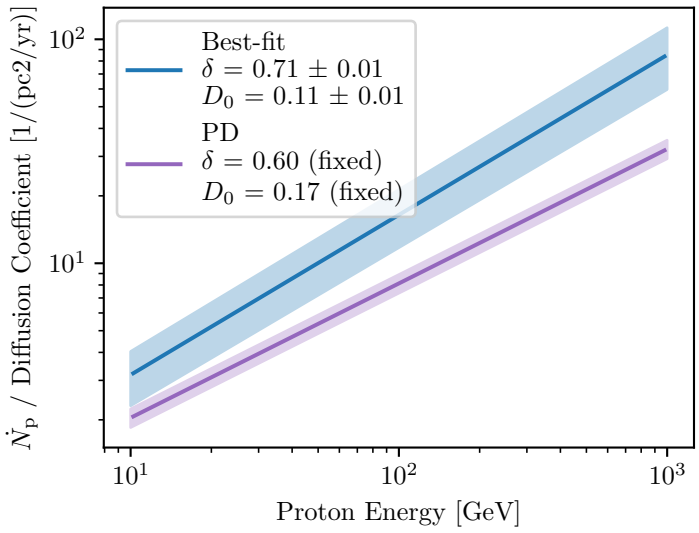

Figure 14.10: Best-fit of the ratio of the rate of protons injected $\dot{N}_p$ and the diffusion coefficient $D(E)$ as a function of proton energy compared to the plain diffusion (PD) model. Note that $\dot{N}_p$ was optimised in both the best-fit result and the PD case.

14.5 Summary of the 3D analysis of the CMZ

The GC is a highly complex region, comprising a multitude of different γ-ray emitting sources. 3D modelling of the GC allows for a simultaneous fit of the morphology and spectrum of the sources, thus enabling the distinction between overlapping sources to be made. The Galactic plane exhibits a high level of diffuse emission, which is attributable to the interaction of CRs with the molecules in the gas, resulting in the emission of γ rays. One component of this emission is attributable to the CR sea, the LSC. The remaining component is attributable to protons originating from an initial source and diffusing outwards. This results in a gradient in the γ-ray emission following a $1/r$ distribution towards the GC, which traces the dense gas component. The modelling of the CMZ diffuse emission was made more complex than in part II. The initial proton source was modeled with a continuous injection, and the protons were then modelled as diffusing into their surrounding medium with a certain energy-dependent diffusion coefficient. The application of a 3D fitting technique to the GC revealed an exponential cutoff in the spectrum of both the LSC and the CMZ. For the LSC, the cutoff was observed at 11.14 ± 2.71 TeV with a significance of 5.13σ. The proton source cutoff was observed at 164.61 ± 32.71 TeV, with a significance of 4.44σ. In a previous analysis of the CMZ with H.E.S.S., no such cutoff was identified, leading to the hypothesis of a PeVatron in the GC. However, the presence of a cutoff challenges this. Prior to comparing the results with the published data and interpreting them physically, it is essential to summarise the systematic uncertainties of the data and the analysis to ensure the reliability of the cutoff.

The results are presented in Table 14.1 and will be explained in more detail in the following section. The first cross-check is with a more straightforward model of the diffuse emission in the CMZ, namely the template-based approach employed in part II. Instead of modelling the spectral shape of the protons, the γ-ray spectrum was fitted. The significant cutoff is larger than 10% of the proton cutoff, which is attributable to the differing cutoff strengths. Despite both

spectra being power laws with exponential cutoffs, the transformation from proton spectrum to γ-ray spectrum resulted in a reduction of the cutoff strength. In light of this, the results are to be regarded as consistent.

The largest systematic uncertainty associated with the other model components is that of the LSC, due to the significant morphological overlap. In order to quantify the impact of this on the cutoff in the CMZ, both the spectral shape and morphology are varied. The LSC was modelled using three distinct approaches: a simple power law, a power law with an exponential cutoff, and a log parabola model. The selection of the LSC spectrum has a pronounced impact on the value of the CMZ cutoff. For all LSC spectra, the CMZ cutoff is found to have a significance of $> 4\sigma$. The morphology of the LSC was modelled by default with a band model, where the Gaussian extension was fitted. The software HERMES was used to create a 2D model of the morphology with greater morphological detail. However, when the fit was performed with this morphology in place of the band model, no change in the best-fit of the CMZ was observed. The significance of the cutoff remains.

The spectral shape of the γ-ray emission resulting from the proton diffusion model is dependent upon both the spectral index of the initial proton source and the energy-dependent diffusion coefficient. As a result, these two parameters are degenerate. Similarly, the number of injected protons is highly correlated with the normalised diffusion coefficient. These degeneracies can be avoided by fixing the two diffusion parameters, δ and D_0, to theoretical predictions. The resulting γ-ray spectrum is consistent with the one obtained when all parameters are fitted. The proton spectrum cutoff was found at a similar value with an even higher significance of 4.77σ.

While the background systematic is always accounted for by nuisance parameters acting as binwise normalisation terms, systematic uncertainties due to the IRF have not yet been addressed. Similarly, these were incorporated into the fit through the use of nuisance parameters and priors, which included an estimation of the magnitude of the systematic. While the point sources remained unaltered, both the LSC and the CMZ cutoff energy were fitted to slightly smaller values. As anticipated, the significance of the cutoff also exhibited a slight reduction due to the expanded parameter space.

The initial proton spectrum was also modelled with a curvature in the form of a log-parabola. This curvature was preferred by 3.78σ over the simple power law. Given that the exponential cutoff power law is slightly preferred over the log-parabola, the former was chosen as the default spectrum.

In conclusion, the proton spectrum in the GC responsible for diffuse emission in the CMZ is not a simple power law; rather, it exhibits a cutoff or curvature at an energy level below $< 1\,\mathrm{PeV}$.

Systematic Test	$E_{\mathrm{c,proton}}$[TeV]	$E_{\mathrm{c},}\gamma$[TeV]	Significance [σ]
Template-based CMZ model		23.59 ± 6.79	4.77
Power law bkg model		24.63 ± 6.73	4.52
LSC spectral shape	114.14 ± 22.30 (PL)		6.26
	164.61 ± 32.71 (ECPL)		**4.44**
	209.16 ± 72.39 (LogP)		4.52
LSC morphology	178.12 ± 45.60		4.22
IRF (ebias + eff.area)	130.15 ± 47.70		3.66
PD diffusion parameters	170.28 ± 20.58		4.53
Curvature	-	-	3.78

Table 14.1: List of the systematic tests and cross-checks with the CMZ energy cutoff value and its significance. The bold line corresponds to the default scenario. All values are expressed in proton energy, except for the first two lines, where the cutoff is in the γ-ray spectrum.

Chapter 15

Exploring the Hypothesis: The Galactic Center as a PeVatron

The γ-ray emission in the CMZ cannot be described by a simple power law. This has been established in the last chapter where multiple systematic uncertainties were taken into account and the model components of the LSC were varied. In any case, a cutoff or curvature of the CMZ spectrum is undeniable. This has implications for the previously proposed PeVatron nature of the parent source at the position of Sgr A* which will be explored in the following chapter. First known PeVatrons in the MW observed with γ-ray telescopes are presented together with their corresponding source candidates and their PeVatron nature. After checking the consistency with published results, several source candidates are presented. Finally, some general remarks are made and an outlook is given.

15.1 Known PeVatrons in the MW and their Source Candidates

In 2021, the LHAASO collaboration published the detection of a source with significant (8.5σ) excess above 100 TeV [106]. In the LHAASO catalogue published in 2024, γ rays above 100 TeV were measured from a total of 43 sources [2]. For some of the LHAASO UHE sources there is an overlap with sources already detected by HAWC beyond 56 TeV [3].

Further PeVatron candidates have been identified among others with H.E.S.S. This includes HESS J1702-420, and as mentioned the GC. The latter was already discussed in detail. One of the components of HESS J1702-420 exhibited a hard spectrum, thereby providing evidence for emission up to 100 TeV [107]. The exact origin of HESS J1702-420 remains uncertain. The Crab Nebula was observed to emit particles with energies exceeding 100 TeV by HAWC, MAGIC and Tibet-ASγ [65]. Furthermore, LHAASO was able to measure the γ-ray flux of the Crab Nebula up to 1 PeV. The Crab nebula is the sole PeVatron with a known source: a pulsar wind nebula (PWN) which was created by a supernova explosion. The central pulsar is a spinning neutron star whose 'spin-down' releases energy, resulting in the production of a magnetised wind consisting of relativistic particles and Poynting flux. The particles are accelerated to the highest energies at the termination shock. If this wind is confined by the surrounding environment, as the case for the Crab, the interactions of the wind with surrounding magnetic fields and seed photon fields produce non-thermal emission via synchrotron radiation and inverse Compton scattering. For a detailed review refer to [108].

It was previously asserted that γ rays with an energy greater than 50 TeV must be produced

via hadronic processes, given that the inverse Compton scattering of electrons becomes highly inefficient as a consequence of the Klein-Nishina suppression [109]. However, it has been demonstrated that the 100 TeV γ rays can be produced via inverse Compton processes despite the Klein-Nishina suppression and the hard γ-ray spectra [110]. For the majority of the LHAASO sources a pulsar is within a region of the same size as the PSF. Therefore, it is a reasonable assumption that the sources are associated with pulsars and are of leptonic nature [108].

Conversely, SNR are considered the primary source of CRs [111]. This implies that they must be capable of accounting for the observed CR flux on Earth up to the knee at 4 PeV which makes them PeVatrons [112]. Assuming that 10% of the total explosion power is converted into CRs and diffusive shock acceleration, the observed intensity and the spectral shape of the CR flux can be explained. However, it is not yet clear whether the SNR are able to accelerate to PeV energies [111]. Even if the SNRs magnetic field and size would be sufficient to reach these energies, the time in which a SNR is in its Pevatron phase is limited. It is only at the end of the free expansion phase and the beginning of the Sedov phase. During the free expansion phase the acceleration rate is high due to the presence of a significant shock velocity. However, in the Sedov phase the shock gradually decelerates. As the velocity of the shock declines, the maximum energy of the particles confined within it also decreases. Consequently, only the most energetic particles (PeV range) can escape the SNR. This period lasts for less than 1000 years, as the spectrum cutoff is shifted to lower energies as the SNR progresses through the Sedov phase [112]. Given the limited time frame within which a SNR can accelerate to PeV energies, it is unlikely that a single SNR can act as a continuous source of CRs in this energy regime. The rate at which SNRs are in this specific phase is approximately 0.1 per century, making it implausible that multiple SNRs can function as PeV CR accelerators, as previously suggested [109].

15.2 Implications on the Pevatron Nature

In the majority of cases, the occurrence of a cutoff in the spectrum of a CR source gives rise to a number of astrophysical interpretations. Firstly, the existence of a cutoff indicates that there is a maximum energy that particles can be accelerated to by the source. The acceleration power of a source is contingent upon its physical conditions and mechanism, such as the magnetic field strength and the dimensions of the acceleration region [113]. Conversely, the particles may be accelerated to high energies but subsequently lose energy through a range of processes. This may include synchrotron radiation, inverse Compton scattering, or interactions with matter and radiation fields. Consequently, the higher energies are diminished in the CR spectrum [113]. Additionally, propagation effects must be considered, as CR travelling through space leads to energy loss and scattering via interactions with interstellar matter and magnetic fields. These effects can result in a cutoff in the observed spectrum [114]. Finally, the age of the CR source may influence its spectral shape. If the source is younger, the time may be insufficient for particles to be accelerated to very high energies [115].

Conversely, in the absence of a cutoff in the CR source spectrum, particles (leptonic or hadronic) can be accelerated to energies exceeding 1 PeV. This makes the source a PeVatron. Through the hadronic process, γ rays are produced, carrying approximately 1/10 of energy of the parent CR's. Therefore, a hadronic PeVatron is expected to produce γ-ray at energies $\sim$100 TeV which is the UHE domain [115]. The detection of these particles is constrained to PeVatrons within our galaxy.

15.2.1 Consistency with Published Studies

In the past years, H.E.S.S. as well as other telescopes published studies on the CMZ. With the exception of MAGIC (2020), the studies all concluded that there is no significant cutoff in the CMZ spectrum. This suggests that the spectrum can be described by a simple power law. The explanation for this is straightforward: the restricted energy range of the fit and the fitting in the spectral dimension only. In the cases of HAWC (2024) and VERITAS (2021), the former is the dominant factor, with the energy range situated in close proximity to the curvature, break, or cutoff point. The cutoff was not detected with a large significance in either the MAGIC (2020) or the H.E.S.S. (2018) analysis due to the ON/OFF approach being unable to adequately disentangle the model components. In a joint fit over a wide energy range of the flux points obtained by H.E.S.S. (2018), MAGIC (2020) and VERITAS (2021), a cutoff was preferred over a simple power law however with $< 5\sigma$ [101]. The value of the proton cutoff was found to be at $157 \pm 87\,\mathrm{TeV}$ which is in perfect agreement with the value found here. Considering the difference in the analysis, the results presented here are consistent with the published results in H.E.S.S. (2018) [60].

The H.E.S.S. publication from 2016 [5] claiming the detection of a PeVatron in the GC was an exciting result that has frequently been cited. Nevertheless, the current definitions of hadronic PeVatrons require a detection above 100 TeV, which is not met here.

15.2.2 Source Candidates in the GC

In this section promising source candidates for the GC are introduced and discussed with a focus on the non-PeVatron nature.

Super Nova Remnants As previously stated, SNRs are capable of accelerating particles to PeV energies within a highly specific and relatively short time frame. In H.E.S.S. (2016) it was highlighted that the maximum proton energy would decline too rapidly below PeV for a single SNR. To sustain a continuous flux of protons $> 1\,\mathrm{PeV}$ a high rate of SNR within the central few parsecs is required, which is considered unlikely [116]. However, this requirement has now been relaxed due to the cutoff found in the γ-ray spectrum. A SNR can accelerate protons up to an energy of [5]:

$$E_{max} \approx 10^{14} \frac{B}{100\,\mu\mathrm{G}} \left(\frac{u_s}{10000\,\mathrm{km\ s^{-1}}} \right)^2 \frac{\Delta t_{\mathrm{PeV}}}{\mathrm{yr}}\,\mathrm{eV}, \tag{15.1}$$

where Δt_{PeV} is the critical time period in which the SNR is capable of accelerating to PeV energies. During this period, the magnetic field strength is expected to be very large $\sim 0.1 - 1\,\mathrm{mG}$. This suggests that depending on the properties of the SNR in the GC, a maximum energy below 1 PeV would be within the predictions. Given that the shock velocity declines by $t^{-3/5}$ in the Sedov phase, this establishes constraints on the SNR age [117]. The position of the CR accelerating source at the centre is coincident with the SNR Sgr A East making it a possible counterpart.

Super Massive Black Hole (SMBH) At the centre of the MW is a SMBH, Sgr A*, of about $4 \cdot 10^6 M_\odot$[118]. The γ-ray source HESS J1745-290 is at a coincident position, but no definite connection has been established. In addition, Fermi-LAT observed prominent γ-ray emission from MeV to TeV at the position of Sgr A*. The SMBH is extremely inactive today, but there is evidence of increased activity over the past few centuries [119]. X-ray observations show rapid variations that can be modelled due to at least two luminous outbursts ($\sim$ 100 and 400 years ago).

While the γ-ray emission shows no time variability, the Fermi bubbles indicate an increased level of activity in the past [120]. The SMBH can accelerate particles through several processes. There are accretion shocks, caused by matter falling into the black hole and forming accretion disks. In addition, when the intense magnetic fields around the black hole undergo reconnection events, energy is released and particles are accelerated to high energies. Finally, there is acceleration by diffusive shock acceleration from jets and outflows produced by the black hole [121]. In H.E.S.S. (2016), a link was made between the γ-ray diffuse emission and Sgr A*. However, it was found that the average acceleration rate over the last 10^{6-7} yrs is sufficient for PeV acceleration [5]. It would therefore also be sufficient to accelerate to the observed proton energy limit of about 170 TeV.

(Millisecond) Pulsars In [52] it was proposed that the diffuse γ-ray emission observed by H.E.S.S. and Fermi-LAT can be explained by $\sim 10^4 - 10^5$ millisecond pulsars. The latter are rotating neutron stars with rotation periods on the order of milliseconds. The fast rotation is thought to be due to accretion of matter as the pulsar ages. It has been argued that a cutoff in the γ-ray spectrum could constrain the magnetic fields of millisecond pulsars. The existence of a cutoff is therefore not ruled out in the millisecond pulsar scenario and could explain the here observed cutoff in the CMZ. Millisecond pulsars have also been proposed as a CR source in the GC along with heavy DM [122].

On the other hand, young and middle-aged pulsars near the GC could produce the observed CMZ diffuse emission [123]. The γ-ray spectrum from H.E.S.S. (2016) is in agreement with spectral predictions from inverse Compton scattering of electrons and positrons. In this case the electron spectrum shows a cutoff at 100 TeV. This theory would explain the cutoff observed in the 3D analysis. However, the correlation between the γ-ray emission and the molecular gas distribution suggests an additional hadronic component.

Association with HESS J1745-290 The CR source causing the CMZ emission is at the position of HESS J1745-290. This necessitates for an investigation of a possible association. Unfortunately the source itself remains unidentified, the proposed counterparts being Sgr A* and the PWN G 359.95-0.0416. The γ-ray spectra of the point source and the diffuse emission were already compared in H.E.S.S. 2016. The obtained best-fit spectra and the flux points are shown in Figure 15.1. The spectral index of the two spectra is compatible which could indicate the same CR source. It has been argued that even though the central source has a cutoff in its spectrum and the diffuse emission does not, there could still be a connection between the two. The cutoff in the spectrum was suggested to be due to the absorption of γ rays via interactions with the ambient infrared radiation field [5]. The spectrum and flux points of HESS J1745-290 and the CMZ diffuse emission obtained in this 3D analysis are also shown in Figure 15.1. The spectral slope has changed slightly compared to H.E.S.S. (2016) which is due to the different analysis methods. The cutoff is now present in both components which favours possible associations even more. However, the value of the γ-ray cutoff differs however by more than 10 TeV and there is a discrepancy in the spectral index. A certain association between the central point source HESS J1745-290 and the CR accelerator responsible for the CMZ diffuse emission cannot be concluded. In [116] it was suggested that the difference in the spectral shapes is due to a fading CR accelerator. Here, the CRs causing the CMZ emission are injected in the past and diffuse outwards, causing no or a higher cutoff. The emission from HESS J1745-290 is more recent and due to its lower energy, a cutoff is developed. According to this model, the cutoff value of the CMZ should be radial dependent. Statistical limitations prevent the determination of a cutoff at

different distances from Sgr A*. However, this theory is compatible with the observed cutoff in the CMZ at a higher γ-ray energy than the HESS J1745-290's cutoff. As the source power decreases, the maximum energy of the CR decreases. A blast wave generated by Sgr A* in a tidal disruption event is proposed as the fading CR source.

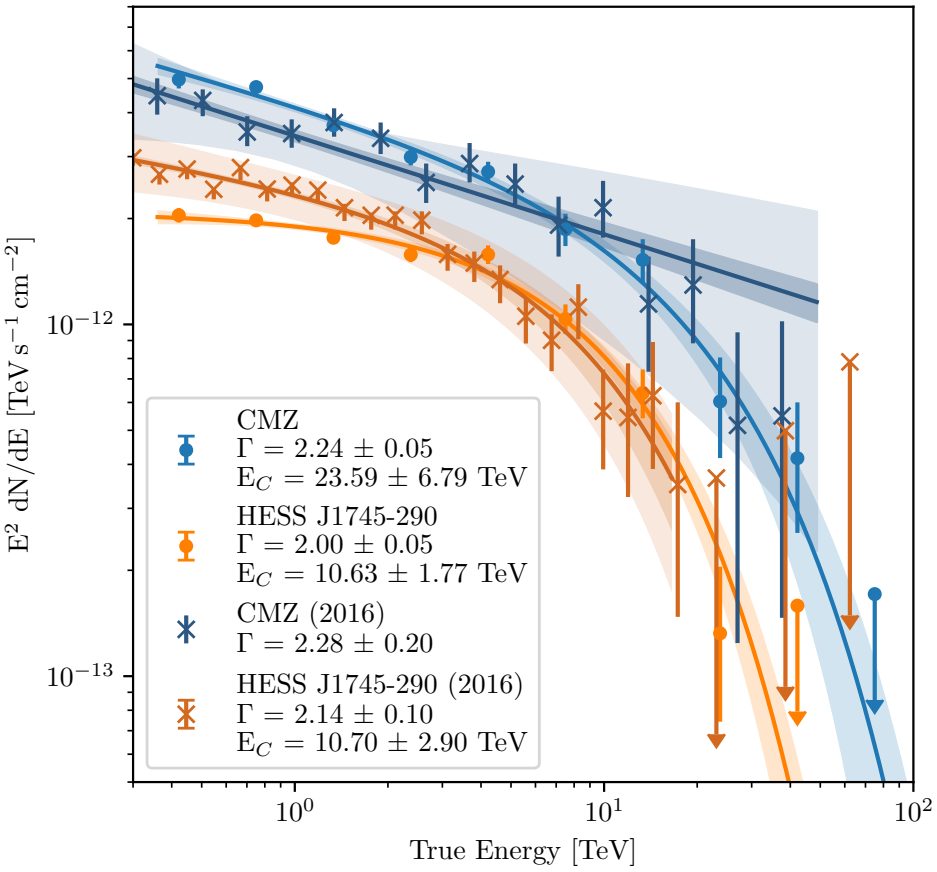

Figure 15.1: Comparison of the best-fit γ-ray spectra and flux points of the CMZ and the central point source HESS J1745-290 obtained in this 3D study and in the ON/OFF study of 2016 [5].

15.3 General Remarks

Leptonic Origins In principle γ rays can be of hadronic or leptonic origin. In the former case, the γ rays receive $\sim 10\%$ of the proton energy which is the reason for the PeVatron hypothesis when 100 TeV γ rays are observed. In the case of a leptonic scenario, the parent particles of a multi-TeV γ ray only carry energies around $\sim$100 TeV. To produce the diffuse emission in the CMZ, electrons have to be accelerated to this energy, despite the severe radiative losses in this region. They must also diffuse over distances of tens of parsecs and reproduce the hard γ-ray spectrum [5]. In some sources, it is claimed that γ-ray above $50 - 100$ TeV have to be of hadronic origin since the Klein-Nishina effect reduces the efficiency of the inverse Compotin scattering causing an exponential suppression of γ rays [109],[112]. However, since here the supression is evident in the spectrum, a leptonic origin might be reasonable and can be explain the CMZ diffuse emission [123]. It was shown how the spectrum of some of the UHE γ-ray sources from

LHAASO could be reproduced via inverse Compton scattering even above 100 TeV [110]. A leptonic scenario can therefore not be ruled out and should be investigated further.

CR Diffusion The CR diffusion used in this model is based on a rather simple but energy dependent CR dynamics. Due to the different gas densities and magnetic field strengths, it is reasonable to assume that the diffusion is anisotropic. In [124] the VHE emission of the the CMZ has been modelled in 3D with an anisotropic diffusion tensor. It was found that an almost isotropic case was favoured. Further modelling of the CMZ with more realistic CR dynamics shows that the GC Pevatron is a composite CR population. This includes the Arches, Quintuplet and nuclear start clusters, as well as Sgr A East [85]. Note that both studies suggest that better angular resolution of the γ-ray telescopes and a more detailed 3D gas distribution would reveal more small-scale structures.

γ-ray Absorption As γ rays propagate through the MW, they interact with matter and radiation fields, leading to absorption and hence a reduction in intensity as measured on Earth. This is due to the photoelectric effect, Compton scattering and pair production. The absorption depends on energy of the particles. For γ rays at the very high energies, around PeV, the dominant radiation field is the cosmic microwave background. At lower energies, absorptions due to the infrared and stellar background are dominant. The diffuse γ-ray in the CMZ can be neglected for energies below a few hundred TeV since due to its large extension the encountering of radiation fields is unlikely [125]. In principle a loss term could be included in the modelling of the diffusion.

15.4 Outlook

Part III of this thesis can be summarised as 'there may be no PeVatron in the GC'. At the first glance, this seems to contradict the H.E.S.S. paper published in 2016 with the sensational title 'Acceleration of Petaelectronvolt protons in the Galactic Centre'. However, a deeper investigation of the spectral analysis and a comparison with the results of other γ-ray telescopes shows that the physical results are consistent. The difference is simply in the astrophysical interpretation. No evidence for a cutoff in a fitting range < 45 TeV as it was used in H.E.S.S. 2018 [60] is no evidence for a hadronic Pevatron. The detection of a γ ray with an energy >100 TeV of clear hadronic origin would be. A straightforward proof of the hadronic origin would be the detection of spatially correlated neutrinos in the multi-TeV range. Additional, though more model-dependent, support could come from X-ray synchrotron emission produced by secondary electrons resulting from hardronic interactions.

The search for evidence of a PeVatron in the GC should be revisited with the next generation of γ-ray telescopes. Figure 15.2 shows the sensitivities of two instruments at different stages (construction, design). Both SWGO and CTA South will be able to obtain new information about the nature of the PeVatron. The CTA collaboration planned a total of 525 h of observing time on the GC [127]. According to simulations this is sufficient to detect γ rays close to 100 TeV [85]. With the fine angular resolution of CTA the morphology of the CMZ can be further studied. The identification of Galactic PeV sources represents a key objective of SWGO. With the additional objective of measuring the GC morphology, the new telescope is poised to yield novel insights into the nature of the diffuse emission in the GC [128].

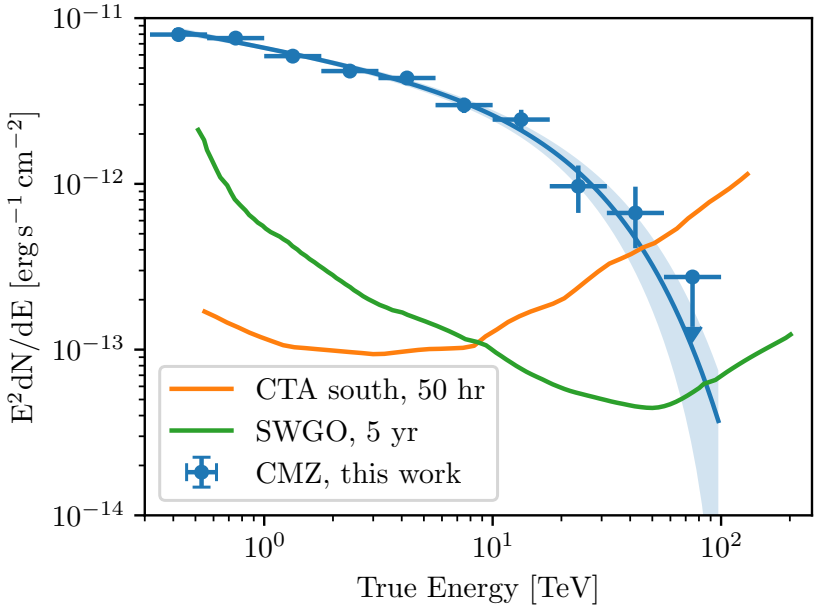

Figure 15.2: Point source sensitivity of different instruments and CMZ spectrum from the analysis carried out here. Figure adapted from [126].

Part IV

WIMP ANNIHILATION IN THE GALACTIC CENTRE

The preceding chapters of this thesis demonstrate that modelling the γ-ray data of the GC in three dimensions is a promising and successful approach. This method not only produces very good results but also reveals new features, such as the cutoff in the CMZ, that would have remained obscured in a traditional ON/OFF approach due to the inherent limitations of that technique. In addition to the aforementioned processes, the GC is also the site of a number of other astrophysical phenomena of interest. One such phenomenon is the existence of DM, matter that does not interact electromagnetically and is therefore invisible to electromagnetic radiation. It is anticipated that the particles will annihilate into a standard model particle pair, which will then produce γ-ray emission. If this is indeed the case and the cross sections are sufficiently large, the emission will be detectable by γ-ray telescopes such as H.E.S.S. Consequently, the objective in this part of the thesis is to utilise the comprehensive models of the γ-ray emitting sources, the background and the systematic uncertainties to search for DM in the GC in 3D.

The initial section of this part presents an introduction to DM, encompassing evidence for DM, prevalent DM candidates, and the search for DM. The subsequent chapter shifts the focus to indirect searches for DM utilising the technique of γ rays in the GC. The spatial and spectral distribution of DM is examined, and the findings of previous studies are presented. Ultimately, the outcomes of the DM search in 3D are presented, followed by a discussion and an outlook.

Chapter 16

Introduction to Dark Matter

The observable Universe is comprised of ordinary matter in the form of galaxies, stars, and gases. Nevertheless, this represents merely a small fraction of the total cosmic energy density. The majority of the Universe's mass is composed of DM, a mysterious and invisible substance that plays a crucial role in the formation and evolution of cosmic structures. This chapter provides a brief introduction to the topic. It begins with a concise overview of the history of the Universe, followed by an examination of the evidence for DM, including the rotation curves of galaxies and observations of galaxy clusters and large and cosmological scales. It then introduces the various DM candidates, and concludes with an overview of the different approaches used to search for DM.

16.1 Evidence for Dark Matter

A Quick Story of the Universe The following section is based on [129]. The standard model of cosmology, designated as the λCDM (cold DM) model, is founded upon the cosmological principle, which asserts that the energy distribution within the Universe is homogeneous and isotropic on large scales. Accordingly, all quantities employed to describe the Universe are contingent on time t, specifically at the initial moment of the Universe's inception, $t = 0$. One of the pivotal cosmological parameters is the scale factor, denoted as $a(t)$, which describes the relative expansion of the Universe and is instrumental in elucidating how distances between objects evolve over time. As the Universe expands, the scale factor increases in proportion to the distances.

The rate of change of the scale factor is proportional to the Hubble parameter, $H(t) = \dot{a(t)}/a(t)$. The scale factor can be related to the redshift, which is a measure of how much the wavelength of light has been stretched by the expansion of the Universe. This relationship can be expressed as $z = a_0/a - 1$ where a_0 is the scale factor today, conventionally normalised to 1. Hence, $z = 0$ corresponds to the present time. Redshift is employed to ascertain the distance and age of distant objects. Furthermore, the global curvature, κ, is defined as a measure of the overall shape and geometry of the Universe on large scales. If $\kappa = 0$, the Universe is said to be flat and follows Euclidean geometry, whereby parallel lines remain parallel. If $\kappa > 0$, the Universe is considered to be closed, which is analogous to the surface of a sphere. Conversely, if $\kappa < 0$, the Universe is regarded as open, which is analogous to the shape of a saddle.

The contents of the Universe, such as radiation, baryonic and dark matter, and dark energy, are descibed in cosmology as perfect fluids. These fluids are composed of a mixture of DM and baryonic matter, radiation (relativistic particles such as photons and neutrinos), and dark

energy. The composition of these fluids has undergone changes over time. Currently, dark energy is the dominant force, characterised by an energy density that fills space homogeneously and is responsible for the accelerated expansion of the Universe. In the recent past, at a redshift of approximately 0.3, matter was the dominant energy source, while at the beginning of the Universe, at a redshift of approximately 3400, radiation was the dominant energy source. The explanation of the early Universe is a highly challenging endeavour, necessitating the development of specific models for each distinct phase. The issue is that these phases cannot be observed directly due to the strong interaction of photons with the plasma, which prevents them from carrying any information. Only after the 'recombination' period can photons be considered as carriers. During this time, the Universe cooled sufficiently for electrons and protons to bind and form neutral hydrogen atoms. Consequently, the number of free electrons and protons was reduced, and the photons' mean free path increased significantly.

The photons are now observed as CMB. Its anisotropies are imprinted with past phenomena, the analysis of which provides constraints on the properties of the Universe, specifically the cosmological parameters. From this, the Planck Collaboration concluded that the Hubble constant today is $67.66 \pm 0.42\,\mathrm{km/s/Mpc}$, that the Universe is almost flat ($\kappa = -0.0007 \pm 0.0037$), and the majority of the Universe is composed of dark energy ($\lambda = 0.6889 \pm 0.0056$) [130]. Approximately 26.8% is cold DM, with a smaller fraction comprising ordinary matter (4.9%). A number of astronomical observations are regarded as evidence for DM and will now be subjected to further discussion.

Rotation Curves of Galaxies In spiral galaxies, the central region and the bulge contain the majority of the visible matter, with a notable decline in density towards the outer regions. The velocity of stars orbiting the centre of the galaxy is $v(r) = \sqrt{GM(r)/r}$, where $M(r)$ is the total mass contained within a sphere of radius r. At large distances, the mass within the sphere from baryonic matter is found to be constant, resulting in $v(r) \propto r^{-1/2}$. However, the observed velocity remains constant with increasing distance. It can be concluded that there is additional mass with a gravitational force exerted on the stars that is not visible, DM. In order to account for the observations, it is necessary to postulate that the DM density is $\propto 1/r^2$ [129]. The Milky Way, a spiral galaxy, exhibits a constant rotation curve, as illustrated in Figure 16.1. The role of DM in galaxies has been the subject of extensive research, with findings indicating that it constitutes approximately $80 - 90\%$ of the total mass in these cosmic structures. It is important to note that the theoretical predictions in this field are largely based on Newtonian mechanics. Consequently, any discrepancies can be attributed to the theory of modified Newtonian dynamics (MOND), which does not necessitate the introduction of additional gravity due to DM. However, despite its success in explaining certain observational phenomena, MOND remains unable to fully account for the full range of relativistic effects observed in nature.

Galaxy Clusters Galaxy clusters provide a popular evidence for the existence of DM. The mass of the cluster can be determined by measuring the X-rays emitted by the accelerated gas within the cluster via thermal Bremsstrahlung. Conversely, the mass of a cluster can be observed via gravitational lensing, whereby deformed images of distant objects are observed. The gravitational force responsible for the deformation in geometry, which causes the deformed image, can be reconstructed. The analysis of multiple galaxy clusters revealed that only $10 - 20\%$ of the mass predicted by gravitational lensing is visible matter [129].

The observation of the Bullet cluster, composed of two colliding galaxy clusters, is considered evidence for DM, as illustrated in Figure 16.2. It has been observed with the Chandra X-Ray

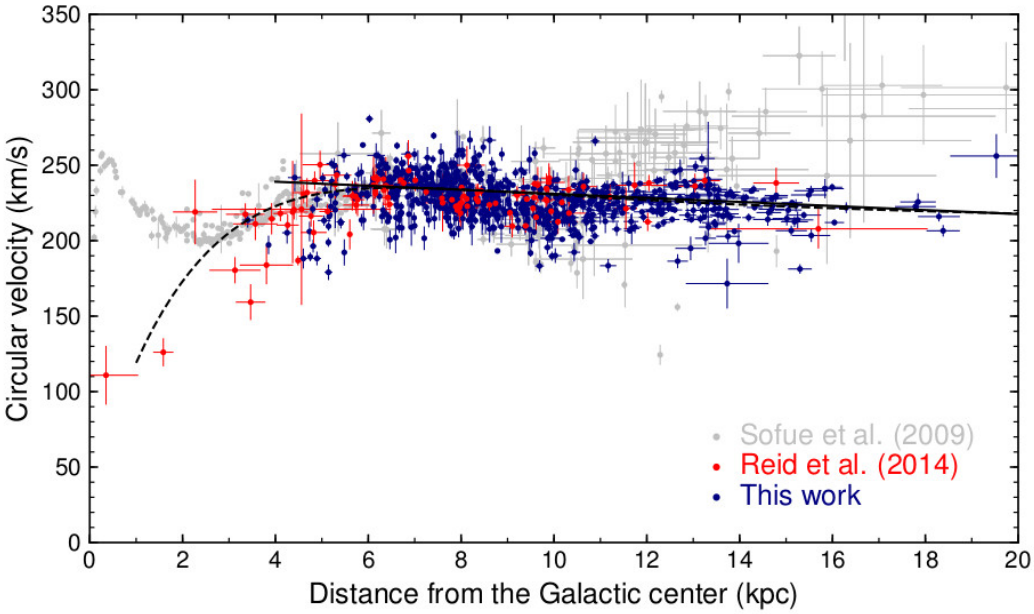

Figure 16.1: Rotation curve of the Milky Way. Figure taken from [131].

Observatory (which detects radiation from hot gas) and via gravitational lensing. However, the distribution of the gas and the mass are spatially distinct, indicating that the baryonic mass and DM are separate entities.

Large and Cosmological Scales Following the recombination and emission of the CMB, larger atoms than hydrogen were formed. The primary interaction was gravity driven, resulting in the formation of large-scale structures in denser regions. This process led to an increase in gravity until the emergence of galaxies. The large-scale structure that exists today has been affected by these very gravitational effects and the expansion of the Universe, resulting in the structures drifting away. The assumption that DM interacts via gravity but is collisionless gives rise to a different role for DM in the formation of large-scale structures than that ascribed to baryonic matter. Simulations are employed to model structures as a function of the age of the Universe, with the results being compared to observations. The observations are drawn from a range of scales, extending from the cosmological scale, where structures of the CMB are measured by Planck, to large-scale structures of matter, including galaxies and galaxy clusters, see Figure 16.3. The power spectrum resulting from predictions of the λCDM model is in excellent agreement with measurements from a variety of observations.

16.2 Dark Matter Candidates

Despite the multitude of observations that are currently considered evidence for DM, its true nature remains a topic of debate, with numerous potential candidates. The astronomical and cosmological observations have revealed that DM is characterised by its mass, stability over extended periods of time, probable lack of collisions and gravitational interaction. The thermal velocity of DM may be relativistic, akin to 'hot' DM, or non-relativistic, akin to 'cold' DM. The

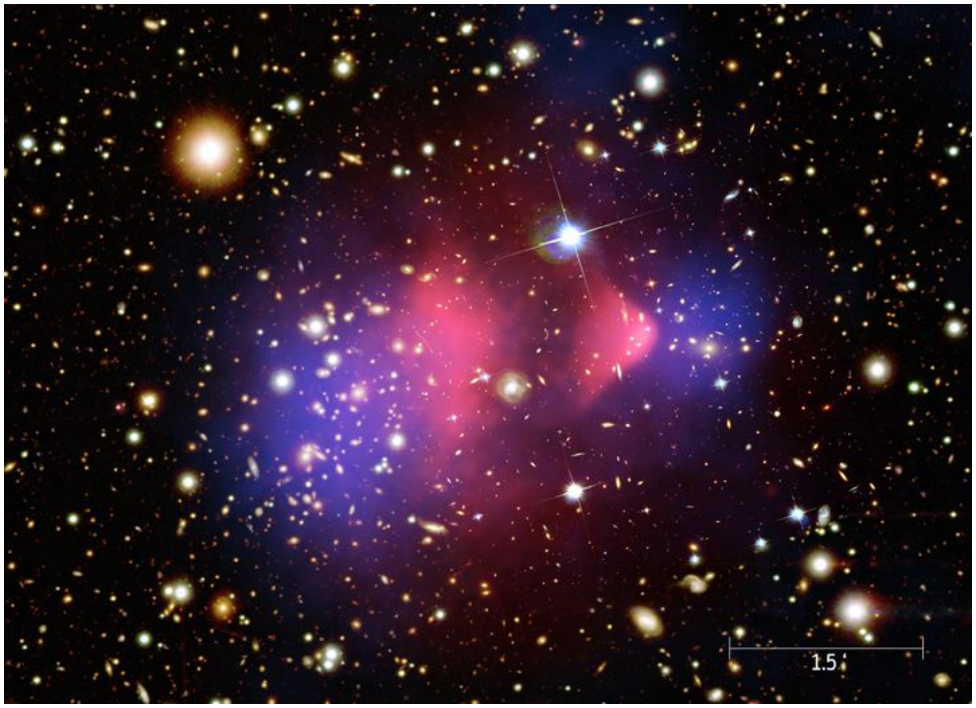

Figure 16.2: The composite image of the Bullet galaxy cluster depicts the red region as hot gas, as observed by the Chandra X-ray Observatory, and the blue region as mass, as observed via gravitational lensing. Image Credit: X-ray: NASA/CXC/CfA/M.Markevitch et al.; Optical: NASA/STScI; Magellan/U.Arizona/D.Clowe et al.; Lensing Map: NASA/STScI; ESO WFI; Magellan/U.Arizona/D.Clowe et al.

Standard Model posits that the only particle matching the properties of DM are neutrinos [1]. However, due to their relativistic speed, neutrinos are candidates for hot DM, whereas simulations modelling the structure of the CMB prefer most of the DM to be cold.

Widely discussed cold DM candidates are ultra-light axions, which emerge from the solution to the strong CP problem; primordial black holes, which are formed in the early Universe; and hypothetical sterile neutrinos, which do not interact via the weak force. Additionally, there are weakly interacting massive particles (WIMPs), which have a mass range of $10\,\mathrm{GeV} - \mathrm{TeV}$ [133].

It is hypothesised that WIMPs are produced through the thermal freeze-out process. Similarly to all other particles, they were in thermal equilibrium. As the temperature of the Universe, T, declines below the mass of the WIMPs, m_χ, their number density becomes Boltzmann-suppressed, scaling as $n_\chi \propto \exp(-m_\chi/T)$. However, the annihilation process is diminished as a consequence of the expansion of the Universe, resulting in a gradual approach towards a constant thermal relic density. This process is referred to as the 'freeze-out'. The relic abundance of DM is determined by the thermal relic cross-section. The velocity-averaged value is $\langle \sigma v \rangle_{\text{thermal relic}} = 3 \cdot 10^{-26}\,\mathrm{cm^3 s^{-1}}$. For typical velocities of 0.1c, this is to be expected for particles interacting via the weak force. The WIMP masses lie around the weak scale of particle physics, and the required annihilation cross-section for the correct relic abundance corresponds to that of a particle interacting via the weak force. This makes WIMPs the perfect candidates for DM, a phenomenon known as the

[1] Baryons have the same properties, however DM is likely seperate from baryonic matter as evidenced by the observations of CMB

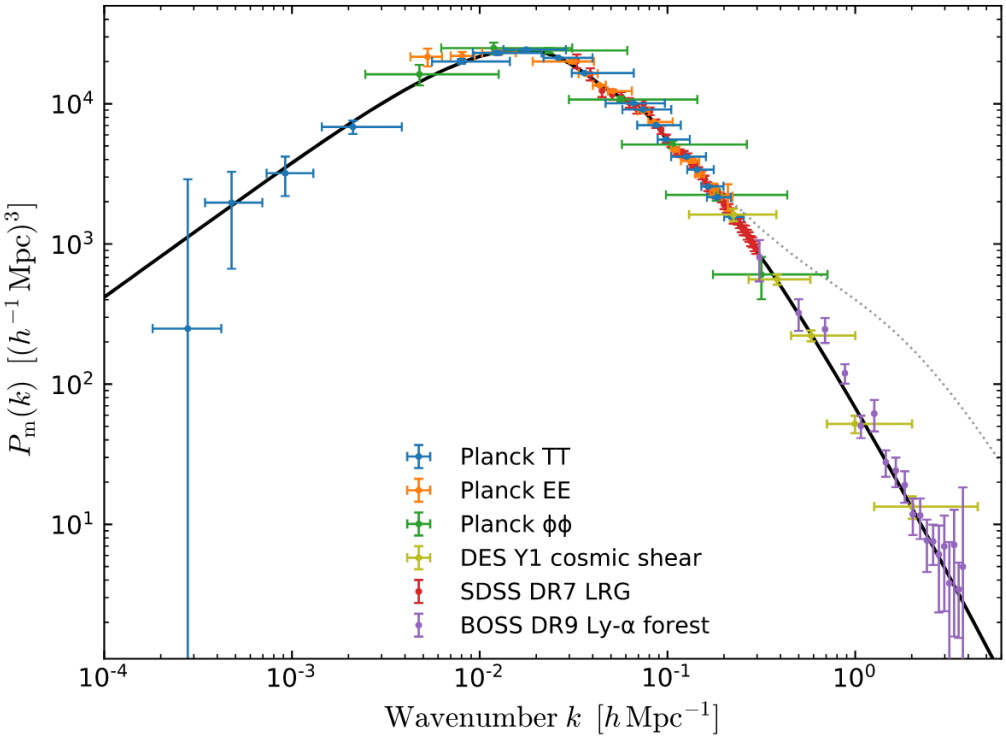

Figure 16.3: Matter power spectrum from different cosmological probes compared to the prediction of the λCDM model (black solid line). Figure taken from [132].

'WIMP miracle'.

A number of theoretical models propose a variety of candidates for WIMPs. One of the most prominent theories is supersymmetry (SUSY) [134]. This theory posits that all particles have a superpartner that has the same quantum numbers and gauge interactions. However, the spin differs by 1/2. The lightest supersymmetric particle (LSP) is stable and may serve as a potential DM candidate. The neutralino is an electrically neutral but weakly interacting particle that is often considered the LSP and therefore a prime candidate. It is a mix of superpartners of the neutral gauge bosons and the Higgs bosons. Other models consider the gravitino, which is the superpartner of the hypothetical graviton that mediates the force of gravity [134]. Furthermore, the theory of universal extra dimensions (UED) posits the existence of additional spatial dimensions beyond the three that are commonly accepted. Due to the quantisation of the momentum in these extra dimensions, each particle is associated with a series of heavier states, known as Kaluza-Klein modes. The lightest Kaluza-Klein particle exhibits properties that are consistent with those of WIMPs.

It should be noted that there are also several non-WIMP candidates, for example baryonic candidates, such as the massive astrophysical compact halo objects (MACHOS), which include neutron stars, brown and white dwarfs. Despite comprising ordinary matter, they have a very faint luminosity due to a very low density.

16.3 The Search for Dark Matter

In the event of an interaction between DM, designated as χ, and a standard model particle SM, three methods for detecting DM are available. These are illustrated in Figure 16.4.

- Particle colliders:
  It can be assumed that the production of DM via SM SM $\rightarrow \chi\chi$ would not result in the detection of the resulting DM particles, but would manifest as missing energy. In the case of SM SM $\rightarrow \chi\chi +$ SM, signatures of DM could be detectable.

- Direct detection:
  In the case of a standard model particle scattering with a DM particle, χSM $\rightarrow \chi$SM, the transferred energy is detectable in sensitive detectors.

- Indirect detection:
  In the event of two DM particles annihilating into two standard model particles, $\chi\chi \rightarrow$ SM SM, the latter or secondary particles are detectable.

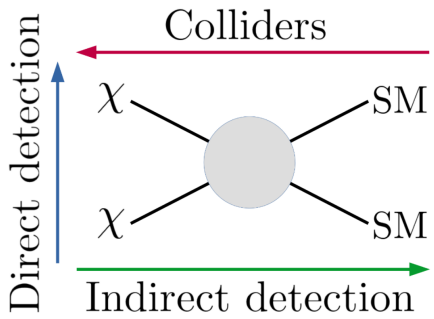

Figure 16.4: Schematic representation of the three types of DM search. Figure taken from [129].

Collider Searches The objective of collider experiments is to produce new particles in high-energy collisions of protons or electrons and positrons. This is the manner in which the majority of the standard model particles' decay rates and branches are constrained. The LHC's centre of mass energy of 14 TeV is sufficient to produce WIMPs through the weak force, provided their mass is below approximately 1 TeV. As the production of a $\chi\chi$ pair is invisible, the optimal targets are mono-jet or mono-photon signals ($\chi\chi j$,$\chi\chi\gamma$). The additional particles are a consequence of initial state radiation [135].

Direct Detection The scattering of WIMPs off nuclei can be detected directly in low-background underground detectors. It is essential to eliminate any interference from CRs and other sources of noise must be sufficiently suppressed to ensure accurate measurements of a DM signal. Residual background noise is distinguished by various discrimination methods, for instance, with the annual modulation of the DM signal occurring due to the relative motion of the Earth with respect to the DM halo. The detection techniques include the measurement of scintillation light, ionisation or heat [135].

Indirect Detection In the event of a DM particle annihilating or decaying into another particle, the latter can be detected on Earth. The majority of research efforts are concentrated on astrophysical regions where it is hypothesised that DM may accumulate, including the centres of galaxies (such as the Milky Way), galaxy clusters and dwarf galaxies. The secondary particles are typically γ rays, neutrinos, positrons and antiparticles. Since only γ rays and neutrinos are chargeless and therefore not deflected by magnetic fields, they are the prime candidates for indirect detection of DM. The advantages and disadvantages of different γ-ray targets regarding the strength of the DM signal and uncertainties is demonstrated in Figure 16.5.

The regions with the largest uncertainties are those of galaxy clusters and extragalactic diffuse emissions, due to the presence of background and other variables. In contrast, dwarf galaxies can be used to obtain robust constraints, although the DM signal is comparably weak. This limitation can be addressed through a combined analysis of dwarf galaxies. The strongest signal is expected to emanate from the GC. However, it is important to acknowledge the non-negligible uncertainties that exist. Given that the GC region was previously analysed in part II and III with a particular focus on the treatment of systematic uncertainties, it is reasonable to conclude that the data and modelling approach is sufficient to handle the large uncertainties and obtain WIMP annihilation signals. The analysis principle will be explained in detail in the following section.

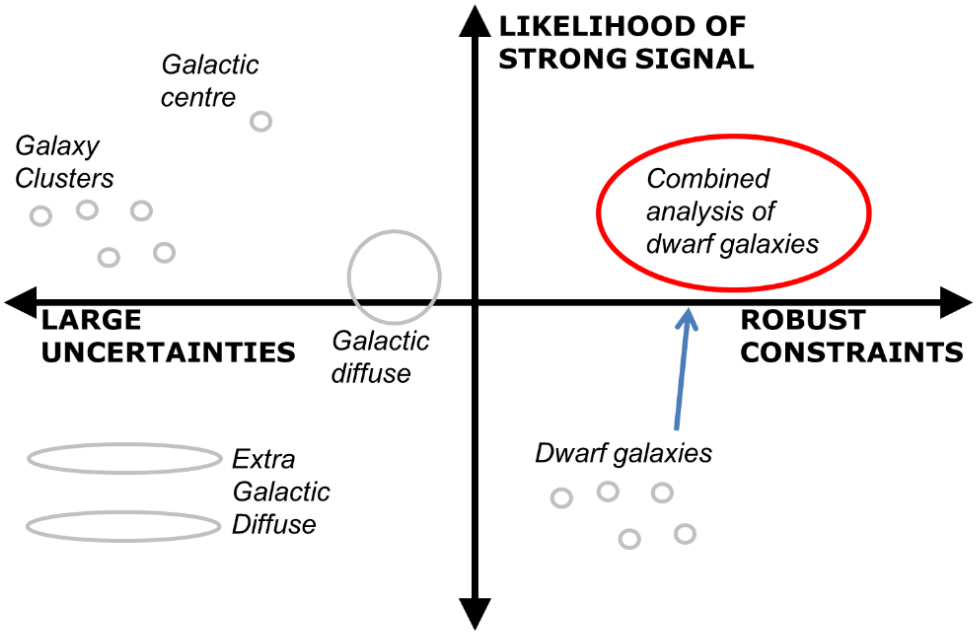

Figure 16.5: Schematic of the usefulness of some γ-ray targets for DM annihilation search. Figure taken from [136].

Chapter 17

Indirect Search for Dark Matter with γ rays in the Galactic Centre

As previously stated, the GC is a common target for indirect DM searches with γ rays due to the elevated DM concentration. The typical methodology employed in DM studies is the ON/OFF analysis. This implies that the known γ-ray sources are not incorporated into the fitting procedure, but are excluded from the analysis. As previously observed, the γ-ray emissions are aligned with the Galactic Plane, extending to the central region, which also exhibits the largest distribution of DM. As a result, a considerable proportion of the potential signal is inevitably lost. However, this issue can be circumvented by utilising a 3D background template and incorporating all the distinct source components, as demonstrated in this thesis. By incorporating a 3D DM model and fitting the associated properties, it is possible to derive constraints on the velocity-averaged annihilation cross section of WIMPs, denoted as $\langle \sigma v \rangle$.

In general, the differential γ-ray flux Φ_γ produced via DM annihilation consists of two components defined as:

$$\frac{d\Phi_\gamma}{d\Omega dE} = \underbrace{\frac{1}{4\pi k m_{\mathrm{DM}}^2} \sum_f \langle \sigma v \rangle_f \frac{dN_\gamma^f}{dE}}_{\text{particle physics}} \cdot \underbrace{\frac{dJ}{d\Omega}}_{\text{astrophysics}}, \tag{17.1}$$

where Ω is the solid angle, $k = 2$ for a Majorana particle and m_{DM} is the mass of the DM particle. $\langle \sigma v \rangle_f$ is the velocity averaged annihilation cross section into a specific SM pair $\chi\chi \to f\bar{f}$ and $\frac{dN_\gamma^f}{dE}$ the energy spectrum of the particles produced directly at the DM annihilation site (primary spectral flux). These particle physics variables define the spectral component of the γ-ray flux. The morphological component is defined by the astrophysics, $\frac{dJ}{d\Omega}$, which is the J-factor. This depends on the target region of the DM search and on the assumed DM distribution, which will be discussed in section 17.1. Section 17.2 focuses on the γ-ray spectrum due to the DM annihilation (particle physics). In section 17.3, a summary of past studies of indirect searches of DM annihilation with γ-ray telescopes, in particular the H.E.S.S. telescope, will be presented.

17.1 Spatial Dark Matter Distribution

A number of profiles have been developed to quantify the distribution of DM in galaxies. These profiles are illustrated as a function of the distance to the DM source in Figure 17.1. In general,

the distinction is made between cored and cusped profiles. The Navarro-Frenk-White (NFW) is a cusped profile that has been traditionally used in the field of astrophysics. It was initially motivated by N-body simulations [137]. Subsequent simulations have yielded the Einasto profile, which is marginally more broader than the NFW profile. Additionally, the Moore profile has been proposed. The Burkert and isothermal profiles have been motivated by observations of galactic rotation curves. However, the two cored profiles are in conflict with numerical simulations. All the profiles assume spherical symmetry and can be parameterised as follows [137]:

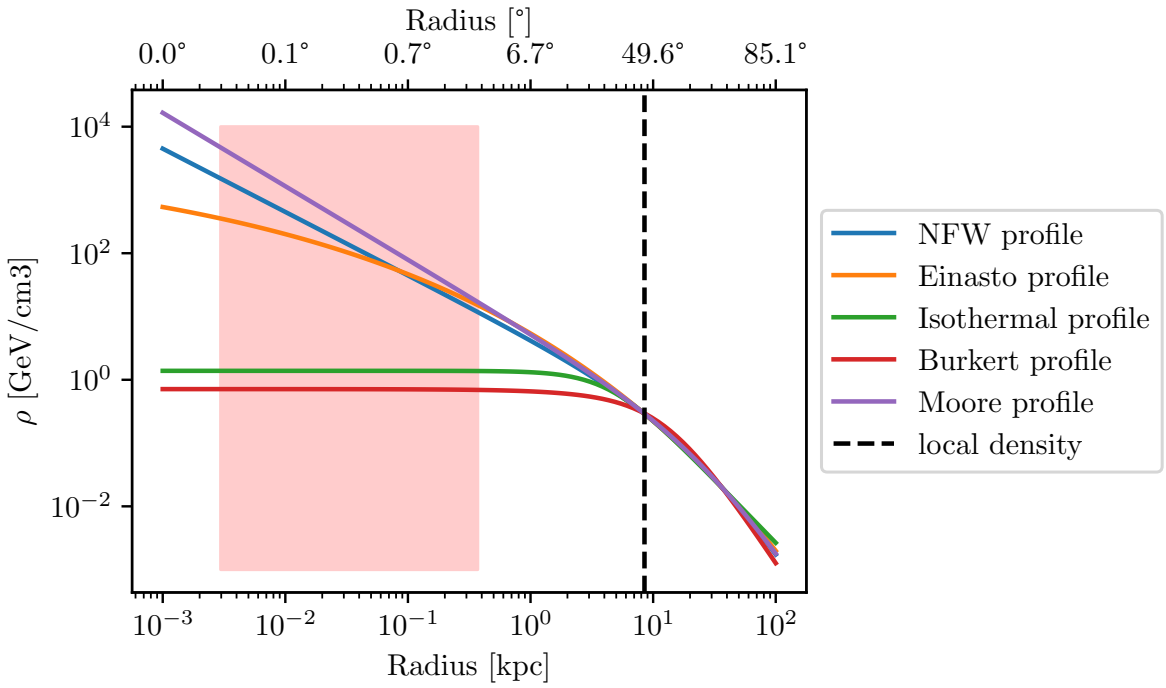

Figure 17.1: Common models for the DM density profiles for the MW as a function of the radius in kpc and in degrees. The dashed line is at the position of the sun (8.5 kpc) where the local density of 0.3 GeV / cm^3 is assumed. The light red area indicates the area used in the analysis here.

$$
\begin{aligned}
\text{NFW}: \quad & \rho_{\text{NFW}}(r) && = \rho_s \frac{r_s}{r}\left(1+\frac{r}{r_s}\right)^{-2} \\
\text{Einasto}: \quad & \rho_{\text{Ein}}(r) && = \rho_s \exp\left\{ -\frac{2}{\alpha}\left[\left(\frac{r}{r_s}\right)^{\alpha} - 1\right]\right\} \\
\text{Moore}: \quad & \rho_{\text{Moo}}(r) && = \rho_s \left(\frac{r_s}{r}\right)^{1.16}\left(1+\frac{r}{r_s}\right)^{-1.84} \\
\text{Isothermal}: \quad & \rho_{\text{Iso}}(r) && = \frac{\rho_s}{1+(r/r_s)^2} \\
\text{Burkert}: \quad & \rho_{\text{Bur}}(r) && = \frac{\rho_s}{(1+r/r_s)(1+(r/r_s)^2)}
\end{aligned}
\tag{17.2}
$$

where r is the distance from the GC, and r_s is the scaling radius and ρ_s the scaling density. In the case of the Einasto profile, $r_s = 28.44\,\text{kpc}$ and $\rho_s = 0.033\,\text{GeV/cm}^3$ is used and the shape

parameter is set to $\alpha = 0.17$. The values have been selected in such a way that the DM density at the position of the sun is equal to $\rho_\odot = 0.3\,\mathrm{GeV/cm^3}$. This corresponds to a distance of 8.5 kpc. The scaling parameters of the other profiles have been chosen in a similar manner.

The one-dimensional profiles can be employed to obtain a 3D distribution of DM. Consequently, the squared profiles, $\rho(r(s,\phi))$, are integrated along the line of sight, s, resulting in the differential J-factor.

$$\frac{dJ}{d\Omega} = \int_{LOS} \rho^2(r(s,\phi))ds \tag{17.3}$$

where ϕ is the angle between the line of sight and the direction of the observation and r is the coordinate in the GC. The coordinates r and s are shown in Figure 17.2.

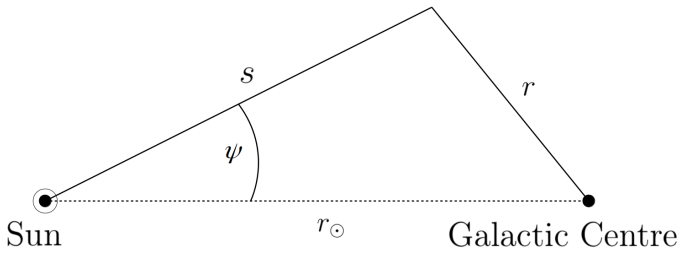

Figure 17.2: Illustration of the line-of-sight integration where s is the line-of-sight and $r_\odot$ is the distance between the sun and the GC.

For the integration the relation between r and s is used:

$$r = \sqrt{r_\odot^2 + s^2 - 2r_\odot \cos\phi} \tag{17.4}$$

The J-factor computation was performed using the open-source software CLUMPY [138], [139], [140]. It is frequently employed for γ-ray or neutrino signals emanating from the annihilation or decay of DM particles. The J-factor map of the GC, computed with CLUMPY and the Einasto profile, is shown in Figure 17.3. The map is used in the following DM analysis as the morphology of the γ-ray signal due to DM annihilation.

17.2 γ-ray Spectrum due to WIMP Annihilation

In the event that the DM analysis is conducted in 3D space, it is necessary to obtain a spectrum of the γ-ray emission resulting from the annihilation of the DM particles, in addition to the morphology. Monte Carlo simulations can be employed to obtain the energy spectra of final-state particles resulting from DM annihilations. In reference [137], the primary fluxes of different final-state particles were computed with Pythia and provided in numerical form. Figure 17.4 illustrates the primary spectra for γ-ray emission from different annihilation channels involving a DM particle of mass 10 000 GeV. All spectra exhibit a cutoff at the DM particle mass, as the maximum mass of the γ-ray spectrum is constrained by the mass of the DM particle. The spectra are broadened due to the intermediate particles involved in the annihilation process, rather than exhibiting a peak as observed in other scenarios [141]. In the case of direct annihilation into γ

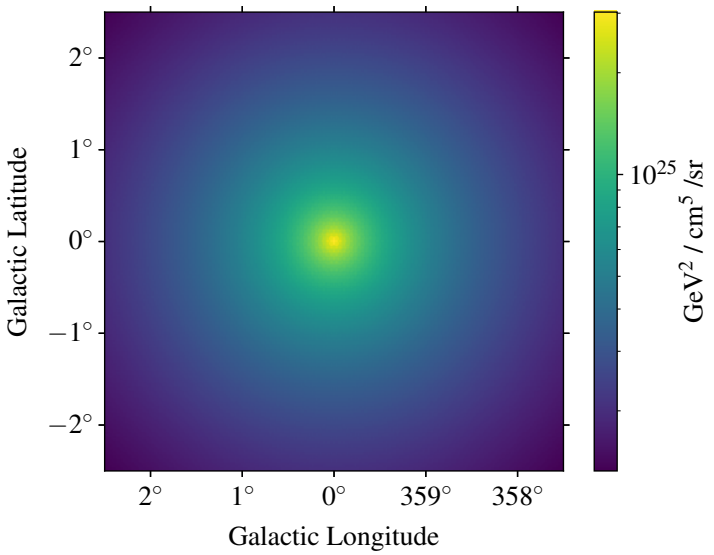

Figure 17.3: J-factor computed with CLUMPY and the Einasto profile of the GC.

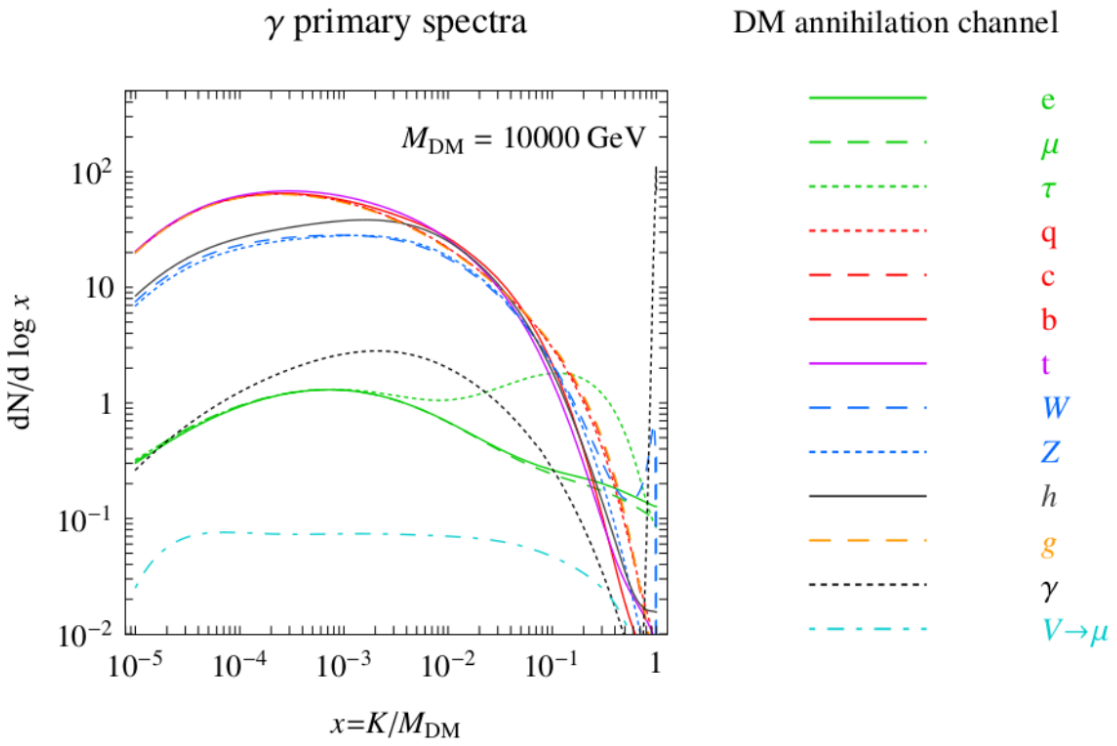

Figure 17.4: Primary spectra of a DM particle with mass 10 000 GeV with different annihilation channels. Figure taken from [137].

rays, however, the absence of intermediate states results in a distinctive 'smoking gun' signal, namely a peak at the mass of the DM particle.

As illustrated in equation 18.1, the total differential γ-ray flux is the superposition of the various annihilation channels. However, since the precise branching ratios remain unknown, an

annihilation via a single channel is assumed in the following analysis, with a branching ratio of 100 %. In accordance with convention, annihilation into the $b\bar{b}$ channel is frequently employed. To ensure compatibility with published results, the same channel will be used as a default in the following analysis.

17.3 Past Studies in the GC

Over the past two decades, the H.E.S.S. collaboration has published 19 papers on DM, with seven of these focusing on the GC as the target region [142]. Some of the papers focus on line signals resulting from direct DM annihilation into γ rays, while others perform searches for continuous γ-ray signals via alternative channels. Notably, the publications from 2016 [143] and 2022 [144] are highly comparable to the analysis presented here in terms of the ROI and the spectra. In the former study, data from 10 years of H.E.S.S. observations (254 hours of live time) of the inner 300 parsecs of the GC were utilised. The spectral and spatial morphologies of the DM signal were compared to those of the background. It should be noted that the analysis was performed using the ON/OFF background estimation method. Consequently, known γ-ray regions along the Galactic Plane or in the vicinity of HESS J1745-303 were excluded (band height: 0.6°, see Figure 17.5). The ON regions were defined as donut shapes with varying radii and a width of 0.1°. The background was estimated from regions with the same angular size at a position where the γ-ray signal due to DM is negligible. By comparing the counts within the ON and OFF regions, no excess DM was identified, thus establishing upper limits on the annihilation cross section. By employing the spectral and one-dimensional spatial information, the sensitivity was enhanced by 30% in comparison to a spectral-only or spatial-only fit. The NFW and the Einasto profiles were utilised to compute the J-factor, and diverse annihilation channels were evaluated. The results for the Einasto profile and the W^+W^- channel are presented in Figure 17.6.

In 2022, the analysis was repeated with the incorporation of supplementary data from the H.E.S.S. inner galactic survey, representing the inaugural comprehensive VHE γ-ray survey of the GC region. The dataset comprises 546 hours of livetime. The excluded, ON and OFF regions are defined in a similar manner to those defined in 2016. However, due to the larger ROI ($10° \times 10°$), 25 annuli are used as the ON region. The photon statistics were computed in each annulus, and since no significant excess due to DM annihilation was found, upper limits were computed.

The upper limits obtained with the Einasto profile and the W^+W^- channel are illustrated in Figure 17.6. It is notable that the larger dataset has led to an improvement in the results obtained in comparison to those from 2016. Furthermore, limits from other experiments and targets are presented, although it should be noted that H.E.S.S. is the most sensitive telescope within the energy range of 0.3 TeV and 70 TeV.

Fermi-LAT observed an excess in γ-ray data in the direction of the GC, designated the Galactic Centre Excess (GCE) [149]. Although several hypotheses have been proposed as an explanation of this excess, it is also consistent with a signal resulting from DM annihilation. The compatibility of the excess with the γ-ray prediction due to DM annihilation via single channels or more complex models was analysed. The hadronic and semi-hadronic channels are excluded based on the antiproton measurements obtained by the Alpha Magnetic Spectrometer (AMS-02) on the International Space Station [150]. Furthermore, the AMS-02 positron data excluded pure or mixed channels with an electron/positron component [149]. The addition of further γ-ray constraints from dwarf spheroidal galaxies resulted in a single compatible DM scenario: $\mu^-\mu^+$, a mass of 60 GeV and approximately the thermal relic cross section.

In the year 2022, a reappraisal of the characteristics of the GCE was undertaken [151]. The

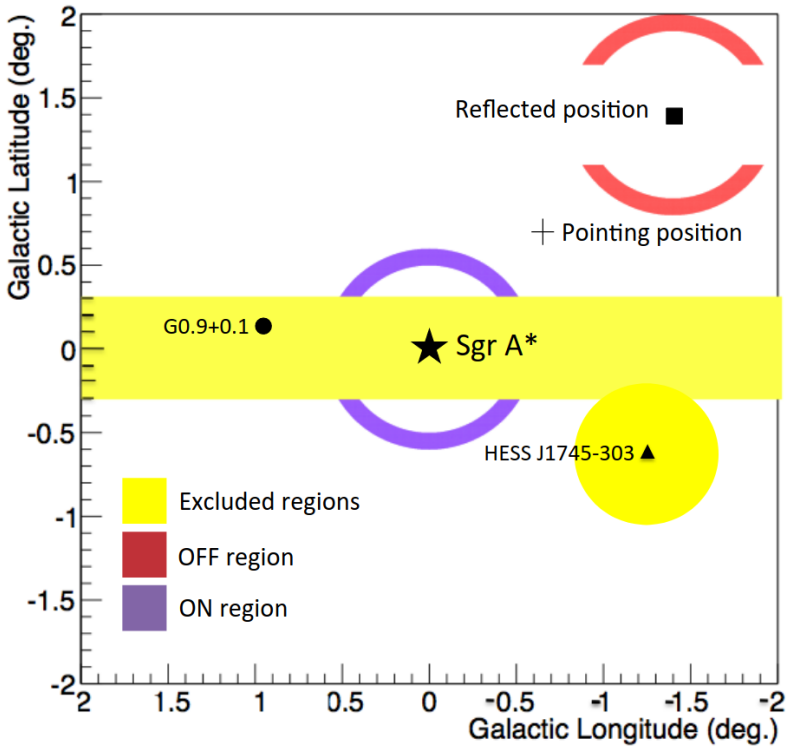

Figure 17.5: Schematic of the excluded, the ON- and OFF-region used in the DM search in the GC with H.E.S.S. in 2016. Figure taken from [143].

systematic uncertainties were accounted for by utilising a comprehensive set of high-resolution templates for the diffuse γ-ray emission in the GC. It was determined that the annihilation of DM via the b quark is more probable than the annihilation via the $\mu^-\mu^+$ channel. The DM mass was found to be 40^{+10}_{-4} GeV, and the annihilation cross-section was calculated to be $\langle\sigma v\rangle = 1.4^{+0.6}_{-0.3} \cdot 10^{-26}\,\mathrm{cm^3 s^{-1}}$.

The forthcoming CTA will achieve a new level of sensitivity in indirect DM searches, thanks to a superior angular resolution and a broad sensitive energy range of 10s of GeV up to 300 TeV. Given the extensive detection area and the resulting large statistics, it is anticipated that systematic uncertainties will have a significant impact. This topic is discussed in detail in the CTA publication [152], with a focus on the instrument and the background systematic uncertainties. The latter is consed of the isotropic CRs and the large-scale diffuse emission, called interstellar emission (IE). The current plan for the survey of the extended GC region would result in a much larger ROI compared to the available H.E.S.S. data in this region. The assumed livetime is 525 hours. In lieu of the conventional ON/OFF methodology for establishing constraints on DM annihilation, a template approach analogous to that utilised herein is employed. In this approach, the CR residual background, the large-scale diffuse emission, point sources below a certain threshold (stronger point sources are masked) and the Fermi bubbles are all taken into account. Systematic uncertainties due to the background are incorporated into the fitting process with nuisance parameters and a prior in the form of a correlation matrix. The latter quantifies the magnitude and the correlation length in both the spatial and the spectral dimension. The

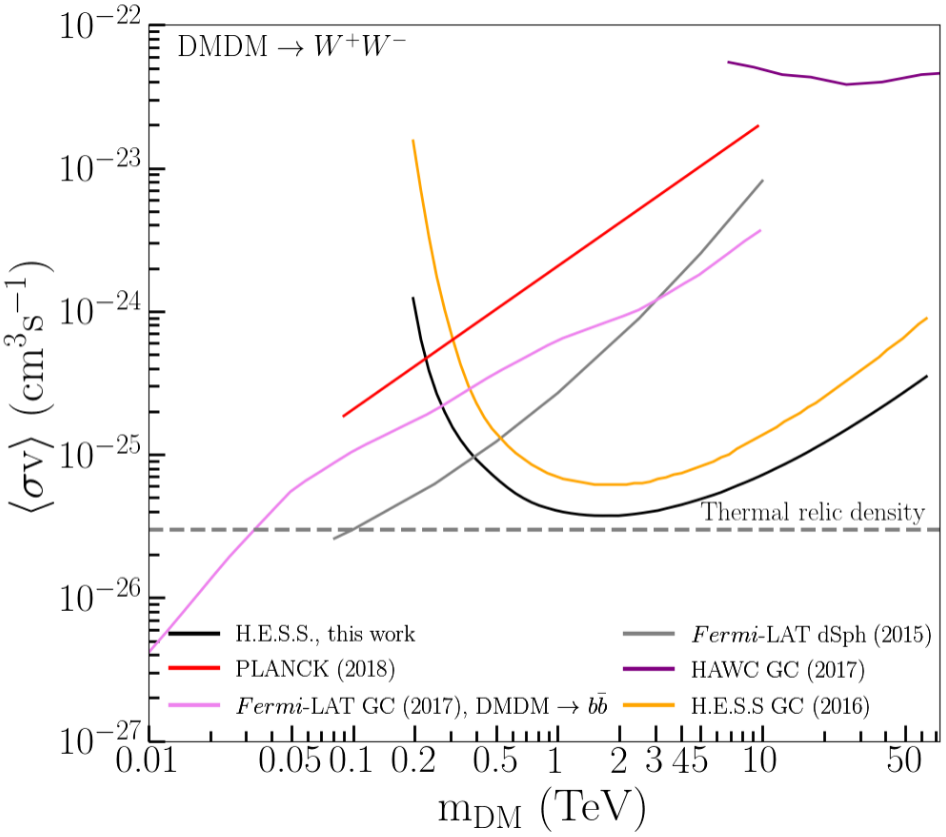

Figure 17.6: Limits on the annihilation cross section in the W^+W^- channel obtained with H.E.S.S. in 2022 and 2016 and HAWC [144], [143], [145]). Additionally, the limits from observations of dawft galaxy satellites of the MW and the GC by Fermi and limits from the CMB with PLANCK are shown [146], [147], [148]. Figure taken from [144].

values of the benchmark goal of CTA are used which is a 1% systematic uncertainty on the hadronic background. However, it was found that the choice of the values has a strong effect on the limits. Furthermore, the effect of the different diffuse emission templates is studied.

The outcomes of the template-based 3D approach were contrasted with the constraints calculated with the conventional ON/OFF methodology. In the absence of an IE in the simulated data, the sensitivities are found to be comparable. Nevertheless, the ON/OFF approach is predicated on the assumption that the large-scale emission is masked at heights of approximately $|b| \leq 0.3°$. In the event that emission persists within the field of view, the DM sensitivity is diminished. This was also observed in the CTA study, wherein the limits derived from the ON/OFF approach exhibited a 1000-fold increase, while the 3D template limits, which accounted for this emission, demonstrated only a slight increase compared to the limits obtained without including the IE. It was determined that the template approach is promising in scenarios involving large-scale emission above the instrument's sensitivity threshold or with a significant gradient within the ROI.

The deployment of survey-style instruments with a large FOV, such as SWGO, will facilitate a deeper comprehension of DM in the GC within the multi-TeV scale. The anticipated constraints resulting from the annihilation and decay of WIMPs are illustrated in [153], which exhibit a

comparable magnitude to the sensitivities attained by CTA, with a marginal enhancement in performance for $m_{\mathrm{DM}} \geq 3\,\mathrm{TeV}$.

Chapter 18

First Application of 3D Analysis Method in WIMP Annihilation Search

As mentioned, the GC is a prime target for DM searches due to its high DM density. Traditional analyses use an ON/OFF method to estimate the background, excluding known γ-ray sources and then search the remaining Galactic Halo for γ-ray signals consistent with expected DM annihilation signatures. In this section, the search for this signature is carried out with the 3D maximum likelihood method analogous to the methodology employed in the remainder of this thesis. The 3D models are used to describe the regions emitting γ rays, and the background rate is not estimated in the OFF regions but is instead derived from archival data. The absence of masking allows for a greater proportion of the DM signal to be retained within the dataset. This chapter begins with an examination of the analysis setup. The computation of expected limits and limits based on random draws is explained. The usage of an uniform prior is discussed to ensure physical limits. Subsequently, the results of the DM search with H.E.S.S. data are presented. This includes the observed limits and the effect the lower energy threshold of the dataset has on the sensitivity. Subsequently, limits via annihilation into different channels are presented. Finally, the results are discussed and an outlook is given.

18.1 Analysis Setup

As introduced in chapter 17, the spectral shape of the γ rays is dependent on the channel through which the DM annihilated, and is typically a superposition of multiple channels. In indirect DM searches, a particular annihilation channel with a branching ratio of 100% is typically assumed. In this case, the $b\bar{b}$ channel is used as the default. Therefore, the predicted γ-ray flux is as follows:

$$\frac{d\Phi_\gamma}{d\Omega dE} = \frac{1}{4\pi k m_{\mathrm{DM}}^2} x_{b\bar{b}} \langle \sigma v \rangle_{\text{thermal relic}} \frac{dN_\gamma^{b\bar{b}}}{dE} \cdot \frac{dJ}{d\Omega} \tag{18.1}$$

Note that the velocity-averaged annihilation cross section of the $b\bar{b}$ channel is substituted as $x_{b\bar{b}}\langle \sigma v \rangle_{\text{thermal relic}}$ where $x_{b\bar{b}}$ is a scaling parameter and $\langle \sigma v \rangle_{\text{thermal relic}} = 3 \cdot 10^{-26}\text{cm}^3/\text{s}$ is the thermal relic cross section. The scaling parameter $x_{b\bar{b}}$ is fitted together with the other model and nuisance parameters.

18.1.1 Expected Limits

In the context of an indirect WIMP search, it is essential to differentiate between the observed and expected limits. While the former employs real γ-ray data, the latter utilises a simulated dataset based on the best-fit description of the real data under the assumption of no DM signal. This simulated dataset is commonly referred to as an Asimov dataset, which represents the expected outcome without statistical fluctuations and is used to estimate the sensitivity of an analysis.

The DM model cube, which contains the J-factor as the morphology and the spectrum based on the $b\bar{b}$ channel and a specific DM mass m_{DM} is fitted to the simulated data as an additional component. For now, all other model parameters are fixed to their best-fit values. As the simulated dataset lacks any DM signal, the best-fit value of the scaling parameter is found to be zero. To set a 95% upper limit (UL) a likelihood ratio test is performed. The value of x_{UL} is found by:

$$-2\log\mathcal{L}(x = x_{\mathrm{UL}}) = -2\log\mathcal{L}(x = 0) + 2.71. \tag{18.2}$$

Figure 18.1 illustrates an example of a $-2\log\mathcal{L}$ scan for a DM mass of 1.2 TeV, with the UL x_{UL} indicated. In the event that a subset of the other model parameters is reoptimised during the fitting process, the likelihood scan will widen as a consequence of the larger parameter space. The case of free normalisations of the LSC, the CMZ and the point sources is demonstrated (see Figure 18.1). Lastly, the nuisance parameters quantifying the systematic uncertainties due to the background model and the IRF are reoptimised, resulting in an even wider likelihood scan. It should be noted that the effect of the background systematic is stronger than that of the IRF systematics.

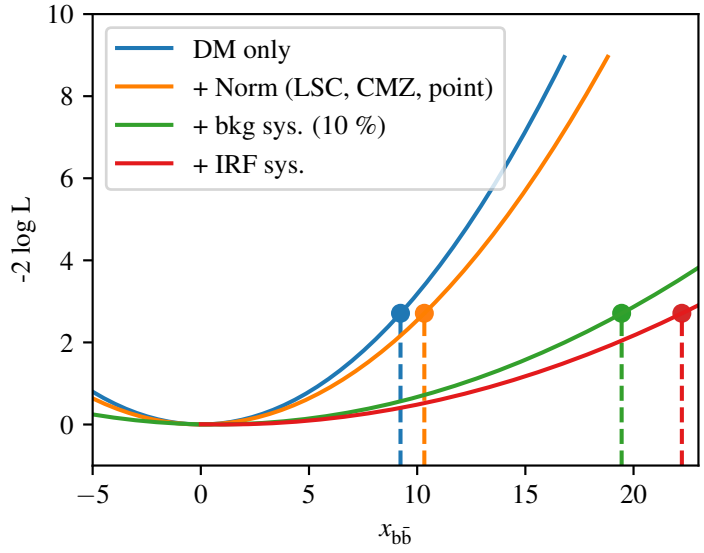

Figure 18.1: $-2\log\mathcal{L}$ scan as a function of the DM scaling parameter $x_{b\bar{b}}$ for $m_{\mathrm{DM}} = 1.2\,\mathrm{TeV}$. In the 'DM only' case all other parameters are fixed to their best-fit value obtained from the data. For the other scans different subsets of the model and nuisance parameters are reoptimised. The dashed lines indicate the UL on the scaling parameter.

The likelihood scan as a function of $x_{b\bar{b}}$ is performed for all assumed DM masses and with different sets of reoptimised model and nuisance parameters. The upper limits on the

annihilation cross section are calculated and plotted as a function of the DM mass in Figure 18.2. As anticipated, the greater the number of parameters that are reoptimised, namely the more systematic uncertainties that are taken into account, the lower the DM sensitivity of this 3D study. A comparison of the limits obtained with and without systematics reveals a deterioration of approximately a factor of two to three. It should be noted that the factor in question is dependent on the mass of the DM particle. This is due to the fact that the count distribution is highly dependent on the γ-ray energy, and decreases with a power law. Furthermore, some of the model components (LSC, CMZ) exhibit additional cutoffs at energies of approximately $\approx 10 - 25\,\mathrm{TeV}$, resulting in significant statistical uncertainties for DM spectra beyond this range. In contrast, both background and IRF systematic uncertainties are dominant at lower energies, leading to a more pronounced increase in the UL for lower DM masses when these are included.

The results are compared to the published H.E.S.S. limits from 2016 [143]. As these limits have been calculated without the inclusion of systematics, it is necessary to compare them to the 'DM only' case. In the reference analysis ([143]), the dataset comprised 254 hours of H.E.S.S. observations, which is comparable to the 264.4 hours used in the present study. While the limits obtained with the ON/OFF method in [143] are superior at lower energies, the limits computed in 3D are more sensitive for masses of the DM greater than 3 TeV. In conclusion, the UL obtained with the 3D method are comparable, and the optimal sensitivity would be achieved by combining the ON/OFF and the 3D approach. However, if systematic uncertainties are correctly incorporated, the 3D results are significantly influenced.

18.1.2 Limits based on Random Draws

In the context of DM searches, the objective is to compute a 68% containment region, which defines the area where 68% of the observed UL are expected to fall. Consequently, a substantial number of artificial datasets are generated, comprising the data predicted by the Asimov dataset and additional statistical fluctuations derived from Poisson distributions. In this case, the number of generated datasets is 1000. Analogous to the expected limit case, the DM model cube is fitted to the data, and the upper limit is computed for the annihilation cross section. The optimal values of $x_{\mathrm{b\bar{b}}}$ and the upper limit are illustrated for $m_{\mathrm{DM}} = 1.2\,\mathrm{TeV}$ in Figure 18.3. The mean of both distributions is computed, yielding values in agreement with those obtained from the Asimov dataset, as anticipated, given that the latter serves as a representative sample of the random draws. However, since the best-fit value of the Asimov dataset is zero, this implies that approximately half of the optimal results of the random draws are negative, which is deemed unphysical. In some instances, even the upper limit is negative. It is important to note that these outcomes are attributed to statistical fluctuations and not any systematic uncertainties, as the random draws are not susceptible to such influences.

In order to preclude the possibility of unphysical values emerging during the fitting process, a prior is set on the DM scaling parameter, the rationale for which will be elucidated in the following subsection.

18.1.3 Uniform Prior

One potential solution to prevent negative values of any fitting parameter is to impose strict constraints on the allowed range. However, to circumvent the discontinuities in the parameter space and the challenges associated with the optimisation process, it is more prudent to utilise a prior distribution. This approach incorporates the prior information on the parameter value

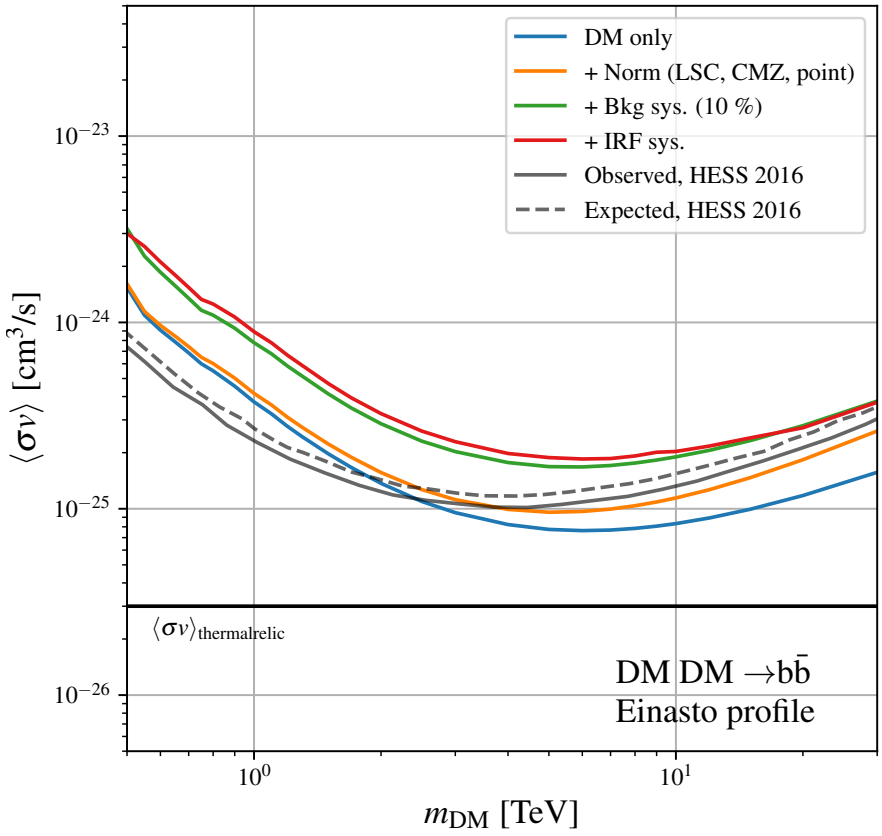

Figure 18.2: Expected limits on the DM annihilation cross section. Different sets of model parameter were refitted and reoptimised during the Likelihood scan.

in a probabilistic manner. The underlying assumption is that $a < x < b$, which consequently motivates the form of the prior distribution, namely a uniform distribution.

$$\pi(x) = \begin{cases} \frac{1}{b-a} & \text{for } a \leq x \leq b \\ 0 & \text{otherwise} \end{cases} \tag{18.3}$$

The probability of the value x being within the range a to b is equal to one:

$$\int_{-\infty}^{\infty} \pi(x)\, dx = \int_a^b \frac{1}{b-a}\, dx = \frac{1}{b-a} \cdot (b-a) = 1 \tag{18.4}$$

The subsequent step is to ascertain the values of a and b. As previously stated, the assumption is that the probability of the DM signal generating a negative γ-ray excess is non-existent; that is to say, the scaling value is not negative. Consequently, a is set to zero. In order to establish the upper limit, the UL of the Asimov dataset and the published H.E.S.S. results are employed. The largest value obtained in the latter is approximately $x = 836$, which corresponds to a DM mass of 180 GeV. Upon fitting the Asimov dataset, the largest value was observed to be approximately

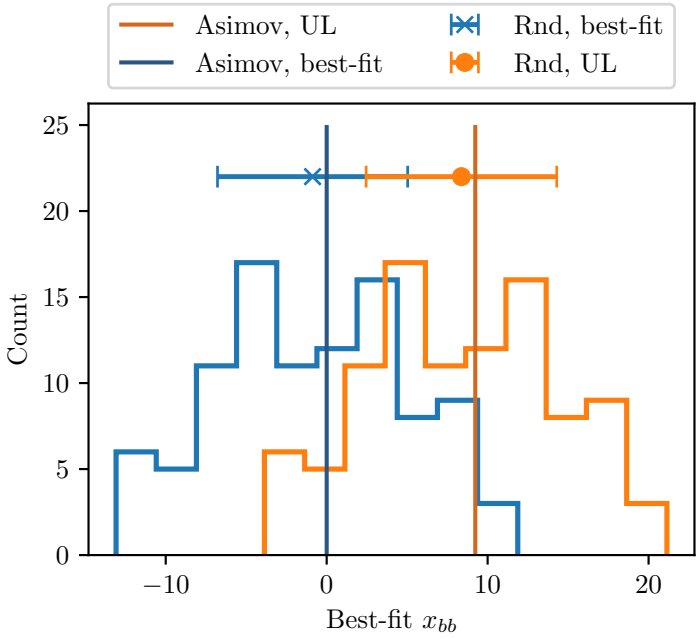

Figure 18.3: Distribution of the best-fit DM scaling parameter $x_{\mathrm{b\bar{b}}}$ of the 1000 datasets containing the astrophysical sources, background, statistical fluctuations but no DM signal. The error bar represents the mean and the 1σ distribution, while the vertical line denotes the best-fit result for the Asimov dataset. The UL for the scaling parameter is shown for comparison.

51. Consequently, the upper bound was set to $b = 10^4$, ensuring that the prior did not affect the upper limit computation. The resulting value, added to the negative log-likelihood, is therefore:

$$-2\log\pi(x) = \begin{cases} -2\log\left(\frac{1}{b-a}\right) = 18.42 & \text{for } a \leq x \leq b \\ \infty & \text{otherwise} \end{cases} \tag{18.5}$$

It should be noted that, instead of ∞, the value of 10^4 has been employed in order to circumvent the potential for not-a-number errors during the optimisation process. The selected value was deemed to be sufficiently large.

The 1000 random draws were refitted with the prior resulting in all best-fit and UL to be positive. The 68% containment region was computed for all masses, and is presented as an error band in Figure 18.4.

18.2 Results of the Dark Matter Search

18.2.1 Observed Limits

In order to ascertain whether DM is present in the data collected by H.E.S.S., the DM model cube is fitted to the counts cube. As a consequence of the prior applied, the optimal values of $x_{\mathrm{b\bar{b}}}$ are non-negative and approximately equal to zero for all DM masses. For masses exceeding 10 TeV, the values are marginally positive. However, a likelihood ratio test for these cases yields a significance of the DM signal below $< 2.7\sigma$, which is considerably below the detection threshold of 5σ. Consequently, upper limits are calculated in accordance with the expected limits (see

equation 18.2), as illustrated in Figure 18.4. The data falls within the 68% containment region, indicating consistency with the anticipated limits derived from the Asimov dataset. This indicates that the data is very well described by the different model components and that there is no excess left or overprediction by the models. If the nuisance and model parameters quantifying the background and IRF systematics and the normalisation of the astrophysical model components are refitted with the DM scaling and reoptimised during the scanning, the limits are considered to be with systematic uncertainties. They are found to worsen by approximately the same factor as the expected limits, which is estimated to be between two and three. Overall, computing DM limits with a 3D likelihood method proves to be a successful approach..

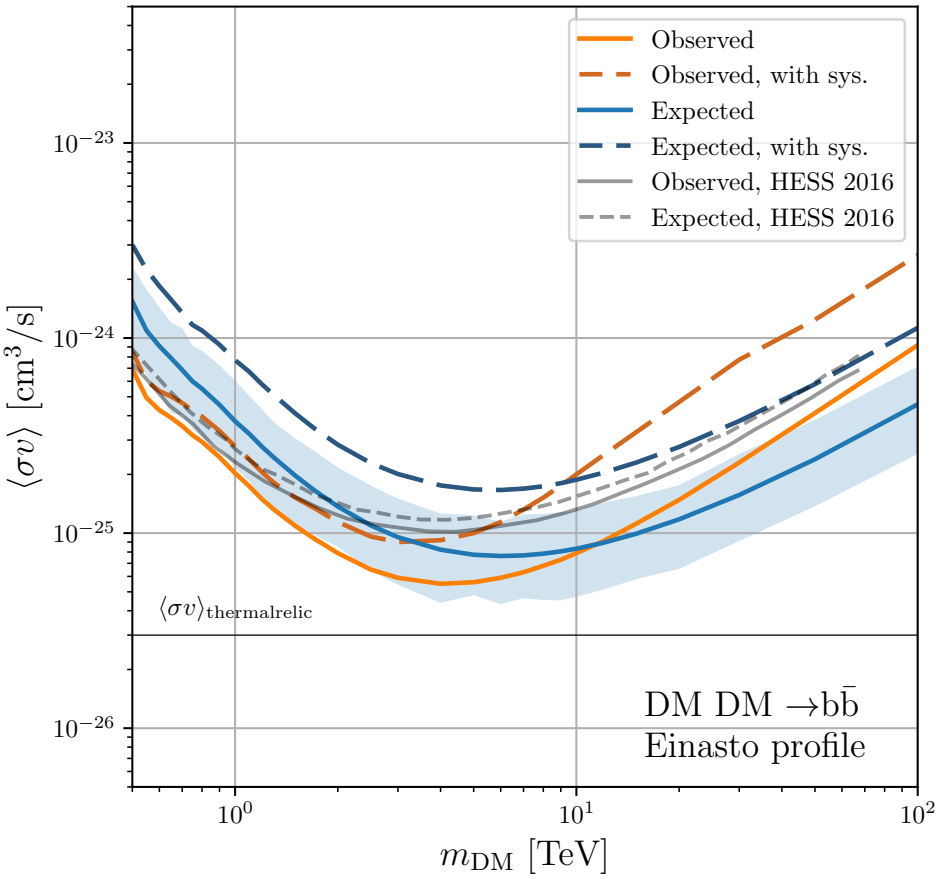

Figure 18.4: This study presents upper limits on the DM annihilation cross section with the Einasto profile and the $b\bar{b}$ channel. The expected limits are obtained from the Asimov dataset, while the observed limits are derived from real H.E.S.S. data. The limits are computed without and with background, IRF, and model components systematic uncertainties. The published ON/OFF limits are taken from [143].

18.2.2 Variation of the Lower Energy Threshold

Given the steep power law distribution of the observed γ-ray flux, the majority of γ rays are conducted at lower energies. Since the sensitivity of any experiment is dependent upon the available statistics, the limits computed here are contingent upon the lower energy threshold. In

this case, the lower limit was set to 0.4 TeV, and as a consequence of the selection of eight bins per decade, the lower bound of the first energy bin is, by default, 0.42 TeV. At lower energies, systematic uncertainties play a more significant role than at the highest energies. To ascertain the impact of the lower bound on the limit, the latter was increased to 0.5 TeV and 1 TeV. In the former case, only the initial energy bin is excluded from the analysis, with the edge of the energy bin situated at 0.56 TeV. However, only 66.06% of the data is retained. In the latter case, the edge is at 1.33 TeV, with only 18.31% of the data included in the analysis.

With these implemented reductions in the lower energy threshold, the anticipated limits were recalculated with and without the incorporation of systematic uncertainties within the fitting process. The outcomes are illustrated in Figure 18.5. As expected the sensitivity is decreased if less data is employed. The behaviour of the limits with systematic uncertainties incorporated are having well. At the highest DM masses, the difference in the limits become smaller.

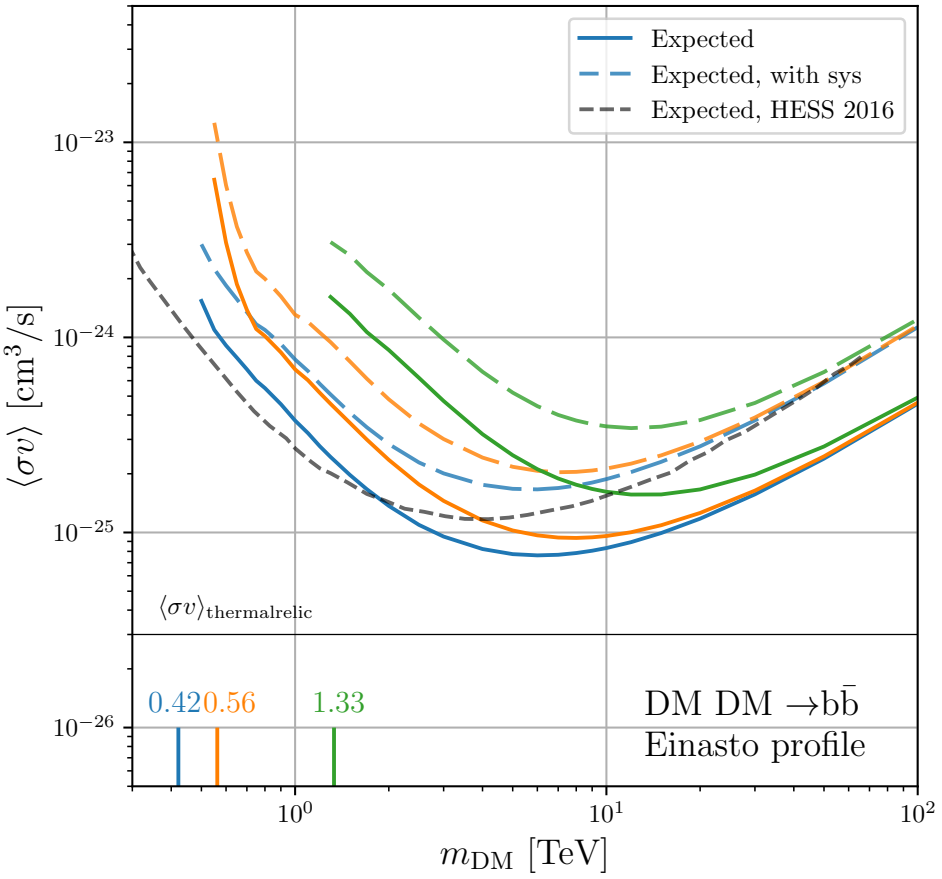

Figure 18.5: Expected UL computed with and without systematic uncertainties, with varying lower thresholds applied to the dataset. The specific threshold values are indicated in the corresponding text at the x-axis.

18.2.3 Annihilation into other Channels

Finally, the expected and observed limits of alternative annihilation channels are calculated. This encompasses the W^+W^-, $\tau^+\tau^-$, $t\bar{t}$ and $\mu^-\mu^+$ channels. The resulting limits are shown

and compared to the H.E.S.S. publication in Figure 18.6. The expected outcomes from the $t\bar{t}$ channel are comparable to the ON/OFF results from H.E.S.S. (2016), exhibiting a marginally enhanced performance at elevated DM masses, analogous to the $b\bar{b}$ results shown in Figure 18.4. In comparison to the expected limits obtained from the ON/OFF analysis, the 3D limits for the remaining three channels exhibit superior performance across almost the entire range of DM masses. In particular, the sensitivity for the $\mu^-\mu^+$ and $\tau^+\tau^-$ channels has increased by a factor of 2.36 and 1.96, respectively. Furthermore, even when incorporating systematic uncertainties, the expected limits remain better than the ON/OFF limits, which do not account for such systematic uncertainties.

The spectral index of the predicted counts of the background template, the LSC and the CMZ are found to be quite similar, with a value of approximately 1.7. The shape of the DM count predictions based on the thermal relic cross section is found to be significantly influenced by the DM mass and the channels involved. In the case of lower DM masses, the spectra are characterised by a high degree of softness, with indices reaching values up to 9. Conversely, at higher DM masses, the spectra exhibit a hardening trend, with indices stabilising at approximately 0.01. In the most extreme cases, both at low and high DM masses, the spectra are those of the $\mu^-\mu^+$ and $\tau^+\tau^-$ channels. The spectral indices of the $b\bar{b}$ and $t\bar{t}$ channels are relatively moderate. This aligns with the ratio of limits obtained with the ON/OFF and 3D approaches. The latter is more sensitive to DM annihilation channels whose spectral shape differs significantly from that of the background template and the two large-scale components (LSC and CMZ).

18.3 Discussion and Outlook

The typical approach to indirect DM searches with γ-ray data is an ON/OFF analysis, whereby the background rate is estimated in OFF regions. This method is considered to be robust, with the effect of background systematics being minimal, given that the rate is estimated within a large region and systematic uncertainties across the field of view are averaged out. The regions of the Galactic Plane where γ-ray emission is observed have been masked. In the case of expected limits, the question of whether the excluded region is sufficiently large to exclude all excess due to large-scale emission is not a significant concern. In the event that the data still exhibits an excess, the observed limits are deemed to be more conservative and therefore do not present a problem. In the event of a positive detection, it is important to address the issue of the LSC with the utmost care in order to guarantee that the DM signal is not erroneously identified as such. The 3D template-based approach precludes the possibility of this occurring, as the LSC is accounted for correctly. Nevertheless, it is imperative to conduct systematic studies of the impact of the LSC on potential detections, akin to the analysis of its influence on the CMZ spectrum presented in chapter 14.2. Given the increased susceptibility of the 3D background template to systematics, it is of critical importance to incorporate the uncertainties arising from this into the fitting process in order to ensure the accuracy of the computed limits. As in the remainder of this thesis, a 10% error is assumed and incorporated into the form of nuisance parameters. Furthermore, the inclusion of instrumental uncertainties associated with the IRF results in a deterioration of the limits by approximately a factor of three. In the published H.E.S.S. study from 2016, which employed a highly analogous dataset, there was no discussion of systematic uncertainties, making it particularly advantageous for comparison.

It is challenging to determine whether a 3D approach is preferable to the ON/OFF methodology. The correct incorporation of systematic uncertainties is a prerequisite for this, as is consideration of the annihilation channel. It was determined that DM spectra exhibiting signifi-

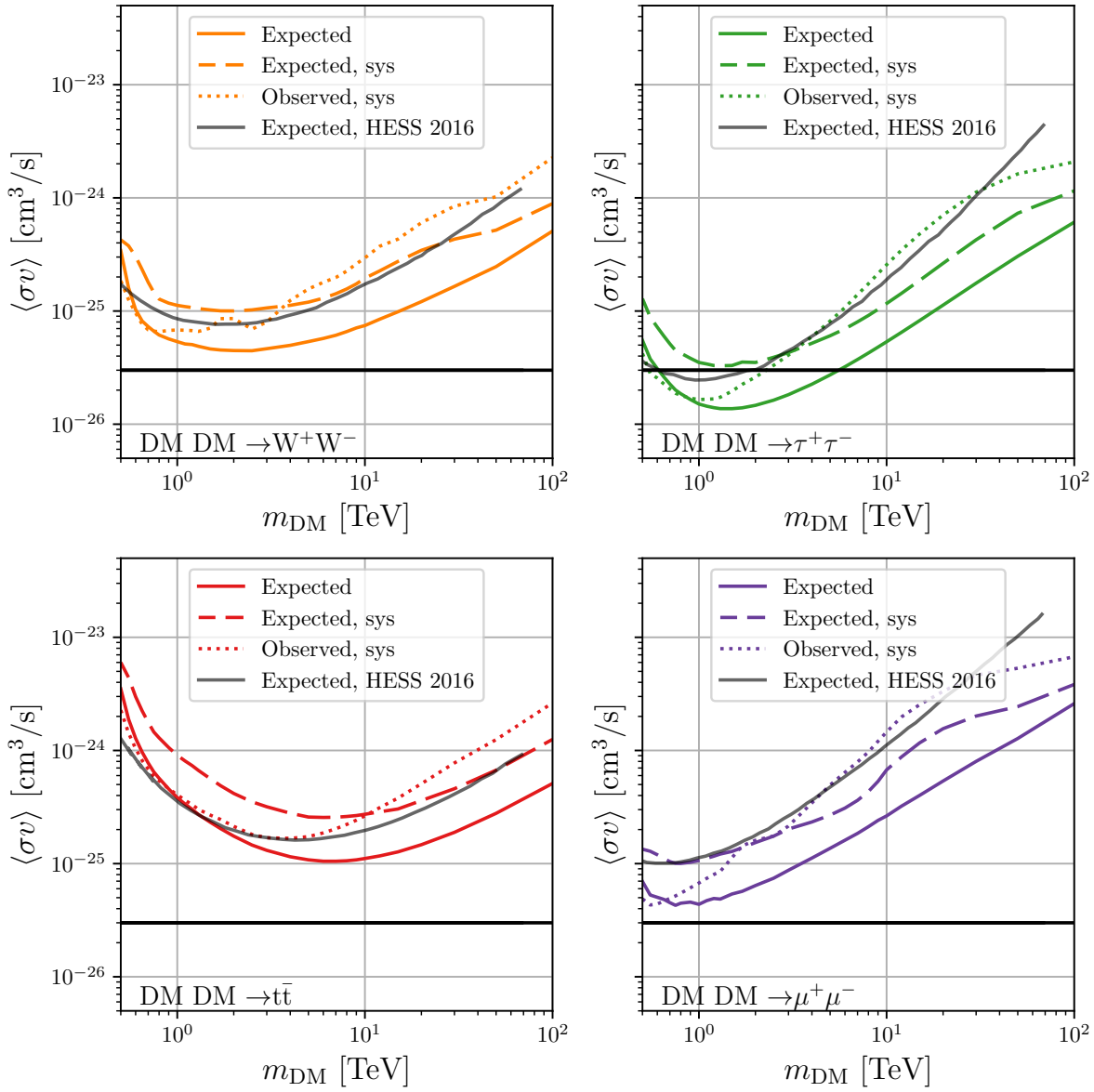

Figure 18.6: Expected limits with and without systematic uncertainties, as well as and the observed limits for the Einasto profile and different annihilation channels. For comparison, the limits computed with the ON/OFF approach in the 2016 H.E.S.S. publication are shown. Data taken from [143].

cant discrepancies from the spectral profile of the background and the LSC and CMZ are more readily discernible in the 3D approach than in the ON/OFF approach. In the case of the $\mu^-\mu^+$ and the $\tau^-\tau^+$ channels, the 3D limits incorporating systematic uncertainties are more stringent than the ON/OFF limits devoid of such uncertainties.

Figure 18.7 shows the limits for the W^-W^+ channel calculated in 3D. The expected limits are shown without and with nuisance parameters to account for the background and IRF systematic uncertainties. For the latter the 68% containment band was calculated from 1000 random draws. The observed limits with systematic uncertainties lie within this band, except for the very first

energy bins which could indicate additional systematic uncertainties or mismodelling of the data. However, due to the small discrepancy, this is negligible in the interpretation. Overall, the calculation of the expected and observed limits in 3D was successful.

It is noteworthy that the H.E.S.S. collaboration conducted γ-ray measurements from the GC post-2015. However, this data was excluded from the current analysis due to the focus on systematic uncertainties and a 3D analysis, which require the use of a well-controlled telescope and dataset. A greater quantity of data was utilised during the Inner Galactic Survey (IGS). In 2022, an ON/OFF DM search was conducted using the aforementioned newer dataset [144]. The resulting limits for the annihilation into W^-W^+ are shown in Figure 18.7. The limits are compared to those obtained by H.E.S.S. in 2016 and in the present work. It should be noted that despite the approximately doubling of the livetime employed, the limits from 2022 improved by more than a factor of $\sqrt{2}$ compared to the 2016 limits. This discrepancy can be attributed to differences in pointing strategies and the field of view employed. A 3D search for DM using the expanded dataset and a comparison of the resulting limits would undoubtedly be interesting. Nevertheless, in view of the considerable challenges that have already been encountered in the management of systematic uncertainties within this relatively stable dataset, it seems likely that such an analysis would prove to be quite labour-intensive. It should be noted that the 2022 DM limits included systematic uncertainties. However, only background systematics with an assumed strength of 1% and systematic uncertainties on the energy scale with an expected strength of 10% were considered, but not included in the analysis. This explains the relatively small increase in the limits and makes a fair comparison to the limits with systematic uncertainties obtained here challenging.

In 2021, the CTA collaboration published their expected DM sensitivity [152]. The authors devoted a considerable amount of space to discussing the impact of systematic uncertainties and additionally undertook a comparison between the ON/OFF approach and the 3D template approach. It was determined that in the absence of significant emission in the simulated dataset, the limits are comparable. However, if the emission is included in the dataset but not excluded sufficiently in the ON/OFF analysis, the limits are inferior to those obtained using the template approach, where the emission is included. This serves to reinforce the assertion made at the outset of this chapter, namely that the large-scale emission can give rise to complications in the ON/OFF approach with regard to the computation of limits, but particularly in the context of a detection. The impact of different assumptions regarding systematic uncertainties on the derived limits was investigated. It was posited that an accurate estimation is challenging due to the telescope's current operational status. The limits obtained without and with the benchmark systematic uncertainties are illustrated in Figure 18.7. Compared to the 2022 H.E.S.S. limits, they are more stringent despite the utilisation of a similar amount of live time. It remains to be seen whether the benchmarks set for the performance of CTA in terms of systematic uncertainties will prove accurate. This will determine whether the 3D template or the ON/OFF approach is more suitable, given that the latter is less affected by systematic uncertainties. The same is true for the larger dataset obtained by H.E.S.S. during the IGS.

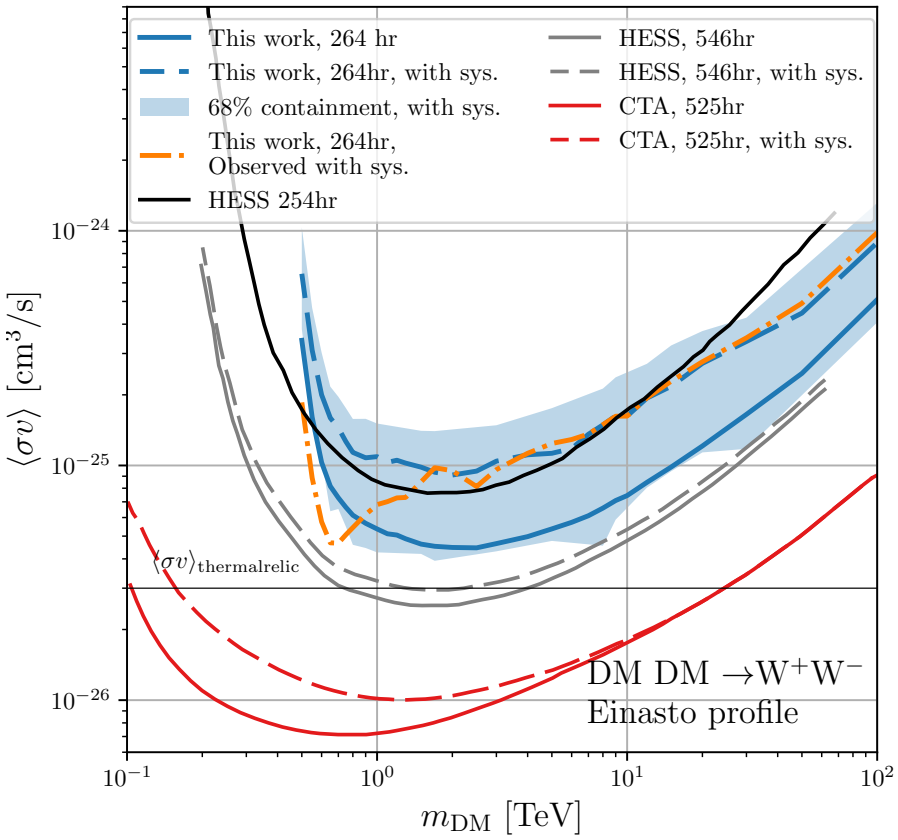

Figure 18.7: Expected limits computed in this thesis in 3D with 264 hours of H.E.S.S. data with and without systematic uncertainties (background and IRF, 10% each) taken into account. 68% containment bands computed with 1000 random draws of the Asimov dataset and with systematic uncertainties and the observed limits from H.E.S.S. data in 3D with systematic uncertainties are shown. Expected limits computed with 264 and 546 hours of H.E.S.S. data using the ON/OFF approach taken from [143, 144]. For the latter, the limits with 1% background systematic are shown. Limits computed with 525 hours of CTA data without and with 1% instrumental and background systematic uncertainties taken from [152].

SUMMARY

The GC region, the centre of the MW, is a region in which a variety of high-energy astrophysical phenomena occur, including intense star formation, strong magnetic activity, and interactions of cosmic rays with dense gas. The region is home to a SMBH at its core, surrounded by a highly concentrated gas region, the CMZ, and numerous other γ-ray emitting sources. The GC was identified as a potential PeVatron, a source capable of accelerating CRs up to PeV energies. PeVatrons are of particular interest as they represent extreme acceleration processes in our Galaxy, potentially contributing to the high-energy end of the CR spectrum and being closely linked to the spectral feature known as the knee at 4 PeV. Investigating these sources can provide critical insight into particle acceleration mechanisms and the maximum energies achievable by Galactic accelerators. The GC was first proposed as a PeVatron candidate in a H.E.S.S. publication in 2016 [5]. The CRs accelerated by the PeVatron would diffuse into the CMZ which would result in the measurement of γ rays of energies up to 100 TeV due to interaction with the particles in the CMZ. The spectrum of this γ-ray diffuse emission was found to be consistent with a power law, with no significant indication of a spectral cutoff. However, no γ rays at energies about 100 TeV were detected.

It should be noted, however, that an ON/OFF method was employed, which has inherent limitations in a crowded region like the GC. This is due to the inability to disentangle overlapping sources and the difficulty in estimating the hadronic background in the OFF-regions. In this instance, a more contemporary yet well-established analysis methodology was employed: the 3D approach, whereby the background is accounted for through the utilisation of a 3D template. In this study, the open-source tool *gammapy* was employed to investigate the region. Four γ-ray emitting sources were identified and modelled as point sources, with a power law and exponential cutoffs applied where appropriate. Furthermore, the two extended γ-ray emitting components have been subjected to detailed analysis. The first of these is the large-scale component, which is thought to be the result of the interaction between the CR sea and the gas along the Galactic Plane. The second is the aforementioned CMZ diffuse emission. The two extended components can be distinguished from each other in a 3D analysis approach due to the difference in the morphology and spectral properties. The distribution of the gas in the CMZ is reflected in the CMZ diffuse emission, which also shows a gradient towards the centre. This is not the case for the large-scale emission. A significant cutoff (4.77σ) was observed in the diffuse CMZ γ-ray spectrum at 23.6 ± 6.79 TeV. This indicates the presence of a cutoff in the primary proton source, which differs from the findings of the previous ON/OFF analysis of H.E.S.S. data.

Further investigation was conducted utilising the modelling of a proton source and particle diffusion. By fitting the proton properties, a cutoff at 164.61 ± 32.71 TeV with a significance of 4.44σ was revealed. The results were compared to the spectra of other instruments, leading to a questioning of the PeVatron hypothesis.

The focus of this work was to address the systematic uncertainties associated with the 3D background template and the IRFs of the telescope system. This was achieved by incorporating additional nuisance parameters and a prior term into the likelihood function. The prior term quantifies the magnitude and correlations of the systematic uncertainties. The efficacy of this method was demonstrated using publicly available H.E.S.S. datasets, which also showed that the model parameter uncertainties were behaving as expected. Subsequently, this method was employed in the analysis of the GC in a series of systematic tests. In addition to further cross-checks, it was demonstrated that a simple power law as the proton spectrum can be excluded with a high degree of confidence.

The GC is a region of particular interest for the search of DM, given the high predicted concentration. It is anticipated that DM particles will annihilate into standard particle pairs causing the production of γ rays. Previous DM searches with γ-ray telescopes employed the ON/OFF method, whereby known γ-ray emitting regions were excluded from the analysis. However, thereby, also a large fraction of the potential DM signal was lost. In this instance, the search was conducted using the 3D analysis method which does not necessitate the exclusion of γ-ray emitting regions. Instead the previously introduced model components are utilised in the analysis. No evidence of a DM signal was identified. Consequently, upper limits were calculated for the annihilation cross-section across a range of DM masses. These results were then compared to the ON/OFF outcomes from H.E.S.S. [143]. It was shown that, for specific annihilation channels, the 3D results are more sensitive. However, it was determined that the 3D results rely on a very good understanding and a correct handling of the systematic uncertainties in the data. Here, this was archieved by including nuisance parameters and priors in the fitting process.

In conclusion, the 3D approach was found to offer distinct advantages over the ON/OFF approach in the GC region. As more data from the GC from H.E.S.S. is collected and analysed, it will become increasingly evident that the systematic uncertainty will have a greater impact than the statistical uncertainties. It is therefore recommended that a correct treatment of the systematic uncertainties is achieved through the use of nuisance parameters and priors. The future CTA is expected to resolve large-scale emission in the TeV energy scale with an improved angular resolution [152]. Consequently, both the analysis of the diffuse emission and the search for DM in the GC could prove to be promising with the 3D analysis approach.

Appendix

Source	*lon*	*lat*
HESS J1745−290	359.943° ± 0.001°	−0.044° ± 0.001°
	[359.942° ± 0.001°]	[−0.044° ± 0.001°]
G0.9+0.1	0.868° ± 0.002°	0.077° ± 0.002°
	[0.865° ± 0.002°]	[0.083° ±0.002°]
HESS J1746−285	0.156° ± 0.008°	−0.144° ±0.002°
	[0.141° ± 0.004°]	[−0.121° ±0.004°]
HESS J1741−302	358.266° ± 0.011°]	0.079° ±0.010°
	[358.281° ± 0.008°]	[0.040° ±0.009°]

Table 1: Best-fit spatial parameters of the known H.E.S.S. point sources for *std-zeta* and for *std-ImPACT* in squared brackets for comparison.

Source	*lon*	*lat*
HESS J1745−290	359.943° ± 0.001°	−0.044° ± 0.001°
G0.9+0.1	0.865° ± 0.002°	0.083° ± 0.002°
HESS J1746−285	0.141° ± 0.004°	−0.121° ± 0.004°
HESS J1741−302	358.281° ± 0.008°	0.040° ± 0.009°

Table 2: Best-fit spatial parameters of the known H.E.S.S. point sources.

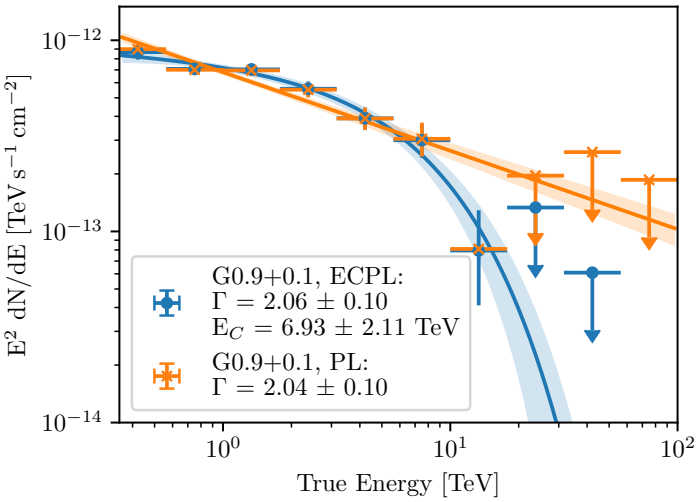

Figure 8: Best-fit spectrum of G0.9+0.1 with and without an exponential cutoff in the power law. The cutoff is preferred by 4.42σ.

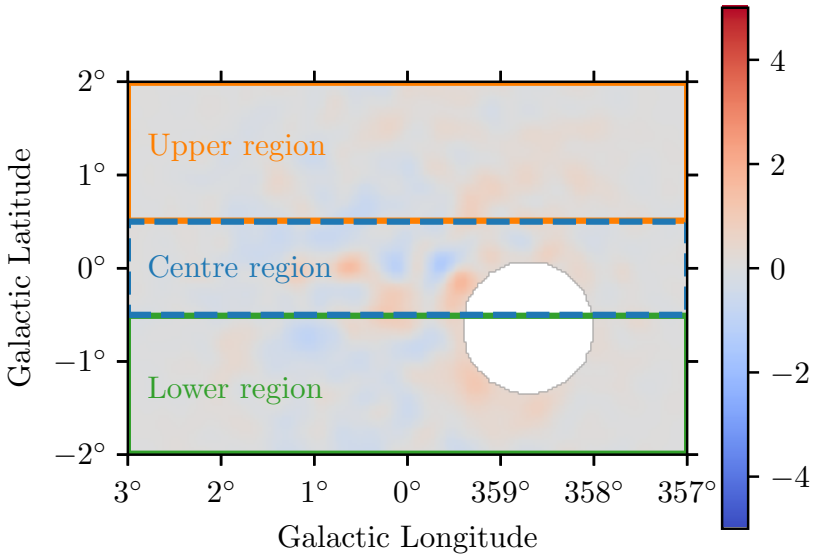

Figure 9: Definition of the control regions of the FoV: upper region ($6° \times 1.5°$), centre region ($6° \times 1°$), lower region ($6° \times 1.5°$)

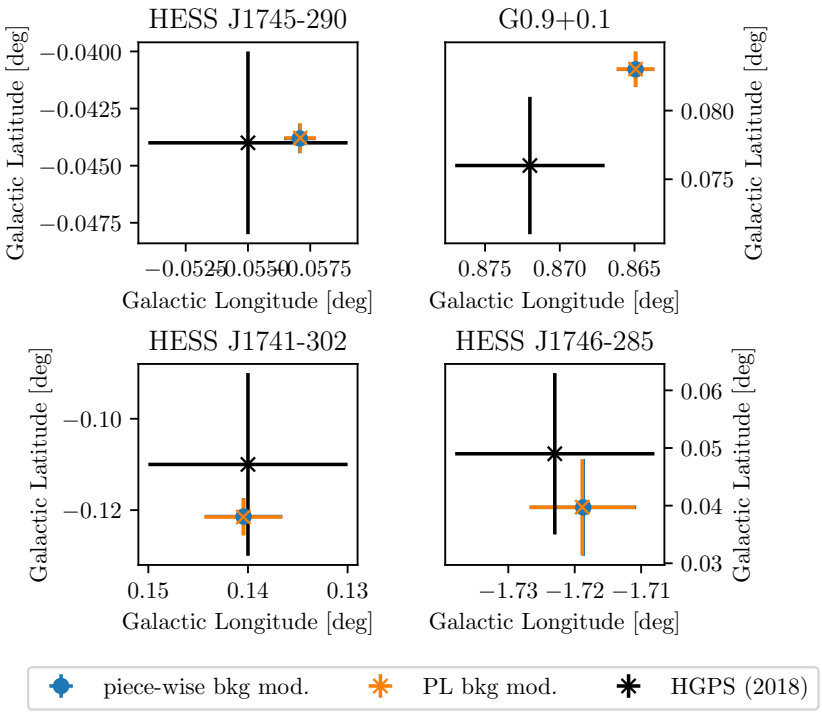

Figure 10: Comparison of the best-fit positions of point sources obtained when fitting the background modifications as a PL and with a piece-wise spectral model with $l_{corr} = 2$ and $\sigma_{bkg} = 10\%$

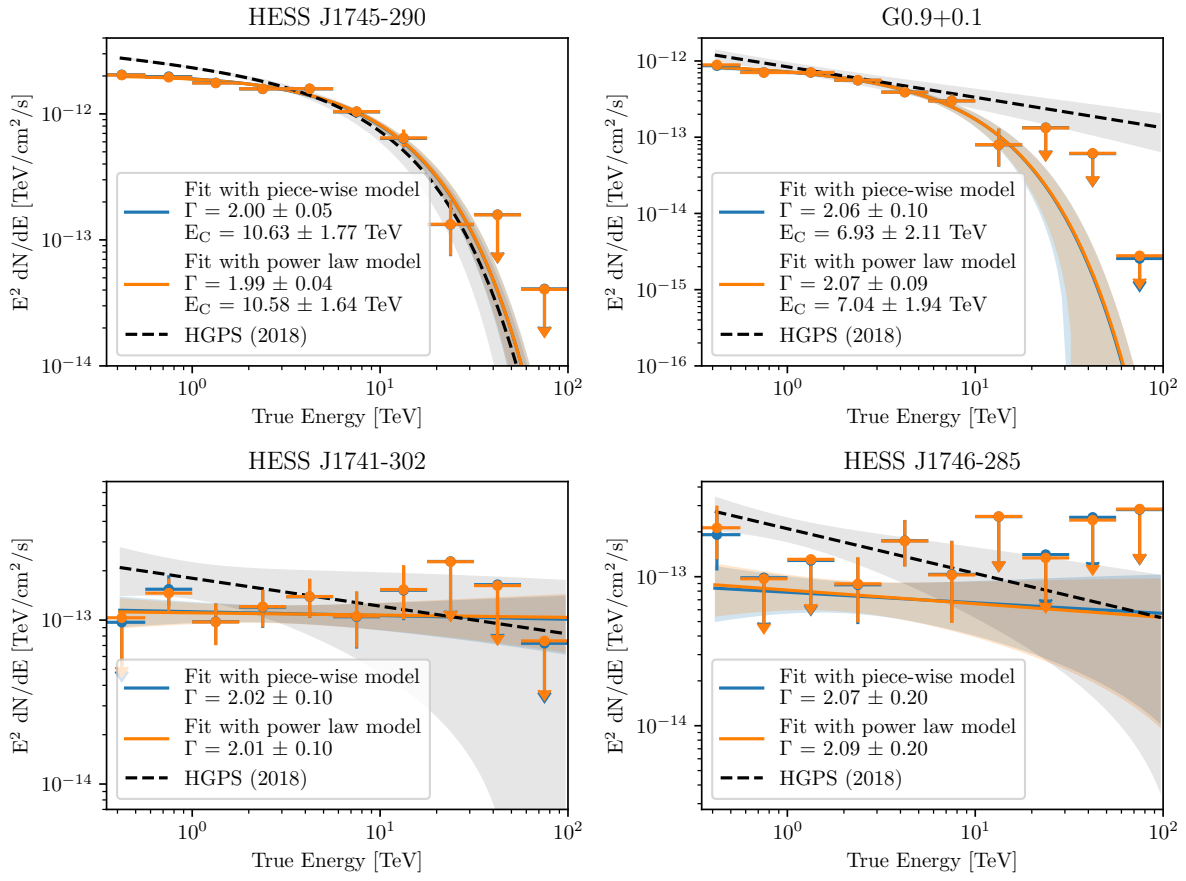

Figure 11: Comparison of the best-fit spectra and flux points of the point sources obtained when fitting the background modifications as a PL and with a piece-wise spectral model with $l_{corr} = 2$ and $\sigma_{bkg} = 10\%$

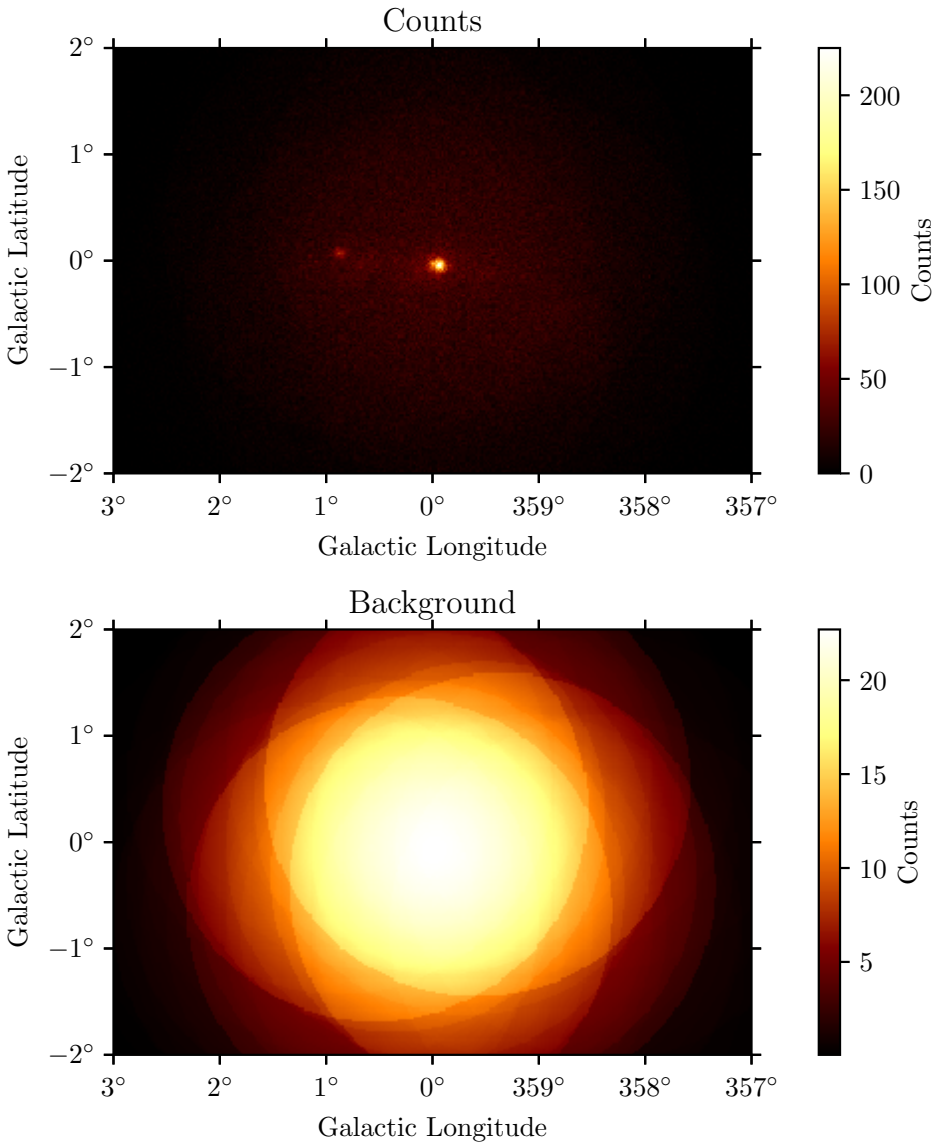

Figure 12: Upper panel: Counts of the stacked *std-zeta* dataset summed up along all energy bins. Lower panel: Background prediction of the stacked *std-zeta* dataset summed up along all energy bins.

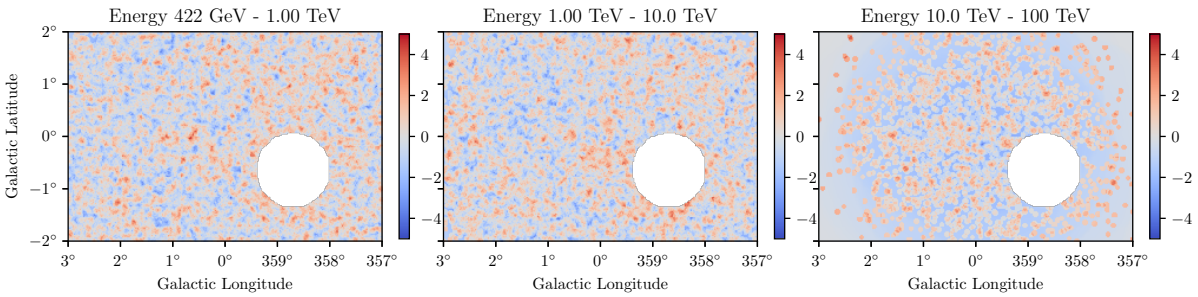

Figure 13: Li&Ma significance map in three energy bins with a 2D top-hat filter with radius 0.05° applied for the *std-zeta* configuration.

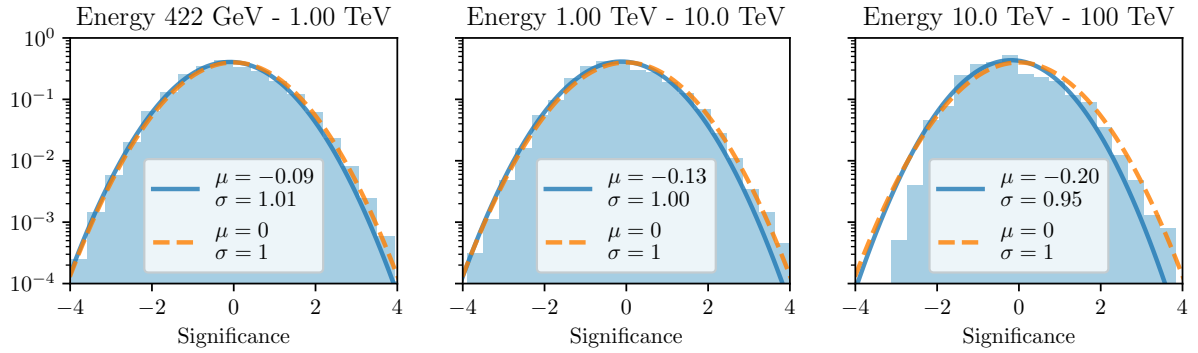

Figure 14: The distribution Li&Ma significance map in three energy bins with a 2D top-hat filter with radius 0.05° applied shown in Figure 9.10 computed with the *std-zeta* configuration. The mean and standard deviation of the distribution were calculated and a Gaussian with the according values is shown (blue). As a comparison, the norm distribution is shown in dashed orange.

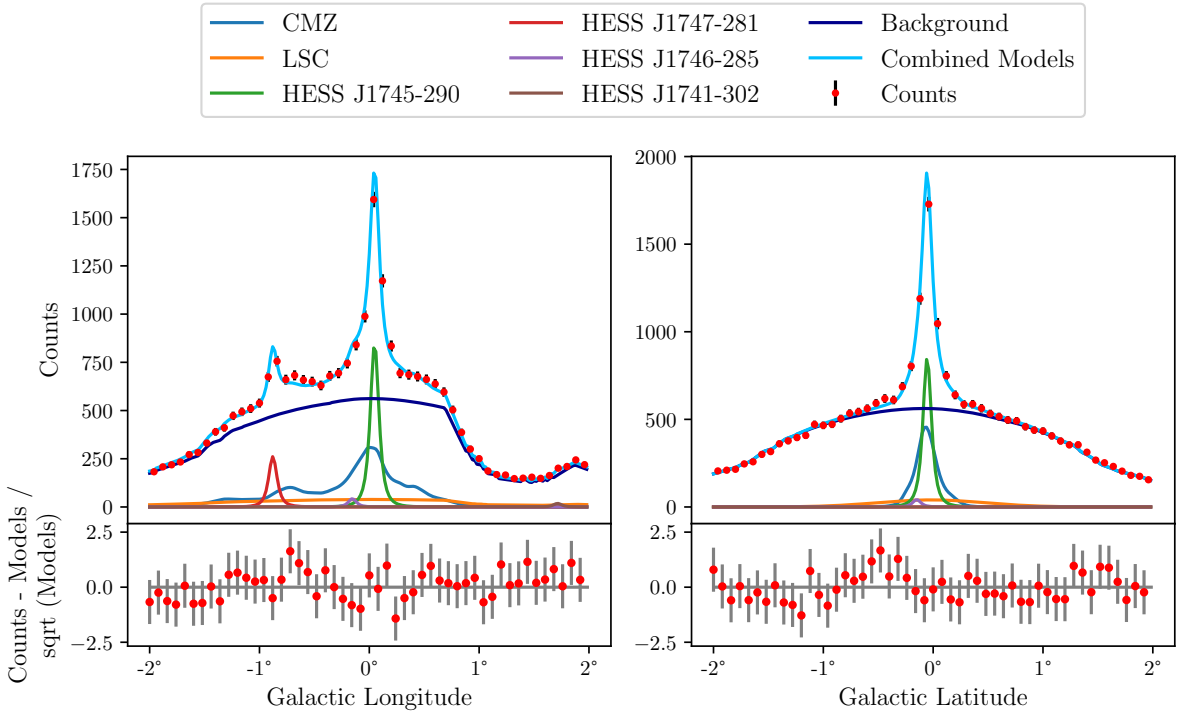

Figure 15: Profiles of the counts and the model prediction maps for the *std-zeta* configuration computed within a (left) 0.5° x 4° and (right) 4° x 0.5° region. The maps are summed up along all energies. For better visibility, the counts are rebinned by a factor of 4 resulting in a spatial binning of 0.08°. The lower panels show the residuals of the counts with the combined models.

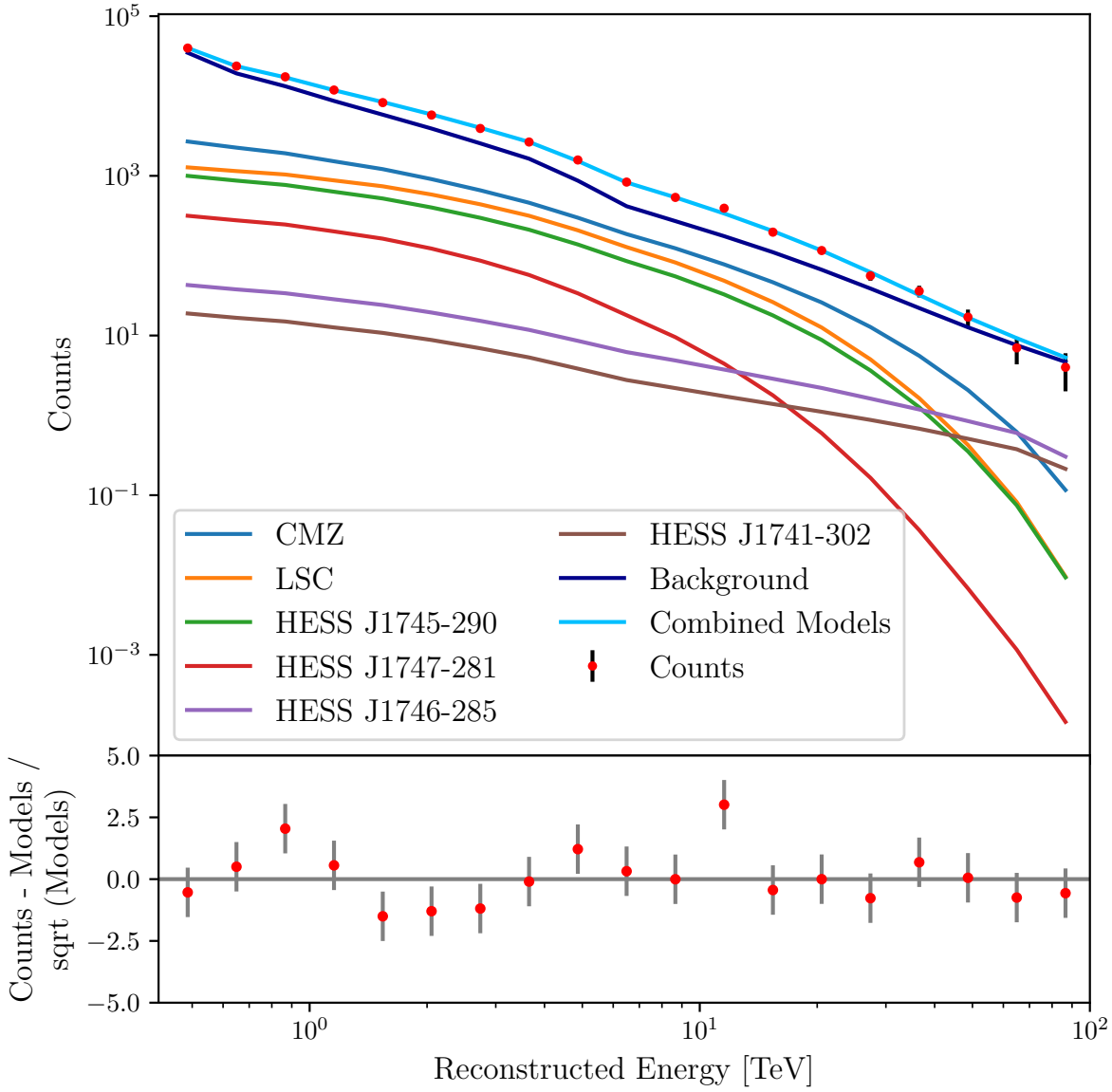

Figure 16: Counts and model predictions of the single components within the complete FoV as a function of reconstructed energy with a piece-wise spectral model with $l_{corr} = 2$ and $\sigma_{bkg} = 10\%$ for the *std-zeta* configuration.

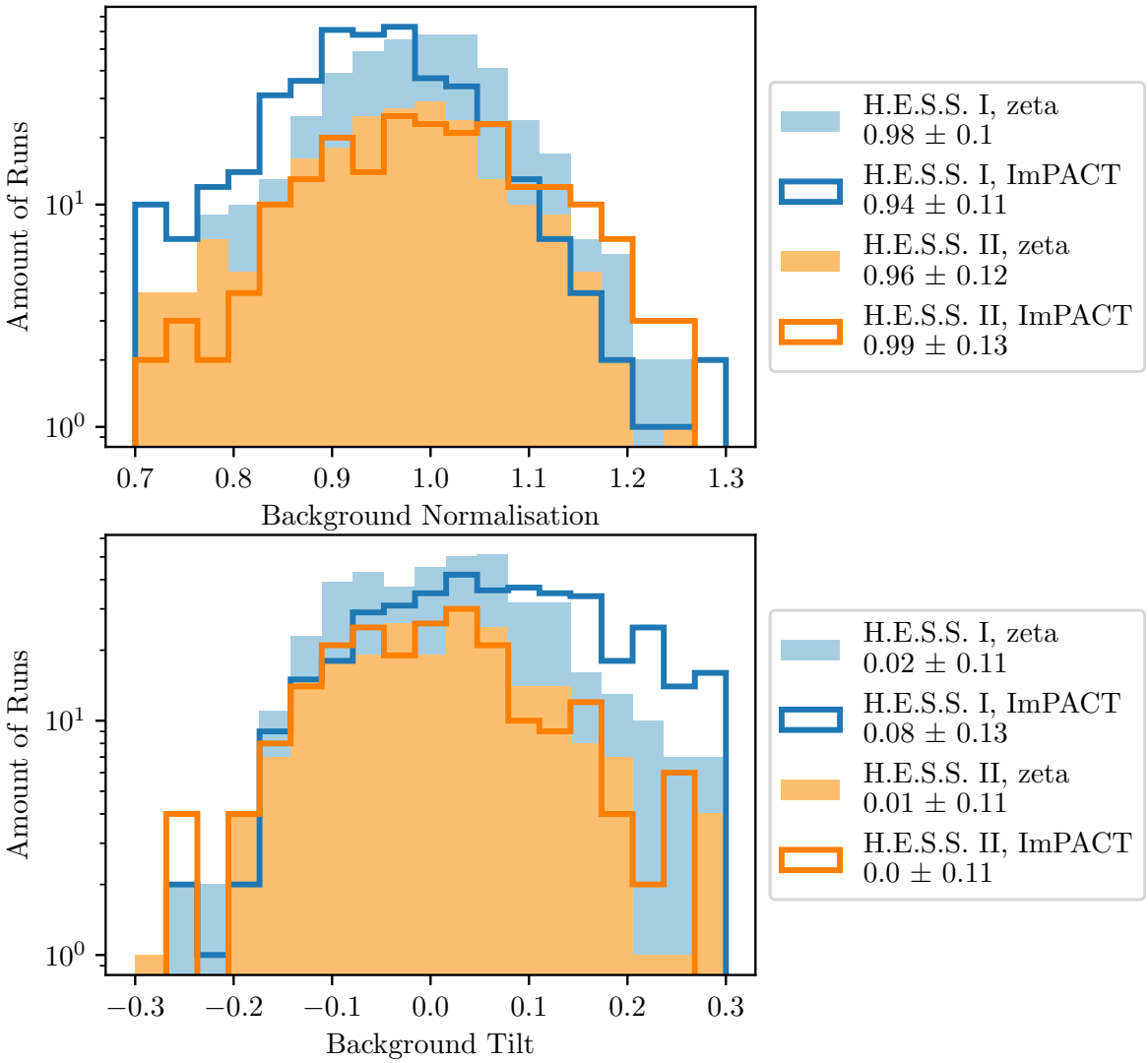

Figure 17: Best-fit results of the run-wise prefit.

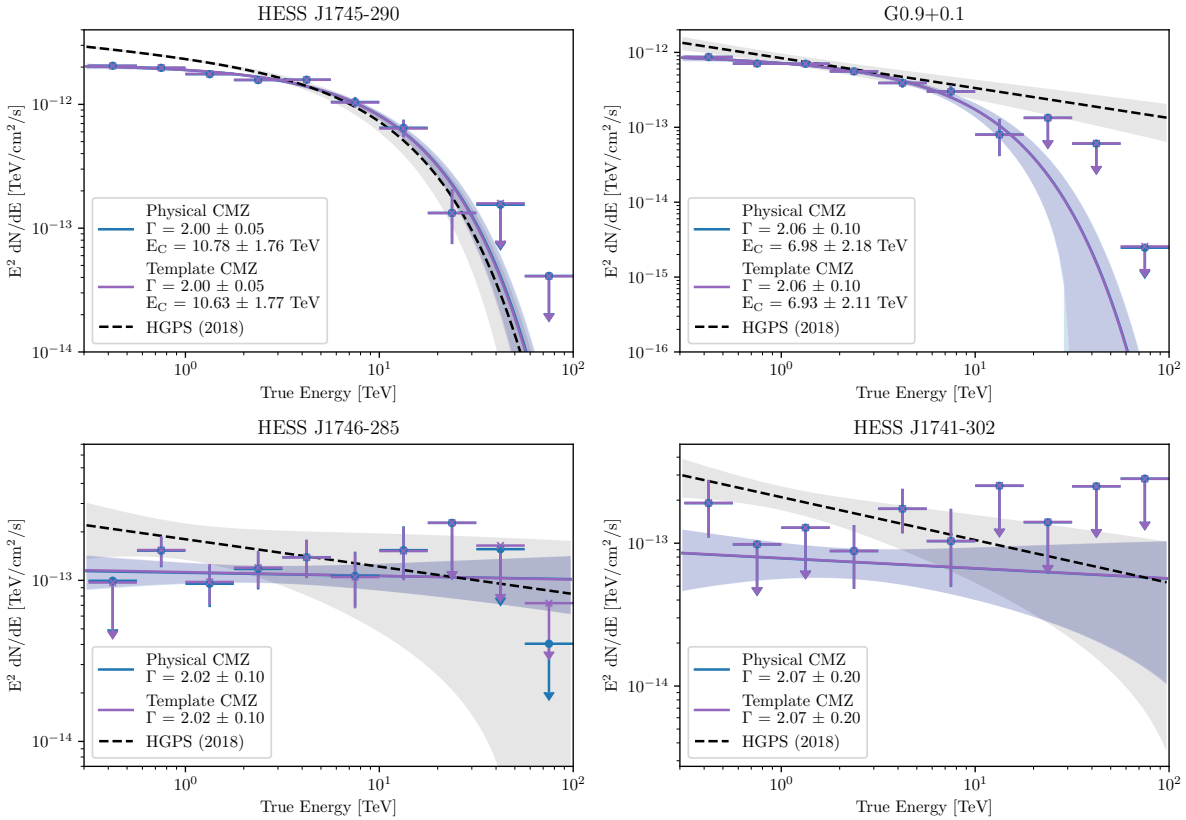

Figure 18: Best-fit spectrum with error band and flux points of the four point sources for the template-based and the physical-based model for the CMZ.

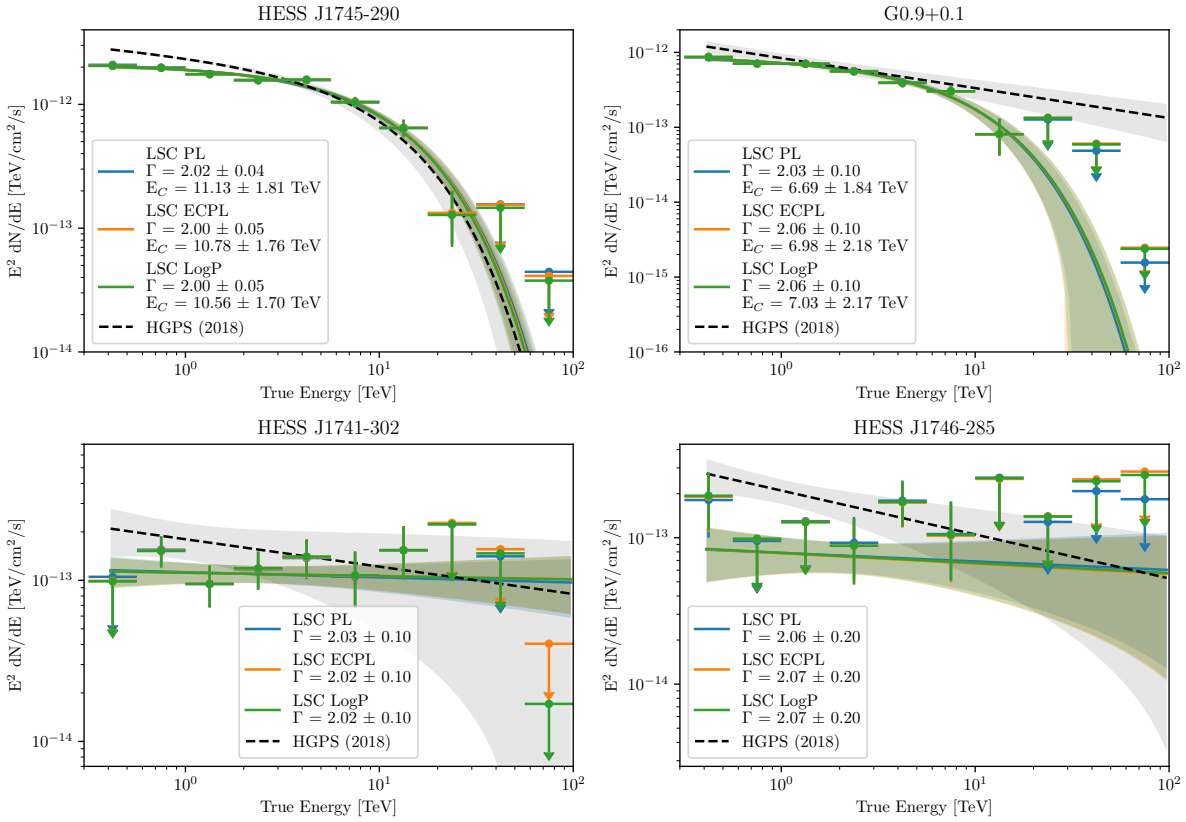

Figure 19: Best-fit spectrum with error band and flux points of the four point sources for different spectral shapes of the LSC.

20194	20195	20198	20199	20549	20550	20551	20552	20553	20554
20567	20568	20572	20573	20580	20581	20582	20583	20584	20596
20597	20598	20608	20609	20922	20923	20924	20925	20929	20968
20979	20989	20990	20991	20992	20998	21006	21007	21016	21017
21027	21028	21146	21147	21148	21149	21150	21152	21165	21166
21167	21168	21169	21190	21194	21238	21270	21272	21275	21323
21327	21347	21348	21349	21350	21372	21373	21376	21377	21389
21390	21452	21492	21493	21494	21496	21497	21508	21862	21863
21894	21895	21896	21897	21909	21910	22258	22266	22270	22271
22272	22273	22277	22278	22279	22280	22281	22290	22291	22292
22293	22294	22322	22384	22385	25330	25331	25349	25350	25353
25379	25380	25402	25403	25404	25405	25709	26080	26081	26082
26083	26084	26085	26086	26087	26088	26089	26090	26105	26106
26107	26108	26109	26110	26111	26112	26113	26114	26115	26129
26177	26178	26789	26790	26810	26811	26812	26813	26844	26845
26874	26875	26931	27376	27377	27378	27498	27499	27500	27501
27502	27503	27504	27505	27506	27507	27535	27536	27537	27539
27540	27541	27542	27543	27544	27545	27566	27567	27568	27569
27570	27571	27572	27573	27574	27575	27592	27593	27594	27595
27599	27600	27601	27602	27603	27625	27626	27627	27628	27629
27630	27631	27632	27633	27634	27662	27663	27664	27665	27666
27667	27668	28127	28128	28129	28130	28167	28168	28169	31031
31106	31539	31578	31579	31593	31594	31595	32666	32668	32669
32692	32693	32694	32695	32765	32766	33135	33136	33137	33138
33159	33160	33161	33162	33207	33208	33458	33467	33468	33469
33482	33483	33484	33485	33499	33500	33501	33502	33536	34148
34187	34209	34310	34313	34314	34949	34950	34951	34976	34977
35001	38832	38833	38835	38862	38863	38865	38895	38896	38897
38898	38930	38931	38932	38959	38960	38961	38962	41036	45378
45445	45446	45448	45449	45466	45467	45468	45469	45470	45471
45472	45487	45488	45489	45490	45491	45492	45493	47027	47028
47029	47030	47031	47032	47033	47034	47064	47065	47066	47067
50653	50654	50679	50680	50681	50682	50683	57804	57805	57821
57860	58728	58751	58802	58805	58829	58860	58887	58911	58912

Table 3: Observation IDs of the H.E.S.S. I runs (first part)

58913	58933	58934	58935	58936	63745	63755	66784	66785	66786
67094	67095	67113	67114	67161	67162	67189	67190	71893	74247
74251	74253	74368	74371	74373	74374	74377	74379	74381	74382
74384	74386	74388	74390	77284					

Table 4: Observation IDs of the H.E.S.S. I runs (second part)

85856	85885	85910	85911	85912	85913	85947	85949	85951	86133
86182	86183	86184	86185	86188	86189	86190	86258	86262	86263
86264	86265	86299	86302	86478	87196	87221	87226	87227	87251
87254	87256	87258	87292	87293	87294	87295	87297	87298	87341
87344	87346	87347	87385	87387	87416	87418	88161	88162	88163
88283	88285	88321	88322	88323	89381	89382	89521	93243	93461
93462	93463	93464	93465	93529	93530	93531	93532	93533	94421
94422	94536	94537	95101	95102	95235	95236	95237	95356	95357
95358	95398	95399	95401	95402	95427	95428	95429	95430	95432
95994	96151	96152	96230	96231	96357	96359	96360	96390	96391
96392	96395	96396	96397	96398	96490	96493	96494	96495	96496
96529	96530	96531	96597	96625	96655	96681	97015	97040	97041
97042	97066	97067	97068	97107	97108	97109	97111	97134	97135
97136	97137	97165	97166	97167	97168	97169	97170	97199	97201
97248	97293	97294	97295	97296	97341	97342	97343	97344	97394
97395	97396	97398	97443	97444	97446	97476	97477	97478	97501
105979	105981	105983	105985	106052	106057	106244	106245	106246	106247
106302	106303	106304	106305	106306	106307	106353	106356	106358	106359
106560	107105	107230	107335	107383	107385	107386	107388	107584	107585
107586	107641	107642	107643	107644	107645	108317	108388	108389	108390

Table 5: Observation IDs of the H.E.S.S. II runs.

Bibliography

[1] J. Sitarek. „TeV Instrumentation: Current and Future“. In: *Galaxies* 10.1, 21 (Jan. 2022), p. 21. DOI: 10.3390/galaxies10010021. arXiv: 2201.08611 [astro-ph.IM].

[2] Z. Cao et al. „The First LHAASO Catalog of Gamma-Ray Sources“. In: *The Astrophysical Journal Supplement Series* 271.1 (Feb. 2024), p. 25. ISSN: 1538-4365. DOI: 10.3847/1538-4365/acfd29. URL: http://dx.doi.org/10.3847/1538-4365/acfd29.

[3] A. U. Abeysekara et al. „Multiple Galactic Sources with Emission Above 56 TeV Detected by HAWC“. In: *Phys. Rev. Lett.* 124 (2 Jan. 2020), p. 021102. DOI: 10.1103/PhysRevLett.124.021102. URL: https://link.aps.org/doi/10.1103/PhysRevLett.124.021102.

[4] A. A. Lagutin and N. V. Volkov. *Where are the Pevatrons that Form the Knee in the Spectrum of the Cosmic Ray Nucleon Component around 4 PeV?* 2023. arXiv: 2309.07421 [astro-ph.HE]. URL: https://arxiv.org/abs/2309.07421.

[5] H.E.S.S. Collaboration et al. „Acceleration of petaelectronvolt protons in the Galactic Centre“. In: *Nature* 531.7595 (Mar. 2016), pp. 476–479. DOI: 10.1038/nature17147. arXiv: 1603.07730 [astro-ph.HE].

[6] J. Bolmont et al. „The camera of the fifth H.E.S.S. telescope. Part I: System description“. In: *Nuclear Instruments and Methods in Physics Research Section A: Accelerators, Spectrometers, Detectors and Associated Equipment* 761 (2014), pp. 46–57. ISSN: 0168-9002. DOI: https://doi.org/10.1016/j.nima.2014.05.093. URL: https://www.sciencedirect.com/science/article/pii/S0168900214006469.

[7] CTAO Collaboration. *Telescopes - CTAO*. https://www.ctao.org/emission-to-discovery/telescopes/. Accessed: 2024-12-03. 2024.

[8] K. Ishio and D. Paneque. „A novel energy reconstruction method for the MAGIC stereoscopic observation“. In: *Astroparticle Physics* 158 (2024), p. 102937. ISSN: 0927-6505. DOI: https://doi.org/10.1016/j.astropartphys.2024.102937. URL: https://www.sciencedirect.com/science/article/pii/S0927650524000148.

[9] F. Krennrich et al. „VERITAS: the Very Energetic Radiation Imaging Telescope Array System“. In: *New Astronomy Reviews* 48.5 (2004). 2nd VERITAS Symposium on the Astrophysics of Extragalactic Sources, pp. 345–349. ISSN: 1387-6473. DOI: https://doi.org/10.1016/j.newar.2003.12.050. URL: https://www.sciencedirect.com/science/article/pii/S1387647303003610.

[10] Z. Cao. „LHAASO Status and Physics Results“. In: *European Physical Journal Web of Conferences*. Vol. 280. European Physical Journal Web of Conferences. Sept. 2023, 01003, p. 01003. DOI: 10.1051/epjconf/202328001003.

[11] R. Alfaro et al. „All-particle cosmic ray energy spectrum measured by the HAWC experiment from 10 to 500 TeV“. In: *Phys. Rev. D* 96 (12 Dec. 2017), p. 122001. DOI: 10.1103/PhysRevD.96.122001. URL: https://link.aps.org/doi/10.1103/PhysRevD.96.122001.

[12] SWGO Collaboration. *SWGO - Start*. https://www.swgo.org/SWGOWiki/doku.php?id=start. Accessed: 2024-12-03. 2024.

[13] M. Baak et al. „HistFitter software framework for statistical data analysis“. In: *European Physical Journal C* 75, 153 (Apr. 2015), p. 153. DOI: 10.1140/epjc/s10052-015-3327-7. arXiv: 1410.1280 [hep-ex].

[14] K. Engel et al. „The Future of Gamma-Ray Experiments in the MeV-EeV Range“. In: *arXiv e-prints*, arXiv:2203.07360 (Mar. 2022), arXiv:2203.07360. DOI: 10.48550/arXiv.2203.07360. arXiv: 2203.07360 [astro-ph.HE].

[15] M. Ajello et al. „Fermi-LAT Observations of High-Energy Gamma-Ray Emission toward the Galactic Center“. In: *Astrophysical Journal* 819.1, 44 (Mar. 2016), p. 44. DOI: 10.3847/0004-637X/819/1/44. arXiv: 1511.02938 [astro-ph.HE].

[16] A. Santangelo C. Bambi, ed. *Handbook of X-ray and Gamma-ray Astrophysics*. Springer Singapore, 2022. ISBN: 978-981-16-4544-0. DOI: 10.1007/978-981-16-4544-0.

[17] R. Conceição and the SWGO Collaboration. „The Southern Wide-field Gamma-ray Observatory“. In: *arXiv preprint arXiv:2309.04577* (2023). URL: https://arxiv.org/abs/2309.04577.

[18] T. Kifune F. Aharonian J. Buckley and G Sinnis. „High energy astrophysics with ground-based gamma ray detectors“. In: *Reports on Progress in Physics* 71.9 (Aug. 2008), p. 096901. DOI: 10.1088/0034-4885/71/9/096901. URL: https://dx.doi.org/10.1088/0034-4885/71/9/096901.

[19] S. Funk. „Ground- and Space-Based Gamma-Ray Astronomy“. In: *Ann. Rev. Nucl. Part. Sci.* 65 (2015), pp. 245–277. DOI: 10.1146/annurev-nucl-102014-022036. arXiv: 1508.05190 [astro-ph.HE].

[20] M. Longair. *High Energy Astrophysics*. 3rd ed. Cambridge University Press, 2011.

[21] C. Fruck. „The Galactic Center resolved with MAGIC and a new technique for Atmospheric Calibration“. PhD thesis. Technische Universität Munchen, 2015.

[22] C. Nigro, T. Hassan, and L. Olivera-Nieto. „Evolution of Data Formats in Very-High-Energy Gamma-Ray Astronomy“. In: *Universe* 7.10 (2021). ISSN: 2218-1997. DOI: 10.3390/universe7100374. URL: https://www.mdpi.com/2218-1997/7/10/374.

[23] A. M. Hillas. „Cerenkov Light Images of EAS Produced by Primary Gamma Rays and by Nuclei“. In: *19th International Cosmic Ray Conference (ICRC19), Volume 3*. Vol. 3. International Cosmic Ray Conference. Aug. 1985, p. 445.

[24] F. Aharonian et al. „Observations of the Crab nebula with HESS“. In: *Astronomy and Astrophysics* 457.3 (Oct. 2006), pp. 899–915. DOI: 10.1051/0004-6361:20065351. arXiv: astro-ph/0607333 [astro-ph].

[25] S. Ohm, C. van Eldik, and K. Egberts. „γ/hadron separation in very-high-energy γ-ray astronomy using a multivariate analysis method“. In: *Astroparticle Physics* 31.5 (2009), pp. 383–391. ISSN: 0927-6505. DOI: https://doi.org/10.1016/j.astropartphys.2009.04.001. URL: https://www.sciencedirect.com/science/article/pii/S0927650509000589.

[26] W. Benbow and H.E.S.S. Collaboration. „The H.E.S.S. Standard Analysis Technique“. In: *Proceedings of the Conference Towards a Network of Atmospheric Cherenkov Detectors VII*. Palaiseau, France, 2005, pp. 163–172.

[27] R. Parsons, T. Murach, and M. Gajdus. „H.E.S.S. II Data Analysis with ImPACT“. In: *34th International Cosmic Ray Conference (ICRC2015)*. Vol. 34. International Cosmic Ray Conference. July 2015, 826, p. 826. DOI: 10.22323/1.236.0826. arXiv: 1509.06322 [astro-ph.IM].

[28] H. E. S. S. Collaboration. „H.E.S.S. first public test data release“. In: *arXiv e-prints*, arXiv:1810.04516 (Oct. 2018), arXiv:1810.04516. DOI: 10.48550/arXiv.1810.04516. arXiv: 1810.04516 [astro-ph.HE].

[29] D. Berge, S. Funk, and J. Hinton. „Background modelling in very-high-energy γ-ray astronomy“. In: *Astronomy and Astrophysics* 466.3 (May 2007), pp. 1219–1229. DOI: 10.1051/0004-6361:20066674. arXiv: astro-ph/0610959 [astro-ph].

[30] L. Mohrmann et al. „Validation of open-source science tools and background model construction in γ-ray astronomy“. In: *Astronomy and Astrophysics* 632, A72 (Dec. 2019), A72. DOI: 10.1051/0004-6361/201936452. arXiv: 1910.08088 [astro-ph.IM].

[31] F. Aharonian et al. „A deep spectromorphological study of the γ-ray emission surrounding the young massive stellar cluster Westerlund 1“. In: *Astronomy and Astrophysics* 666, A124 (Oct. 2022), A124. DOI: 10.1051/0004-6361/202244323. arXiv: 2207.10921 [astro-ph.HE].

[32] H. E. S. S. Collaboration et al. „HESS J1809−193: A halo of escaped electrons around a pulsar wind nebula?“ In: *Astronomy and Astrophysics* 672, A103 (Apr. 2023), A103. DOI: 10.1051/0004-6361/202245459. arXiv: 2302.13663 [astro-ph.HE].

[33] H. E. S. S. Collaboration et al. „The H.E.S.S. Galactic plane survey“. In: *Astronomy and Astrophysics* 612, A1 (Apr. 2018), A1. DOI: 10.1051/0004-6361/201732098. arXiv: 1804.02432 [astro-ph.HE].

[34] A. Donath et al. „Gammapy: A Python package for gamma-ray astronomy“. In: *Astronomy and Astrophysics* 678, A157 (Oct. 2023), A157. DOI: 10.1051/0004-6361/202346488. arXiv: 2308.13584 [astro-ph.IM].

[35] Samuel S. Wilks. „The Large-Sample Distribution of the Likelihood Ratio for Testing Composite Hypotheses“. In: *Annals of Mathematical Statistics* 9.1 (1938), pp. 60–62. DOI: 10.1214/aoms/1177732360.

[36] P. Ongmongkolkul et al. H. Dembinski. „scikit-hep/iminuit“. In: (Dec. 2020). DOI: 10.5281/zenodo.3949207. URL: https://doi.org/10.5281/zenodo.3949207.

[37] F. James and M. Roos. „Minuit: A System for Function Minimization and Analysis of the Parameter Errors and Correlations“. In: *Comput. Phys. Commun.* 10 (1975), pp. 343–367. DOI: 10.1016/0010-4655(75)90039-9.

[38] J. V. Wall and C. R. Jenkins. *Practical Statistics for Astronomers*. Second. Cambridge, UK: Cambridge University Press, 2012. ISBN: 978-0-521-73249-9.

[39] G. Cowan, K. Cranmer, E. Gross, and O. Vitells. „Asymptotic formulae for likelihood-based tests of new physics“. In: *European Physical Journal C* 71, 1554 (Feb. 2011), p. 1554. DOI: 10.1140/epjc/s10052-011-1554-0. arXiv: 1007.1727 [physics.data-an].

[40] D. Yadolah. *The Concise Encyclopedia of Statistics*. Springer New York, NY, 2008. DOI: 10.1007/978-0-387-32833-1. URL: https://link.springer.com/referencework/10.1007/978-0-387-32833-1.

[41] S. Watanabe and J.-T. Chien. „Maximum a-posteriori approximation“. In: *Bayesian Speech and Language Processing*. Cambridge University Press, 2015, pp. 137–183.

[42] D.S. Moore, G.P. McCabe, and B.A. Craig. *Introduction to the Practice of Statistics*. W. H. Freeman, 2014. ISBN: 9781464133633. URL: https://books.google.de/books?id=pX1_AwAAQBAJ.

[43] W. T. Sullivan III. „Karl Jansky and the discovery of extraterrestrial radio waves“. In: *The Early Years of Radio Astronomy*. Cambridge University Press, 2010, pp. 3–42. DOI: 10.1017/CBO9780511564956.003.

[44] I. Heywood et al. „The 1.28 GHz MeerKAT Galactic Center Mosaic“. In: *Astrophysical Journal* 925.2, 165 (Feb. 2022), p. 165. DOI: 10.3847/1538-4357/ac449a. arXiv: 2201.10541 [astro-ph.GA].

[45] Event Horizon Telescope Collaboration et al. „First Sagittarius A* Event Horizon Telescope Results. VII. Polarization of the Ring“. In: *Astrophysical Journal, Letters* 964.2, L25 (Apr. 2024), p. L25. DOI: 10.3847/2041-8213/ad2df0.

[46] A. Boehle et al. „An Improved Distance and Mass Estimate for Sgr A* from a Multistar Orbit Analysis“. In: *Astrophysical Journal* 830.1, 17 (Oct. 2016), p. 17. DOI: 10.3847/0004-637X/830/1/17. arXiv: 1607.05726 [astro-ph.GA].

[47] N. Scepi, J. Dexter, and M.C. Begelman. „Sgr A* X-ray flares from non-thermal particle acceleration in a magnetically arrested disc“. In: *Monthly Notices of the RAS* 511.3 (Apr. 2022), pp. 3536–3547. DOI: 10.1093/mnras/stac337. arXiv: 2107.08056 [astro-ph.HE].

[48] S. Markoff, F. Melia, and I. Sarcevic. „On the Nature of the EGRET Source at the Galactic Center“. In: *Astrophysical Journal, Letters* 489.1 (Nov. 1997), pp. L47–L50. DOI: 10.1086/310958. arXiv: astro-ph/9708068 [astro-ph].

[49] F. Cafardo, R. Nemmen, and Fermi LAT Collaboration. „Fermi-LAT Observations of Sagittarius A*: Imaging Analysis“. In: *Astrophysical Journal* 918.1, 30 (Sept. 2021), p. 30. DOI: 10.3847/1538-4357/ac0efe. arXiv: 2107.00756 [astro-ph.HE].

[50] M. Ackermann, A. Albert, W. B. Atwood, et al. „The Spectrum and Morphology of the Fermi Bubbles“. In: *The Astrophysical Journal* 793.1 (2014), p. 64. DOI: 10.1088/0004-637X/793/1/64. URL: https://arxiv.org/abs/1407.7905.

[51] T. Liu et al. „Morphological Evidence for the eROSITA Bubbles Being Giant and Distant Structures“. In: *The Astrophysical Journal Letters* 967 (2024), p. L27. DOI: 10.3847/2041-8213/ad47e0. URL: https://arxiv.org/abs/2405.04264.

[52] C. Guépin et al. „Pevatron at the Galactic Center: multi-wavelength signatures from millisecond pulsars“. In: *Journal of Cosmology and Astroparticle Physics* 2018.07 (July 2018), pp. 042–042. ISSN: 1475-7516. DOI: 10.1088/1475-7516/2018/07/042. URL: http://dx.doi.org/10.1088/1475-7516/2018/07/042.

[53] C. van Eldik. „Gamma rays from the Galactic Centre region: A review“. In: *Astroparticle Physics* 71 (2015), pp. 45–70. DOI: 10.1016/j.astropartphys.2015.05.002.

[54] A. Neronov and D. Semikoz. „Galactic diffuse gamma-ray emission at TeV energy“. In: *Astronomy and Astrophysics* 633, A94 (Jan. 2020), A94. DOI: 10.1051/0004-6361/201936368. arXiv: 1907.06061 [astro-ph.HE].

[55] K. Kosack et al. „TeV Gamma-Ray Observations of the Galactic Center“. In: *Astrophysical Journal, Letters* 608.2 (June 2004), pp. L97–L100. DOI: 10.1086/422469. arXiv: astro-ph/0403422 [astro-ph].

[56] F. Aharonian et al. „Very high energy gamma rays from the direction of Sagittarius A*“. In: *Astronomy and Astrophysics* 425 (Oct. 2004), pp. L13–L17. DOI: 10.1051/0004-6361:200400055. arXiv: astro-ph/0408145 [astro-ph].

[57] F. Aharonian et al. „Spectrum and variability of the Galactic center VHE γ-ray source HESS J1745-290“. In: *Astronomy and Astrophysics* 503.3 (Sept. 2009), pp. 817–825. DOI: 10.1051/0004-6361/200811569. arXiv: 0906.1247 [astro-ph.GA].

[58] F. Acero et al. „Localizing the VHE γ-ray source at the Galactic Centre“. In: *Monthly Notices of the RAS* 402.3 (Mar. 2010), pp. 1877–1882. DOI: 10.1111/j.1365-2966.2009.16014.x. arXiv: 0911.1912 [astro-ph.GA].

[59] F. Aharonian et al. „Very high energy gamma rays from the composite SNR G 0.9+0.1“. In: *Astronomy and Astrophysics* 432.2 (Mar. 2005), pp. L25–L29. DOI: 10.1051/0004-6361:200500022. arXiv: astro-ph/0501265 [astro-ph].

[60] H. E. S. S. Collaboration et al. „Characterising the VHE diffuse emission in the central 200 parsecs of our Galaxy with H.E.S.S.“ In: *Astronomy and Astrophysics* 612, A9 (Apr. 2018), A9. DOI: 10.1051/0004-6361/201730824. arXiv: 1706.04535 [astro-ph.HE].

[61] M. de Naurois and D. Mazin. „Ground-based detectors in very-high-energy gamma-ray astronomy“. en. In: *Comptes Rendus. Physique* 16.6-7 (2015), pp. 610–627. DOI: 10.1016/j.crhy.2015.08.011.

[62] *H.E.S.S. High Energy Stereoscopic System*. https://www.mpi-hd.mpg.de/hfm/HESS/. Accessed: 2024-06-13.

[63] J. Devin. *private communication*. devin@lupm.in2p3.fr, CNRS-LUPM (France). 2024.

[64] TeVCat Collaboration. *TeVCat Gamma-Ray Source Summary: H 2356-309*. http://tevcat.uchicago.edu/?mode=1&showsrc=111. Accessed: 2024-10-23. 2024.

[65] A. M. W. Mitchell. „Status of Ground-based and Galactic Gamma-ray Astronomy“. In: *Proceedings of the 37th International Cosmic Ray Conference (ICRC 2021)*. 2021. URL: https://arxiv.org/abs/2109.13753.

[66] T. Sawada, T. Hasegawa, T. Handa, and R. J. Cohen. „A molecular face-on view of the Galactic Centre region“. In: *Monthly Notices of the Royal Astronomical Society* 349.4 (Apr. 2004), pp. 1167–1178. ISSN: 0035-8711. DOI: 10.1111/j.1365-2966.2004.07603.x. eprint: https://academic.oup.com/mnras/article-pdf/349/4/1167/3037500/349-4-1167.pdf. URL: https://doi.org/10.1111/j.1365-2966.2004.07603.x.

[67] M. Tsuboi, T. Handa, and N. Ukita. „Dense Molecular Clouds in the Galactic Center Region. I. Observations and Data“. In: *Astrophysical Journal Supplement Series* 120.1 (Jan. 1999), pp. 1–39. DOI: 10.1086/313165.

[68] E. Moulin, A. Montanari, D. Malyshev, and Dm. Malyshev. *Search for TeV emission from the Fermi Bubbles at low Galactic latitudes with H.E.S.S. inner Galaxy survey observations*. 2021. arXiv: 2108.10028 [astro-ph.HE]. URL: https://arxiv.org/abs/2108.10028.

[69] K. Nakashima. „Systematic Errors of a 3D Template Background Model for IACTs and its Application to the Galactic Center“. PhD Thesis. Erlangen, Germany: Friedrich-Alexander-Universität Erlangen-Nürnberg, 2023.

[70] M. Spurio. *Probes of Multimessenger Astrophysics. Charged cosmic rays, neutrinos, γ-rays and gravitational waves*. Astronomy and Astrophysics Library. Springer, 2018. DOI: 10.1007/978-3-319-96854-4.

[71] T. K. Gaisser, R. Engel, and E. Resconi. *Cosmic Rays and Particle Physics*. Cambridge University Press, 2016. ISBN: 978-0-521-01646-9.

[72] J. Abraham et al. „Observation of the Suppression of the Flux of Cosmic Rays above 4×10^{19}eV“. In: *Physical Review Letters* 101.6, 061101 (Aug. 2008), p. 061101. DOI: 10.1103/PhysRevLett.101.061101. arXiv: 0806.4302 [astro-ph].

[73] W. Hanlon. *Cosmic Ray spectra of various experiments*. [Online; Accessed 17/06/2023]. 2021. URL: https://web.physics.utah.edu/~whanlon/spectrum.html.

[74] D. Caprioli. „Particle Acceleration at Shocks: An Introduction“. In: *arXiv e-prints*, arXiv:2307.00284 (July 2023), arXiv:2307.00284. DOI: 10.48550/arXiv.2307.00284. arXiv: 2307.00284 [astro-ph.HE].

[75] D. Bose, V. R. Chitnis, P. Majumdar, and A. Shukla. „Galactic and extragalactic sources of very high energy gamma rays“. In: *European Physical Journal Special Topics* 231.1 (Jan. 2022), pp. 27–66. DOI: 10.1140/epjs/s11734-022-00434-8. arXiv: 2201.06789 [astro-ph.HE].

[76] M. Pimenta A. De Angelis. *Introduction to Particle and Astroparticle Physics: Multimessenger Astronomy and its Particle Physics Foundations*. Undergraduate Lecture Notes in Physics. Springer, 2018. ISBN: 978-3-319-78180-8. DOI: 10.1007/978-3-319-78181-5.

[77] B. Zhang. „Hadronic Processes“. In: *The Physics of Gamma-Ray Bursts*. Cambridge University Press, 2018, pp. 221–227.

[78] S. Navas et al. (Particle Data Group). *Review of Particle Physics*. Vol. 110. 030001. Phys. Rev. D, 2024. URL: https://pdg.lbl.gov/.

[79] S. R. Kelner, F. A. Aharonian, and V. V. Bugayov. „Energy spectra of gamma rays, electrons, and neutrinos produced at proton-proton interactions in the very high energy regime“. In: *Physical Review D* 74.3, 034018 (Aug. 2006), p. 034018. DOI: 10.1103/PhysRevD.74.034018. arXiv: astro-ph/0606058 [astro-ph].

[80] Y. W. Wong. „Diffuse γ-Ray Emission from the Galactic Centre with H.E.S.S.“ PhD Thesis. Erlangen, Germany: Friedrich-Alexander-Universität Erlangen-Nürnberg, 2024.

[81] K. Ferrière, W. Gillard, and P. Jean. „Spatial distribution of interstellar gas in the innermost 3 kpc of our Galaxy“. In: *Astronomy and Astrophysics* 467.2 (2007), pp. 611–627.

[82] E.A.C. Mills. „The Milky Way's Central Molecular Zone“. In: *arXiv* 1705.05332 (2017). Jansky Fellow, University of Arizona Steward Observatory. URL: https://arxiv.org/abs/1705.05332.

[83] R. E. M. Hedges, D. L. Drummond, and Gallagher A. „Extreme-Wing Line Broadening and Cs-Inert-Gas Potentials“. In: *Physical Review A* 6.4 (1972), p. 1519. DOI: 10.1103/PhysRevA.6.1519.

[84] P. Blasi. „The origin of galactic cosmic rays“. In: *Astronomy and Astrophysics Review* 21, 70 (Nov. 2013), p. 70. DOI: 10.1007/s00159-013-0070-7. arXiv: 1311.7346 [astro-ph.HE].

[85] A. Scherer, J. Cuadra, and F. E. Bauer. „Modeling the Galactic center gamma-ray emission with more realistic cosmic-ray dynamics“. In: *Astronomy and Astrophysics* 679, A114 (Nov. 2023), A114. DOI: 10.1051/0004-6361/202245822. arXiv: 2310.01226 [astro-ph.HE].

[86] O. Bakunin. *Turbulence and diffusion. Scaling versus equations*. Jan. 2008. ISBN: 978-3-540-68221-9. DOI: 10.1007/978-3-540-68222-6.

[87] F.A. Aharonian. *Very high energy cosmic gamma radiation : a crucial window on the extreme Universe*. 2004. DOI: 10.1142/4657.

[88] A. N. Kolmogorov. „The Local Structure of Turbulence in Incompressible Viscous Fluid for Very Large Reynolds Numbers“. In: *Proceedings of the Royal Society of London Series A* 434.1890 (July 1991), pp. 9–13. DOI: 10.1098/rspa.1991.0075.

[89] M. Aguilar et al. „Precision Measurement of the Boron to Carbon Flux Ratio in Cosmic Rays from 1.9 GV to 2.6 TV with the Alpha Magnetic Spectrometer on the International Space Station“. In: *Physical Review Letters* 117.23, 231102 (Dec. 2016), p. 231102. DOI: 10.1103/PhysRevLett.117.231102.

[90] R. H. Kraichnan. „Inertial-Range Spectrum of Hydromagnetic Turbulence“. In: *Physics of Fluids* 8.7 (July 1965), pp. 1385–1387. DOI: 10.1063/1.1761412.

[91] A. Obermeier, P. Boyle, J. Hörandel, and D. Müller. „The Boron-to-carbon Abundance Ratio and Galactic Propagation of Cosmic Radiation“. In: *Astrophysical Journal* 752.1, 69 (June 2012), p. 69. DOI: 10.1088/0004-637X/752/1/69. arXiv: 1204.6188 [astro-ph.HE].

[92] A.W. Strong, I.V. Moskalenko, and V.S. Ptuskin. „Cosmic-Ray Propagation and Interactions in the Galaxy“. In: *Annual Review of Nuclear and Particle Science* 57.1 (Nov.

2007), pp. 285–327. DOI: 10.1146/annurev.nucl.57.090506.123011. arXiv: astro-ph/0701517 [astro-ph].

[93] F. Aharonian et al. „Discovery of very-high-energy γ-rays from the Galactic Centre ridge“. In: *Nature* 439.7077 (Feb. 2006), pp. 695–698. DOI: 10.1038/nature04467. arXiv: astro-ph/0603021 [astro-ph].

[94] A. Archer et al. „TeV Gamma-Ray Observations of the Galactic Center Ridge by VERITAS“. In: *Astrophysical Journal* 821.2, 129 (Apr. 2016), p. 129. DOI: 10.3847/0004-637X/821/2/129. arXiv: 1602.08522 [astro-ph.HE].

[95] M. L. Ahnen et al. „Observations of Sagittarius A* during the pericenter passage of the G2 object with MAGIC“. In: *Astronomy and Astrophysics* 601, A33 (May 2017), A33. DOI: 10.1051/0004-6361/201629355. arXiv: 1611.07095 [astro-ph.HE].

[96] V. A. Acciari et al. „MAGIC observations of the diffuse γ-ray emission in the vicinity of the Galactic Centre“. In: *Astronomy and Astrophysics* 638 (2020), A14. DOI: 10.1051/0004-6361/202037678.

[97] C. B. Adams et al. „VERITAS Observations of the Galactic Center Region at Multi-TeV Gamma-Ray Energies“. In: *Astrophysical Journal* 913.2, 115 (June 2021), p. 115. DOI: 10.3847/1538-4357/abf926. arXiv: 2104.12735 [astro-ph.HE].

[98] A. Albert et al. „Observation of the Galactic Center PeVatron Beyond 100 TeV with HAWC“. In: *arXiv e-prints*, arXiv:2407.03682 (July 2024), arXiv:2407.03682. DOI: 10.48550/arXiv.2407.03682. arXiv: 2407.03682 [astro-ph.HE].

[99] Z. Cao et al. „Measurement of Ultra-High-Energy Diffuse Gamma-Ray Emission of the Galactic Plane from 10 TeV to 1 PeV with LHAASO-KM2A“. In: *Physical Review Letters* 131.15, 151001 (Oct. 2023), p. 151001. DOI: 10.1103/PhysRevLett.131.151001. arXiv: 2305.05372 [astro-ph.HE].

[100] Y. W. Wong. *private communication*. yuwunwong@fau.de, ECAP (Germany). 2023.

[101] E. O. Angüner, G. Spengler, E. Amato, and S. Casanova. „Search for the Galactic accelerators of cosmic rays up to the knee with the Pevatron test statistic“. In: *Monthly Notices of the RAS* 523.3 (Aug. 2023), pp. 4097–4112. DOI: 10.1093/mnras/stad1674. arXiv: 2306.01484 [astro-ph.HE].

[102] D. Bose, V. R. Chitnis, P. Majumdar, and A. Shukla. „Galactic and Extragalactic Sources of Very High Energy Gamma-rays“. In: *The European Physical Journal Special Topics* (2022). DOI: 10.48550/arXiv.2201.06789. arXiv: 2201.06789 [astro-ph.HE].

[103] Q.-Z. Yan et al. „Towards a three-dimensional distribution of the molecular clouds in the Galactic Centre“. In: *Monthly Notices of the RAS* 471.3 (Nov. 2017), pp. 2523–2536. DOI: 10.1093/mnras/stx1724. arXiv: 1707.02378 [astro-ph.GA].

[104] A. Dundovic, C. Evoli, D. Gaggero, and D. Grasso. „Simulating the Galactic multi-messenger emissions with HERMES“. In: *Astronomy and Astrophysics* 653, A18 (Sept. 2021), A18. DOI: 10.1051/0004-6361/202140801. arXiv: 2105.13165 [astro-ph.HE].

[105] A. E. Vladimirov, G. Jóhannesson, I. V. Moskalenko, and T. A. Porter. „Testing the Origin of High-energy Cosmic Rays“. In: *Astrophysical Journal* 752.1, 68 (June 2012), p. 68. DOI: 10.1088/0004-637X/752/1/68. arXiv: 1108.1023 [astro-ph.HE].

[106] Z. Cao et al. „Discovery of the Ultrahigh-energy Gamma-Ray Source LHAASO J2108+5157“. In: *The Astrophysical Journal Letters* 919.2 (Sept. 2021), p. L22. ISSN: 2041-8213. DOI: 10.3847/2041-8213/ac2579. URL: http://dx.doi.org/10.3847/2041-8213/ac2579.

[107] H. Abdalla et al. „Evidence of 100 TeV γ-ray emission from HESS J1702-420: A new PeVatron candidate“. In: *Astronomy and Astrophysics* 653, A152 (Sept. 2021), A152. DOI: 10.1051/0004-6361/202140962. arXiv: 2106.06405 [astro-ph.HE].

[108] E. Amato and B. Olmi. „The Crab Pulsar and Nebula as Seen in Gamma-Rays“. In: *Universe* 7.11 (2021). ISSN: 2218-1997. DOI: 10.3390/universe7110448. URL: https://www.mdpi.com/2218-1997/7/11/448.

[109] P. Cristofari. „The Hunt for Pevatrons: The Case of Supernova Remnants“. In: *Universe* 7.9 (Aug. 2021), p. 324. ISSN: 2218-1997. DOI: 10.3390/universe7090324. URL: http://dx.doi.org/10.3390/universe7090324.

[110] M. Breuhaus, B. Reville, and J. A. Hinton. „Pulsar wind nebula origin of the LHAASO-detected ultra-high energy γ-ray sources“. In: *Astronomy and Astrophysics* 660, A8 (Apr. 2022), A8. DOI: 10.1051/0004-6361/202142097. arXiv: 2109.05296 [astro-ph.HE].

[111] P. Cristofari, S. Gabici, R. Terrier, and T. B. Humensky. „On the search for Galactic supernova remnant PeVatrons with current TeV instruments“. In: *Monthly Notices of the Royal Astronomical Society* 479.3 (June 2018), pp. 3415–3421. ISSN: 0035-8711. DOI: 10.1093/mnras/sty1589. eprint: https://academic.oup.com/mnras/article-pdf/479/3/3415/25161517/sty1589.pdf. URL: https://doi.org/10.1093/mnras/sty1589.

[112] S. Gabici. „Cosmic Rays and Molecular Clouds“. In: *Cosmic Rays in Star-Forming Environments*. Ed. by Diego F. Torres and Olaf Reimer. Vol. 34. Astrophysics and Space Science Proceedings. Jan. 2013, p. 221. DOI: 10.1007/978-3-642-35410-6_16. arXiv: 1208.4979 [astro-ph.HE].

[113] T. Sudoh and J.F. Beacom. „Where is the end of the cosmic-ray electron spectrum?“ In: *Physical Review D* 108.10, 103015 (Nov. 2023), p. 103015. DOI: 10.1103/PhysRevD.108.103015. arXiv: 2308.13600 [astro-ph.HE].

[114] V. Verzi, D. Ivanov, and Y. Tsunesada. „Measurement of energy spectrum of ultra-high energy cosmic rays“. In: *Progress of Theoretical and Experimental Physics* 2017.12 (Nov. 2017), 12A103. ISSN: 2050-3911. DOI: 10.1093/ptep/ptx082. eprint: https://academic.oup.com/ptep/article-pdf/2017/12/12A103/22075708/ptx082.pdf. URL: https://doi.org/10.1093/ptep/ptx082.

[115] S. Liu, H. Zeng, Y. Xin, and Y. Zhang. „The origin of galactic cosmic rays“. In: *Reviews of Modern Plasma Physics* 6.1 (2022), p. 19. ISSN: 2367-3192. DOI: 10.1007/s41614-022-00080-6. URL: https://doi.org/10.1007/s41614-022-00080-6.

[116] R. Liu, X. Wang, A. Prosekin, and X. Chang. „MODELING THE GAMMA-RAY EMISSION IN THE GALACTIC CENTER WITH A FADING COSMIC-RAY ACCELERATOR“. In: *The Astrophysical Journal* 833.2 (Dec. 2016), p. 200. DOI: 10.3847/1538-4357/833/2/200. URL: https://dx.doi.org/10.3847/1538-4357/833/2/200.

[117] L. O'C. Drury, F. A. Aharonian, D. Malyshev, and S. Gabici. „On the plasma temperature in supernova remnants with cosmic-ray modified shocks“. In: *Astronomy and Astrophysics*

496.1 (Mar. 2009), pp. 1–6. DOI: 10.1051/0004-6361/200811394. arXiv: 0811.3566 [astro-ph].

[118] L. Jouvin, A. Lemière, and R. Terrier. „Does the SN rate explain the very high energy cosmic rays in the central 200 pc of our Galaxy?“ In: *Monthly Notices of the Royal Astronomical Society* 467.4 (Feb. 2017), pp. 4622–4630. ISSN: 0035-8711. DOI: 10.1093/mnras/stx361. eprint: https://academic.oup.com/mnras/article-pdf/467/4/4622/11041368/stx361.pdf. URL: https://doi.org/10.1093/mnras/stx361.

[119] G. Ponti, R. Terrier, A. Goldwurm, G. Belanger, and G. Trap. „DISCOVERY OF A SUPERLUMINAL Fe K ECHO AT THE GALACTIC CENTER: THE GLORIOUS PAST OF Sgr A* PRESERVED BY MOLECULAR CLOUDS“. In: *The Astrophysical Journal* 714.1 (Apr. 2010), p. 732. DOI: 10.1088/0004-637X/714/1/732. URL: https://dx.doi.org/10.1088/0004-637X/714/1/732.

[120] F. Cafardo and R. Nemmen. „Fermi-LAT Observations of Sagittarius A*: Imaging Analysis“. In: *The Astrophysical Journal* 918.1 (Sept. 2021), p. 30. ISSN: 1538-4357. DOI: 10.3847/1538-4357/ac0efe. URL: http://dx.doi.org/10.3847/1538-4357/ac0efe.

[121] F. Aharonian and A. Neronov. „High-Energy Gamma Rays from the Massive Black Hole in the Galactic Center“. In: *The Astrophysical Journal* 619.1 (Jan. 2005), pp. 306–313. ISSN: 1538-4357. DOI: 10.1086/426426. URL: http://dx.doi.org/10.1086/426426.

[122] T. Lacroix, J. Silk, E. Moulin, and C. Bœhm. „Connecting the new H.E.S.S. diffuse emission at the Galactic Center with the Fermi GeV excess: A combination of millisecond pulsars and heavy dark matter?“ In: *Physical Review D* 94.12 (Dec. 2016). ISSN: 2470-0029. DOI: 10.1103/physrevd.94.123008. URL: http://dx.doi.org/10.1103/PhysRevD.94.123008.

[123] D. Hooper, I. Cholis, and T. Linden. „TeV gamma rays from Galactic Center pulsars“. In: *Physics of the Dark Universe* 21, 40 (Sept. 2018), p. 40. DOI: 10.1016/j.dark.2018.05.004. arXiv: 1705.09293 [astro-ph.HE].

[124] J. Dörner et al. „Impact of Anisotropic Cosmic-Ray Transport on the Gamma-Ray Signatures in the Galactic Center“. In: *The Astrophysical Journal* 965.2 (Apr. 2024), p. 180. DOI: 10.3847/1538-4357/ad2ea1. URL: https://dx.doi.org/10.3847/1538-4357/ad2ea1.

[125] S. Celli, A. Palladino, and F. Vissani. „Neutrinos and γ-rays from the Galactic Center Region after H.E.S.S. multi-TeV measurements“. In: *The European Physical Journal C* 77.2 (Feb. 2017). ISSN: 1434-6052. DOI: 10.1140/epjc/s10052-017-4635-x. URL: http://dx.doi.org/10.1140/epjc/s10052-017-4635-x.

[126] E. de Oña Wilhelmi et al. *The hunt of PeVatrons as the origin of the most energetic photons observed in our Galaxy*. 2024. arXiv: 2404.16591 [astro-ph.HE]. URL: https://arxiv.org/abs/2404.16591.

[127] Cherenkov Telescope Array Consortium et al. *Science with the Cherenkov Telescope Array*. 2019. DOI: 10.1142/10986.

[128] P. Abreu et al. *The Southern Wide-Field Gamma-Ray Observatory (SWGO): A Next-Generation Ground-Based Survey Instrument for VHE Gamma-Ray Astronomy*. 2019. arXiv: 1907.07737 [astro-ph.IM]. URL: https://arxiv.org/abs/1907.07737.

[129] A. Arbey and F. Mahmoudi. „Dark matter and the early Universe: A review“. In: *Progress in Particle and Nuclear Physics* 119 (July 2021), p. 103865. ISSN: 0146-6410. DOI: 10.1016/j.ppnp.2021.103865. URL: http://dx.doi.org/10.1016/j.ppnp.2021.103865.

[130] N. Aghanim et al. „Planck2018 results: VI. Cosmological parameters“. In: *Astronomy and Astrophysics* 641 (Sept. 2020), A6. ISSN: 1432-0746. DOI: 10.1051/0004-6361/201833910. URL: http://dx.doi.org/10.1051/0004-6361/201833910.

[131] P. Mróz et al. „Rotation Curve of the Milky Way from Classical Cepheids“. In: *The Astrophysical Journal Letters* 870.1 (Jan. 2019), p. L10. ISSN: 2041-8213. DOI: 10.3847/2041-8213/aaf73f. URL: http://dx.doi.org/10.3847/2041-8213/aaf73f.

[132] N. Aghanim et al. „Planck2018 results: I. Overview and the cosmological legacy ofPlanck“. In: *Astronomy and Astrophysics* 641 (Sept. 2020), A1. ISSN: 1432-0746. DOI: 10.1051/0004-6361/201833880. URL: http://dx.doi.org/10.1051/0004-6361/201833880.

[133] J. L. Feng. „Dark Matter Candidates from Particle Physics and Methods of Detection“. In: *Annual Review of Astronomy and Astrophysics* 48.1 (Aug. 2010), pp. 495–545. ISSN: 1545-4282. DOI: 10.1146/annurev-astro-082708-101659. URL: http://dx.doi.org/10.1146/annurev-astro-082708-101659.

[134] J. L. Feng. „The WIMP paradigm: Theme and variations“. In: *SciPost Physics Lecture Notes* (June 2023). ISSN: 2590-1990. DOI: 10.21468/scipostphyslectnotes.71. URL: http://dx.doi.org/10.21468/SciPostPhysLectNotes.71.

[135] L. Roszkowski, E.M. Sessolo, and S. Trojanowski. „WIMP dark matter candidates and searches—current status and future prospects“. In: *Reports on Progress in Physics* 81.6 (May 2018), p. 066201. ISSN: 1361-6633. DOI: 10.1088/1361-6633/aab913. URL: http://dx.doi.org/10.1088/1361-6633/aab913.

[136] J. Conrad. „Indirect Detection of WIMP Dark Matter: a compact review“. In: *arXiv e-prints*, arXiv:1411.1925 (Nov. 2014), arXiv:1411.1925. DOI: 10.48550/arXiv.1411.1925. arXiv: 1411.1925 [hep-ph].

[137] M. Cirelli et al. „PPPC 4 DM ID: a poor particle physicist cookbook for dark matter indirect detection“. In: *Journal of Cosmology and Astroparticle Physics* 2011.3, 051 (Mar. 2011), p. 051. DOI: 10.1088/1475-7516/2011/03/051. arXiv: 1012.4515 [hep-ph].

[138] C. A. Charbonnier, Combet, and D. Maurin. „clumpy: A code for γ-ray signals from dark matter structures“. In: *Computer Physics Communications* 183.3 (Mar. 2012), pp. 656–668. ISSN: 0010-4655. DOI: 10.1016/j.cpc.2011.10.017. URL: http://dx.doi.org/10.1016/j.cpc.2011.10.017.

[139] V. Bonnivard et al. „CLUMPY: Jeans analysis, γ-ray and ν fluxes from dark matter (sub-)structures“. In: *Computer Physics Communications* 200 (Mar. 2016), pp. 336–349. DOI: 10.1016/j.cpc.2015.11.012. arXiv: 1506.07628 [astro-ph.CO].

[140] M. Hütten, C. Combet, and D. Maurin. „CLUMPY v3: γ-ray and ν signals from dark matter at all scales“. In: *Computer Physics Communications* 235 (Feb. 2019), pp. 336–345. ISSN: 0010-4655. DOI: 10.1016/j.cpc.2018.10.001. URL: http://dx.doi.org/10.1016/j.cpc.2018.10.001.

[141] N. A. Kevork, A. Prateek, C. Zackaria, and K. Can. „Lower limits on the strengths of gamma ray lines from WIMP dark matter annihilation“. In: *Physical Review D* 85 (2012), p. 123543. DOI: 10.1103/PhysRevD.85.123543.

[142] H.E.S.S. Collaboration. *H.E.S.S. Publications*. Accessed: 2024-10-14. 2024. URL: https://www.mpi-hd.mpg.de/HESS/pages/publications/pubs_jour.shtml.

[143] H. Abdallah et al. „Search for Dark Matter Annihilations towards the Inner Galactic Halo from 10 Years of Observations with H.E.S.S.“ In: *Physical Review Letters* 117.11, 111301 (Sept. 2016), p. 111301. DOI: 10.1103/PhysRevLett.117.111301. arXiv: 1607.08142 [astro-ph.HE].

[144] H. Abdalla et al. „Search for Dark Matter Annihilation Signals in the H.E.S.S. Inner Galaxy Survey“. In: *Physical Review Letters* 129.11, 111101 (Sept. 2022), p. 111101. DOI: 10.1103/PhysRevLett.129.111101. arXiv: 2207.10471 [astro-ph.HE].

[145] A.U. Abeysekara et al. „A search for dark matter in the Galactic halo with HAWC“. In: *Journal of Cosmology and Astroparticle Physics* 2018.02 (Feb. 2018), pp. 049–049. ISSN: 1475-7516. DOI: 10.1088/1475-7516/2018/02/049. URL: http://dx.doi.org/10.1088/1475-7516/2018/02/049.

[146] M. Ackermann et al. „Searching for Dark Matter Annihilation from Milky Way Dwarf Spheroidal Galaxies with Six Years of Fermi Large Area Telescope Data“. In: *Physical Review Letters* 115.23 (Nov. 2015). ISSN: 1079-7114. DOI: 10.1103/physrevlett.115.231301. URL: http://dx.doi.org/10.1103/PhysRevLett.115.231301.

[147] M. Ackermann et al. „The Fermi Galactic Center GeV Excess and Implications for Dark Matter“. In: *The Astrophysical Journal* 840.1 (May 2017), p. 43. ISSN: 1538-4357. DOI: 10.3847/1538-4357/aa6cab. URL: http://dx.doi.org/10.3847/1538-4357/aa6cab.

[148] N. Aghanim et al. „Planck2018 results: VI. Cosmological parameters“. In: *Astronomy and Astrophysics* 641 (Sept. 2020), A6. ISSN: 1432-0746. DOI: 10.1051/0004-6361/201833910. URL: http://dx.doi.org/10.1051/0004-6361/201833910.

[149] M. Di Mauro and M.W. Winkler. „Multimessenger constraints on the dark matter interpretation of the Fermi-LAT Galactic center excess“. In: *Phys. Rev. D* 103.12 (2021), p. 123005. DOI: 10.1103/PhysRevD.103.123005. arXiv: 2101.11027 [astro-ph.HE].

[150] F. Calore et al. „AMS-02 antiprotons and dark matter: Trimmed hints and robust bounds“. In: *SciPost Physics* 12.5 (May 2022). ISSN: 2542-4653. DOI: 10.21468/scipostphys.12.5.163. URL: http://dx.doi.org/10.21468/SciPostPhys.12.5.163.

[151] I. Cholis, Y.-M. Zhong, S.D. McDermott, and J.P. Surdutovich. „The Return of the Templates: Revisiting the Galactic Center Excess with Multi-Messenger Observations“. In: *Phys. Rev. D* 105 (2022), p. 103023. DOI: 10.1103/PhysRevD.105.103023. arXiv: arXiv:2112.09706 [astro-ph.HE].

[152] A. Acharyya et al. „Sensitivity of the Cherenkov Telescope Array to a dark matter signal from the Galactic centre“. In: *Journal of Cosmology and Astroparticle Physics* 2021.1, 057 (Jan. 2021), p. 057. DOI: 10.1088/1475-7516/2021/01/057. arXiv: 2007.16129 [astro-ph.HE].

[153] A. Viana et al. „Searching for dark matter in the Galactic halo with a wide field of view TeV gamma-ray observatory in the Southern Hemisphere“. In: *Journal of Cosmology and Astroparticle Physics* 2019.12 (Dec. 2019), pp. 061–061. ISSN: 1475-7516. DOI: 10.1088/1475-7516/2019/12/061. URL: http://dx.doi.org/10.1088/1475-7516/2019/12/061.

Acknowledgements

I'm excited to get started on the last chapter of my thesis, which I'm sure will be the easiest for me because it's so obvious. I'd like to thank everyone who helped me get this far:

I'd like to start by thanking my supervisor, Christopher. Thanks for giving me the chance to work on this project and for always making time to talk through the issues and results along the way. You had a great deal of insight and were a huge help.

I'd also like to thank the diffuse emission group, especially Justine, Régis and Anne. It was a great experience working on this topic together and I learned a lot. And of course, Wun, thanks for all the work you've already put in and your help along the way while you were still here, and afterwards through your thesis, which I now know by heart.

I'd also like to thank the Gammapy development team for setting up the software and for all the feedback. Thanks also for letting me get my code into the official version and for giving me the chance to visit Sicily.

Thank to all the people who took the time to read some of this thesis and give me helpful feedback: Benedetta, Dima, Johannes, Pedro, Tina and Tim.
On this behalf, thanks to the whole gamma group for making the past few years so much fun. The corner office with lots of decorations, crafting, popcorn and stadt-land-fluss, the lunch breaks, all the time spent abroad during collaboration meetings and workshops and for everything else. It was a real pleasure working with such a friendly, helpful and funny group!

And of course, a big thanks to my parents. You have always believed in me, helped me and been there for me for as long as I can remember. I would not have made it to this point in my life without you.

I'd also like to thank the mystery-solving group, the physicists and the senior meeting. You made this physics study a lot more bearable. I don't know what I would have done without you (probably quit and finally get a backery). Thanks to the Homies, I love you and I am so happy for all of you to be part of my life for so long. Flo, thank you for the amazing years we've shared and for always being there for me, I am excited for what lies ahead. And finally, even though you can't read this, Trischie, thanks for making me go outside and for being the best dog on Earth.